Investigating correlated charge, lattice and spin degrees of freedom in layered perovskite ruthenates

विद्या वाचस्पति की उपाधि की अपेक्षाओं की आंशिक पूर्ति में प्रस्तुत शोध प्रबंध

A thesis submitted in partial fulfillment of the requirements of the degree of

Doctor of Philosophy

द्वारा / By

श्रुति चक्रवर्ती / **SHRUTI CHAKRAVARTY**

पंजीकरण सं. / Registration No.

20152041

शोध प्रबंध पर्यवेक्षक / Thesis Supervisor:

प्रो. सुनील नायर / **Prof. Sunil Nair**



भारतीय विज्ञान शिक्षा एवं अनुसंधान संस्थान पुणे

Indian Institute of Science Education and Research Pune

2024

©2024 -- SHRUTI CHAKRAVARTY
all rights reserved.

Dedicated to Savitrimai

and

my family.

Declaration

I declare that this written submission represents my ideas in my own words and where others' ideas have been included, I have adequately cited and referenced the original sources. I declare that I have acknowledged collaborative work and discussions wherever such work has been included. I also declare that I have adhered to all principles of academic honesty and integrity and have not misrepresented or fabricated or falsified any idea/data/fact/source in my submission. I understand that violation of the above will be cause for disciplinary action by the Institute and can also evoke penal action from the sources which have thus not been properly cited or from whom proper permission has not been taken when needed.

The work reported in this thesis is the original work done by me under the guidance of **Prof. Sunil Nair**.



Pune
February 4, 2025

Shruti Chakravarty
(Reg. No. 20152041)

Certificate

Certified that the work incorporated in the thesis entitled **"Investigating correlated charge, lattice and spin degrees of freedom in layered perovskite ruthenates"** submitted by **Shruti Chakravarty** was carried out by the candidate, under my supervision. The work presented here or any part of it has not been included in any other thesis submitted previously for the award of any degree or diploma from any other university or institution.



Pune
February 4, 2025

Prof. Sunil Nair
(Supervisor)

Acknowledgments

This thesis is truly a culmination of the steadfast support I have had the fortune to receive over the years. The first and foremost among them is my supervisor, *Prof. Sunil Nair*, who in 2015, had a fledgling neophyte knock on his door, never having worked in a materials lab or held a soldering gun, and yet agreed to accept her as his mentee. Almost a decade has passed since then, with him academically guiding me with patience and consideration. He supported me during times of immense distress and through losing close ones, something not usually on the job description of a PhD supervisor. He did that anyway, and I will forever be indebted for that. His friendly nature and wit ensured our communication remained transparent and open. He has let me learn and grow at my own pace while also nudging me in the right direction by pulling me out of my many local minima. I must also thank him for tolerating my (*often insufferable*) verbosity in speech and writing and always having my back despite all my shortcomings. Even though my time in Lab 211 comes to a close, I will always cherish my time as his graduate student.

I must also extend my heartfelt thanks to my Review Advisory Committee (RAC) members, *Prof. Surjeet Singh* and *Prof. Mukul Kabir*, for their continual support. Their valuable input during my routine RAC presentations was crucial in improving the quality of this work. I hope to continue actively collaborating with them throughout my academic career.

I would be remiss to not mention the women who have profoundly influenced the values I strive to embody as an academic. In my very first semester at IISER, *Dr. Suneeta Vardarajan*'s teaching left an indelible mark on me. It shaped my perspective of physics and left me with a permanent appreciation for the history of science. *Dr. Ashna Bajpai*, who, apart from giving me opportunities to participate in exciting collaborative projects very early on, has also been a constant source of support and encouragement. I hope to emulate her brilliant experimental insight and relentless drive as I make my way through academia. In my very first interaction with *Prof. Seema Sharma*, the coordinator of our lab course, instilled in me the value of speaking up and being unafraid of confrontation. Since then, she has continued to be a friend, often dropping dollops of encouragement in the soup of my life. I hope to carry forward all of these values.

A heartfelt thanks also to *Prof. Stephen Blundell*, who earlier this year, in a short yet significant conversation, rekindled a self-worth that had been stifled under disillusionment and cynicism.

Much of my PhD work required measurements performed at large-scale facilities like synchrotron and neutron beamlines, which would not have been possible without the technical support of the instrument scientists - *Dr. Arpan Bhattacharyya*, *Dr. Gangadhar Das*, *Dr. Pascal Manuel*, *Dr. Antonio Cervellini* and *Dr. Francois Fauth*. I also acknowledge the generous funding extended by DST, JNCASR, AOARD (AFRL), Infosys Foundation and I-Hub QTF, allowing me the privilege of performing experiments at some of these facilities and travelling to various conferences and workshops to build my academic network.

I must thank IISER Pune for providing outstanding research and residential infrastructure. I am especially thankful to the academic office, which is always available to help streamline various bureaucratic processes, be it coursework, international travel, or any other administrative matter. A special thanks to Prabhakar Sir and Dhanashree Ma'am, the backbone of the Physics department, who are always ready to assist students with a smile, no matter the issue. I would also like to extend my appreciation to the technical team at $\hbar$ - Nilesh Sir, Anil Sir, Sudhir Sir, and Karthikeyan - who consistently went above and beyond to keep our research going, spending countless hours troubleshooting and repairing instruments. Lastly, my gratitude goes out to the housekeeping staff, who worked tirelessly to ensure we had a safe and hygienic environment to work in - something that remains a privilege for many in our country.

I also extend my gratitude to the members of Lab 211, who taught me much of what I know today. My seniors - *Dr. Soumendranath Panja* and *Dr. Charu Garg* introduced me to my first lab skills - solid-state synthesis, magnetic and dielectric measurements, during instrumentation, discussions with *Dr. Avirup De* helped me immensely, and *Dr. Jitender Kumar* continues to hold his door open to answer my numerous queries to date. My special thanks to *Haritha SV* for her continued friendship, and her curiosity, which helped me become a better science communicator. I also thank my current labmates - *Anna M Francis*, *Rohit Mandlik*, *Harshdip Meshram*, *Dr. Vikram Singh* - for their warm companionship and support, and also all Lab 211 alums for making my extended time here so enjoyable and fruitful.

I am also thankful to all my iPhD 2015 batchmates for the fond memories of my time at IISER. Especially, *Dr. Avisikta Upadhyay*, who stuck around nearly every day and happily lent her ears to my generally morbid and nihilist take on life.

A special mention for *Tanvi Damle* and *Dr. Poorva Mehendale*, who pulled me out of rock bottom and without whom I might not be here.

Alina Suhail and *Ambika Srikrishnan* are the sisters I never had. Distance and (15+ years of) time have only made our hearts fonder. From teenage to adulthood, thank you for always being my ultimate cheerleader.

The three years I spent in Miranda House remain the peak of my life. It was here that I discovered my love for research, experiments, outreach, and writing. It would be an understatement to say that it was a transformative period of my life. It was there that I met *Dr. Pragya Chawla*, aka *my person* on the very first day of college. She and her sister, *Damini Chawla*, have generously opened their hearts and home to me year after year. *Your unwavering faith in me kept me going in the hardest times. And for that, and much much more, gamsahamnida. Jinjja neomu saranghamnida.*

When I joined IISER in 2015, I thought that my days of making friends who stick around for life were over. Who knew attending classes with the BS-MS batch of 2013 would make me a tetrahedral vertex? *Dr. Saurabh Kadam*, one of the most brilliant physicists I have known in life, is also an obsessive crackhead in his free time, and the latter is the true foundation of our friendship. Also covalently bonded to me is *Dr. Nandini Hazra*, who was often mistaken for me while at IISER (and vice versa). Between the two of us, there exists only one brain cell. Both *Nandini* and *Saurabh* are now indistinguishable from family, and I am immensely fortunate to have their friendship in my life. And finally, *Rajeev*, who has held my hand firmly through the 7+ years we have spent geographically apart. Even on my worst days, I have thought of you as the one thing I did right. *Thank you for sticking with me in sickness and health. I love you.*

Ultimately, it comes down to the reason I exist: my family. To my parents - who always prioritized my well-being and education above their own needs - *Mumma, Baba, thank you for always being in my corner*. To my grandparents - who were my first best friends and will forever be my core - *Dadu, Didu, and Thamma, even though you left this world before you could see me graduate, I hope you are having a gala time in the afterlife and will clink glasses when my grad life finally comes to an end. And Thakurdada, thank you for patiently waiting year after year for me to close this chapter and come back home to you. This is all for you. I hope I could make you proud.*

The unwavering support of all these people is the seed that has incrementally grown this crystal. And despite imperfections, it remains unyielding to discover its future.

Contents

1 Introduction **1**

1.1 Magnetism in Transition-Metal Oxides . . . 1

1.1.1 The Crystal Field . . . 1

1.1.2 Hund's coupling . . . 2

1.1.3 Spin orbit coupling . . . 3

1.1.4 Exchange . . . 5

1.1.5 Exchange Mechanisms . . . 6

1.1.5.1 Direct exchange and the hubbard model . . . 6

1.1.5.2 Superexchange . . . 8

1.1.5.3 Double Exchange . . . 9

1.2 Geometrical frustration . . . 9

1.3 Disorder . . . 10

1.4 The spin glass state . . . 11

1.5 The Perovskite structure . . . 11

1.5.1 Layered Perovskites . . . 14

1.5.2 Why Ruthenates? . . . 20

1.6 Orbital Molecules . . . 21

1.7 Motivation and plan of the thesis . . . 22

2 Instrumentation and Experimental Methods **24**

2.1 Solid-state synthesis . . . 25

2.2 X-Ray Diffraction . . . 26

2.2.1 X-ray Sources . . . 28

2.2.2 X-ray diffraction geometries . . . 28

2.2.3 X-ray Detectors . . . 29

2.2.4 Synchrotron x-ray sources and instruments . . . 30

2.2.4.1 BL-18B at Photon Factory, KEK (Japan) . . . 31
2.2.4.2 ADDAMS at SLS, PSI (Switzerland) . . . 31
2.3 Neutron scattering . . . 32
2.3.1 Nuclear scattering . . . 32
2.3.2 Magnetic scattering . . . 33
2.3.3 Neutron sources and instruments . . . 33
2.3.3.1 Reactor-based sources . . . 33
2.3.3.2 Spallation sources . . . 34
2.3.4 Neutron Powder Diffraction . . . 35
2.3.4.1 Constant wavelength diffraction . . . 35
2.3.4.2 time-of-flight diffraction . . . 35
2.4 Diffraction data analysis . . . 36
2.4.1 The Rietveld Method . . . 36
2.4.1.1 The reduced χ^2 . . . 38
2.4.1.2 The profile factor . . . 38
2.4.1.3 The weighted profile factor . . . 38
2.4.1.4 The expected weighted profile factor . . . 38
2.4.1.5 The Bragg R-factor . . . 39
2.5 Scanning Electron Microscopy and Energy Dispersive X-ray Spectroscopy . . . 40
2.6 Magnetometry . . . 41
2.6.1 Vibrating Sample and squid Magnetometry . . . 42
2.6.1.1 ac susceptibility . . . 43
2.7 Thermal and electronic transport . . . 44
2.7.1 Specific Heat . . . 44
2.7.2 Resistivity . . . 45
2.8 Broadband Dielectric Spectroscopy . . . 46
2.9 Instrumentation: Nonlinear Dielectric Susceptibility . . . 49
2.9.1 The Setup . . . 51
2.9.1.1 The lock-in amplifier, SR830 . . . 52
2.9.1.2 The current pre-amplifier, SR570 . . . 53
2.9.1.3 Temperature control and wiring . . . 54
2.9.1.4 Vacuum techniques . . . 56

2.9.1.5 Grounding 56

3 Ba_2CoRuO_6: A disorder-driven cluster glass **58**

3.1 Introduction 58
3.2 Synthesis and preliminary characterization 59
3.3 Crystal structure 60
3.4 The spin state of *Co* 62
3.5 Magnetic properties 64
3.5.1 dc magnetization 64
3.5.2 ac magnetic susceptibility 67
3.5.3 Thermoremnant magnetization 69
3.5.4 Aging, memory and rejuvenation 69
3.5.5 Exchange anisotropy 73
3.6 Influence of temperature on structure 73
3.7 Magnetic structure within the clusters 75
3.8 Electronic and thermal transport behaviour 77
3.8.1 Specific heat 77
3.8.2 Resistivity 78
3.9 Dielectric spectroscopy 79
3.10 Conclusions 80

4 Nonlinear dielectric response of $A_3M\mathrm{Ru_2O_9}$ (A = Ba, Sr), (M = Co, Bi, Ca) **81**

4.1 Introduction 81
4.2 Sample preparation 85
4.3 The Measurement Setup 85
4.4 Calibration 86
4.5 Nonlinear dielectric susceptibilities of $Ba_3CoRu_2O_9$ 88
4.6 Nonlinear dielectric susceptibilities of $Ba_3BiRu_2O_9$ 90
4.7 Nonlinear dielectric susceptibilities of $Sr_3CaRu_2O_9$ 93
4.8 Conclusion 96

5 Evolution of the magnetism in $Ba_4NaRu_3O_{12}$ **98**

5.1 Introduction . . . 98
5.2 Synthesis and preliminary characterization . . . 100
5.3 Crystal structure . . . 101
5.4 Magnetic properties . . . 104
5.5 Influence of temperature on structure . . . 108
5.6 Magnetic structure . . . 110
5.7 Electronic and thermal transport . . . 114
5.7.1 Specific Heat . . . 114
5.7.2 Resistivity . . . 116
5.8 Conclusions . . . 119

6 Summary and future scope **120**
6.1 Ongoing and future work . . . 122

Appendix A Solving magnetic structures using FULLPROF **126**
A.1 The structure above the transition . . . 126
A.2 Adding the magnetic phase . . . 128
A.2.1 How to find the *k-vector* . . . 128
A.3 Magnetic representation analysis . . . 129
A.3.0.1 step 1: SARAh Rep Analysis . . . 130
A.3.0.2 step 2: SARAh Refine . . . 130
A.3.1 Which IR describes the magnetic structure? . . . 131
A.3.2 for Ba_2CoRuO_6 . . . 133
A.3.2.1 Elements in the group G_0 . . . 136
A.3.2.2 Elements in the group G_k . . . 139
A.3.3 For $Ba_4NaRu_3O_{12}$ . . . 139
A.3.3.1 Elements in the group G_0 . . . 140
A.3.3.2 Elements in the group G_k . . . 142

Appendix B Microstructure Analysis in FULLPROF **144**
B.1 Contributions to broadening . . . 145
B.1.1 Optics . . . 145
B.1.2 Sample Geometry . . . 145

B.1.2.1 Intrinsic resolution of the detector 145
B.1.2.2 Capillary size 146
B.1.2.3 Wobbling 146
B.1.2.4 Axial divergence 146
B.1.3 Microstructure 147
B.1.3.1 Experimental Results for MYTHEN at SLS XRPD 147
B.2 Format of the `*.irf` file 149
B.2.1 Profile functions in `FULLPROF` and calculation of `Size` and `Strain` . . 150

References **186**

List of Tables

1.1 Classification of possible octahedral tilt systems in perovskites given by Glazer[1] . 13

3.1 Structural Parameters of Ba_2CoRuO_6 obtained from Rietveld refinement of the neutron diffraction pattern measured at 310K 62

3.2 Bond Angles and Lengths for Ba_2CoRuO_6 obtained from Rietveld refinement of neutron diffraction data collected at 310K 63

3.3 Summary of magnetic structure models obtained from refining neutron powder diffraction data measured at 1.7 K. 75

4.1 Structural parameters of the three compounds under investigation[2,3,4] 84

5.1 Lattice and structural parameters of $Ba_4NaRu_3O_{12}$ calculated from combined synchrotron x-ray and neutron powder diffraction. 104

5.2 Bond angles and lengths for $Ba_4NaRu_3O_{12}$ estimated from Rietveld refinement of neutron diffraction data collected at 300 K 105

5.3 The point symmetries and Shubnikov space groups associated with each basis vector calculated from the parent space group $P6_3mc$ with $\mathbf{k} = (0,\ 0,\ 0)$. . . . 111

5.4 Universality classes and their critical exponents[5] 115

A.1 Basis vectors for the space group $P6_3/mmc$ with $k = (\frac{1}{2},\ 0,\ 0)$.The decomposition of the magnetic representation for the $Co1$ site $(0,\ 0,\ 0)$ is $\Gamma_{Mag} = 1\Gamma_1^1 + 0\Gamma_2^1 + 2\Gamma_3^1 + 0\Gamma_4^1 + 1\Gamma_5^1 + 0\Gamma_6^1 + 2\Gamma_7^1 + 0\Gamma_8^1$. Atoms of the non-primitive basis are defined according to 1: $(0,\ 0,\ 0)$, 2: $(0,\ 0,\ \frac{1}{2})$. 134

A.2 Basis vectors for the space group $P6_3/mmc$ with $k = (\frac{1}{2},\ 0,\ 0)$. The decomposition of the magnetic representation for the Ru site $(\frac{1}{3},\ \frac{2}{3},\ 0.15561)$ is $\Gamma_{Mag} = 1\Gamma_1^1 + 2\Gamma_2^1 + 2\Gamma_3^1 + 1\Gamma_4^1 + 1\Gamma_5^1 + 2\Gamma_6^1 + 2\Gamma_7^1 + 1\Gamma_8^1$. The atoms of the nonprimitive basis are defined according to 1: $(\frac{1}{3},\ \frac{2}{3},\ 0.15561)$, 2: $(\frac{1}{3},\ \frac{2}{3},\ 0.65561)$, 3: $(\frac{1}{3},\ \frac{2}{3},\ 0.84439)$, 4: $(\frac{1}{3},\ \frac{2}{3},\ 0.34439)$. 136

A.3 Symmetry operators of the space group $P6_3/mmc$. The notations used are of the International Tables, where the elements are separated into rotation[6] and translation components, and the *Jones faithful representations*[7]. 138
A.4 Symmetry elements of the little group $G_{\mathbf{k}}$. The notations used are of the International Tables, where the elements are separated into rotation[6] and translation components, and the *Jones faithful representations*[7]. 139
A.5 Basis vectors for the space group $P6_3mc$ with $\mathbf{k} = (0,\ 0,\ 0)$. Decomposition of the magnetic representation for the sites $Ru1(\frac{1}{3},\ \frac{2}{3},\ 0.93858)$, $Ru2(0,\ 0,\ 0.32126)$, and $Ru3(0,\ 0, 0.18269)$ is $\Gamma_{Mag} = 0\Gamma_1^1 + 1\Gamma_2^1 + 0\Gamma_3^1 + 1\Gamma_4^1 + 1\Gamma_5^2 + 1\Gamma_6^2$ 140
A.6 Atoms of the nonprimitive cell of $Ba_4NaRu_3O_{12}$ 140
A.7 Symmetry operators of the space group P 63 m c. The notations used are of the International Tables, where the elements are separated into rotation[6] and translation components, and the *Jones faithful representations*[7]. 142
A.8 Symmetry elements of the little group $G_{\mathbf{k}}$. The notations used are of the International Tables, where the elements are separated into rotation[6] and translation components, and the *Jones faithful representations*[7]. 143

B.1 Si refinement values[8] 147
B.2 NAC refinement values[8] 148
B.3 Size and microstrain parameters in FULLPROF 153
B.4 Models for Anisotropic Size broadening 155
B.8 Models for Anisotropic Strain broadening 158

List of Figures

1.1 The splitting of *d* orbitals in presence of an octahedral (left) and tetrahedral (right) crystal field. 2

1.2 The superexchange mechanism. Examples of orbital symmetries when (a), (b) antiferromagnetic, and (c), (d) ferromagnetic coupling is favoured. 8

1.3 The double exchange mechanism. The AFM case is restricted by Hund's first rule. 9

1.4 Various types of geometrically frustrated lattices and their possible ground states 10

1.5 The octahedral tilt systems $a^0a^0a^0$, $a^0a^0c^+$ and $a^0a^0c^-$ in perovskite structures. . 12

1.6 The perovskite crystal structure in (a) 3C, (b) 4H, (c) 6H and (d) 9R variants . 14

1.7 The various types of A- and B-site cation order possible in ideal double perovskite structure 15

1.8 (a) 6H structure of $A_3BB'2O_9$ with face and corner-shared octahedra, (b) A-site orderings in $AA'_3B_4B_{12}$ and (c) $A_2A'A''B_4B_{12}$ quadruple perovskite systems (Reproduced from A. Belik[9] with permission from the Royal Society of Chemistry) (d) Crystal structure of $A_4B'B_3O_{12}$ showing the B_3O_{12} trimers found in B-site substituted quadruple perovskites. 16

1.9 The various types of antiferromagnetic order found in (a) layered and (b) simple perovskites. 19

2.1 (a) A typical synthesis protocol. (b) Construction of a KBr press. 25

2.2 A crucible (with lid) containing the sample is placed in a larger one, covered from top by another crucible and the edges are packed by filling in a non-reactive oxide (MgO/Al_2O_3). 26

2.3 Bragg Diffraction 28

2.4 (a) The reflection (Bragg-Brentano) diffraction geometry. (b), (c) The transmission (Debye-Scherrer) diffraction geometry. 29

2.5 Layout of the two sources at Photon Factory (KEK, Japan) showing the electron storage rings and the placement of various beamlines (BLs). Image source: KEK-IMSS Website[10]. Copyright KEK IMSS. 30
2.6 Left: The Versatile Hard x-ray station (BL-18B) at Photon Factory, KEK (Japan). Right: Sample stage used for PD experiments. Image source: SINP Website[11]. Copyright SINP. 31
2.7 The PD setup at ADDAMS. (a) Robotic sample changer holding a capillary (b) Zoomed view of sample holder aligned with the diffractometer axis (c) the MYTHEN detector - 1: detector modules, 2: He-filled housing, 3: multi-crystal analyzer detector, 4: diffractometer center, 5: x-ray beam tube. Images reproduced with permissions[12,8]. Copyright IUCr Journals. 32
2.8 (a) The spallation process of neutron production (b) Instrument layout of the ISIS Neutron and Muon Source with the location of WISH circled. Image source:[13] 34
2.9 (a) Schematic of a SEM. (b) Origins of backscatter and secondary electrons, and characteristic x-rays due to electron-matter interaction. (c) An FESEM images showing μm sized hexagonal crystallites within $Ba_4LiRu_3O_{12}$ under a primary electron beam energy of 20 keV. 41
2.10 B, H and M field lines in- and outside a bar magnet. Attribution: Geek3, VFPt magnets BHM, adapted for this thesis, License: CC BY-SA 4.0 42
2.11 (a) Schematic of the QD MPMS-XL SQUID Magnetometer (b) Schematic of a longitudinal SQUID system and a typical measured SQUID response 43
2.12 An ac-χ measurement being performed on Ba_2CoRuO_6 using the MPMS-XL . 44
2.13 Schematic showing the (a) side and (b) top-view of the QD PPMS heat capacity puck. 45
2.14 (a) A schematic showing the measurement of sheet resistivit of a sample in the four-probe method. (b) Sample stage and probe end of the resistivity option from CRYOGENICS LTD. Image source: CFMS Brochure[14] (c) Image of samples loaded onto the PPMS puck with gold wire and silver paste contacts. 46

2.15 (a) The Alpha-A mainframe front panel. The GEN channel is the signal generator output, sent to the sample via the ZG4 interface (b) The ZG4 test interface. The sample leads are connected to the BNC inputs I high and I low on the front panel. The V1 and V2 rear panel outputs are connected to the mainframe V1 and V2 analyzer inputs. (c) The circuit schematic for an impedance measurement[15] 48
2.16 A schematic of the custom-built setup for measuring nonlinear dielectric susceptibility $\chi_{n>1}$ 51
2.17 Snippets of the LabVIEW program front panel 52
2.18 Block diagram of a (a) functional SR830 LIA[16] and (b) SR570 pre-amplifier[17]. The (c) current and (d) gain characteristics of SR570 in the low-noise mode[18]. . 54

3.1 (a) Hexagonal perovskite structure of Ba_2CoRuO_6 showing the face- and corner-sharing octahedra with Co/Ru site-disorder, (b) the buckled honeycomb layers formed by the Co and Ru octahedra in the ab-plane, (c) intra- and inter-dimer bond lengths and angles 60
3.2 Constant wavelength (CW) neutron powder diffraction pattern obtained at 310 K and a fit to the structural model given in Table 3.1 using Rietveld method. Open circles are the experimental data, solid red line is the calculated pattern, blue line shows the difference curve and green ticks mark the Bragg positions expected for the space group $P6_3/mmc$. 61
3.3 Room temperature synchrotron x-ray powder diffraction patterns fitted to the structural model refined using the Rietveld method. 61
3.4 dc magnetic susceptibility (χ_{dc}) data from $T = 5 - 330$ K measured under an external magnetic field, $H = 5$ kOe showing irreversibility below 47 K. Inset shows χ_{dc} measured at low-field H = 20 Oe showing the onset of correlations ~ 280 K. 65
3.5 Left: Linear fits attempted for inverse susceptibility $\chi^{-1}(T)$ in various temperature ranges. Right: Variation in fit parameters and derived values of Curie constant (C) and Curie-Weiss temperature θ_{CW} with fitting range. 66

3.6 Linear magnetization isotherms $M(H)$ for $T \geq 150$ K without any signs of saturation. Development of an S-shaped curvature and a finite hysteresis loop below 47 K, indicating the presence of finite ferromagnetic correlations. 66
3.7 (a) Real part of $\chi_{ac}(T)$ showing a dispersive cusp below 60 K. Inset shows the variation of the cusp temperature ($10^3 T_f^{-1}$) with $\ln\tau$. (b) shows a non-linear (NL) curve fit to the VFT equation and the inset shows the linear scaling done using T_0 returned by the NL fit, (c) shows the fit to mean-field power law model and the inset shows the excellent fit to the linearized plot. 68
3.8 The thermal evolution of thermoremnant magnetization ($M_{TRM}(T, H = 0)$) measured for different cooling fields. The inset shows the same data as a semi-log plot, highlighting the slope change seen close to room temperature. 69
3.9 Left: The FC memory effect observed at $T = 28$ K with a waiting time of 6 hours and applied magnetic field of 100 Oe. Right: The ultrametric order in the spin glass phase space. Reproduced with permission from Springer Nature[19]. 70
3.10 Aging behaviour of Ba_2CoRuO_6. The isothermal remnant magnetization $-M_{IRM}(t)$ plotted against t for (a) different waiting periods t_w at $T = 10$ K and $H = 250$ Oe, (c) different fields at $T = 10$ K and $t_w = 100$ s, and (e) different fields at $T = 30$ K and $t_w = 100$ s. Solid lines show fits to the modified stretched exponential function. The derivative of $-M_{IRM}(t)$ shown in (a), (c) and (e) with respect to t is shown in (b), (d) and (f), respectively. Insets of (d) and (f) show the (lack of) dependence of t_w^{eff} on H. 72
3.11 The field dependence of the cusp in static χ_{ZFC} . The inset shows the nonlinear fit to $T_f(H)$ using eq.3.7 74
3.12 The c/a ratio as a function of temperature showing two distinct features across T_N and 250 K. 74
3.13 CW NPD data collected at 1.7 K showing presence of additional magnetic peaks (marked by $*$). Solid lines show fits to these peaks corresponding to three different irreps: Γ1, Γ5, and Γ7. 76
3.14 Magnetic structure within frozen antiferromagnetically correlated spin clusters corresponding to irreps (a) Γ3 and (b) Γ7. 76

3.15 (a) The featureless molar heat capacity $C_P(T)$ shown upto 100 K, (b) $\frac{C_P}{T^3}$ vs T showing a strong upturn at low-temperatures. Inset: linear fit to $\frac{C_P}{T}$ vs T^2 showing the low-temperature deviation from the Debye Law. 77
3.16 Left: Temperature dependence of resistivity ρ. The inset shows a zoomed view of the feature close to T_f. Right: The 3D VRH model fit to $\ln\rho$ vs $1/T^{1/4}$. . . . 79
3.17 Dielectric loss tangent $\tan\delta = \varepsilon''/\varepsilon'$ plotted as a function of T for frequencies $f = 333$ Hz - 1 MHz 79

4.1 The room temperature crystal structures of (a) $Ba_3CoRu_2O_9$, (b) $Ba_3BiRu_2O_9$, and (c) $Sr_3CaRu_2O_9$ 84
4.2 Temperature dependence of real (left) and imaginary (right) parts of fundamental susceptibility χ_1 of KDP (KH_2PO_4). Both the discontinuous FE transition and the shoulder peak associated with the domain freezing are measured, attesting to the accuracy of the setup. 86
4.3 The nonlinear dielectric response of KDP (a) Real part of $\chi_2'(T)$ for KDP. Polarization remains negative throughout for all frequencies except 13.3 kHz. (b) Real part of $\chi_3'(T)$ for KDP. The first-order FE transition as well as the domain freezing process are captured. (c) Scaled nonlinear susceptibility a_3 of KDP as a function of temperature. Arrows mark the two distinct features. Frequency dispersion is present for $T < 70$ K. $a_3 < 0$ for all temperatures. 87
4.4 Fundamental and first harmonic dielectric response of $Ba_3CoRu_2O_9$. (a) $\chi_1'(T)$ plotted for various frequencies on a log scale. The magnetoelastic transition is captured as a distinct slope changed marked by the dashed line. For $T > 150$ K, the dielectricity is lost as conduction effects become dominant. (b) $\chi_2'(T)$ for various frequencies plotted on a log scale. P drops sharply above 100 K and shows intense frequency dependence. Beyond 150 K, conduction effects dominate. . . 89
4.5 The second harmonic dielectric response of $Ba_3CoRu_2O_9$. (a) $\chi_3'(T)$ plotted for frequencies 1.3 - 33.3 kHz in log scale. χ_3' falls sharply above 100 K with similar dynamics as χ_2'. Inset shows the variation of τ with the temperature corresponding to χ_3 (negative) peaks. The dotted line is a guide to the eye. (b) Log of the absolute nonlinear susceptibility, $\log|a_3(T)|$ plotted for frequencies 1.3 - 33.3 kHz. Dashed arrows mark the transition temperatures 90

4.6 Linear dielectric response of $Ba_3BiRu_2O_9$. (a) $\chi_1'(T)$ plotted for various frequencies on a log scale. χ_1' sharply drops to negative values close to 175 K due to conduction. Feature below 100 K is most pronounced at 33.3 kHz and is suppressed at lower frequencies. (b) Derivative $d\chi_1'/dT$ plotted as a function of temperature for frequencies 0.3 - 33.3 kHz to discern the spin-gap opening transition. (c) Zoom-in of $d\chi_1'/dT$ at $f = 33.33$ kHz showing the slope change marking the spin-gap transition. (d) relaxation below 100 K seen to follow an exponential T-dependence. 91

4.7 First harmonic response of $Ba_3BiRu_2O_9$. (a) $\chi_2'(T)$ is plotted for frequencies 1.3 - 33.3 kHz. Three features are noticeable: peak → dip → peak ($T_{P1} \rightarrow T_{dip} \rightarrow T_{P2}$) shown with arrows. (b) Critical slowing down behavior followed by $\tau(T_{P1})$ (c): linearity in $\ln\tau$ vs $\ln(T_{P1}/T_0\text{-}1)$ confirming the validity of the nonlinear fit. (d) Relaxation process across T_{dip}, dotted lines are only a guide to the eye (not a fit) 92

4.8 Second harmonic response of $Ba_3BiRu_2O_9$. (a) $\chi_3'(T)$ as a function of temperature for various frequencies in the temperature range 75 - 190 K. The coexistence of two types of relaxation processes is captured in the dynamics of the two observed features. The inset shows τ plotted as a function of T_1 and T_2. 93

4.9 The fundamental and first harmonic response of $Sr_3CaRu_2O_9$. (a) $\chi_1'(T)$ is shown for frequencies 0.3 - 33.3 kHz. The sharp feature (T_dip) corresponding to the magnetic transition at ~ 160 K. (b) $\chi_2'(T)$ for frequencies 0.3 - 33.3 kHz. Inset: zoomed view of $T < 150$ K, highlighting the small frequency-dependent negative polarization observed before $\chi_2'(T)$ rose sharply. 94

4.10 (a) Second harmonic response of $Sr_3CaRu_2O_9$. (a) $\chi_3'(T)$ measured at frequencies 0.3 - 33.3 kHz. Inset: zoomed view of $T < 150$ K, highlighting the minuscule magnitude of χ_3 maxima on a positive scale, (b) The scaled nonlinear susceptibility, $a_3(T)$ shown for frequencies 0.3 - 33.3 kHz. Horizontal dotted lines show the position of zero for each curve. 95

5.1 Formation of molecular orbitals in a (a) $Ru_2^{5+}O_9$ dimer, and (b) a $Ru_3^{4+}O_{12}$ trimer. The structural geometry of the dimer/trimer and the hopping within the a_{1g} (bottom) and e_g (top) orbitals is also shown. 99

5.2 FESEM image $Ba_4NaRu_3O_{12}$ showing micron-sized hexagonal crystallites. . . . 100
5.3 Room temperature synchrotron XRD (top) and neutron (bottom) powder diffraction patterns of $Ba_4NaRu_3O_{12}$ refined using FULLPROF SUITE[20] 102
5.4 (a) Crystal structure of $Ba_4NaRu_3O_{12}$. The triangular network formed in the ab-plane by (b) Ru1/Na and (c) Ru2/Ru3 ions viewed along the *c*-axis. (d) The 8-layered unit cell viewed along the *a*-axis, (e) Bond lengths and angles of the exchange path calculated from at room temperature neutron diffraction data. . 103
5.5 Magnetic Properties of $Ba_4MRu_3O_{12}$ (a) dc Molar susceptibility χ_{mol} measured as a function of T in ZFC, FCC and FCW protocols. The temperature derivative $d\chi_{mol}/dT$ shows the antiferromagnetic transition at $T_N \sim 265$ K along with other subtler features within the AFM phase. (b) Curie-Weiss fit to the inverse magnetic susceptibility ($\chi^{-1}_{mol}(T)$) 106
5.6 (a) $M(H)$ isotherms measured in the range [-8 T, 8T] for 8 temperatures between 2 - 400 K, (b) - (i) show low field regions showing a finite loop and low-field features, insets of (b) and (c) show dM/dH in the H range [-8 T, 8 T] and (l) for $H \in$ [-0.1 T, 0.1 T], (j) and (k) show the coercivity (H_c) and Retentivity (or Remnant Magnetization, M_R) as function of temperature. 107
5.7 Thermal evolution of (a) lattice constants a, c and the unit cell volume (obtained from NPD) and (b) the axial ratio c/a obtained from SXRD. 108
5.8 Thermal variation of the (a,b) Ru3—O, (c,d) Ru2—O and (e,f) Ru1—O bond lengths. The colors of the curves correspond to the color coding on the pictorial representation of the octahedral bonds. T dependence of the (g) inter- and (h) intra-dimer Ru—O—Ru bond angles. 109
5.9 (a) T dependence of the Ru-Ru bond lengths. (b) Variation in maximum strain (%) calculated from synchrotron XRD microstructure analysis with Temperature 109
5.10 Additional reflections observed in NPD at $T = 13$ K corresponding to the magnetic structure. 110
5.11 (a) The A-type AFM structure of $Ba_3NaRu_3O_{12}$ at 13 K. (b) The staggered arrangement of the Ru1 triangular layers, AFM coupled to each other along *c*. (c) The cubic packing of the Ru2,3 dimers - characterized by intra-dimer and interlayed AFM coupling. Both sublattices are intra-layer FM coupled. 112

5.12 Rietveld fit of the IR Γ_4 magnetic model to neutron powder diffraction data collected at 13 K. 113
5.13 Increase in moment values with decreasing temperature 114
5.14 (a) Temperature dependence of specific heat capacity of $Ba_4NaRu_3O_{12}$ in the vicinity of T_N. Inset (i) shows $C_P(T)$ for the whole T range (2 - 300 K) and inset (ii) shows a plot of C_P vs T^3 showing the range of temperatures for which the Debye term is dominant. (b) A plot of C_P/T vs T^2 with the linear fit along with the parameters obtained from the fit. (c) A graph showing the variation in C_P/T^3 as a function of T. 116
5.15 Transport behaviour of $Ba_4NaRu_3O_{12}$. (a) ρ vs T, showing a semiconducting behaviour, and the derivative $d\rho/dT$ shows the discontinuity at T_N. (b) Linear fit to $\ln\rho$ vs $10^3/T$ for $T > T_N$. Insets show the deviation from linearity and the sharp change in the slope below T_N. (c) Linear fit to the Efros-Shklovskit Variable Range Hopping (ES-VRH) model below T_N. 117
5.16 (a) log-log plot of $d(ln\rho)/d(ln(1/T))$ showing the two distinct transport regimes characterized by different slopes (p). (b) $\ln\rho$ vs $100/T^{0.642}$ yielding an improved linear fit with a lower T_0 118

6.1 (a) Powder x-ray diffraction of $Ba_4LiRu_3O_{12}$ at room temperature compared to a simulated 6H structure (using vesta). (b) DC magnetization measurements showing magnetic irreversibility below 100 K. 123
6.2 (a) Le-Bail fit performed on the room temperature XRD pattern to a hexagonal unit cell in space group $P6_3/mmc$ for $Ba_4MgRu_3O_{12}$. (b) Powder x-ray diffraction of $Ba_4ZnRu_3O_{12}$ at room temperature compared to a simulated 6H structure (using VESTA) 123
6.3 DC Magnetization measurements on (a) $Ba_4MgRu_3O_{12}$ and (b) $Ba_4ZnRu_3O_{12}$ showing absence of any paramagnetic region and a dimer-like susceptibility. . . 124
6.4 Additional reflections at low temperature corresponding to the magnetic structure at 8 K observed in NPD data. 125

A.1 `.pcr` file format for WISH 127
A.2 SARAH Refine dialogue box with a `.mat` file loaded showing the basis vectors resulting from the representation analysis. 130

A.3 The `.pcr` file output by SARAh 131
A.4 Magnetic moment values obtained from `FPStudio` for a given refined Γ 133

B.1 Refinement of Si NIST 640C using `FULLPROF`. Reproduced with permission from Bergamaschi et al., 2010[8]. Copyright IUCr Journals. 147
B.2 WPPM of $Na_2Ca_3Al_2F_{14}$ (NAC) using `FULLPROF`. Reproduced with permission from Bergamaschi et al., 2010[8]. Copyright IUCr Journals. 148
B.3 IRF measured using NAC for a 0.2 mm capillary at 25 keV[8] 148
B.4 Format of `.irf` files provided in `FullProf_Suite` folder 149
B.5 Profile fitting dialogue box in `WinPLOTR` for manually creating an IRF file . . . 150
B.6 Format of `.irf` file generated using `WinPLOTR` 150

Thesis advisor: Prof. Sunil Nair Shruti Chakravarty

Investigating correlated charge, lattice and spin degrees of freedom in layered perovskite ruthenates

ABSTRACT

This thesis explores the magnetic and dielectric properties of B-site substituted perovskite systems, specifically double-, triple-, and quadruple-perovskites, with an emphasis on ruthenium-based compounds. Perovskite oxides with ABO_3 crystal structure, are well-known for their diverse physical and chemical properties, owing to their immense flexibility in accommodating a majority of elements in the periodic table as A- and B-site substitutions. These alterations can modify the structural geometry from the ideal cubic form, affecting various properties, including magnetism. In particular, the study focuses on systems with A = Ba/Sr and B = Ru, investigating how the arrangement of corner- and face-shared octahedra influences their magnetic interactions.

Ruthenium-based perovskites are of great interest due to the plethora of unexpected physics they exhibit, such as quantum critical behavior[21], unconventional superconductivity[22], and altermagnetism[23]. Ruthenium, with its 4*d* orbital character, has notable spin-orbit coupling (SOC) and spatially extended orbitals that enhance the exchange interactions and orbital overlap, resulting in complex magnetic behaviors.

We employ a range of experimental techniques, including x-ray and neutron powder diffraction, magnetometry, electronic and thermal transport, and linear and nonlinear dielectric susceptibility measurements, in order to investigate these materials. Additionally, we detail the construction and functioning of a homemade automated dielectric susceptometer which allows us to explore the multifunctionality of these materials at criticality.

The first section focuses on Ba_2CoRuO_6 (BCRO), a double-perovskite system which structurally mimics its triple-perovskite sibling. The presence of significant antisite disorder (about 30%) on the metal sites located within the face-shared octahedra, combined with the geometrically frustrated hexagonal structure, prevents long-range magnetic ordering. Instead, BCRO exhibits a cluster-glass (CG) ground state below $\sim$43 K, characterized by classic glassy behaviour such as frequency-dependent ac-susceptibility, ageing, and memory effects. These features differentiate BCRO from typical spin-glass systems. The presence of exchange anisotropy leads to locally dominant antiferromagnetic spin clusters, which persist even at high temperatures, as demonstrated

by the absence of a pure paramagnetic behaviour in susceptibility measurements.

In the second section, the nonlinear dielectric properties of three triple-perovskite ruthenates - $Ba_3CoR_2O_9$, $Ba_3BiRu_2O_9$, and $Sr_3CaRu_2O_9$ - are explored. These materials show significant coupling between their spin, charge, lattice, and polar degrees of freedom. For instance, $Ba_2CoRu_2O_9$ exhibits a frequency-dependent relaxation in $\chi_{2,3}$ just above a magneto-elastic transition around 100 K, followed by a loss of polarization. $Ba_2BiRu_2O_9$ displays a more complex relaxation behavior, strongly influenced by the spin-gap opening at 175 K. Meanwhile, $Sr_2CaRu_2O_9$ shows strong dispersion effects around its magnetic transitions, highlighting a robust interaction between magnetic and dipolar orders. The study of higher-order susceptibilities provides deeper insights into these systems' dynamics, revealing information that is otherwise masked in the linear polarization responses alone.

The final section examines the quadruple-perovskite $Ba_4NaRu_3O_{12}$, which exhibits a spin-lattice coupled ground state with long-range magnetic order below 257 K. The magnetic properties of this system are strongly influenced by its structural motif, where RuO_6 octahedra are linked to Ru_2O_9 dimers, separated by nonmagnetic NaO_6 layers. Neutron diffraction at 13 K reveals antiferromagnetic order, with Ru2 and Ru3 dimer moments oppositely aligned, while the Ru1 triangular layers show a staggered arrangement along the c-axis. Specific heat measurements reveal a boson peak contribution associated with optical modes at low temperature, with a maximum vibrational energy of around 55 cm^{-1}. Charge transport below the magnetic transition follows a variable-range hopping (VRH) mechanism, though the power law energy dependence of the Coulomb gap with an exponent > 2 suggests the presence of multiparticle correlation effects.

Overall, this work provides an in-depth exploration of the magnetic and dielectric properties of B-site substituted perovskites, highlighting the complex interplay of spin, charge, and lattice degrees of freedom in these systems. The findings underscore the richness of ruthenium-based perovskites in hosting diverse and unconventional physical phenomena.

Science, my lad, is made up of mistakes, but they are mistakes which it is useful to make, because they lead little by little to the truth.

Jules Verne

1 Introduction

1.1 Magnetism in Transition-Metal Oxides

Transition Metals (TM), which make up the *d*-block (groups 3-12) of the periodic table are progenitors of some of the most interesting magnetism studied by humans. The word *magnet* itself owes its etymology (from *magnētis lithos* (Greek), "the Magnesian stone") to the discovery of magnetite (Fe_3O_4) - a transition-metal oxide. Their unique ability to have multiple stable oxidation states, along with their frequent defiance of established chemical rules (e.g. Madelung rule) - allows them to bond with a variety of anions (ligands) and show complex (and colourful) chemistry and physics. Origins of magnetic properties in materials are traced back to this block. Elements with partially filled *d* shells i.e. the unpaired electrons residing in the valence *d* orbitals are the source of magnetism.

1.1.1 The Crystal Field

The interesting properties of TMs is observable when they are placed in a local environment which perturbs their otherwise degenerate valence orbitals and promotes a preferential electron filling - paving the way for intra-ion inter-orbital transitions which can be detected. This environment, called the *crystal field* is defined by the geometry in which negatively charged ions are

placed around the TM, each of them exerting a finite electrostatic field at the central cation (due to the repulsion between the electrons in the anion *p*-orbitals and the cation *d*-orbitals). As a result, the *d*-orbitals lose their degeneracy and are split by an energy difference called the *crystal field splitting energy*. This interaction disproportionally affects the *d* orbitals due to their pronounced angular dependence (shown in Fig. 1.1). The most common crystal field symmetries encountered in oxides are the octahedron (where the TM sits at the centre of 6 negatively charged O^{2-}) and the tetrahedron (TM at the centre of 4 O^{2-}). The octahedral environment has a cubic symmetry which raises the $d_{x^2-y^2}$ and $d_{z^2-r^2}$ orbitals (called the doubly-degenerate e_g or $d\sigma$ manifold), and lowers the energy states d_{xy}, d_{yz} and d_{zx} (the triply-degenerate t_{2g} or $d\varepsilon$ manifold). The difference between them is 10 Dq, the crystal field splitting energy. The situation is reversed in case of a tetrahedra, as shown in Fig. 1.1. The tetrahedral splitting energy (Δ_t) is related to the octahedral splitting energy (Δ_o) by the relation $\Delta_t = \frac{4}{9}\Delta_o$.

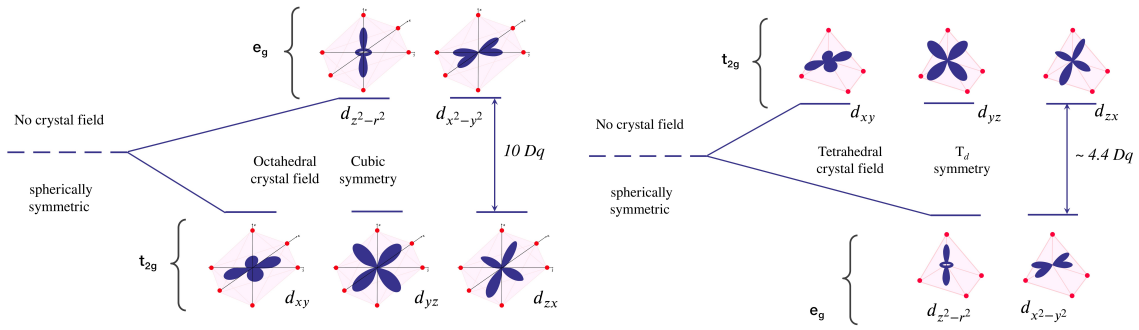


Figure 1.1: The splitting of *d* orbitals in presence of an octahedral (left) and tetrahedral (right) crystal field.

An important consequence of placing the TM ion in a crystal field is the quenching of orbital angular momentum ($\boldsymbol{L}$). This happens because when the imaginary $\boldsymbol{L}$ operator ($= -i\hbar\boldsymbol{r}\times\frac{\partial}{\partial\boldsymbol{r}}$) acts on the real eigenfunctions of the Schrödinger's equation ($\boldsymbol{\Psi}$), the expectation value $\int \boldsymbol{\Psi}^*(\boldsymbol{r})\boldsymbol{L}\boldsymbol{\Psi}(\boldsymbol{r})\mathrm{d}^3\boldsymbol{r} = 0$, due to the requirement that the diagonal part of a Hermite operator $\boldsymbol{L}$ must be real[24]. Thus, in absence of strong spin-orbit coupling (SOC), a TM ion's magnetic moment μ can be approximated to its spin-only value.

1.1.2 Hund's coupling

The Hund's coupling rules govern an atom's electronic configurations, and by extension, their electronic and chemical properties when placed in an external environment. The rules say:

1. *Maximize S*. Hund's first rule requires that the energy levels of an atom are filled in a way such that the total spin angular momentum S is maximized. In other words, the lowest energy configuration is given by the maximum number of unpaired electrons. The basis of this rule lies in the energy cost that Coulomb repulsion extracts when 2 electrons occupy the same energy state, i.e. Pauli's exclusion principle.
2. *Maximize L*. For a given S, the total energy is minimized when the total angular momentum L is maximized.
3. *J and the valency*. For a given electronic configuration, the lowest lying energy state is the one with lowest J if the outermost subshell is $\leq$ half-filled, and with maximum J if it is more than half-filled.

These rules are valid in the $L-S$ coupling regime when SOC for a given atom is weak, and L and S are still good quantum numbers. When SOC is strong, $J = L + S$ is considered instead.

The Hund's coupling competes with the crystal field energy to decide the ground state electronic configuration of the TM ion. When the crystal field splitting is small in comparison to the Hund's coupling energy, high-spin (HS) configurations are favored, whereas when the split between e_g and t_{2g} levels is large, it is energetically favorable for electrons to completely fill the low-lying states first, and thus yielding low-spin (LS) configurations.

When writing the Hamiltonian $\mathcal{H}$ for a real material, the Hund term ($\sim$ 1 eV in TMOs) encapsulates the interactions between two electrons in distinct orbitals but of the same ion, and favors parallel alignment of spins. This term results gives the atomic multiplet structure as well as ferromagnetic coupling in metallic TMOs.

1.1.3 Spin orbit coupling

Spin-orbit coupling is a relativistic quantum-mechanical interaction between a particle's spin (the spin angular momentum **S**) and its orbital motion (the orbital angular momentum **L**) - which causes otherwise degenerate energy levels (especially those near the Fermi level) to split. The underlying mechanism of the phenomenon involves two aspects - the apparent magnetic field observed from the particle's perspective, due to special relativity, and the magnetic moment of the particle ($\boldsymbol{\mu}$). An electron orbiting a nucleus, experiences a magnetic field in its rest frame which can be written as

$$\mathbf{B} = -\frac{\mathbf{v}\times\mathbf{E}}{c^2} = \frac{1}{m_e e c^2}\frac{1}{r}\frac{\partial U(r)}{\partial r}\mathbf{L} \tag{1.1}$$

implying that the field is parallel to **L** and perpendicular to the electron motion. The spin magnetic moment of the electron is

$$\boldsymbol{\mu}_{\mathbf{S}} = -g_s \mu_B \frac{\mathbf{S}}{\hbar} \tag{1.2}$$

whose energy (E) in presence of an external magnetic field (**B**) is given by $E = \boldsymbol{\mu} \cdot \mathbf{B}$. Here g_s is the electron spin g-factor and μ_B is the Bohr magneton. This results in the total spin-orbit interaction energy of the form

$$E \approx \frac{\mu_B}{\hbar m_e e c^2} \frac{1}{r} \frac{\partial U(r)}{\partial r} \mathbf{L} \cdot \mathbf{S} \tag{1.3}$$

As mentioned in Section 1.1.2, L and S are not good quantum numbers in presence of SOC and so the total angular momentum $\mathbf{J} = \mathbf{L} + \mathbf{S}$ needs to be considered instead.

$$\Rightarrow \mathbf{J} \cdot \mathbf{J} = \mathbf{J}^2 = \mathbf{L}^2 + \mathbf{S}^2 + 2\,\mathbf{L} \cdot \mathbf{S} \tag{1.4}$$

And since **L** and **S** commute,

$$\mathbf{L} \cdot \mathbf{S} = \frac{1}{2}(\mathbf{J}^2 - \mathbf{L}^2 - \mathbf{S}^2) \tag{1.5}$$

$$\Rightarrow \langle \mathbf{L} \cdot \mathbf{S} \rangle = \frac{1}{2}\big(\langle \mathbf{J}^2 \rangle - \langle \mathbf{L}^2 \rangle - \langle \mathbf{S}^2 \rangle\big) = \frac{\hbar^2}{2}\big[j(j+1) - \ell(\ell+1) - s(s+1)\big]. \tag{1.6}$$

where j, ℓ, s are the total, orbital and spin angular momentum quantum numbers, respectively.

Substituting eq.1.6 into eq.1.3 gives the total energy shift due to SOC as

$$\Delta E = \frac{\beta}{2}\left[j(j+1) \;-\; \ell(\ell+1) \;-\; s(s+1)\right] \qquad \text{with} \tag{1.7}$$

$$\beta \;=\; \beta(n,\ell) \;=\; Z^4 \frac{\mu_0}{4\pi} g_s \mu_B^2 \frac{1}{n^3 a_0^3} \ell\left(\ell + \tfrac{1}{2}\right)(\ell+1) \tag{1.8}$$

where n is the principal quantum number, a_0 is the Bohr radius, and μ_0 is the permeability of vacuum.

SOC has profound consequences on the magnetic properties of materials. It is the first order contribution to magnetocrystalline anisotropy through the coupling of the electron's orbital motion to the crystal electric field. In systems without an inversion symmetry, SOC can result in the antisymmetric Dzyaloshinskii-Moriya Interaction (DMI) which can stabilize chiral and helical spin structures like skyrmions via spin canting[25], and give rise to topological effects in spintronic

devices[26]. Presence of SOC in systems with broken inversion symmetry can lead to the Rashba effect which can generate spin polarized currents through spin-momentum locking[27]. Materials capable of such spin transport are of immense importance for the development of next-generation information storage and low-loss devices.

1.1.4 Exchange

The key player in deciding the magnetic ground states of transition-metal oxides is the competition between exchange interactions. *Exchange* is a purely quantum-mechanical term that arises due to the exchange symmetry imposed upon the wavefunctions of indistinguishable particles (like electrons). This symmetry requires fermion states to be antisymmetric under a coordinate swap. A simple intuitive description of this comes from by simply combining two independent H-atom wavefunctions to calculate the total energy of the system (H_2 molecule). The Hamiltonian can be broken down into a combination of the potential and kinetic terms plus an *extra* perturbative term related to the interactions between the two nuclei and electrons of the two atoms (i.e. n_1–n_2, e_1–e_2, n_1–e_2, e_1–n_2; $n_{1,2}$ are the two nuclei and $e_{1,2}$ are the two electrons). The latter is the exchange term and is parametrized by the exchange integral J and the overlap integral $\mathcal{S}$.

Including the particle spins in this picture adds more combinations from their symmetric and antisymmetric contributions and the resulting wavefunction is written in the form of Slater determinants. There is an overall antisymmetry constraint on this wavefunction which requires the orbital and spin contributions to be antisymmetric with respect to each other, so that the result of the above calculation yields a symmetric spin-singlet solution ($\varepsilon = \frac{-4t^2}{U}$) and an antisymmetric spin-triplet solution ($\varepsilon = 0$). t and U reflect the kinetic and Coulomb interaction of the electrons, and the energy solutions reflect the preference toward the antiparallel spin configuration.

More generally, the exchange interaction between electrons is considered as a perturbative energy term

$$\mathcal{H}_{Heis} = -J_{12} < \vec{s_1} \cdot \vec{s_2} > \tag{1.9}$$

called the Heisenberg exchange Hamiltonian with J_{12} as the exchange constant (derived from J) (van Vleck[28], Dirac[29], Heisenberg[30]). $J_{12} > 0$ prefers a parallel alignment of spins while $J_{12} < 0$ favours an anti-parallel arrangement, and that the ground state energy of a two-particle system depends on their relative spin.

1.1.5 Exchange Mechanisms

Competition among various different types of J_{12} in real materials helps stabilize various interesting magnetic states including complex, non collinear ones like helical and spiral magnetic arrangements. The discussion above considering the diatomic system is often called the two-state Hubbard Model and its extension to an infinite lattice helps reveal the correlation between magnetism and transport properties as we see below.

1.1.5.1 Direct exchange and the hubbard model

The Hubbard Model is the starting point in exploring electronic correlation in real materials. It starts with the tight-binding model, with each atom described as a nucleus + electron system, and then introduces the interaction term - allowing electrons to *hop* to neighbouring sites, with a probability t - this is the hopping integral. The Hubbard Hamiltonian thus becomes:

$$\mathcal{H} = -t \sum_{i,j,\sigma} c^{\dagger}_{j,\sigma} c_{i,\sigma} + U \sum_{i} n_{i\uparrow} n_{i\downarrow} \tag{1.10}$$

where the first term encapsulates hopping of the electron from $i \rightarrow j$ state - using the creation and annihilation operators $c^{\dagger}$ and c, and the second (Hubbard) term corresponds to electrons on the same orbital and same site ($\sim$ 6 - 8 eV for TMOs).

Solving this Hamiltonian for the simplest case of 1D chains yields the following results:

- if $U \gg t$, electrons remain localized - this is the case for magnetic (Mott-Hubbard) insulators - atomic limit - band gap opens within the d bands.
- if $U \approx t$, finite electron hopping is allowed, and as a result antiferromagnetic (AFM) interaction is favored.
- if $U \ll t$, the electrons are free to move across the crystal - this is the case for metals - band limit

This means that the Hubbard model defines the boundary between an insulating and metallic phase and provides the critical value of U for which the crossover - the *Mott transition* occurs. Applying the mean-field approximation in the low U limit allows one to obtain an effective single-

particle $\mathcal{H}$ which is solved self-consistently to reach the *Stoner Criterion*

$$Ud(E_F) \geq 1$$

where $d(E_F)$ is the density of states at Fermi level. This defines the condition for itinerant ferromagnetism to occur in a given system. The product $Ud(E_F)$ competes with the kinetic energy cost of the up-down spin splitting. If large enough, it allows the system to form a spin-polarized state by compensating the energy cost. Despite its seeming simplicity, the Hubbard model remains unsolved for more than one dimension. This model is the basis of DMFT (Dynamic Mean-Field Theory) calculations that model the band structures and magnetic ground states of real materials within certain approximations.

The spectrum between the localized and itinerant behaviour of electrons is particularly relevant for ruthenates due to their moderate electron correlation (as we will discuss in Section 1.5.2). These systems also often have complicated band structures with multiple bands crossing the Fermi level. This can result in a mix of localized and itinerant behaviour depending on the type of bands contributing to the magnetic interactions[31,32]. The degree of localization of the orbitals involved in magnetism also plays a role. *d* orbital based magnetism will be localized, while delocalized conduction bands will result in an itinerant picture[33]. In this context, it is worthwhile to mention the *Slater* insulators in which the insulating behaviour is a consequence of a magnetic transition (usually AFM) breaking the translational symmetry and splitting the electronic bands. Because the electrons are not strongly localized, band theory sufficiently describes the electron conduction in these systems and the magnetism results from phenomena like band nesting or spin polarization. In *borderline* materials like ruthenates, it can be particularly challenging to differentiate between these two extremes of insulating character[34]. Other notable types of correlated insulators include charge-transfer insulators - a Mott insulator variant where the gap opens up between the *d* and *p* states instead[35], Kondo (heavy fermion) insulators - where a strong hybridization between localized *f* electrons and delocalized conduction electrons leads to a low temperature gap[36], and spin-orbit Mott insulators - where the presence of SOC (e.g. in 5*d* compounds) entangles the spin and orbital degrees of freedom leading to gap opening along with unusual magnetic or topological states even with modest electron correlation[37].

The prerequisite for direct exchange is an overlap between the spin and orbital wavefunctions of the nearby ions participating in the interaction. However, most materials do not have such

proximally placed cations (Coulomb repulsion!) and yet show bulk physical properties which can only be interpreted in terms of a cooperative behaviour. *Indirect* exchange mechanisms, with a *mediator* anion, helps facilitate these long-range interactions, by enabling localized electrons to *hop* across the crystal.

1.1.5.2 Superexchange

Superexchange is the type of indirect exchange where localized electrons interact with each other via the nearest-neighbour anion *p* orbitals by forming covalent bonds and sharing electrons with opposite spins (restricted by Pauli's exclusion principle, and spin angular momentum conservation). The exchange between two half-filled *d* orbitals is always AFM, while that between a partially filled and empty *d* orbital is FM.

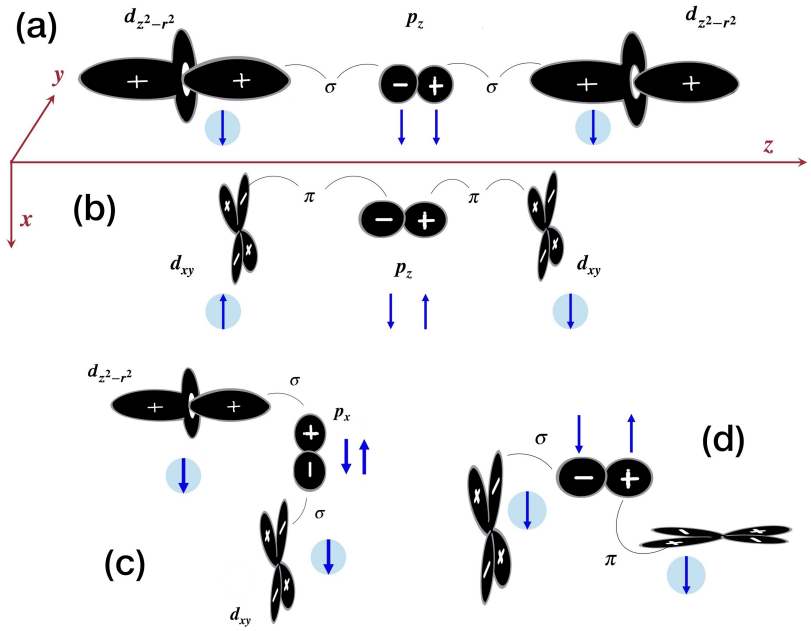


Figure 1.2: The superexchange mechanism. Examples of orbital symmetries when (a), (b) antiferromagnetic, and (c), (d) ferromagnetic coupling is favoured.

The configurations favoured by superexchange depend strongly on the degree of orbital overlap and the orthogonality of the participating orbitals governed by the (semi-empirical) Goonenough-Kanamori rules[38,39] which say:

- When the overlapping orbitals are linear (i.e. the bond angle at the anion is $\sim 180°$, σ bond), strong AFM coupling is favoured.

- When the two *d*-orbitals are oriented 90° - which means different anion orbitals participate in exchange - a weak FM coupling is favoured.
- When the interaction is betweem a partially filled and an empty *d* orbital - a weak intra-site FM coupling is favoured.

These rules highlight the deep relationship shared by the spin and orbital order and suggests that extent of long-range order in real materials is strongly dependent on the orientation of the different orbitals.

1.1.5.3 Double Exchange

Double Exchange, proposed by Zener[40], is a type of exchange encountered in mixed-valent compounds and gives a framework to understand the very special class of ferromagnetic metals. The electron from one ion can hop to the other via O^{2-} and occupy the empty e_g orbital. The final state then results in the two ions swapping oxidation states. This resonance can only be sustained if the moments on the two ions are parallel to each other (Hund's coupling). This results in a cooperative occurrence of ferromagnetism and metallicity. Fig. 1.3 shows a schematic of the double exchange process between a Mn^{3+} and Mn^{4+} ion via the O $2p$ orbital.

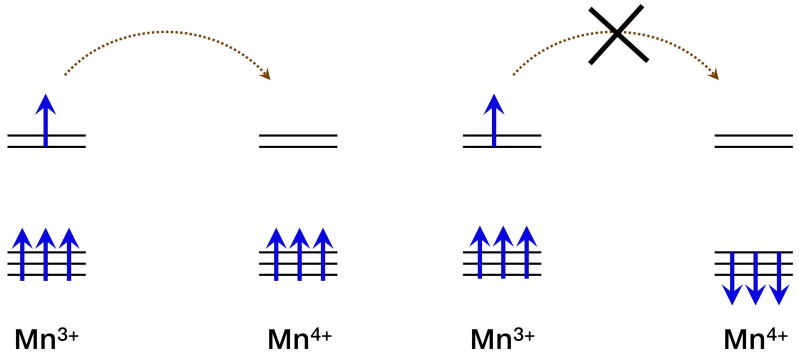


Figure 1.3: The double exchange mechanism. The AFM case is restricted by Hund's first rule.

1.2 Geometrical frustration

Like humans, spins also tend to get frustrated when trying to simultaneously fulfill two incongruent constraints. The concept of frustration was introduced by Anderson in 1950s in his work on identifying different types of AFM structures[41]. The canonical example is always of the triangular lattice, where 2/3 vertices are antiparallel to each other, so the third one is unable to choose

a minimum energy state and is frustrated. When originating purely from the topology of the structure, the frustration is called geometrical, however there are more types possible. For example, an ideal square lattice can also be frustrated if the NNN interactions become comparable to the NN ones - a form of exchange frustration. The tetrahedron, the kagomé (corner-shared triangular lattice), the pyrochlore (connected network of tetrahedra) (Fig. 1.4 (a)) - are all standard models where the origins and effects of frustration are explored in real systems.

Some frustrated systems do order - albeit in a compromised arrangement. For example, the relative 120° arrangement in a triangular lattice or the 109° arrangement in a tetrahedron (Fig. 1.4(b)). However, the system has more than one way to attain these ground states, often with very little cost between them - this is the origin of the large ground state degeneracy observed frustrated materials.

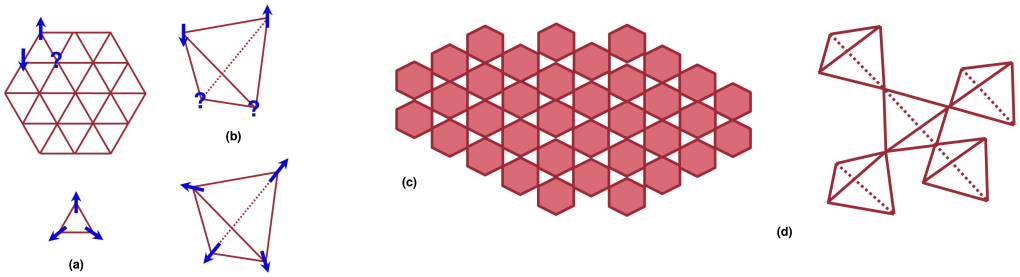


Figure 1.4: Various types of geometrically frustrated lattices and their possible ground states

1.3 Disorder

Although in theoretical models, ideal, perfect arrays of atoms allow us to simplify complex physical problems in order to make connections with their macroscopic observables, real materials are never *perfect*. Defects and disorder are ubiquitous and their manifestation in physical properties is inevitable. Usually, it is regarded as something unwanted, making it difficult for a system to achieve a perfect, pristine ground state. However, consensus has been growing on the usefulness of controlling and manipulating disorder in the endeavour to achieve true correlated ground states. For example, the spin-liquid state in $H_3LiIr_2O_6$ is understood to be closely linked to the hydrogen disorder[42,43], and in an experiment on 1D atomic chains in an optical lattice, it was found that introducing disorder stabilized the BEC superfluid state instead of Mott phase[44]. Disorder in the form of spatial randomness of interactions has also been proposed as an explanation for the unusual experimental signatures of strange metals[45]. Research on disorder is active

and emerging, and exploring the numerous types of possible disorder in real systems - positional, compositional, orientational etc. - presents an alternative way of understanding the nontrivial correlations in quantum materials.

1.4 The spin glass state

A configuration of spins *frozen* in random directions as a combined result of frustration and disorder is called a spin-glass. These materials have long puzzled experimentalists and theorists alike, the former, for their experimental signatures including magnetic irreversibility, aging and memory and the elusive *true* phase transition. Their curious behaviour stems from the topology of their phase space, which consists of infinitely many energy valleys, separated by very small energy differences - so that, there exists infinitely many ways for a system to achieve a ground state without any path preference. This is the basis of the *ground state degeneracy* in these systems - which leads to dynamics over extremely long timescales and a hierarchical distribution of these states. We will explore this fascinating non-Néel state in detail in Chapter 3.

1.5 The Perovskite structure

The material class of perovskites (named after Russian mineralogist L. A. Perovski) is one of the most celebrated in condensed matter physics. These chemically flexible structures find wide technological applicability from dielectric and piezoelectric sensors[46] to photovoltaics where they have have carved up their own field of research (*Perovskite Solar Cells*[47]). Apart from this they also show a variety of intriguing magnetic and transport properties[48,49,50], as well as multifunctionality[51], thus making them choice subjects for studying the interplay of spin, lattice, charge and orbital degrees of freedom.

In the simplest case, a perovskite is any material with the chemical formula ABX_3, with 12-coordinated A-cations occupying the corners of a cubic unit cell and the B-cation located at the body center, sixfold coordinated by the X anions forming an octahedra around it. In this thesis, we focus on the oxides subset of materials having $X = O^{2-}$. An ideal cubic perovskite structure is shown in Fig. 1.6(a). The unit cell symmetry is strongly influenced by the relative size of the cations and is quantified in the *Goldschmidt tolerance factor*, t:

$$t = \frac{r_A + r_O}{\sqrt{2}(r_B + r_O)} \tag{1.11}$$

where r_A, r_B, and r_O are ionic radii of the A, B, and O ions, respectively. For an ideal cubic perovskite, $t = 1$. When $t < 1$, the BO_6 octahedra distort to compensate for the cation mismatch and often a monoclinic symmetry is favored. When $t > 1$, the strain is too large, and face-sharing between octahedra is promoted and hexagonal or rhombohedral symmetries are preferred[52]. In most real perovskites, different types of octahedral distortions - tilting, rotation, elongation or compression of octahedral bonds and atomic displacements from the center - lower the symmetry from cubic, and strongly influence physical properties. In 1972, A.M. Glazer classified perovskites into 23 distinct tilt systems[1] and further work on group theoretical classifications to predict distortion-induced structural phase transitions have continued[53,54,55]. Recently, even more complex tilts beyond those tabulated by Glazer have been predicted in $BiFeO_3$[56], attesting to the strong impact of distortions on perovskite properties. The nomenclature of the tilt-type is as follows:

- a, b, and c denote the axes along which the tilting occurs
- the superscripts $0, +, -$ indicate no tilting (in a given direction), in-phase tilting (all octahedra tilt in the same orientation), or out-of-phase tilting (octahedra tilt alternately) (see Fig. 1.5).
- same letter use for more than one direction indicates that the magnitude of tilting is same in those directions.

The list of Glazer tilts along with their corresponding space groups are given in Table 1.1[1] and a schematic showing the commonly seen tilt systems $a^0a^0a^0$, $a^0a^0c^+$ and $a^0a^0c^-$ are shown in Fig. 1.5.

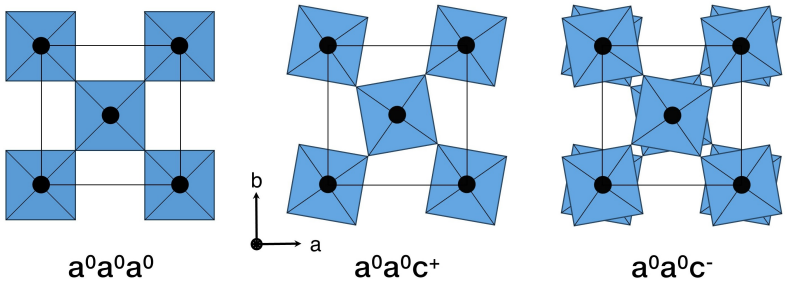


Figure 1.5: The octahedral tilt systems $a^0a^0a^0$, $a^0a^0c^+$ and $a^0a^0c^-$ in perovskite structures.

Tilt System number	Tilt system symbol	Space group
	Zero-tilt systems	
23	$a^0a^0a^0$	Pm3m (#221)
	One-tilt systems	
22	$a^0a^0c^-$	F4/mmc (#140)
21	$a^0a^0c^+$	C4/mmb (#127)
	Two-tilt systems	
20	$a^0b^-b^-$	Imcm (#74)
19	$a^0b^-c^-$	F2/m (#12)
18	$a^0b^+b^-$	Bmmb (#63)
17	$a^0b^+c^-$	Bmmb (#63)
16	$a^0b^+b^+$	I4/mmm (#139)
15	$a^0b^+c^+$	Immm (#71)
	Three-tilt systems	
14	$a^-a^-a^-$	R3c (#167)
13	$a^-b^-b^-$	I2/a (#15)
12	$a^-b^-c^-$	F1 (#2)
11	$a^+a^-a^-$	Pmnb (#62)
10	$a^+b^-b^-$	Pmnb (#62)
9	$a^+a^-c^-$	$A2_1/m$ (#11)
8	$a^+b^-c^-$	$A2_1/m$ (#11)
7	$a^+a^+a^-$	Pmmn (#59)
6	$a^+b^+b^-$	Pmmn (#59)
5	$a^+a^+c^-$	Pmmn (#59)
4	$a^+b^+c^-$	Pmmn (#59)
3	$a^+a^+a^+$	Im3 (#204)
2	$a^+b^+b^+$	Immm (#71)
1	$a^+b^+c^+$	Immm (#71)

Table 1.1: Classification of possible octahedral tilt systems in perovskites given by Glazer[1]

Perovskites also show a large structural variety based on their unit cell packing. The typical cubic

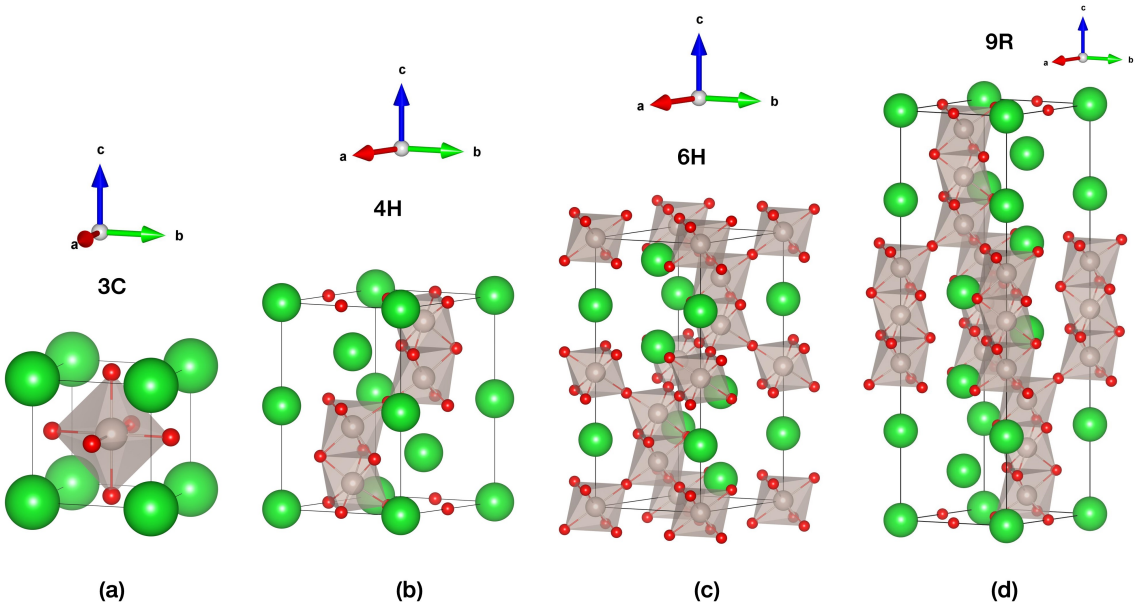


Figure 1.6: The perovskite crystal structure in (a) 3C, (b) 4H, (c) 6H and (d) 9R variants

ABO_3 is a 3C structure, i.e. it has 3 cubic layers per cell (see Fig. 1.6(a)). Numerous other types like 2H, 4H, 6H, 9R are also known (H = hexagonal, R=rhombohedral). One compound exemplifying this vast diversity is $BaRuO_3$, which adopts four different polymorphs (Fig. 1.6(b)-(d)) depending on the synthesis conditions[57,58,59,60]. Often applying a higher pressure is required in order to stabilize a high symmetry structure.

1.5.1 Layered Perovskites

The great appeal of this packing flexibility lies in the option of chemically substituting either of the cation sites to the n^{th} degree. Substituting exactly half of the B-sites with a different cation (B') results in the $A_2BB'O_6$ subset of compounds, dubbed "double perovskites" (DPs) in literature, due to the "doubling" of unit cell along all three crystallographic axes with respect to the ABO_3 cell. One can also have mixed DPs ($AA'BB'O_6$) where both A and B sites are substituted. DPs are one of the most extensively researched class of compounds in materials science owing to the expansive breadth of physical properties that they cover. The numerous types of cation ordering allowed in these systems has profound impact on their physical properties. For example, the celebrated high temperature ferromagnet Sr_2FeMoO_6 with a $T_C = 420$ K is strongly influenced by the degree of cation order on B-site[61,62,63]. Based on the degree of disorder, DPs can be classified as - disordered (may or may not have short-range order), weakly ordered, partially ordered,

and highly ordered with or without an anti-phase boundary[64]*. They can show charge disproportionation among the B-site cation - leading to a different kind of cation order on the B-site - based on alternating oxidation states of the same ion - like in $Ba_2Bi^{3.5+}Bi^{4.5+}O_6$ (T_{co} $\geq$723 K)[65], $Y_2Ni^{2.65+}Ni^{3.35+}O_6$ (T_{co} =580 K)[66]and $Ca_2Fe^{3.45+}Fe^{4.55+}O_6$ (T_{co} =290 K)[67]. This also points to the ability of these compounds to stabilize unusual oxidation states at their B-sites including mixed-valences. For instance, Sr_2RuMnO_6[68,69] shows a Mn^{3+}/Ru^{5+} - Mn^{4+}/Ru^{4+} mixing and A_2FeMoO_6 (A = Ca,Sr,Ba) show combinations of $Fe^{2+/3+}$ and $Mo^{5+/6+}$ states[70]. The B-site oxidation states can also be tuned structurally, by doping or by altering synthesis conditions. A large A (e.g. Ba) in A_2FeMoO_6 favors a Fe^{2+}/Mo^{6+} combination, while a smaller A (e.g. Ca) leans toward a Fe^{3+}/Mo^{5+} combination - attributed to the system's attempt at reducing strain and other structural distortions and push t towards 1[52]. Ca_2MnRuO_6 is also seen to favor the Mn^{3+}/Ru^{4+} combination as compared to the mixed valency observed in its Sr counterpart. Likewise, Ca_2NiOsO_6 is mixed-valent, but Sr_2NiOsO_6 has a combination of Ni^{2+}/Os^{6+}. This highlights the fact that structure is a key player in determining the stable oxidation states of cations comprising these layered perovskites, providing high tunability of physical and functional properties. Similarly sized B-cations can also swap places, generating *anti-site* disorder like Ba_2CoRuO_6 (discussed in Chapter 3) and Ca_2LnRuO_6 (Ln= Y, La-Lu)[71].

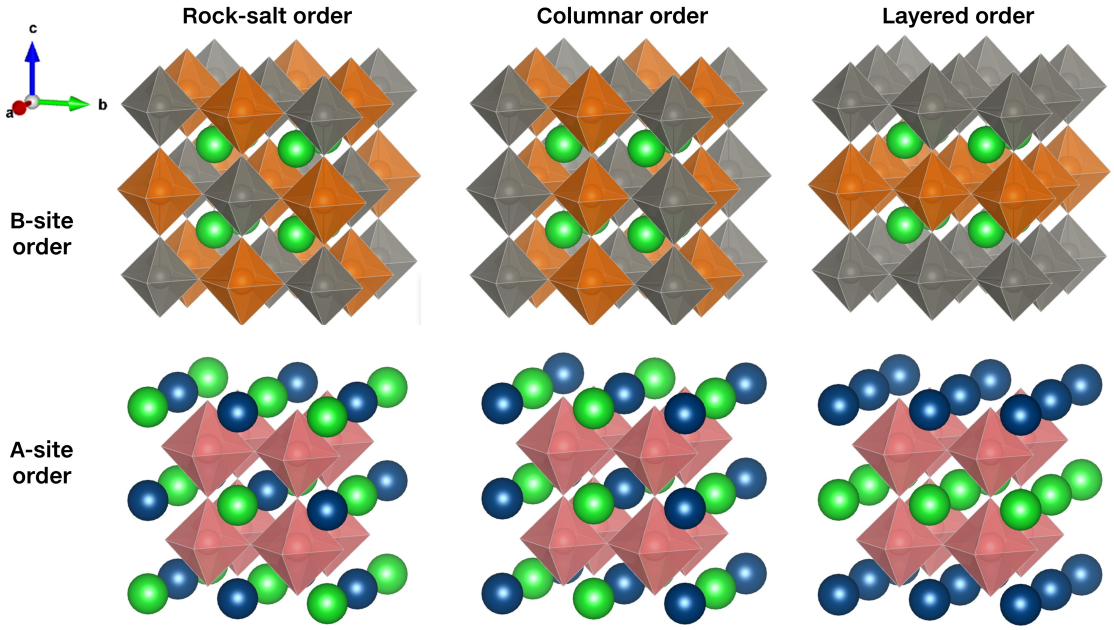


Figure 1.7: The various types of A- and B-site cation order possible in ideal double perovskite structure

*An anti-phase boundary divides two ordered domains within the DP with inverse B' and B occupancies[63,52]

B-site substitution of the perovskite structure in ratio 1:2 and 1:3 generate the "triple-perovskite" (TP) and the "quadruple-perovskite" structures, respectively. The latter are quite interesting, since their A-site substituted versions have been shown to possess and intrinsic triple-order which becomes apparent only when three different ions occupy the A-site[9]. This family shows extraordinary dielectric[72] and catalytic properties[73], but poses a significant obstruction in synthesis as it requires both high temperatures and high pressures to be stabilized. This is consistent with their structure where extremely high tilting of the B-site octahedra forces one of the A-sites to settle in a square planar geometry - markedly different from the octahedral network common in B-site doped QPs.

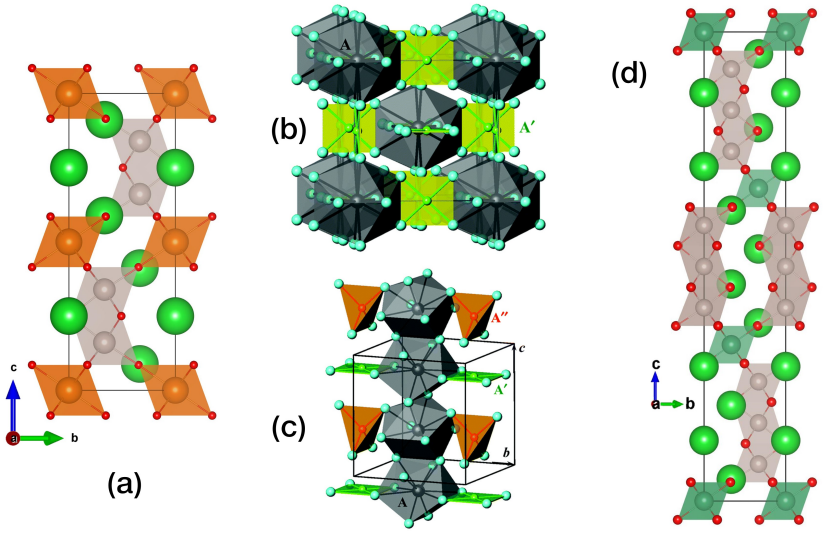


Figure 1.8: (a) 6H structure of $A_3BB'2O_9$ with face and corner-shared octahedra, (b) A-site orderings in $AA'_3B_4B_{12}$ and (c) $A_2A'A''B_4B_{12}$ quadruple perovskite systems (Reproduced from A. Belik[9] with permission from the Royal Society of Chemistry) (d) Crystal structure of $A_4B'B_3O_{12}$ showing the B_3O_{12} trimers found in B-site substituted quadruple perovskites.

From the point of view of electronic transport, most layered perovskite oxides are insulators, however, the choice of B-cation is again important here, since the degree of overlap between the cation and anion orbitals is what facilitates the pathway for electron conduction through the crystal. Now, since the orbital overlap is also influenced by structure, internal distortions under change in temperature, pressure, field, etc. can change the degree of overlap and in turn, alter the conduction mechanism (e.g. $Ba_3NaRu_2O_9$). We will see an example of this in Chapter 5. Some of them have been reported to have semiconducting behaviour with small resistivities and Seebeck coefficients e.g. La_2NiFeO_6, Sr_2CoIrO_6 and $Ba_3MnRu_2O_9$ with $\rho = 10^{-3}$ - 10^{-4}

Ω-cm at room temperature, presenting the possibility of them being close to a metal-insulator transition (MIT)[52]. Indeed, MIT has been seen in some DPs like Sr_2CoTiO_6 (T_{MIT} =700 K) and Ca_2MnMoO_6 (T_{MIT} =209 K)[74]. What about superconductivity? High T_c cuprates, being perovskite-derived structures, with Cu-O layers being responsible for the superconductivity, raises this question. Some superconducting properties have been seen in a non-stoichiometric compound $Sr_2Y(Ru_{1-x}Cu_x)O_6$ (0.05<x<0.2), although their origins remain controversial. There are even rare, half-metallic DPs - where one spin channel is metallic while the other insulating (Sr_2FeMoO_6[62,75]) - allowing one to have spin polarized electron transport, a property of immense value for spintronic applications. $Ba_4NbRu_3O_{12}$ is an interesting example of a geometrically frustrated trimer Mott insulator with an enhanced electronic contribution to the specific heat[76].

Of particular interest to us is the spectrum of magnetic behaviour covered by layered hexagonal perovskites. Magnetic order in these systems is greatly influenced by the cation order and degree of octahedral distortions and thus, it is an appealing prospect to tune their structures and observe the crossovers between various magnetic phases in these materials. The magnetism in these systems is primarily governed by the superexchange between the B and B' - with different pathways having different strengths. For example, in some Ru-based compounds (Ru being the only magnetic ion), due to its empty e_g orbital can only participate in π bonding, which leads to the 90° B—O—O—B exchange being stronger than the ideal 180° B—O—B'—O—B[77] (as expected from the GK rules). Things get more interesting when both B and B' are magnetic, because now, the quality of orbital overlap influences the relative strength between the nearest-neighbour (NN) B—O—B' and next-nearest-neighbour (NNN) B—O—B'—O—B. When the former is weak, for instance, in case of B = *Ln* and B' = TM, the two magnetic sublattices order independently at different temperatures (e.g. Sr_2TbIrO_6, Ba_2NdOsO_6[52]). A magnetic ion on the A-site adds even more complexity and can stabilize delicate and incommensurate orderings like elliptical spin-spiral in Mn_2FeSbO_6[78]. Additionally, the magnetism in many of these compounds is governed by double-exchange like electron hopping and Jahn-Teller (JT) distortions. For instance, in Ba_2(Sm/Nd)MoO_6, JT distortion (and the resultant orbital ordering) coincides with the magnetic ordering. In Ba_2NaOsO_6, the dynamic distortion does not show up in the structure but manifests itself in magnetic measurements, where orbital degeneracy breaking causes a weak FM order to develop. In contrast, its sibling compound, Ba_2LiOsO_6, is a simple AFM. Such a variety in physical properties despite similar compositions, is also seen in the TPs Ba_3(Na/Li)Ru_2O_9. The Li compound preserves its hexagonal structure down to 100 K, whereas,

the Na one undergoes a structural transition to a lower (orthorhombic, monoclinic) symmetry due to a charge ordering of the B-site Ru ions[79]. A small oxygen deficiency is seen to destroy the order and make the compound paramagnetic down to 1.7 K (although CW analysis indicates the presence of AFM correlations)[80]. This is true for the Ir compounds as well - even though both $Ba_3(Na/Li)Ir_2O_9$ have the same structure $P6_3/mmc$ at room temperature, only the Na system undergoes a structural transition to a monoclinic symmetry ($C2/c$) below 100 K. This is a clear example of how subtle changes in the local environment of the magnetic ions translate into drastic changes in macroscopic observed quantities - a hallmark of truly *quantum* materials.

Another important influence on magnetic properties is the choice between $3d/4d/5d$ ions - which have successively increasing SOC and spin delocalization due to enhanced orbital spatial extension. Ironically, in trying to understand the magnetism of these materials, we often gravitate towards materials with no magnetic order at all. One reason for this is the search for strongly correlated but non-ordered spin liquid ground states, whose large energy degeneracy at low T make them uniquely appealing for quantum information and computing applications. But another reason is to simply understand in what ways a system starting with magnetic ions can reach a ground state where their individual magnetism is *quenched*. This is often the case for $4d$ and $5d$ materials, where observed magnetic moment values are much smaller than that expected from a spin-only calculation. In the very special case of Ir^{5+} (d^4), the SOC strength becomes comparable to the crystal-field splitting and inter-electron interaction strengths, which then splits the degeneracy of the t_{2g} orbitals and stabilize a nonmagnetic ground state with no ordering (e.g. Sr_2FeIrO_6[77], Sr_2YIrO_6[81]). Although rare, high-spin $3d$ ions can also have notable SOC due to their finite orbital moment which results in observed moments larger than those expected from a spin-only calculation, like for Sr_2CoMoO_6[82] and Sr_2FeWO_6[52]. SOC can also be quenched by structural distortions, as seen in Sr_2YIrO_6[81], where at low temperature the crystal field becomes non-cubic and leads to a magnetically ordered state.

Various types of AFM arrangements of the B cations are achievable in these systems depending on the relative strengths of the NN and NNN interactions, which in turn depend on the energetic and orbital overlap and symmetry. When the NN interactions are stronger, a type I AFM order is established where intra-layer spins are ferromagnetically aligned, but inter-layer coupling is AFM. When the converse is true (NNN>NN), the type II order is established where every nearest neighbour is AFM coupled. Type III is a mix of I and II, and the structure is such that

corner spins of each layer are FM with each other, but AFM to the spin at the centre of the layer. The second layer, formed by the spins on the faces has spins on the adjacent faces AFM linked, while those on opposite faces FM linked. The set of these two layers are inverted and repeated to form 1 magnetic unit cell. Typically, B-site combinations of *Ln* and TM ions are seen to have the type I arrangement while type II is more prevalent for systems where both B-cations are TM elements[52]. When both B and B' are magnetic, interpenetrating sublattices (Sr_2CoOsO_6[83]), or unusual up-up-down-down (Lu_2CoMnO_6[84], $Ba_3NiNb_2O_9$[85]) and incommensurate structures La_2NaRuO_6[86] can be stabilized. These AFM types are derived from the more basic AFM types A, C, D, E, F and G found in the ideal perovskite system. All of these arrangements are schematically shown in Fig. 1.9

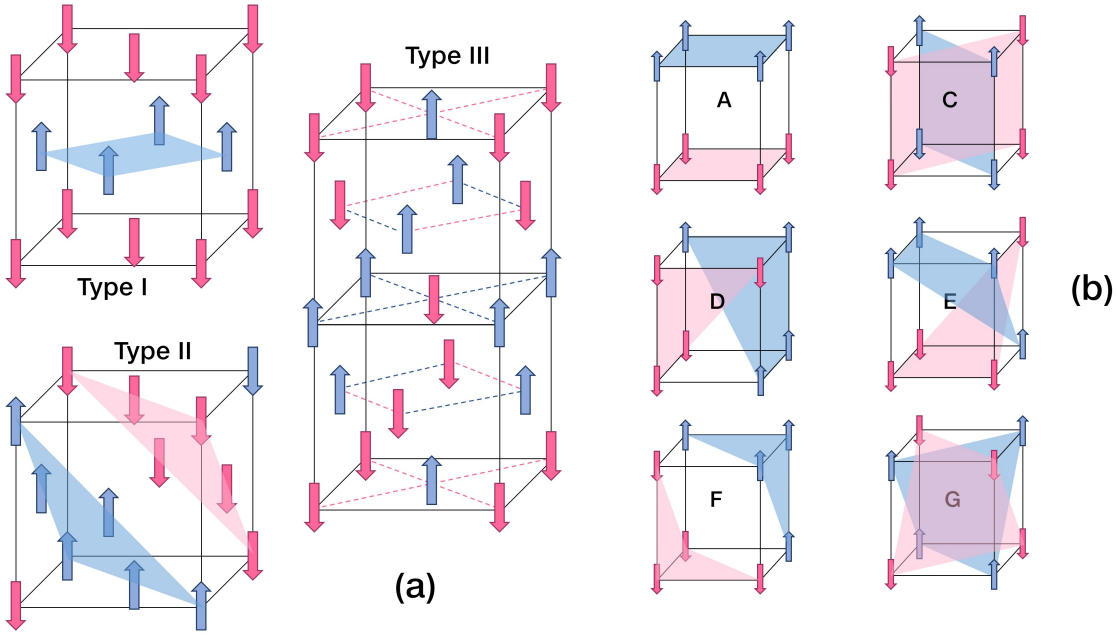


Figure 1.9: The various types of antiferromagnetic order found in (a) layered and (b) simple perovskites.

The diversity of NN and NNN interactions in layered perovskites presents the possibility of magnetic frustration. The ideal cubic DP is made up of a tetrahedral network of NN AFM interactions which can potentially be geometrically frustrated. The total spin (S) of the cations also seems to be important - La_2LiMO_6 and Ba_2YMO_6 with $S = 3/2, 1$ and $1/2$ for M = Ru, Re and Mo, respectively, exhibit long-range order only for M = Ru. For M = Re and Mo, only have features that could be interpreted as broad anomalies owing to short-range correlations. The frustration in the NN network can be relieved by the NNN interactions, but often when NN and

NNN of comparable strengths favour two opposing magnetic ground states - it can rather give rise to an exchange frustration. This is even more severe in cases where site-disorder can occur and leads to spin-glass -like frozen magnetic ground states inhibiting long range order. We discuss this case in Chapter 3 in detail.

Oxide ferro- and ferrimagnets are quite uncommon, since superexchange predominantly favours AFM arrangements and very specific symmetry and overlap requirements need to be satisfied for superexchange mediated long-range FM to exist. Layered perovskites seem to structurally fulfill this requirement with a full cation order, and permit FM interactions to not only compete with but also prevail over the usually dominant AFM order. Double-exchange is the leading mechanism for this, acting between partially filled and empty TM ions - most of which are 3*d* manganites.

The layered structure of these systems also allows them to sometimes show low-dimensional magnetism, especially when magnetic ions are isolated by nonmagnetic spacer layers. For example, in A_2CuB'O_6 with diamagnetic B' = Mo, W or Te, Cu^{2+} octahedra undergo JT distortion and form a square array perpendicular to the *c*-axis[87,88].

And finally, layered perovskites have been reported to show useful multifunctional properties, most sought after of them being multiferroicity - a coupling of the ferromagnetism and ferroelectricity. It is an unusual occurence though, since a displacive ferroelectric distortion needs empty *d* orbitals, while magnetism needs partially filled *d* orbitals. The resolution lied in creating materials with a polarizable ion like Pb or Bi - with an extra lone pair of electrons - on the A site, while a magnetic ion on the B-site. The lone pair on Pb/Bi also enhances the magnetism by mediating exchange and enhancing T_c[89]. Bi_2NiMnO_6 is a known multiferroic although the two orders occur at different temperatures - $T_{FE} \sim 470$ K and $T_c = 140$ K.

1.5.2 Why Ruthenates?

Ruthenium stands out as a special element even within the 4*d* TMs since it seems to tread a fine line between itinerant and localized electron behaviour. Compression of lattice increases electron delocalization due to increased orbital overlap. This is interesting in the view of the (Ca/Sr)RuO_3 perovskites which are metallic oxides. On the other hand, localized/itinerant behaviour of electrons in transition metal oxides is largely a product of the spatial and energetic overlap and the symmetry of the orbitals. The π^* conduction bands are primarily derived from the B' t_{2g} and if

their mixing with the B orbitals is prohibited by symmetry the latter do not contribute to conduction and an insulating state is likely. If mixing is allowed, its degree is defined by the energy cost of the overlap and a large difference in the band energies of the B' and B will favor insulating states. Structural distortions can change this and sometimes encourage σ—π bonding. In this respect, Ru-based oxides are worth paying attention to, since their spatially extended orbitals lead to a reduction of the inter-electronic repulsion U making it comparable to the narrow bandwidth W. In addition, their moderate SOC, adds another competing interaction to the ring, thus placing Ru-based materials prone to crossovers in conduction behaviour (like close to metal-insulator transitions). These are only a few reasons why ruthenates have been known to show such a marvelous breadth of unusual magnetic properties, and have consequently been a subject of continued interest in the quantum materials community. Compounds like - Sr_2RuO_4 [22,90,91] showing unconventional spin-triplet superconductivity, the high T_N honeycomb antiferromagnet $SrRu_2O_6$ [92] exhibiting spin-waves and spin-state transitions, (Sr/Ca)RuO_3 [93,94] showing strong distortion effects and orbital ordering, the altermagnet RuO_2 [23], $Sr_3Ru_2O_7$ displaying metamagnetic quantum criticality [21], and α-$RuCl_3$ being a strong Kitaev spin-liquid candidate [95,96] - provide only a glimpse of the broad spectrum of fascinating physics embodied by ruthenates, making them truly deserving of the distinguished focus they receive in fundamental condensed matter research.

1.6 Orbital Molecules

A relatively new concept in the realm of complex quantum magnetism, the term *orbital molecules* was introduced by Attfield [97] to describe systems characterized by extremely short metal-metal (M–M, where M is a cation) bonds, enabling direct interactions between localized t_{2g} orbitals. These direct orbital overlaps result in the formation of hybridized molecular orbitals with lower energy than the individual atomic t_{2g} orbitals. As a result, the coupled ions in these structures become the true building blocks or "motifs".

The simplest example of an orbital molecule is the $BB'O_9$ dimer, previously discussed in section 1.5.1, which forms via direct t_{2g} B–B' bonding in the face-sharing octahedra. However, larger orbital clusters, such as trimers and tetramers, can also form, demonstrating the versatility of these systems. Beyond layered perovskites, even more complex clusters like heptamers have been identified!

For these clusters to function as fundamental units, their formation must correspond to a thermodynamically favorable equilibrium state. Therefore, it is not surprising that the formation of these multimers are often accompanied by phenomena such as orbital ordering, spin-gap openings[98], and metal-insulator transitions[79], strongly coupled to the lattice and charge degrees of freedom, as evidenced by structural distortions and charge redistribution in compounds[99].

More intricate motifs, such as triangular spin-singlet clusters and their interconnected networks (*trimerons*), have been observed in materials like $BaV_{10}O_{15}$[100] and Fe_3O_4[101]. For the latter, it seems there is no end to finding new facets of its incredibly rich phase diagram. A particularly striking example of an orbital molecule is the seven-atom heptamer found in AlV_2O_4, which exhibits a charge-ordering transition at a remarkably high temperature of $T \sim 700$ K. In this system, 18 *d* electrons spread across nine bonding orbitals, resulting in the spin-gap observed in magnetization measurements.

These materials mark the beginning of a new era in quantum materials research, driven by the pursuit of subtler correlations that stabilize ground states beyond the conventional single-ion spin, charge, or orbital degrees of freedom. Orbital physics offers a pathway to achieving multifunctionality in materials, with potential applications in the emerging field of *orbitronics*. By enhancing spin-orbit coupling (SOC), these systems may play a key role in the development of next-generation technologies. The recent discovery of *altermagnetism*, a novel form of magnetic ordering based on the orientation of orbitals alongside spins, exemplifies the future trajectory of quantum materials research. This interdisciplinary approach, blending methods and physical concepts, will undoubtedly drive innovation in both fundamental science and technological applications.

1.7 Motivation and plan of the thesis

Although layered perovskite-based transition-metal oxides have been extensively studied, several aspects of their complex behaviour remain insufficiently understood. This thesis seeks to address these gaps through a detailed experimental investigation of three compounds from the layered hexagonal perovskite family.

This thesis is organized as follows:

Chapter 2 outlines the experimental methodologies employed, providing a detailed overview of

the instruments and facilities used, including diffraction, magnetometry, specific heat measurements, and dielectric characterization techniques.

Chapter 3 investigates the evolution of the magnetic ground state in the hexagonal double perovskite Ba_2CoRuO_6. Through an analysis of its structural, magnetic, thermal, and electronic properties, the study reveals a strongly correlated cluster spin-glass state driven by significant antisite disorder between Co and Ru. The low-temperature magnetic structure, characterized by antiferromagnetically correlated spin clusters and a canted geometry, offers new insights into the role of disorder in shaping the material's ground state.

Chapter 4 focuses on the polar domain, presenting results from nonlinear dielectric susceptibility measurements using a custom-built setup. The chapter delves into the utility of this technique for probing disordered ferroelectrics, followed by a comparative study of three triple perovskite systems: two with hexagonal symmetry and one monoclinic. Differences in their higher harmonic dielectric responses are explained in the context of their magnetic and structural characteristics.

Chapter 5 examines the magnetic ground state of the B-site substituted quadruple perovskite $Ba_4NaRu_3O_{12}$. Detailed temperature-dependent magnetization, specific heat, and resistivity measurements are conducted, alongside structural investigations using neutron and synchrotron x-ray powder diffraction to capture temperature-dependent structural evolution. Neutron time-of-flight (*tof*) measurements resolve the low-temperature magnetic structure, revealing an A-type antiferromagnetic arrangement, consistent with the other experimental findings.

Chapter 6 provides a summary of the thesis, highlights ongoing research, and suggests potential directions for future work.

Appendices A and B offer practical guides for beginners on analyzing diffraction data to solve magnetic structures and extract microstructural information using the FULLPROF SUITE.

I have not failed. I've just found 10,000 ways that won't work.

Thomas Edison

2

Instrumentation and Experimental Methods

The foundation of a thorough exploration of a material lies in being able to perform accurate and sensitive measurements of its physical and magnetic properties as a function of an external perturbation (temperature, pressure, light etc.). Results obtained from a detailed analysis of such experimental data can provide a profound insight into the microscopic interactions at the heart of these complex systems. In our work, we synthesize polycrystalline samples of three different families of B-site substituted perovskite ruthenates and study in detail their crystal and magnetic structures by using neutron and x-ray powder diffraction (NPD, XRPD) techniques, their morphology and composition using Field Emission Scanning Electron Microscopy (FESEM) and Energy Dispersive X-ray Spectroscopy (EDS), and their magnetic and thermal and electronic transport using temperature- and field-dependent magnetization, specific heat, resistivity and dielectric measurements. Additionally, in order to specifically probe subtler dynamics within these systems we design a home-made automated setup capable of measuring the real and imaginary higher-order dielectric susceptibilities as a function of external ac field and temperature without the need of a dc bias to probe the non-linear response. A detailed description of each of these techniques will be provided in this chapter.

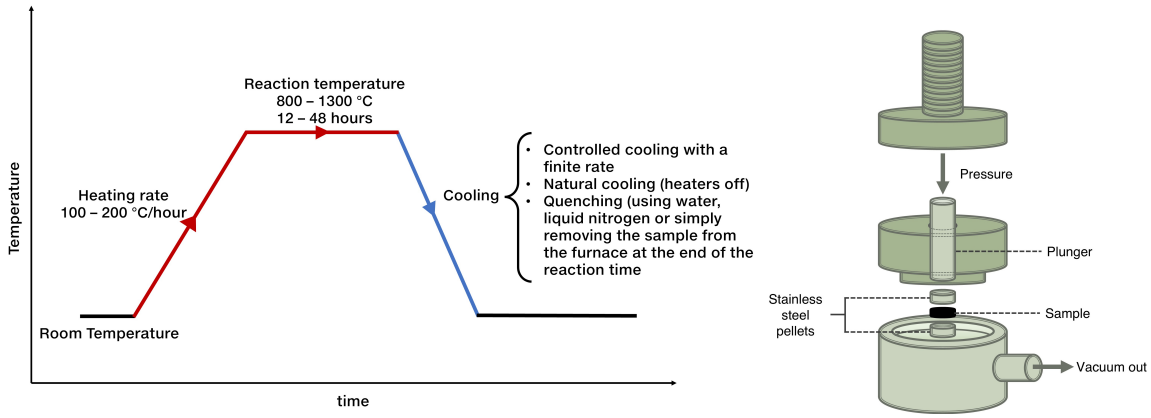


Figure 2.1: (a) A typical synthesis protocol. (b) Construction of a KBr press.

2.1 Solid-state synthesis

All the polycrystalline samples in this thesis have been prepared using solid-state reaction, the method of choice for synthesizing novel oxide materials. Stoichiometric quantities of high-purity (typically >99.99%) raw materials (based on balanced chemical equation) were weighed and mixed in a mortar using a pestle. The first grinding is done for at least 3-4 hours using small amounts of high-purity ethanol to create a slurry while mixing, to ensure homogeneity. Hygroscopic compounds are pre-heated to 200 – 300°C before weighing to remove the water weight. The physical mixture is then placed in alumina crucibles and fired in high-temperature box/tube furnaces at temperatures ranging from 800 – 1500°C in air or an oxygen flow for 12 – 48 hours. The samples, after being cooled to room temperature, are re-ground and checked for phase purity using XRD and EDS. Partially reacted samples are re-ground to break up existing reactant/product interfaces and refresh contact surfaces, pelletized using a KBr press* and re-heated. This process is repeated to optimize the temperature and time required for the completion of the reaction, until a pure phase is obtained. A typical temperature protocol is shown in Fig. 2.1(a).

In some cases, when volatile reactants are involved (like in the case of $Ba_4(Na,Li)Ru_3O_{12}$), the required excess of alkali-metal oxide must also be optimized through repeated trials. To suppress the loss of Na in this case, we use the double sealing method (Fig. 2.2) where the sample is placed

*A KBr press is a hydraulic press usually used for preparing samples for infrared (IR) spectroscopy analysis. The potassium bromide (KBr) acts as a transparent matrix allowing the IR to reach the sample and analyse its molecular structure. The KBr itself is not required for making pellets for solid-state synthesis, and only the sample powder is placed between cylindrical discs and compressed uniaxially by a hydraulic cylinder. A typical construction of a KBr press is shown in Fig. 2.1(b).

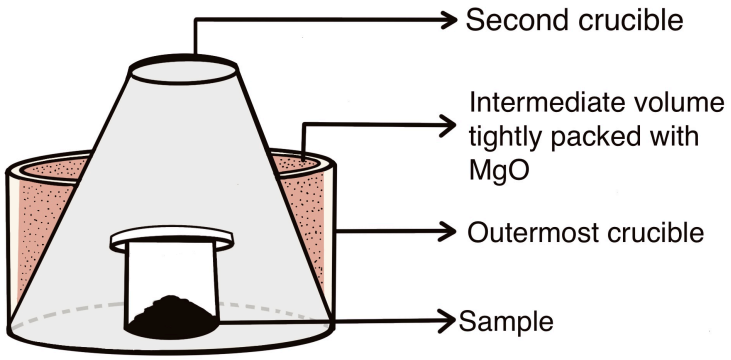


Figure 2.2: A crucible (with lid) containing the sample is placed in a larger one, covered from top by another crucible and the edges are packed by filling in a non-reactive oxide (MgO/Al_2O_3).

in a box air furnace sealed from the outside by a non-reactive oxide like MgO or Al_2O_3.

2.2 X-Ray Diffraction

X-rays were discovered in 1895 by Röntgen[102]. Lying on the high frequency end of the electromagnetic spectrum, they are ubiquitous in condensed matter physics research. Their wavelength range of $0.01 - 100$Å makes them optimal probes of atomic and molecular structure. When a monochromatic and coherent x-ray beam (of wavelength λ) is incident on a crystalline material, it interacts with the electron cloud surrounding the nuclei constituting the crystal and is scattered. When the scattering is elastic, momentum and energy are conserved leading to a constructive interference of scattered rays and a diffraction spot is obtained on the detector. A crystal thus works like a diffraction grating for a given incident wavelength λ. This discovery was first made my Max von Laue in 1912 and the necessary condition for diffraction to occur was first given by W.H. Bragg, which is now the famous *Bragg's Law*[103]:

$$n\lambda = 2\,d\,sin\theta \tag{2.1}$$

where, d is the spacing between the hkl planes occupied by the scattering atoms and the θ is the angle at which the x-ray beam is incident on the surface of the sample (2.3). Knowing λ and measuring across θ, one can calculate d corresponding to each diffraction peak and assign to it a specific hkl value. This allows identification the unit cell geometry and the crystal space group of the material. This is called *indexing*. Scattering of x-rays is strongly dependent on the atomic

number Z of the scatterer. This is because the x-ray atomic form factor f_j (i.e. the amplitude of x-ray scattering from the j^{th} atom) is a Fourier transform (FT) of the electron charge density distribution around the nucleus given by

$$f_j(\mathbf{Q}) = \int \rho_j(\mathbf{r}) e^{i\mathbf{Q}\cdot\mathbf{r}} d^3\mathbf{r},$$

$\rho_j(\mathbf{r})$ being the spatial density of the j^{th} atom around its center of mass ($\mathbf{r} = 0$) and $\mathbf{Q}$ being the momentum change. The vector sum of the scattered waves from all (N) atoms in the crystal is given by

$$\Psi(\mathbf{q}) = \sum_{j=1}^{N} f_j e^{-i\mathbf{q}.\mathbf{R}_j}$$

where $\mathbf{q}$ is the scattering vector ($|\mathbf{q}| = \frac{4\pi}{\lambda} sin(\theta/2)$, θ is the scattering angle) and R_j is the position vector of scatterer. This sum depends on the structure. The product of $\Psi(\mathbf{q})$ with its complex conjugate $\Psi^*(\mathbf{q})$ gives the scattered intensity. The structure factor is then defined as the normalization of this intensity

$$S(\mathbf{q}) = \frac{1}{\sum_{j=1}^{N} f_j{}^2} \sum_{j=1}^{N} \sum_{k=1}^{N} f_j f_k \, e^{-i\mathbf{q}\cdot(\mathbf{R}_j - \mathbf{R}_k)}$$

In case of a powder (isotropic), the intensity depend s on $q = |\mathbf{q}|$ and $r_{jk} = |r_j - r_k|$, simplifying to the Debye scattering equation in three dimensions:

$$S(\mathbf{q}) = \frac{1}{\sum_{j=1}^{N} f_j{}^2} \sum_{j=1}^{N} \sum_{k=1}^{N} f_j f_k \frac{sin(qr_{jk})}{qr_{jk}}$$

For crystals, the structure factor is also expressed as

$$F_{hkl} = \sum_{j=1}^{N} f_j \, e^{[-2\pi i(hx_j + ky_j + lz_j)]}$$

whose modulus squared $|F_{hkl}|^2$ gives the scattering intensity. The above expression is equivalent to $\Psi((q))$. This is why x-rays are less sensitive to light atoms since their $\rho_j(\mathbf{r})$ is small. The angle dependence of $S(\mathbf{q})$ also explains why x-ray diffraction peaks diminish at higher 2θ. All these

reasons contribute to this technique's moniker as a *fingerprint* of a material. The use of powders for XRD was independently invented by Debye and Scherrer [104] and Hull [105] allowing structural analysis of materials for which single-crystals could not be obtained.

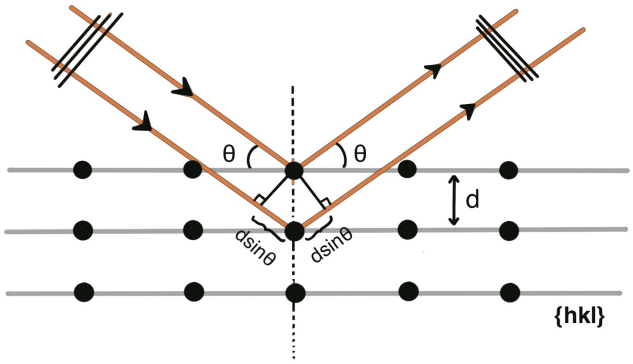


Figure 2.3: Bragg Diffraction

2.2.1 X-ray Sources

Usually, x-rays are generated as a result of impinging a target metal with high-energy electrons. When the incident electrons have an energy higher than a certain threshold energy (specific to the metal target), they are able to knock out an electron from the core (K) shell of the atom. The remaining electrons then redistribute between the atomic energy levels to attain equilibrium. The photons emitted in this process have characteristic energies equal to the difference between the transition states, and thus called *characteristic* x-rays. For a copper target, the characteristic x-rays are emitted at energies 8.05 ($K_{\alpha 1}$) and 8.91 ($K_{\beta 1}$) keV which correspond to wavelengths $\sim$1.54 ($K_{\alpha 1}$) and 1.39 ($K_{\beta 1}$)Å. Additionally, the x-ray spectrum also consists a smooth continuous background called *bremsstrahlung* (literally 'braking radiation' in German) due to the scattering of electrons by the nuclear field. Another increasingly popular way of producing x-rays is by accelerating charged particles in a circular path called *synchrotron* x-rays. We will discuss them in section 2.2.4.

2.2.2 X-ray diffraction geometries

There are two main types of diffraction geometries used in modern diffraction setups. In the reflection or the *Bragg-Brentano* geometry the source and the detector are kept at a fixed radius from the sample and rotated along the goniometer circles as shown in Fig. 2.4 (a). A divergence slit directs the beam onto the sample and filters remove the additional K_β and white radiation. This

is the geometry used in the BRUKER D8 ADVANCE DIFFRACTOMETER at IISER, Pune, which is used for the preliminary characterization of all the materials in this thesis. The x-ray source is a copper (Cu) target with characteristic wavelengths $K_\alpha = 1.542$ Å and $K_\beta = 1.392$ Å. The sample is also rotated about the normal so as to minimize preferred orientation effects. In the transmission or *Debye-Scherrer* geometry, the sample (a cylindrical capillary) is placed perpendicular to the beam path and rotated to expose the entire sample. The diffracted rays form a three-dimensional cone, which is stereographically projected onto a detector (Fig. 2.4(b), (c)). Most synchrotron (and neutron) powder diffraction (PD) facilities use this geometry.

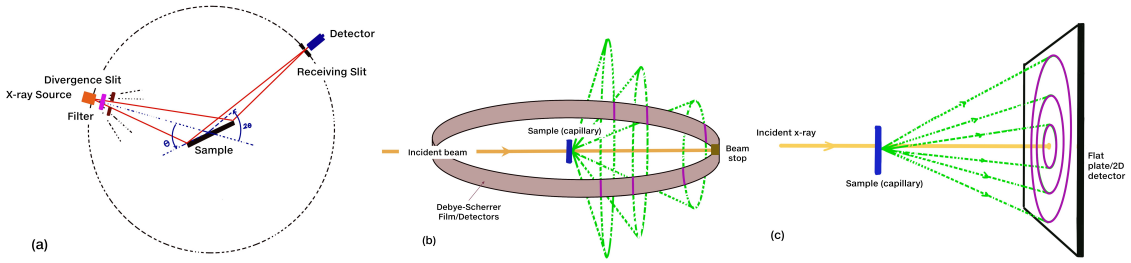


Figure 2.4: (a) The reflection (Bragg-Brentano) diffraction geometry. (b), (c) The transmission (Debye-Scherrer) diffraction geometry.

2.2.3 X-RAY DETECTORS

Most commonly used x-ray detectors are indirect, scintillator-based point (0D) crystal analyzer detectors. When a diffracted photon strikes a phosphor screen, it produces secondary photons that are forwarded to a photomultiplier array generating a voltage proportional to the energy of the incident photon. While these detectors have limited energy resolution and typically cover only about 0.1° in 2θ (making long-range diffraction scans time-consuming) they offer high quantum efficiency. This makes them valuable for thin-film, high-resolution and grazing-angle diffraction purposes. Semiconductor-based point detectors can overcome this limitation and separate K_α and K_β, but require a cooling unit to function. They are useful for characterizing materials that exhibit fluorescence.

Linear (1D) or *position-sensitive* detectors (PSDs) are gas filled detectors containing an anode wire (metal or quartz) which acts as a photon counter aided by a multi-channel analyzer (MCA) setup. Even small PSDs offer a larger angular range and can typically record across ∼10° simultaneously, allowing faster data acquisition. These detectors are useful for time-resolved PD experiments, but they require careful calibration of the wire position for each MCA channel. A novel 1D detector

based on the Si-microstrip technology (used in detectors in particle physics experiments) called MYTHEN (Microstrip sYstem for Time rEsolved experimeNts) was developed at Paul Scherrer Institute (PSI) showing exceptional performance [106,107,8]. It covers an angular range of 120° and continues to evolve [108,109,110]. It has been commercialized for large-scale use by PSI's spin-off company DECTRIS.

Area (2D) detectors (e.g. imaging plates and charge-coupled device (CCD) cameras) also allow a large spatial sensitivity and are the standard choice in single-crystal x-ray diffraction [111]. Presently, the state of the art 2D detectors are the hybrid photon counting detectors (HPCDs) in which incoming x-rays strike a doped-Si or CdTe sensor layers and create electron-hole pairs. The electrons drift under a bias and are amplified by a readout application-specific integrated circuit (ASIC) bonded to the sensor. These detectors are the standard in most synchrotron light sources and notable examples include PILATUS [112] (also developed at PSI) and EIGER detectors both marketed by DECTRIS.

2.2.4 Synchrotron X-ray sources and instruments

When charged particles moving at relativistic velocities are accelerated in a direction perpendicular to their velocity (usually under an external magnetic field), they emit a linearly polarized radiation called synchrotron (also, *magnetobremsstrahlung*) radiation. They are the ultra-relativistic special case of cyclotron emission.

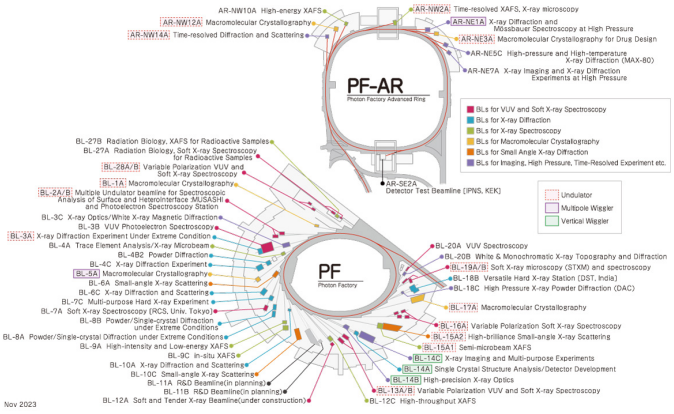


Figure 2.5: Layout of the two sources at Photon Factory (KEK, Japan) showing the electron storage rings and the placement of various beamlines (BLs). Image source: KEK-IMSS Website [10]. Copyright KEK IMSS.

In a synchrotron light source, typically electrons undergo an initial acceleration in a linear accelerator (linac) and then injected into a long, circular evacuated tube (the *storage ring*), lined by

numerous magnets, where they attain relativistic speeds. The synchrotron x-rays produced by these zooming electrons are then guided into different beamlines by a series of magnets (*undulators*) where they undergo an optics train (monochromators, collimators, filters, mirrors etc.) to be optimized for a specific experimental endstation depending on the required wavelengths (or energies). The layout of the Photon Factory light sources at KEK is shown in Fig. 2.5. In the following subsections, we briefly describe the PD endstations at synchrotron facilities used for this thesis.

2.2.4.1 BL-18B at Photon Factory, KEK (Japan)

The versatile hard x-ray station (BL-18B) at Photon Factory has a four-circle goniometer and typically uses Bragg-Brentano ($\theta - 2\theta$) geometry to perform temperature-dependent PD on samples. Fig. 2.6 (right) shows the copper sample stage used for loading the powder samples. It is attached to a cryogen-free cryostat capable of achieving $T \sim$10 K. The radiation energy available is 7 - 20 keV and two types of detectors - a point detector (cyberstar) and a 100K 2D pilatus detector are available for data acquisition[11].

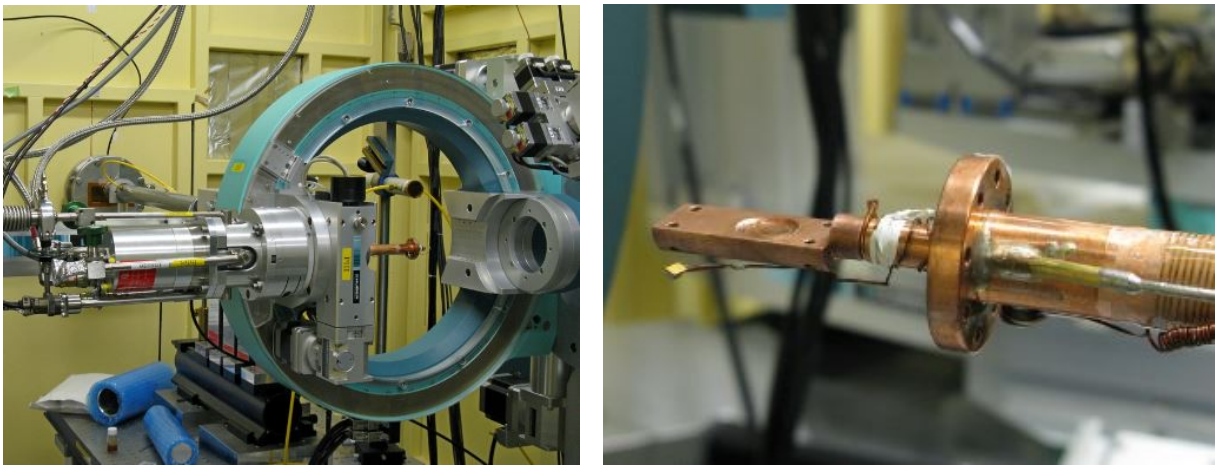


Figure 2.6: Left: The Versatile Hard x-ray station (BL-18B) at Photon Factory, KEK (Japan). Right: Sample stage used for PD experiments. Image source: SINP Website[11]. Copyright SINP.

2.2.4.2 ADDAMS at SLS, PSI (Switzerland)

The ADvanced DiffrAction for Materials Science (ADDAMS) at the Synchrotron Light Source (SLS) uses an in-vacuum, cryogenically cooled permanent magnet undulator (CPMU) with a magnet period of 14 mm as a source[12]. After passing through the beam optics, x-rays (energy range 5 - 40 keV) are incident upon the sample loaded in capillaries. A robotic sample changer

is available for quick and remote access (Fig. 2.7 (a)). Fig. 2.7 (b) shows a mounted sample aligned with the diffractometer axis. A Janis cryostat allows access to low temperatures up to 4.5 K. MYTHEN (see section 2.2.3) is primarily used for data collection. Its instrumental resolution with respect to microstructure analysis is discussed in more detail in Appendix B. A scintillator multi-crystal analyzer detector (MAD) is also available for high-resolution diffraction requirements.

2.3 Neutron scattering

Similar to x-rays, neutrons also interact with matter through scattering. Being chargeless, neutrons can penetrate deep into materials and interact directly with the nucleus via the strong nuclear force, called *nuclear scattering*. Because of their finite spin, neutrons also interact with unpaired electrons in the outermost shells of magnetic ions, called *magnetic scattering*. Both are briefly discussed as follows:

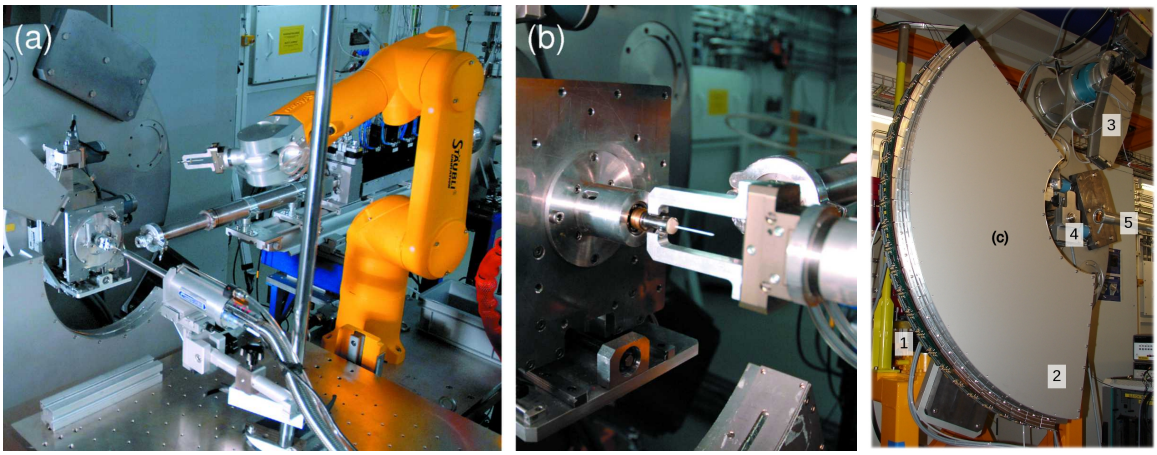


Figure 2.7: The PD setup at ADDAMS. (a) Robotic sample changer holding a capillary (b) Zoomed view of sample holder aligned with the diffractometer axis (c) the MYTHEN detector - 1: detector modules, 2: He-filled housing, 3: multi-crystal analyzer detector, 4: diffractometer center, 5: x-ray beam tube. Images reproduced with permissions [12,8]. Copyright IUCr Journals.

2.3.1 Nuclear scattering

An atomic nucleus can generally be approximated as a point source, which means that its spatial density distribution is a delta function with respect to the incident neutron wavelength. The atomic form factor (introduced in section 2.2), i.e. the FT of this delta function is 1, rendering the neutron scattering amplitude (or scattering length), b, independent of the scattering vector,

Q. Thus, it is often said that neutrons have no form factor. Elemental dependence of b is not well-defined and it is only estimated experimentally. This makes neutrons very sensitive to positions of even the lightest of atoms within a material, unlike x-rays which are unable to *see* low-Z atoms very well. This is also why fairly intense diffraction peaks can be obtained even at high angles whereas XRD peak intensities diminish significantly at large 2θ. This also allows neutrons to differentiate between isotopes of the same element.

2.3.2 Magnetic scattering

Additionally, neutrons being fermionic $s = 1/2$ particles also interact with the unpaired electrons present in the outermost orbitals of magnetic ions. The form factor for this process involves the diffuse spatial distribution of outermost electrons and hence, falls off rapidly at high angles. This also allows neutrons to distinguish between different oxidation states of the same element and visualize magnetic order within materials. The use of polarized neutron beams (with all incident neutron spins pointing in a chosen direction) is particularly valuable for solving nontrivial magnetic structures.

2.3.3 Neutron sources and instruments

For performing neutron scattering experiments, coherent and stable beams of neutrons are required which are produced in large nuclear reactors or spallation sources. NPD can be performed in either a constant wavelength mode or a time-of-flight mode. These concepts are discussed in the following subsections.

2.3.3.1 Reactor-based sources

The original way of producing neutrons was in nuclear reactors. In these sources, a radioactive nuclei like ^{235}U is bombarded with neutrons to trigger a chain reaction producing more neutrons as products. These neutrons are then slowed down (*moderated*) to produce a Maxwellian distribution in the desired energy (wavelength) ranges - called *thermal* or *cold* neutrons - and guided to various endstations using (typically Al) beam tubes. Reactor sources provide a continuous neutron flux and are often run in periodic cycles with regular downtime required for replacement of reactor fuel cells. Examples of some operational reactor-based facilities include the High-Flux Reactor (HFR) at the Institut Laue Langevin (ILL) at Grenoble, France, the High-Flux Isotope

Reactor (HFIR) at Oak Ridge National Lab (ORNL), USA and the Dhruva Reactor at Bhabha Atomic Research Institute (BARC), India.

2.3.3.2 Spallation sources

The modern, more efficient way to produce neutrons is through the *spallation* process (Fig. 2.8). In these sources, an accelerated proton beam is collided with a heavy metal target, resulting in the nucleus heating up and releasing $\sim$ 10 - 15 neutrons in all different directions. These neutrons are then moderated by a cold source of liquid deuterium and directed towards instruments via a neutron guide. The moderators contribute to instrumental parameters and the observed diffraction peak shapes.

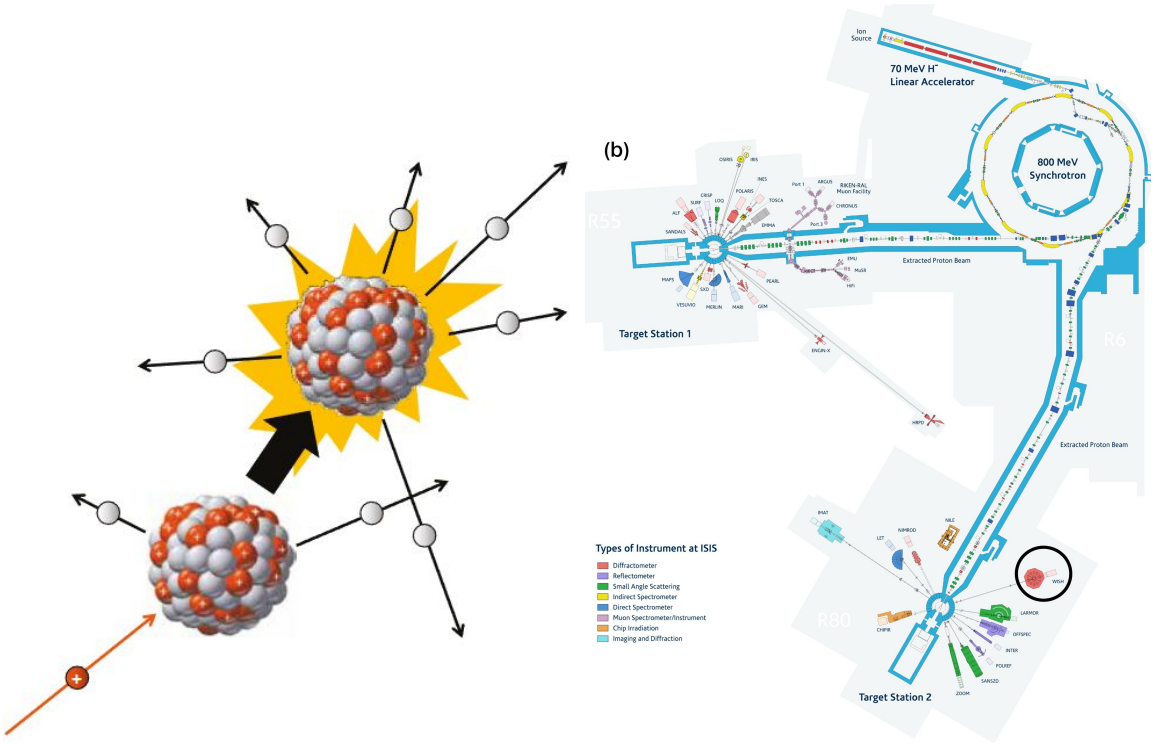


Figure 2.8: (a) The spallation process of neutron production (b) Instrument layout of the ISIS Neutron and Muon Source with the location of WISH circled. Image source: [13]

Most spallation sources are pulsed sources like the ISIS Neutron and Muon source at the Rutherford Appleton Laboratory (RAL), UK which uses a tungsten (W) target to produce neutrons [13]. SINQ at PSI is the only continuous spallation source in the world and uses a Pb target to generate neutrons [113].

2.3.4 Neutron Powder Diffraction

The principles of Bragg diffraction discussed in section 2.2 are applicable for neutrons as well, the particles constituting the incident beams being the only difference. NPD is the *elastic* case of the scattering process discussed in section 2.3 and returns information complementary to XRD. For a complete analysis of a material's structure, often both NPD and XRPD measurements are performed in tandem. Below we discuss the NPD techniques and related instruments used for the work in this thesis.

2.3.4.1 Constant wavelength diffraction

In a constant wavelength diffractometer, like the cold neutron diffractometer (DMC) at SINQ (PSI), the moderated neutron beam is passed through a monochromator which selects a chosen wavelength to strike the sample. The range available at DMC is 2.3 - 5 Å. Samples are loaded in cyndrical Vanadium cans since it is transparent to neutrons and rotated about the axis for complete powder averaging in a Debye-Scherrer geometry. Diffracted neutrons are then passed through a set of collimators before being detected by a ^{3}He gas-proportional detector with a 2D readout. The detector at DMC covers an in-plane angular range of 132° (2θ) and a simultaneous recording of count rates across 14° (2θ) with a maximum $q = 5.3\text{Å}^{-1}$. It offers high-intensity and high-resolution data at low q and numerous sample environments (T = 50mK - 1800 K, $H_z \leq 10$ T, $P = 9$ - 100 kbar), desirable for probing phase transitions and low magnetic moment structures[114].

2.3.4.2 time-of-flight diffraction

In time-of-flight (*tof*) diffraction, the incident neutron beam from the moderator contains a distribution of energies. The faster neutrons hit the sample first and are diffracted, thus a velocity-sorting occurs at the sample and a time-dependent diffraction pattern is measured at a fixed angle/resolution. At WISH (ISIS), there are five different detector banks, each with a specified resolution providing information from a wide q-range with high flux, especially useful for complex magnetic structures spanning large d-spacings. The wavelength range at WISH is 0.35 - 20 Å and 2×10^5 1D ^{3}He tube detectors are spread across an angular range of 320° giving access to exceptionally large q-values. Each ^{3}He tube can record neutron count rates across $\sim$15° (2θ) at once.

2.4 Diffraction data analysis

Powder diffraction data is often obtained in the form of intensities (I) vs 2θ (or d). As discussed in section 2.2, the first step is to index the peaks to find the unit cell parameters of the sample. The d-spacing of a particular hkl peak is given by

$$\frac{1}{d^2} = Ah^2 + Bk^2 + Cl^2 + Dkl + Ehl + Fhk \tag{2.2}$$

where A, B, C, D, E and F are parameters of the reciprocal unit cell. There are various free softwares available (DICVOL, NTREOR, McMaille etc.) that iteratively go through many combinations of these parameters to suggest possible unit cells (with associated figures of merit) corrresponding to a given list of peak positions. Usually at least 20 - 30 peaks, with intensities above a certain tolerance threshold need to be provided for the analysis to return viable results. This highlights the importance of collecting good powder patterns with intense and well-resolved peaks over a reasonable angular range (typically >80° (2θ)), to have any chance at solving the crystal structure of an unknown compound using PD.

A more common (and easier) way is to match the obtain patterns with those already reported in literature and then refine the starting model to obtain the accurate structural parameters. For this, one can use the various crystal databases (ICDD, COD etc.) to perform pattern matching or directly use structural parameters reported for similar compounds to simulate an XRD pattern using softwares like VESTA[115] or web resources like The Materials Project[116] as a starting model.

2.4.1 The Rietveld Method

Once an initial structural model is at hand, the next step is to refine it. This is done by using the Rietveld method, named after Hugo Rietveld who first described this method for analyzing NPD data using a least square fitting procedure[117]. Put simply, the program tries to minimize the difference between the observed data and the calculated profile from the input structural model. The list of softwares that allow structural refinement using this method is ever growing, however, FULLPROF[20], GSAS[118,119], TOPAS[120], JANA[121], EXPO and RIETAN[122] are some of the most popular and reliable ones, widely used among crystallographers.

The minimized function in FULLPROF is:

$$\chi^2 = \sum_{i=1}^{n} w_i \{y_i - y_{c,i}(\boldsymbol{\alpha})\}^2 \tag{2.3}$$

where y_i and $y_{c,i}$ are the observed and calculated i^{th} intensity, respectively, n is the total number of data points collected, $w_i = \frac{1}{\sigma_i^2}$ is the weight, σ_i being the uncertainty in y_i and $\boldsymbol{\alpha} = (\alpha_1, \alpha_2, ..., \alpha_p)$ is the set of parameters which are simultaneously refined iteratively until the convergence criteria is satisfied. p is the total number of varied parameters[123]. The calculated peak profile is given by:

$$y_{c,i} = \sum_{\varphi} S_{\varphi} \sum_{\mathbf{h}} I_{\varphi,\mathbf{h}} \Omega(x_i - x_{\varphi,\mathbf{h}}) + b_i \tag{2.4}$$

where $\mathbf{h}$ is the position of the peaks, S_{φ} is the scale factor of each phase φ included in the refinement (relevant for multiphase or magnetic structure refinement), $I_{\varphi,\mathbf{h}}$ is the calculated integrated intensity at $\mathbf{h}$ for each φ, Ω is the mathematical function (e.g. Gaussian, Lorentzian, Pseudo-Voigt etc.) that are used for peak modeling and b_i is the background at each i. The integrated intensity has many contributions mathematically represented as:

$$I_{\varphi,\mathbf{h}} = \{LAPCF^2\}_{\varphi,\mathbf{h}} \tag{2.5}$$

where, L combines the Lorentz, polarization and multiplicity factors, A is the absorption correction, P is the preferred orientation function, C includes special corrections, and F is the structure factor[123]. Various strategies are undertaken to refine a structural model depending upon the sample type and diffraction techniques and requires careful variation of parameters while keeping the physicality of the obtained values in mind[124,125]. The profile functions used to model diffraction peaks depend strongly on the type of instrument used and should be chosen carefully. For example NPD peaks are have a more Gaussian profile, whereas SXRD peaks are strongly Lorentzian in shape. XRD peaks are usually best modeled by a pseudo-voigt function, a convolution of the Lorentzian and Gaussian functions. A detailed discussion on the analysis of peak broadening (or FWHM, the full width at half maxima) to decouple instrumental contribution from the peak shapes to deduce the microstructural features is laid out in Appendix B for the interested reader.

The agreement between the calculated and observed pattern is measured by the various types of statistical R-factors. Some of the relevant ones are listed below[126,20]:

2.4.1.1 The reduced χ^2

The goodness-of-fit or reduced χ^2 is given by:

$$\chi^2_v = \frac{\chi^2}{(n-p)} = \left[\frac{R_{wp}}{R_{exp}}\right]^2 \tag{2.6}$$

where $(n-p)$ is the number of degrees of freedom. For a successful refinement, it is imperative that $n \gg p$.

2.4.1.2 The profile factor

The profile factor is calculated as:

$$R_p = 100\frac{\sum_{i=1}^{n}|y_i - y_{c,i}|}{\sum_{i=1}^{n} y_i} \tag{2.7}$$

2.4.1.3 The weighted profile factor

The square root of the minimized function χ^2 is the weighted R-factor R_{wp} given by:

$$R_{wp} = 100\sqrt{\frac{\sum_{i=1}^{n} w_i|y_i - y_{c,i}|^2}{\sum_{i=1}^{n} w_i y_i^2}} \quad \% \tag{2.8}$$

The conventional R-factors in FULLPROF cR_p, cR_{wp} are calculated by substituting $y_i \rightarrow y_i - b_i$, i.e. by using the background-corrected intensities[123].

2.4.1.4 The expected weighted profile factor

In case of an ideal model, the average of $(y_i - y_{c,i})^2 = (\sigma_i)^2$, i.e. $w_i(y_i - y_{c,i})^2 = 1$ - the best possible value that can be obtained for a given pattern data[127]. This *best possible* R_{wp} is called the

expected weighted profile factor R_{exp} and is given by:

$$R_{exp} = 100\sqrt{\frac{n-p}{\sum_i w_i y_i^2}} \quad \% \tag{2.9}$$

2.4.1.5 The Bragg R-factor

The Bragg R-factor only includes contribution from intensities of Bragg reflections and is defined as

$$R_{Bragg} = 100\frac{\sum_{\mathbf{h}} |I_{obs,\mathbf{h}} - I_{calc,\mathbf{h}}|}{\sum_{\mathbf{h}} |I_{obs,\mathbf{h}|}} \quad \% \tag{2.10}$$

with $I_{obs,\mathbf{h}}$ calculated as

$$I_{obs,\mathbf{h}} = I_{calc,\mathbf{h}} \sum_i \left\{ \frac{\Omega(x_i - x_{\mathbf{h}})(y_i - b_i)}{(y_{c,i} - b_i)} \right\} \tag{2.11}$$

This is a *proportional sharing* of intensities between overlapped reflections based on the model[123,127]. So in calculating R_{Bragg} the program makes $I_{obs,\mathbf{h}} = 0$ if the model expects $I_{calc,\mathbf{h}=0}$ at a given **h**. This also means that R_{Bragg} is not truly a statistical parameter and can be misleading for highly asymmetric peaks because of portions of the observed peaks being excluded from intensity calculations[127]. The magnetic Bragg R-factor (R_{mag}) is also calculated according to equation 2.10, except only magnetic intensities are used for its estimation[123].

Often, it can be difficult to reduce the χ^2 values beyond a certain threshold even when the fits obtained are visually very good. Better quality data, with a high number of counts will often increase the difference between R_{wp} and R_{exp} leading to a larger χ^2. This is because the discrepancies between the observed and calculated data are magnified as compared to the uncertainties in observed intensities[127]. It is important to carefully analyze the sources of errors (especially for strongly correlated parameters) during refinement to avoid getting stuck in local minima or ending up with unphysical parameters and divergent fits.

The refined parameters along with their uncertainties can be used to visualize the crystal structure and estimate bond lengths and angles using softwares like VESTA[115].

The morphology and elemental composition of a powder sample can be assessed using scanning electron microscopy (SEM) and energy dispersive x-ray spectroscopy (EDS). In a typical field-emission (FE) SEM, like the one at IISER Pune, an electron beam generated by a field emission gun is focused by condenser lenses to a nanometer sized spot on the sample. The final lens deflects the electron beam in the x and y directions allowing a raster scanning of a chosen rectangular area of the sample. The incident electrons interact with the sample in a teardrop shaped volume by a multitude of processes (selected ones shown in Fig. 2.9(b)), and produce secondary and backscattered electrons as well as characteristic x-rays specific to the elements in the sample. Secondary electrons are typically measured by a collector-scintillator-photomultiplier detector and the output voltage is displayed as an image after undrgoing analog-to-digital conversion. Since the brightness of the image is proportional to the number of secondary electrons reaching the detector, SEM is able to resolve changes in surface depth and the three-dimensional morphology upto nm resolution can be viewed. Backscattered electrons are captured by a circular-ring shaped detector concentric with the electron beam placed right above the sample and allow mapping of elemental composition across the sample surface due to their strong dependence on the Z, thus enabling sample homogeneity confirmation [128].

By tuning the energy of the electron beam, characteristic x-rays can also be generated from the sample. The number and energies of the x-ray photons allow the estimation of the atomic weight% of the of the element present in the sample. This measurement is also a Z dependent process and usually only heavier elements are used to estimate the elemental ratios and stoichiometry. A large number of scans ($\geq$ 30) at random regions of the samples are usually taken to improve statistical accuracy. A schematic of a SEM is shown in Fig. 2.9(a). For a typical SEM measurement on a polycrystaline sample, well-ground, fine powders are sprinkled on a carbon tape stuck to a stainless steel stub. The sample is kept in a dessicator and dried under vacuum for at least 0.5 - 1 hour in order to remove any moisture before loading into the FESEM sample chamber. An FESEM image obtained for $Ba_4LiRu_3O_{12}$ showing hexagonal crystallites is shown in Fig. 2.9(c).

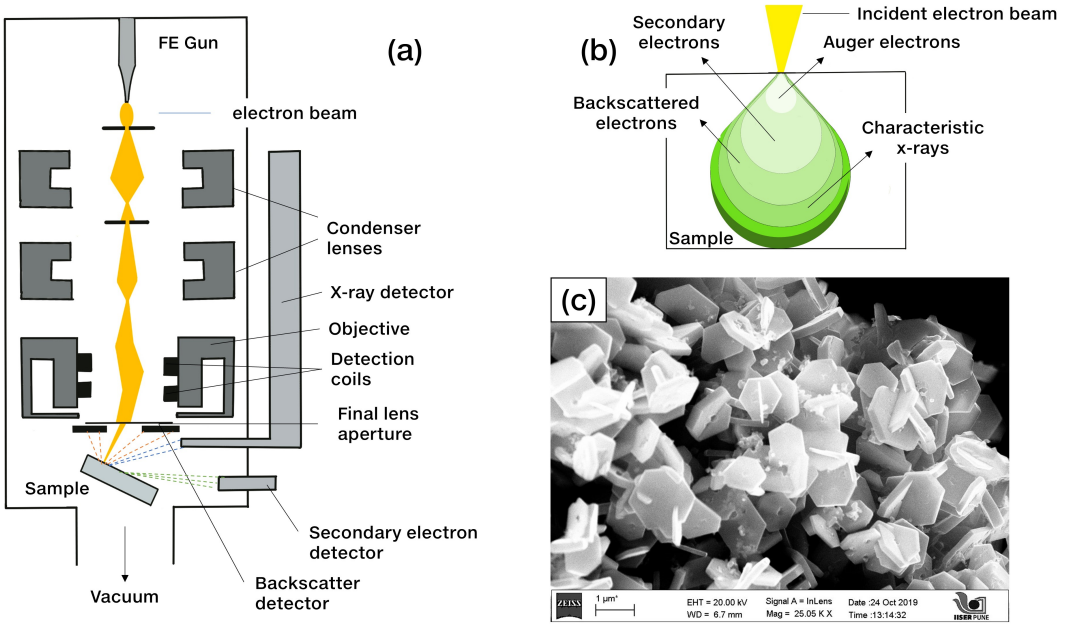


Figure 2.9: (a) Schematic of a SEM. (b) Origins of backscatter and secondary electrons, and characteristic x-rays due to electron-matter interaction. (c) An FESEM images showing μm sized hexagonal crystallites within $Ba_4LiRu_3O_{12}$ under a primary electron beam energy of 20 keV.

2.6 Magnetometry

The fundamental basis of magnetism is the magnetic moment, μ representing a magnetic dipole. When placed in an external magnetic field B, this moment has an energy equal to $E = \mu \cdot B$. A magnetic material is an overall collection of numerous such moments and the average magnetization M is defined as the magnetic moment per unit volume. Inside a solid, $B = \mu_0(H + M)$ and H is called the magnetic field strength and measured in A/m. In vacuum, H and B can be used interchangeably and only differ by a factor of vacuum permeability μ_0 [129]. Typically in magnetic measurements, the cgs system is preferred and moment is measured in units of electromagnetic units (emu). It is important to remember the relationship between these values when calculating magnetic properties from magnetization data. A visual representation of difference between the B, H and M is shown in Fig. 2.10.

In the linear approximation, $M = \chi H$ where χ is dimensionless magnetic (volume) susceptibility. χ is an important material property which measures the degree to which a material can be magnetized (or, is *susceptible* to an external field). In literature, materials are often categorized based on their molar susceptibilities $\chi_{mol} = \chi V_{mol}$, V_{mol} being the molar volume. The mass susceptibility

$\chi_{mass} = \frac{\chi}{\rho}$ (ρ is the material density) is another related value commonly used in literature[129].

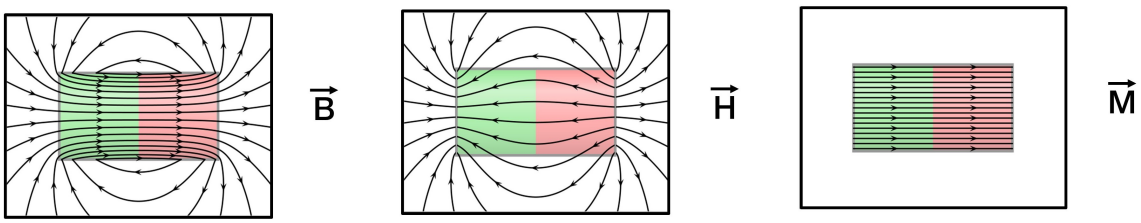


Figure 2.10: B, H and M field lines in- and outside a bar magnet.
Attribution: Geek3, VFPt magnets BHM, adapted for this thesis, License: CC BY-SA 4.0

2.6.1 Vibrating Sample and squid Magnetometry

A material's response to an external field B can be measured by moving the sample (*induction* method) between a set of copper pickup coils. The working principle is Faraday's law, according to which, the periodic sample motion induces change of magnetic flux and in turn, a voltage proportional to the magnetization inside the coils. The signals are detected through a lock-in detection (discussed in section 2.9.1.1) so as to isolate the sample response from contribution from other unwanted frequencies.

In modern commercial magnetic property measurement systems like the quantum design (qd) mpms, the copper pickup coils are substituted by a SQUID (Superconducting Quantum Interference Device), which provides enhanced sensitivity and is especially useful for probing low moment samples and magnetic phase transitions. A SQUID consists of Josephson junctions (superconductoring layers separated by thin insulating layers) which show a quantized flux change when placed under a time-varying current.

In the MPMS-XL, the sample is moved through a set of superconducting pickup coils wound in a second-derivative arrangement (as shown in Fig. 2.11 (b)). The changing magnetic flux induces a coil current which in turn produces a magnetic field which is inductively measured by the SQUID. The voltage response produced at the SQUID (Fig. 2.11(b)) is proportional to the average magnetic moment of the sample and is calibrated using standard paramagnetic samples like Pd. In a typical measurement, a sample (powder, pellet, crystals or films) are placed inside a gelatin capsule inserted into a plastic straw which is attached at the end of a sample rod. The rod is then inserted vertically into the sample space and pushed down until the sample is placed at the center of the magnet and the pickup coils. This is called *centering* the sample and is impor-

tant to obtain accurate moment values. The sample space is filled with low pressure He exchange gas which provides contact with a cooling annulus. Holes are punched into the plastic straw to allow the exchange gas to enter and cool the sample. The temperature of the sample space can be varied between 2 - 400 K and is controlled by two sets of heaters and sensors driven by a temperature controller board. The whole probe (including the coils and the magnet) are dipped in a dewar filled with liquid He whose level is measured by a sensor. The He recirculation is done through a closed cycle compressor attached at the top of the dewar space, connected to a high purity (>99.9999%) He gas cylinder. A simplified schematic of the MPMS probe is shown in Fig. 2.11(a) (not to scale).

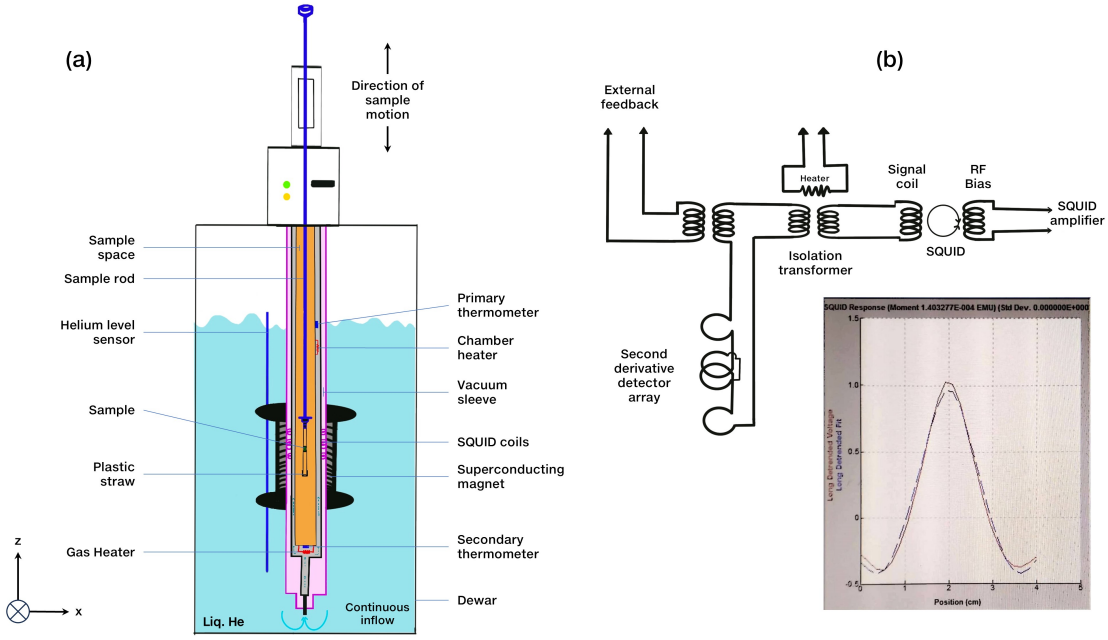


Figure 2.11: (a) Schematic of the QD MPMS-XL SQUID Magnetometer (b) Schematic of a longitudinal SQUID system and a typical measured SQUID response

2.6.1.1 AC SUSCEPTIBILITY

The above discussion applies to measurements under a static magnetic field. The dynamic magnetization response of a sample to a time-varying magnetic field can also be measured by the MPMS and provides a way to probe magnetic relaxation effects. This is particularly useful for characterizing materials like spin glasses, superparamagnets, superconductors and also investigate spin dynamics close to criticality in phase transitions. In a typical ac-susceptibility (ac-χ) measurement, the sample is perturbed by an oscillating magnetic field $H(t) = H_0 sin\omega t$, where H_0 and $\omega = 2\pi f$

are the amplitude and frequency of the applied field, respectively. $H(t)$ produces a time-varying moment $\mu(t)$ inducing a current in the pickup coil without moving the sample. The ac-χ technique is sensitive to the slope of the M(H) curve of the sample (and not the absolute moment) allowing the detection of subtle changes in the magnetic state of the sample. As f is increased, moments inside the sample find it increasingly difficult to follow the external field and M lags behind H. Thus, the measured susceptibility is a complex quantity with the in-phase (real) χ' giving the magnitude and the out-of-phase (imaginary) χ'' yielding the loss component. Image of an ac-χ measurement in progress on the MPMS-XL for the sample Ba_2CoRuO_6 (a cluster spin-glass discussed in Chapter 3) across its freezing transition is shown in Fig. 2.12.

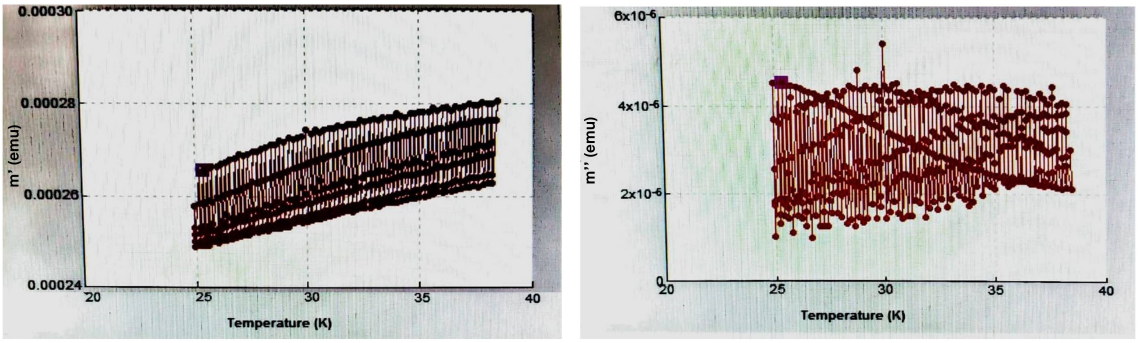


Figure 2.12: An ac-χ measurement being performed on Ba_2CoRuO_6 using the MPMS-XL

2.7 Thermal and electronic transport

Thermal and electronic transport measurements in this thesis were performed on QD PPMS (Physical Property Measurement System) as well as a VTI based setup in conjunction with a 7T cryomagnet from CRYOGENICS LTD. and a KEITHLEY DAQ6510 DMM with a cryogen-free closed cycled refrigerator (CCR). The basic principle and relevant details of these measurements are described in the following sections:

2.7.1 Specific Heat

The heat capacity at constant pressure C_P is defined as the rate of change of heat within a material with respect to temperature at constant pressure. The thermal dependence of C_P can offer a deeper look into the lattice, electronic and magnetic properties of a material. At low temperatures, C_P is able to directly probe the density of states and entropy change across phase transitions can

provide valuable information about the distribution of energies across quasiparticle modes.

In a typical $C_P(T)$ measurement, the sample is heated for a fixed duration of time (with constant power) and then cooled. The temperature of the sample is monitored as a function of time and the cooling curve is fitted to known models to compute C_P. This is known as *relaxation calorimetry*. The top and side view of the calorimeter option provided with the PPMS is shown in Fig. 2.13 (a) and (b). First, an *addenda* measurement is performed where the heat capacity of the sample platform along with a thin layer of Apiezon-N grease is measured across the desired temperature range. Then, the sample is gently placed on top of the grease layer and the total heat capacity is measured. The sample C_P is calculated by subtracting the addenda values from the total measured C_P. It is recommended to use samples smaller than 1 mm$\times$3 mm$\times$3 mm since larger samples increase the equilibriation time. This is pertinent for insulating samples which often have poor thermal conductivity, since only phonons modes are available to distribute the heat across the sample. In such cases, it becomes important to optimize thermal contact to avoid underestimating the sample C_P. The PPMS offers a temperature range of 2 - 300 K, limited only by the sample thermal coupling with the platform. Measurements can also be performed in presence of a magnetic field upto 9 T.

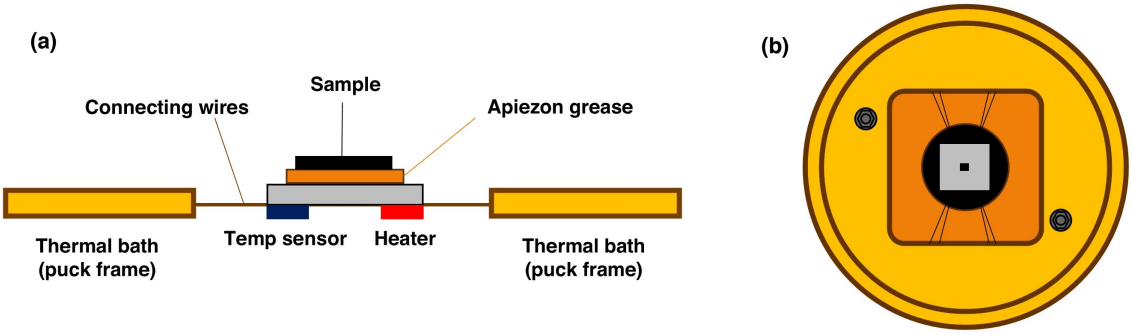


Figure 2.13: Schematic showing the (a) side and (b) top-view of the QD PPMS heat capacity puck.

2.7.2 Resistivity

Sheet resistivity of samples is measured in the four-probe arrangement. A schematic showing the lead connections for a typical measurement is shown in Fig. 2.14 (a). In this configuration, two outermost leads connected to a current source pass current through the sample leading to a voltage drop proportional to the resistance of the sample. Two inner voltage leads separated by a distance l measure the potential difference across l. The cross-sectional area A is given by

the product of the thickness and breadth of the sample ($t \times b$) and using these values and the measured resistance R the resistivity (ρ) can be calculated as $R = \frac{\rho l}{A}$. Fig. 2.14 (b) shows the resistivity probe and 8-pin sample stage from CRYOGENICS LTD. and Fig. 2.14 (c) shows samples stuck onto a PPMS Electrical Transport Option (ETO) puck with gold wire contacts affixed on the sample using conductive silver paste. For insulating samples, the two-wire configuration can also be used and for samples with R > 10MΩ, it is recommended.

Resistivity of materials is a temperature-dependent quantity and this can be exploited to investigate the evolution of the electron transport mechanisms dominant in different temnperature regimes. All the samples studied in this thesis are semiconductors and $\rho(T)$ measurements allow us to study the correlation between the spin and charge degrees of freedom, especially across phase transitions.

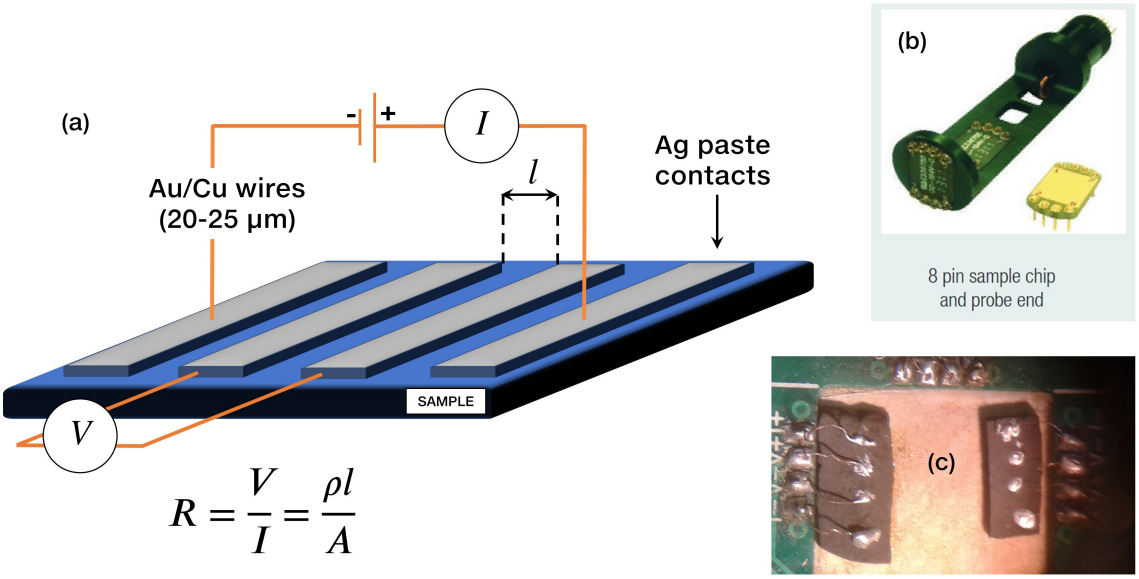


Figure 2.14: (a) A schematic showing the measurement of sheet resistivit of a sample in the four-probe method. (b) Sample stage and probe end of the resistivity option from CRYOGENICS LTD. Image source: CFMS Brochure [14] (c) Image of samples loaded onto the PPMS puck with gold wire and silver paste contacts.

2.8 Broadband Dielectric Spectroscopy

Broadband dielectric spectroscopy (BDS) is a popular technique to study the electric polarization response as a function of frequency spanning many decades. This allows access to variation relaxation mechanisms that electric dipoles follow when subjected to an oscillating electric field $E(t)$. When a dielectric material is placed in a static electric field E, it leads to separation of charge

density within the material, giving rise to an internal electric field, called the *displacement* field D. Additionally, the dipole moment density develops, called the *Polarization P*. These three quantities are related as $D = \varepsilon_0(\varepsilon^* + \chi_E^*)E$. This is analogous to the relationship between B, H and M discussed in section 2.6. χ_E^* and ε^* are complex quantities called the electric susceptibility and the dielectric permittivity, respectively. Under $E(t)$, ε^* is frequency dependent and is given by:

$$\varepsilon^*(\omega) = \varepsilon'(\omega) - i\varepsilon''(\omega) \tag{2.12}$$

where $\omega = 2\pi f = 2\pi/t$[130].

In this work, BDS in the linear approximation has been performed in the parallel-plate capacitor configuration with the help of NOVOCONTROL Alpha-A high-performance frequency analyzer in the 2-wire impedance measurement mode. The Alpha-A mainframe (Fig. 2.15) contains a frequency response analyzer (FRA) along with a dc bias generator (GEN) and two analysis channels V1 and V2. The Alpha-A sends a periodic voltage $U(t) = U_0 cos\omega t = Re(U^* e^{i\omega t})$ to the sample, generating a response current $I(t) = I_0 cos(\omega t + \varphi) = Re(I^* e^{i\omega t})$, where φ is the phase difference between $U(t)$ and $I(t)$. The complex quantities U^* and I^* are related to U_0 and I_0 as $U_0 = U^*$ and $I_0 = |I^*| = \sqrt{I'^2 + I''^2}$ so that $\varphi = tan^{-1}\left(\frac{I''}{I'}\right)$. The impedance of the sample is then given by

$$Z^* = \frac{U^*}{I^*} = Z' + iZ''$$

The voltage across the sample U^* is directly measured at the mainframe channel V1. The current I^* is passed through a current-to-voltage (I-V) converter with a variable resistance R_x. The resultant voltage $U_2^* = -I^* R_x$ is measured at channel V2. Alpha-A then performs a Fourier correlation analysis to calculate the sample impedance

$$Z^* = \frac{U^*}{I^*} = -\frac{U^*}{U_2^*} R_x \tag{2.13}$$

Z^* is related to the sample permittivity $\varepsilon^*(\omega)$ as

$$\varepsilon^*(\omega) = \frac{-i}{\omega Z^*(\omega) C_0} \tag{2.14}$$

$C_0 = \frac{A\varepsilon_0}{d}$ being the vacuum capacitance[15]. $\varepsilon'(\omega)$ and $\varepsilon''(\omega)$ can be calculated from the real and

imaginary components of Z^* as

$$\varepsilon' = \frac{-1}{\omega C_0}\frac{Z''}{|Z^*|^2} \qquad\qquad \varepsilon'' = \frac{1}{\omega C_0}\frac{Z'}{|Z^*|^2}$$

with the loss factor tanδ is given by

$$tan\delta = \frac{\varepsilon'}{\varepsilon''} = \frac{-Z'}{Z''}$$

The contact electrodes are prepared by coating conductive silver paste and affixing thin copper wires on the top and bottom surfaces of a cylindrical pellet samples of thickness 0.5 - 1 mm. The samples are then stuck onto a sample stage to the CCR cold finger (see Fig. 2.16) using GE Varnish and measurements are performed in the temperature range 20 - 300 K and a frequency range of 0.3 Hz - 1 MHz. The sample chamber is evacuated using a oil diffusion pump (HIND HIGH VACUUM) to typical pressures of $< 1 \times 10^{-3}$ mbar. The measurements are automated by a program written in LABVIEW allowing simultaneous frequency and temperature measurements.

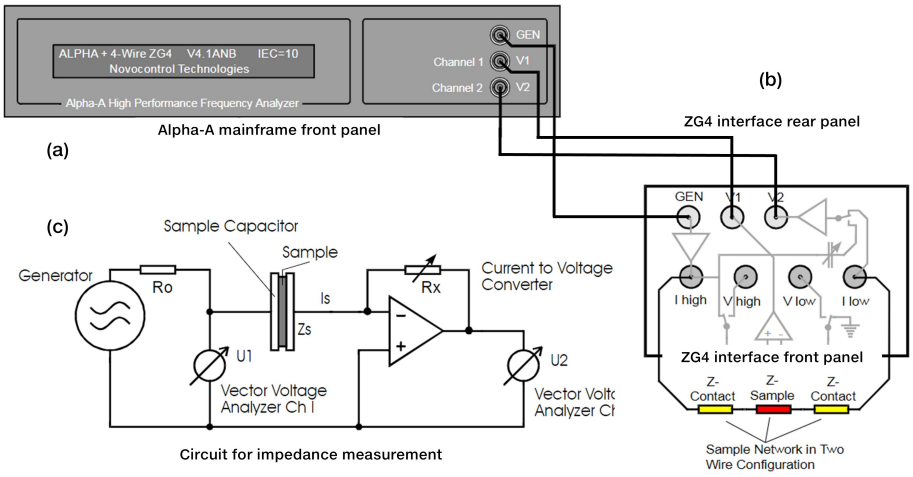


Figure 2.15: (a) The Alpha-A mainframe front panel. The GEN channel is the signal generator output, sent to the sample via the ZG4 interface (b) The ZG4 test interface. The sample leads are connected to the BNC inputs I high and I low on the front panel. The V1 and V2 rear panel outputs are connected to the mainframe V1 and V2 analyzer inputs. (c) The circuit schematic for an impedance measurement [15]

During a measurement, the program goes through a temperature control loop, establishing temperature stability, then communicates with the Alpha-A through the NOVO GPIB Card setting the input voltage amplitude (typically 1 V). The program then recursively loops through the

list of frequencies provided by the user at which impedance is to be measured. The program allows both discrete frequencies as well as a range of frequencies measured at a specified interval. Apart from this stepwise scan of (T, f) it is also possible to let Alpha-A measure $Z^*(\omega)$ recursively at defined time-intervals without controlled cooling/warming. This is sometimes preferable for quicker routine measurements, since the extra time required for temperature stability is eliminated.

2.9 Instrumentation: Nonlinear Dielectric Susceptibility

Section 2.8 discusses dielectric spectroscopy when it is limited to measuring the polarization response of a sample to an applied AC field in the linear approximation. However, the total polarization response (P) can be expressed as a power series:

$$P = \varepsilon_0(\chi_1 E + \chi_2 E^2 + \chi_3 E^3 + ...) \tag{2.15}$$

including higher-order terms with respect to the time-varying external electric field E[131,132]. For a sinusoidal applied field $E = E_0\, sin(\omega t)$, eq.2.15 becomes:

$$P(t) = \varepsilon_0 \sum_{i=1}^{n} \chi_i E^i = \varepsilon_0 \sum_{i=1}^{n} \chi_i E_0^i\, sin^i(\omega t) \tag{2.16}$$

Simply using the trigonometric identities for $sin^i(\omega t)$ for $i = 1, 2, 3$ gives:

$$\frac{P(t)}{\varepsilon_0} = \frac{1}{2}\chi_2 E_0^2 + \left(\frac{3}{4}\chi_3 E_0^3 + \chi_1 E_0\right) sin(\omega t) - \left(\frac{1}{2}\chi_2 E_0^2\right) cos(2\omega t) - \left(\frac{1}{4}\chi_3 E_0^3\right) sin(3\omega t) \tag{2.17}$$

demonstrating how the polarization is actually dependent on the higher harmonics of the fundamental frequency ω[132].

The displacement current, I through a dielectric material is related to P as:

$$I = S\,\frac{\partial(\varepsilon_0 E + P)}{\partial t} \tag{2.18}$$

where S is the cross-sectional surface. Differentiating eq.2.17 with respect to time and inserting it in eq.2.18 gives us an expression relating the displacement current with the applied ac-field[132]:

$$I = \varepsilon_0 \omega S \left[\left((\chi_1 + 1)E_0 + \frac{3}{4}\chi_3 E_0^3 \right) cos(\omega t) + \left(\chi_2 E_0^2 \right) sin(\omega t) - \left(\frac{3}{4}\chi_3 E_0^3 \right) cos(\omega t) \right] \quad (2.19)$$

This also tells us that the odd harmonics of the response current are out of phase with the applied field (voltage) and must be taken care of during the measurement. The prefactors of the sin and cos arguments are the harmonics $I_{1,2,3}$ and each depends linearly on $\chi_{1,2,3}$ which allows us to obtain:

$$\begin{aligned}
\chi_1 &= \frac{1}{\varepsilon_0 S\omega}\frac{d}{V_0}(I_1 + I_3) - 1 \\
\chi_2 &= \frac{1}{\varepsilon_0 S\omega}\left(\frac{d}{V_0}\right)^2 I_2 \\
\chi_3 &= \frac{1}{\varepsilon_0 S\omega}\left(\frac{d}{V_0}\right)^3 \left(-\frac{4}{3} I_3 \right)
\end{aligned}$$

where $E_0 = V_0/d$, V_0 and d being the amplitude of the applied sinusoidal voltage and thickness of the sample respectively.

For lossy dielectrics, I becomes complex (I^*) and the above equations can be reinterpreted to give the real and imaginary susceptibilities χ_i', χ_i'' as follows:

$$\begin{aligned}
\chi_1' &= Im\left[\frac{1}{\varepsilon_0 S\omega}\frac{d}{V_0}(I_1 + I_3) - 1\right] & \chi_1'' &= Re\left[\frac{1}{\varepsilon_0 S\omega}\frac{d}{V_0}(I_1 + I_3) - 1\right] \\
\chi_2' &= Re\left[\frac{1}{\varepsilon_0 S\omega}\left(\frac{d}{V_0}\right)^2 I_2\right] & \chi_2'' &= Im\left[\frac{1}{\varepsilon_0 S\omega}\left(\frac{d}{V_0}\right)^2 I_2\right] \\
\chi_3' &= Im\left[\frac{1}{\varepsilon_0 S\omega}\left(\frac{d}{V_0}\right)^3 \left(-\frac{4}{3} I_3 \right)\right] & \chi_3'' &= Re\left[\frac{1}{\varepsilon_0 S\omega}\left(\frac{d}{V_0}\right)^3 \left(-\frac{4}{3} I_3 \right)\right]
\end{aligned}$$

This method of measuring the higher-order susceptibilities of a dielectric by measuring the harmonics of the displacement current was proposed by Miga, Dec and Kleemann[132] and remains a niche technique, due to the challenge in measuring the relatively miniscule nonlinear terms as compared to the fundamental response. However, in many cases, especially for disordered and correlated ferroelectric materials, they can potentially provide crucial information that is not available in the fundamental response.[131,132]

2.9.1 The Setup

To probe the nonlinear dielectric behaviour of layered perovskite materials we custom-built a susceptometer based on the technique proposed by Miga, Dec and Kleeman[132] but with small modifications. Instead of using an A/D converter on a KPCI card, we use a Lock-in amplifier (LIA) (Stanford Research Systems, SR830) both as an ac-voltage source and as a measurement unit. This ensures that no phase discrepancies are present between the source and the signal input. The sample's time-varying current response is amplified and converted to a voltage using a current pre-amplifier (Stanford Research Systems, SR570) in the low-noise mode. This significantly improves the signal to noise ratio for the harmonic signals and enables their simultaneous measurement with the much larger linear response. The temperature of the sample is controlled using a Lakeshore 335 Temperature Controller, a Lakeshore Diode sensor (DT-670-CU) and a 50 W Cartridge Heater. Cryogenic temperatures down to 20 K attained using a Cryo Industries Model-204 Cryogen-free CCR and the sample space is evacuated using an oil diffusion pump. The schematic of the setup is shown in Fig. 2.16

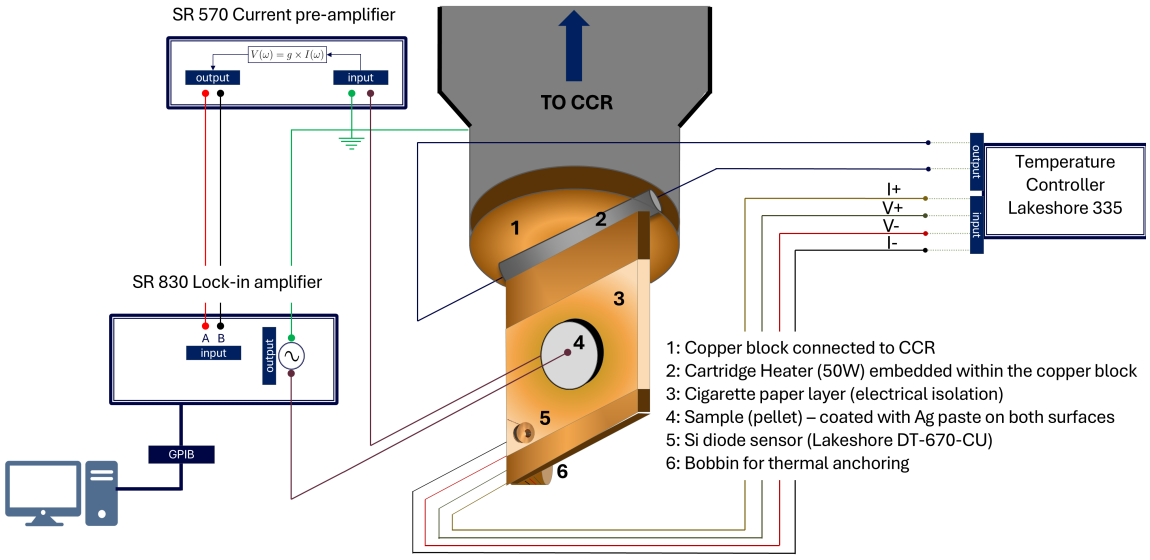


Figure 2.16: A schematic of the custom-built setup for measuring nonlinear dielectric susceptibility $\chi_{n>1}$

The sensitivity threshold of the setup is in the range of a few μVs, with data acquisition being fully automated through a LabVIEW program (Fig. 2.17). The program first establishes temperature control and waits until the temperature setpoint is reached. Once temperature stability is con-

firmed, the LIA is initialized the sine voltage is applied. The noise at the X and Y LIA channels is monitored until they are below a certain threshold value (decided based on the SNR of the measured harmonic voltage) and finally the X and Y voltages are measured. The whole $T \rightarrow f \rightarrow h$ loop is repeated for each harmonic h and a .csv file is generated at the end of the measurement. To protect the input amplifiers of the LIA from being overloaded, the program also automatically decides the optimum sensitivity for a given f, h. The communication between the computer and the instruments is established using a KEITHLEY USB-GPIB controller.

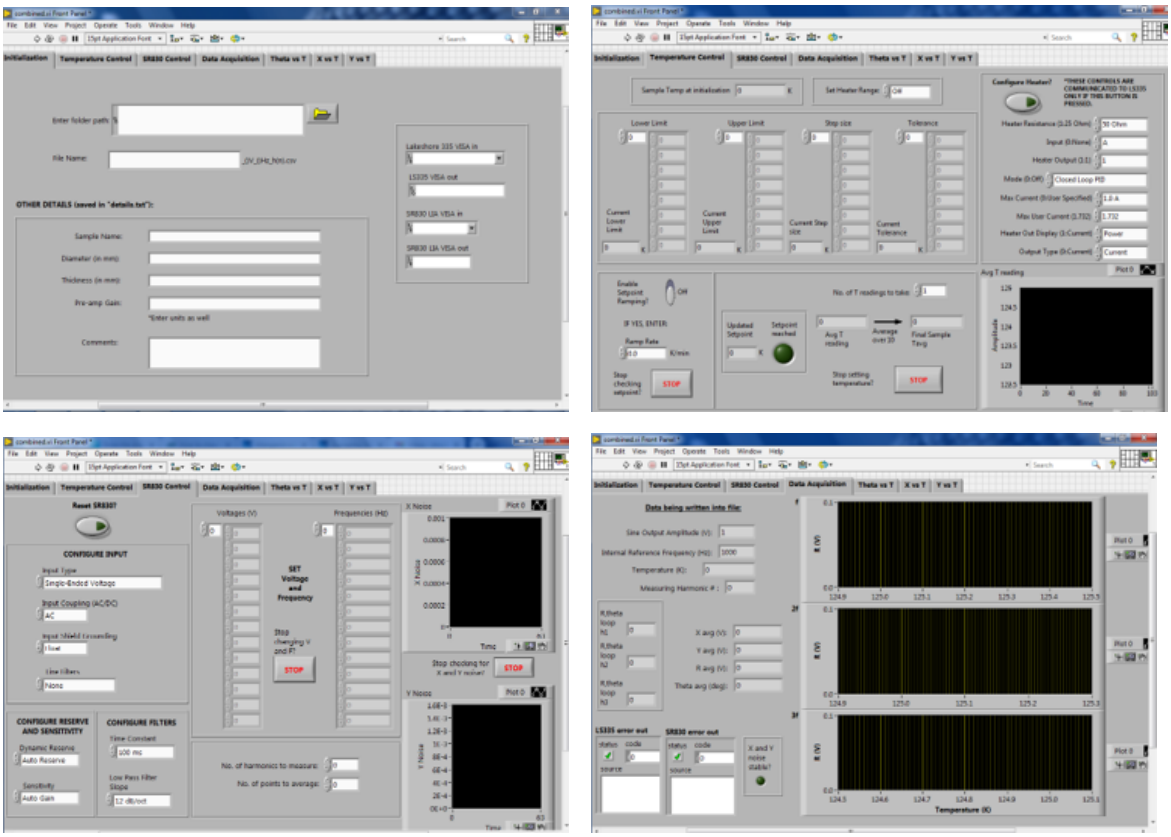


Figure 2.17: Snippets of the LabVIEW program front panel

A brief overview of the components used in the setup are described as follows:

2.9.1.1 THE LOCK-IN AMPLIFIER, SR830

Lock-in amplifiers (LIAs) use the phase-sensitive detection (PSD) technique to *lock-in* to a specified (*reference*) frequency and phase. Signal contribution from all other frequencies are rejected and do not influence the measurement. This allows a LIA to accurately measure even weak signals buried in a noisy background. In order to measure an input signal $V(t) = V_0 sin(\omega t + \varphi)$,

the LIA generates its own reference its own reference signal $V_{ref} = V_L sin(\omega_L t + \theta)$, amplifies $V(t)$ and then multiplies it by V_{ref} using a PSD. The PSD output then is

$$\begin{aligned} V_{PSD} &= V_0 V_L sin(\omega t + \varphi) sin(\omega_L t + \theta) \\ &= \frac{1}{2} V_0 V_L [cos\{(\omega - \omega_L)t + \varphi - \theta\} - cos\{(\omega + \omega_L)t + \varphi + \theta\}] \end{aligned}$$

having contribution from two frequencies (ω-ω_L) and (ω+ω_L). Now, if $\omega = \omega_L$, the low-pass filtered V_{PSD} is

$$V_{PSD} = \frac{1}{2} V_0 V_L cos(\varphi - \theta) \tag{2.20}$$

i.e. a dc voltage proportional to the signal amplitude[16]. The low-pass filter attenuates all frequencies differing from ω_L depending on its bandwidth. A narrower bandwidth results in a PSD output closer to dc values. Further, a LIA uses a *phase locked loop* (PLL) to make $\omega = \omega_L$ as well as to keep the phase difference $\varphi - \theta$ constant (*phase locking*). In our experiments, we use the internal oscillator of SR830 as the excitation source, so that lock-in reference is internal and the source and the reference are always *locked in*. SR830 has two PSDs for each output channel - X and Y. Channel X measures the voltage proportional to $cos(\varphi - \theta)$ (eq.2.20). The Y output is obtained by multiplying the signal with the reference phase-shifted by 90°yielding a PSD output[16]

$$V_{PSD2} = \frac{1}{2} V_0 V_L cos(\varphi - \theta + 90) = \frac{1}{2} V_0 V_L sin(\varphi - \theta) \tag{2.21}$$

The voltages obtained in eqs.2.20 and 2.21 are the in- and out-of-phase components - V_X and V_Y of the signal measured by the LIA. The magnitude of the signal is given by $R = \sqrt{V_X^2 + V_Y^2}$ and the phase difference between the input and the reference is $\varphi - \theta = tan^{-1}\left(\frac{V_Y}{V_X}\right)$. LIA outputs are always rms voltages and the phase is measured in degrees[16]. The block diagram of the SR830 is shown in Fig. 2.18(a).

2.9.1.2 The current pre-amplifier, SR570

As mentioned in section 2.9, the difficulty in measuring the higher harmonics of the sample current arises from their significantly smaller magnitudes compared to the fundamental signal. The SR570 low-noise current pre-amplifier is used to overcome this challenge. It outputs a voltage proportional to the input current with discrete sensitivity options from 1 mA/V to 1 pA/V[17]. The block diagram of the internal circuit of the SR570 is shown in Fig. 2.18(b). To further con-

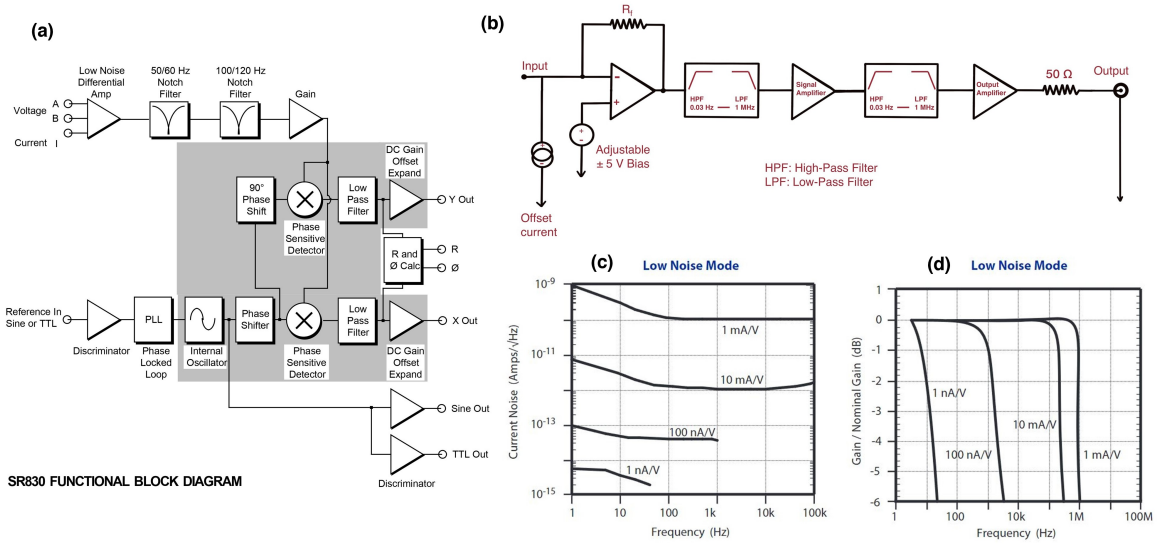


Figure 2.18: Block diagram of a (a) functional SR830 LIA [16] and (b) SR570 pre-amplifier [17]. The (c) current and (d) gain characteristics of SR570 in the low-noise mode [18].

figure the output voltage, various combinations of (+/-) voltage bias, (+/-) current offsets, filters (high/low/band-pass), inverters and gain modes (low noise/high bandwidth/low drift) are available. We perform all our measurements in the low noise gain mode which quickly lifts low-level signals above the instrument's noise floor [17]. Although the chassis is connected to the common ground of the whole instrument, the SR570 itself operates on a floating ground, thus protecting the amplification circuit from ground voltage fluctuations from the ac power supply or elsewhere [17]. Fig. 2.18 (c) and (d) show the current noise and gain characteristics for different sensitivities in the low noise mode [18]. It is important to check these characteristics before deciding the operational mode of the intrument, which must be optimally matched to the measurement ranges.

2.9.1.3 Temperature control and wiring

The LAKESHORE 335 temperature controller is the versatile centerpiece of the temperature control circuit. It provides two channels each for current output (50 W, 25 W or 75 W and 1 W combination) and sensor input, with default calibrations available for RTD (resistance temperature detector), diode and thermocouple sensors. The user also has the option to input their own sensor calibration file. The outputs are closed-loop PID (proportional-integral-derivative) controlled and the parameters can be manually adjusted or autotuned. The instrument can be automated using a GPIB or USB interface [133].

In our setup, cooling is achieved using a Gifford-McMahon (GM) cyrocooler with a cold-finger. In a GM cycle, the coolant He gas undergoes a 4-step pressurization-expansion cycle, driven by a displacer oscillating at $\sim$ 1 Hz, extracting heat from the first stage and transferring it to a sink (water). The first and second stage are thermally connected to transport heat from the thermal load at the second stage, and a 50 W cartridge heater located between the cold-finger and the sample allows controlled heating and cooling. Cartridge heaters are Joule heating elements with precisely wound resistive wires (Ni-Cr, here) and insulated solid pins provided for current supply. Two diode sensors, one at the CCR second stage and one close to the sample, monitor the temperature and provide the input feedback for the heater control. The temperature sensor must be chosen according to the experiment and attributes like temperature range, accuracy and resolution, magnetic and radiation resilience, ease of installation, and price need to be considered. For the present case, Si diode sensors are the best choice since they can be used over a wide T range (1.5 - 400 K), offer reasonable average temperature accuracy of < 0.1 K ($\sim$ 0.03 K below 30 K), a wide variety of package options and nominal pricing. We use a bolt-down package (CU) of the DT-670 Si diode sensor from LAKESHORE here, in which the sensor is indium soldered to a gold-plated copper bobbin along with the four thermally anchored 0.91 m 36 AWG long insulated leads, both wrapped in Stycast epoxy. The bobbin has a flat base with a small hole in it which allows installation either by adhesion (using GE Varnish, Apiezon grease or epoxy) or using a 4-40/M3 screw. The sensor and heater leads (4+2) are finely soldered to counter wound copper wires firmly wrapped around the CCR second stage and taped with a cryogenic tape. This is to ensure that the wires have good thermal contact with the CCR stages and no thermal gradient induced voltages accompany the sensor voltage, as the two ends of the wires would be at very different temperatures when the sample is cooled[134]. They are then connected to LS 335 through a vacuum compatible 9-pin connector located near the CCR head. It is important to be careful while soldering the sensor leads to the copper wires since keeping the thin leads in contact with a soldering gun for too long can heat the sensor and damage it. Often the sensor is kept in contact with a thermal bath to protect it from damage and dissipate the heat flowing to it. The same is done for the two signal carrying cables connecting the sample to the pre-amplifier. The temperature control and sample current response circuits are kept isolated from each other to ensure there is no interference or coupling between them. Specialized cryogenic ultra-miniature coaxial cables with stranded copper (SC) center conductors (32 AWG) are used. These cables have a nominal attenuation of 0.108 dB/m for signals with $f < 1$ MHz and are mechanically

flexible due to their braided construction. The shields are a 12×3 matrix of 42 AWG braided gold-plated copper wires and both the center conductor and shield has a Teflon FEP insulation. These cables have superior conductance and should be preferred when minimizing signal loss due to conductor resistance is of prime importance[135].

2.9.1.4 Vacuum techniques

The sample space is evacuated to chamber pressures <1 $\times 10^{-3}$ mbar with the help of an oil diffusion pump. These are convection-driven pumps that use high-speed jets of oil vapors to direct gas molecules to the bottom of the pump and out toward the backing rotary pump. The vapor jets are created by heating oil stored in a reservoir and the pump walls are cooled by a liquid nitrogen cold trap to prevent backstreaming of oil into the vacuum chamber. The oil vapors on contact with the cool surface condense and are recovered back into the reservoir. The vacuum in the roughing and backing lines are monitored by using Pirani gauges and the high vacuum is measured by a Penning gauge. The sample chamber as load is connected to the vacuum chamber by using a KF25 baffle and continuously pumped during the measurement. It is important to ensure that there are no leaks in the joints, otherwise condensation of water vapor and other gases may occur at low temperatures inside the sample space and on the CCR stages, which will not only restrict the system from attaining desired T setpoints but also can damage the CCR body.

2.9.1.5 Grounding

The final (and probably one of the most important) consideration for low-level measurements is ensuring proper grounding of the measurement circuit. It is an essential part of instrumentation to ensure uncontaminated measurement signals and protect instruments from being damaged by random voltage surges. The most common way is to have a star ground - a single point where the grounds and shields of all the components of the circuit are connected. If frequency-dependent noise is observed, electromagnetic interference from nearby instruments should be investigated. This includes other high power instruments connected on the power supply line, air conditioners, and even mechanical vibrations from instruments like the CCR or vacuum pumps (which contribute to low-frequency noise). In case there are random fluctuations in the measured signal, the earth line of the power supply should be investigated. Often, the metallic conductors connected to the literal earth, needs refreshing and begin to develop a voltage which contributes to forming ground loops. Instrument racks often have their own sockets connected to a main power supply.

The earth pins of these sockets should have proper contact with the main earth line as well. Some instruments, like the FRA, LIA, and preamplifier, discussed in sections 2.8 and 2.9.1.1, require to be operated at a float/open ground to protect their internal circuitry from interference. User manuals should be consulted and paid attention to, since mishandling can damage sensitive circuit boards within these instruments permanently. There is no *cookbook* for ensuring clean signals really, but frequent troubleshooting and careful analysis of the circuit along with some patience and care for the instruments can help one obtain accurate and reproducible measurement signals, contributing to the advancement of good science.

Bring forward what is true. Write it so that it is clear. Defend it to your last breath.

Ludwig Boltzmann

3

Ba_2CoRuO_6: A disorder-driven cluster glass

This work has been published as Chakravarty et al., "*Disorder-driven cluster glass state in a geometrically frustrated hexagonal perovskite*" *Physical Review B* **107**, 134414 (2023)[136]

3.1 Introduction

As discussed in Chapter 1, the structure of perovskites is strongly influenced by the ratio of the ionic radii of A and B cations, quantified in the *Goldschmidt ratio, t* (eq.1.11) and when $t > 1$ face-sharing and hexagonal crystal structures are favored[52]. The *6H* perovskite structure is commonly found in triple perovskite layered systems with the chemical formula $A_3BB'_2O_9$, where the B and B' cations occupy two distinct crystallographic sites. These structures feature face-sharing octahedra, or dimers, where strong orbital overlap between the B' cations can occur, competing with both intra- and inter-octahedra superexchange interactions. In some *6H* perovskites, the strong hybridization between B' and oxygen orbitals suggests that the B'_2O_9 dimers might act as "molecular units" instead of individual ions[79,137]. The ongoing debate about whether these face-shared dimers should be considered as molecules with defined molecular orbitals is a curious aspect of *6H* perovskites[138].

The combination of $3d/4d$ cations in B and B' sites is especially intriguing due to the contrast-

ing spatial extents of 3*d* and 4*d* orbitals and the increased significance of spin-orbit coupling in 4*d* systems. Ru^{5+}, in particular, stands out as a 4*d* ion because it borders between localized and delocalized electron behaviour[52], owing to the high correlation energy of its t_{2g}^3 configuration and a broad 4*d* valence band. The ability to tune these dimers from localized (superexchange) to itinerant (direct exchange or metal-metal bonding) behaviour allows Ru-based perovskites to exhibit a wide range of electronic and magnetic phenomena, such as orbital/charge ordering[79], frustrated molecular quantum magnets[139], large zero-field splitting[140], orbital-selective Mott insulating behaviour at the molecular, incommensurate magnetic structures[141], glassy dynamics and magnetic frustration[142,143,144], colossal dielectric constants[145], spin-liquid behaviour[146], and even superconductivity[147].

Ba_2CoRuO_6, unlike a prototypical double perovskite with rock-salt order, mimics a 6*H* structure with $t = 1.071$ random distribution of Co and Ru within the face-sharing octahedra, and its chemical formula can be rearranged as $Ba_3Co[Co_{0.25}Ru_{0.75}]_2O_9$. The ordered triple-perovskite version $Ba_3CoRu_2O_9$ is an intriguing material in itself, with strong evidence of spin, charge and orbital ordering. It undergoes a $P6_3/mmc \rightarrow Cmcm$ structural transition, an antiferromagnetic transition, and an electronic transition at $T_N = 93$ K. An orbital ordering arising from the distortion of the Ru_2O_9 dimers has been proposed as the reason for this strong coupling[148]. When disorder is introduced, the oxidation state of Co increases from +2 to +3 and all three types of long-range order are suppressed. A thorough analysis of the influence of disorder on the magnetic ground state is detailed in the following sections.

3.2 Synthesis and preliminary characterization

Polycrystalline Ba_2CoRuO_6 samples were synthesized using a solid-state method with stoichiometric amounts of high-purity $BaCO_3$ (Alfa Aesar, 99.95%), Co_3O_4 (Alfa Aesar Puratronic, 99.9985%), and RuO_2 (Alfa Aesar, Anhydrous, 99.9%), following the procedure described in[149]. The raw materials were mixed and ground in ethanol using a mortar until a fine, homogeneous mixture was achieved. The mixture was then heated twice at 1150°C for 24 hours each, with intermediate regrinding and pelletization. Room temperature laboratory XRD measurements, conducted on a Bruker D8 Advance diffractometer (CuKα, $\lambda = 1.5406$ Å), confirmed the sample to be pure and single-phase. The homogeneity and elemental composition were further verified using an energy dispersive X-ray spectrometer (Zeiss Ultra Plus). Statistical analysis

of the EDS data showed an average stoichiometry of $Ba_2Co_{0.97}Ru_{1.03}O_6$, matching the expected Ba:Co:Ru ratio of 2:1:1 within error margins, confirming the sample's homogeneity and single-phase nature.

3.3 Crystal structure

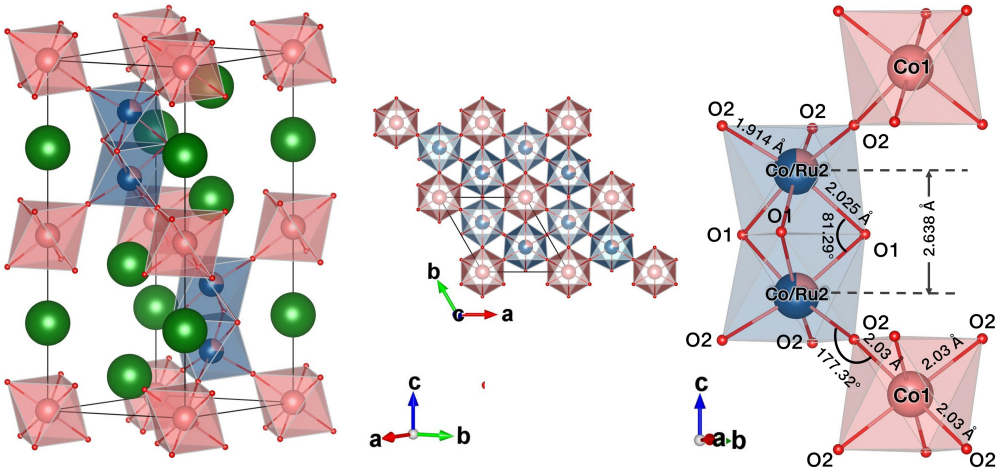


Figure 3.1: (a) Hexagonal perovskite structure of Ba_2CoRuO_6 showing the face- and corner-sharing octahedra with Co/Ru site-disorder, (b) the buckled honeycomb layers formed by the Co and Ru octahedra in the ab-plane, (c) intra- and inter-dimer bond lengths and angles

The crystal structure of Ba_2CoRuO_6 was ascertained by a combined neutron and synchrotron x-ray diffraction analysis. Neutron Powder Diffraction (NPD) was performed at DMC (COLD NEUTRON DIFFRACTOMETER) at SINQ (PSI) using a neutron beam wavelength of 2.458Å. Synchrotron XRD (SXRD) measurements were performed at the Indian Beamline (PF-I8B) at PHOTON FACTORY, KEK, JAPAN using an x-ray wavelength of 0.8313Å. The diffraction patterns were indexed to a 6-layered hexagonal (*6H*) structure in the space group $P6_3/mmc$ shown in Fig. 3.1 consistent with previous literature[149,150]. Figs. 3.2 and 3.3 show the experimental and calculated neutron and synchrotron x-ray diffraction profiles measured at 310 K and 300 K respectively. The lattice parameters obtained from Rietveld refinement of the data were $a = b = 5.700(4)$ Å and $c = 13.970(1)$ Å. The refined atomic positions, thermal parameters and occupancies are tabulated in Table 3.1. The corner sites are found to be fully populated by Co^{3+} ions forming layers of triangular lattices in the *ab*-plane (Fig.3.1(b)). Significant anti-site disorder is observed in the $4f(\frac{1}{3}, \frac{2}{3}, z)$ sites within the face-shared octahedra, with $\sim 30\,\%$ Co^{3+} occupancy.

Table 3.2 displays the bond parameters calculated from the refined structure, shown visually in

Fig. 3.1(c). The average distance between the B' sites is 2.638 Å, which is shorter than the Ru—Ru metallic bond length (2.6725 Å [116]), indicating that the intradimer antiferromagnetic (AFM) direct exchange is relatively strong. The average (Ru/Co2)—O bond length is approximately 1.97 Å, which closely matches the expected value for a Ru^{5+}—O^{2-} bond [151], confirming that the material has a Co^{3+}/Ru^{5+} distribution rather than Co^{4+}/Ru^{4+} or Co^{2+}/Ru^{6+}. Additionally, the Ru^{5+} ions are slightly displaced from their centers due to Coulomb repulsion, as evidenced by the difference in the (Ru/Co2)—O1 bond length (∼2.0246 Å) and the (Ru/Co2)—O2 bond length (∼1.9141Å).

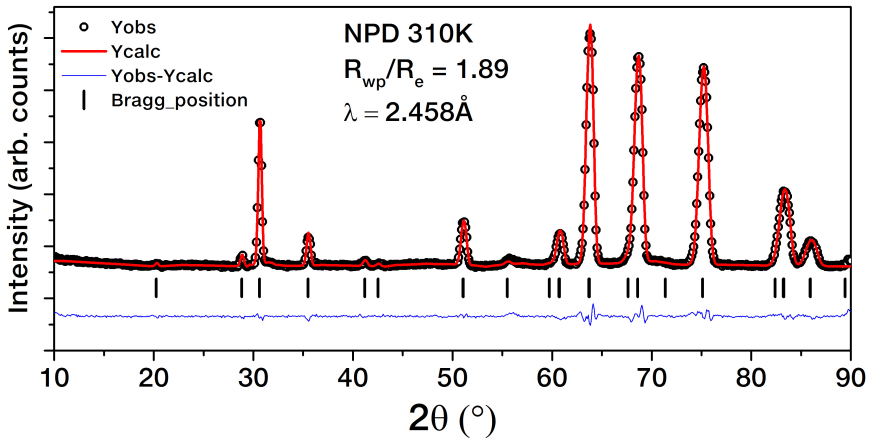


Figure 3.2: Constant wavelength (CW) neutron powder diffraction pattern obtained at 310 K and a fit to the structural model given in Table 3.1 using Rietveld method. Open circles are the experimental data, solid red line is the calculated pattern, blue line shows the difference curve and green ticks mark the Bragg positions expected for the space group $P6_3/mmc$.

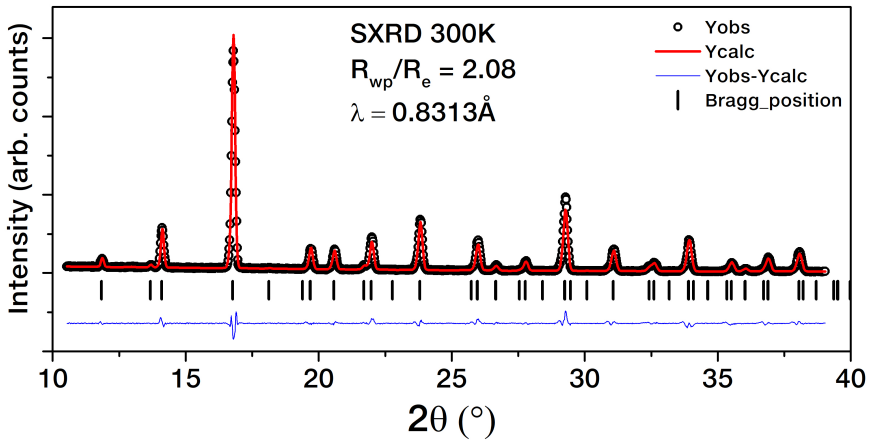


Figure 3.3: Room temperature synchrotron x-ray powder diffraction patterns fitted to the structural model refined using the Rietveld method.

Space Group: $P6_3/mmc$ (Hexagonal)

a = b = 5.700(4) Å c = 13.970(1) Å $\alpha = \beta = 90°$ $\gamma = 120°$

Atom	Wyckoff	x	y	z	B	Occ
Ba1	2b	0	0	1/4	0.0005	1
Ba2	4f	1/3	2/3	0.90963	0.0005	1
Co1	2a	0	0	0	0.24289	1
Co2	4f	1/3	2/3	0.15561	0.21454	0.30
Ru2	4f	1/3	2/3	0.15561	0.21454	0.70
O1	6h	0.48892	-0.02223	0.25	0.25418	0.97
O2	12k	0.16892	0.33811	0.41713	0.52233	1

Table 3.1: Structural Parameters of Ba_2CoRuO_6 obtained from Rietveld refinement of the neutron diffraction pattern measured at 310K

The competitive interaction between the Co/Ru2—O—Co/Ru2 superexchange, characterized by a bond angle of 81.29°, and the intradimer direct exchange leans towards a subtle ferromagnetic (FM) coupling. The direct exchange among Co^{3+} ions is unlikely due to the insufficient extension of the 3*d* orbitals. The nature of the interaction between $(Ru^{5+}: t_{2g}^3)$ and $(Co^{3+}: t_{2g}^4 e_g^2)$ ions - whether ferromagnetic (FM) or antiferromagnetic (AFM) - hinges on the specific Co orbital involved in the exchange, with t_{2g} and e_g orbitals favoring FM and AFM interactions, respectively. Further, a significant role is played by the exchange with next-nearest neighbors (NNN). These intricate interactions distributed randomly across the crystal due to site disorder crucially influence the physical properties by introducing exchange randomness. The O1—O1 separation is notably short, approximately 2.661 Å, facilitating the octahedra's shared face in effectively mitigating cationic repulsion [152], a phenomenon observed in other *6H* Perovskites as well [153,154].

3.4 The spin state of *Co*

The ability of Co^{3+} ions to toggle between low-spin (LS), high-spin (HS), and intermediate spin (IS) states is influenced by several factors including their oxidation state, the crystal field surrounding them, their coordination number, local symmetry, and the types of ions nearby. Notably, a LS state of Co^{3+} is commonly observed and has been reported in compounds such as $LiCoO_2$ [155] and $La_2Li_{0.5}Co_{0.5}O_4$ [156]. Conversely, an HS state of Co^{3+} is typically seen in environments with weaker crystal fields, such as in $YBaCo_4O_7$, which has a tetrahedral local symmetry [157], and in

Sr_2CoO_3Cl[158] and $BiCoO_3$[159], both of which have a square pyramidal local symmetry. Finding HS Co^{3+} in octahedral coordination is more unusual, seen primarily in systems that exhibit a mix of LS and HS states ($LaCoO_3$[160], $Pr_{0.5}Ca_{0.5}CoO_3$[161]) or have an oxygen deficiency ($RBaCo_2O_{5.5}$ (R=Rare-earth metal)[162,163], $Sr_{1-x}Y_xCoO_{3-\delta}$)[164]). It remains to be concluded if the observed spin state is truly a HS-LS mixture or a purely IS state.

Ba1 — O1	× 6	2.85(3) Å
Ba1 — O2	× 6	2.87(0) Å
Ba2 — O1	× 3	2.83(8) Å
Ba2 — O2	× 6	2.85(3) Å
Ba2 — O2'	× 3	2.91(4) Å
Co1 — O2	× 6	2.03(2) Å
(Ru/Co2) — O1	× 3	2.02(5) Å
(Ru/Co2) — O2	× 3	1.91(4) Å
(Ru/Co2) — O (avg)		1.96(9) Å
Co1 — (Ru/Co2)		3.94(5) Å
(Ru/Co2) — (Ru/Co2)		2.63(9) Å
O1 — (Ru/Co2) — O1		82.13(9)°
O1 — (Ru/Co2) — O2		91.39(1)°
O2 — (Ru/Co2) — O1		171.41(1)°
O2 — Co1 — O2		90.74(4)°
Co1 — O2 — (Ru/Co2)		177.32(8)°
(Ru/Co2) — O1 — (Ru/Co2)		81.29(1)°

Table 3.2: Bond Angles and Lengths for Ba_2CoRuO_6 obtained from Rietveld refinement of neutron diffraction data collected at 310K

Research into the spin state of Co^{3+} in an octahedral setting within $SrCo_{0.5}Ru_{0.5}O_{2.96}$ under varying pressures[165] found that at room temperature and standard pressure, the Co ions are in an HS state. Introducing pressure results in a HS → LS transition, bypassing the IS state entirely, at around a Co—O bond length of 1.93 Å. This shift allows for some flexibility in the local lattice structure. Configuration interaction cluster model calculations suggest that significant distortions are required to stabilize an IS state. Similarly, a study on the spin state evolution

of Co^{3+} in a CoO_6 octahedral environment in $Sr_2Co_{0.5}Ir_{0.5}O_4$ [166] found that for an IS state to be stable, there must be significant elongated tetragonal distortion along with a short in-plane Co—O bond length. When the in-plane Co—O bonds are longer than 1.9 Å, the IS state becomes highly unlikely. At high temperatures and normal pressures, a stable HS state is observed, which shifts entirely to an LS state under pressures above 9.7GPa, without transitioning through an IS state. In $LaCoO_3$, the transition from a mixed HS-LS state to a pure LS state occurs with increasing pressure, which is attributed to the decrease in Co—O bond length. This indicates a close relationship between the spin state of Co^{3+} ions and their distance from oxygen atoms.

Based on this understanding, Ba_2CoRuO_6 is expected to predominantly exhibit an HS state due to the absence of distortion in its octahedral sites and the relatively large average bond lengths observed. The similar Co—O bond lengths in the corner-shared CoO_6 octahedra (2.0315 Å) suggest that the crystal field is weak enough to favor an HS state at higher temperatures. The same is observed for the face-shared octahedra (1.9694 Å). These values are consistent with the distances observed in $Sr_2Co_{0.5}Ir_{0.5}O_4$ and $SrCo_{0.5}Ru_{0.5}O_{2.96}$. This is further supported by the stoichiometry obtained from neutron diffraction analysis, $Ba_2Co_{1.03}Ru_{0.97}O_{5.93}$, showing a small oxygen deficiency similar to $SrCo_{0.5}Ru_{0.5}O_{2.96}$, reinforcing the expectation of an HS state for Co^{3+} in this compound. Minimal changes in bond lengths upon cooling (Co1—O (average) = 2.0226 Å and Co/Ru2—O (average) = 1.9617 Å) indicate that the HS state of Co^{3+} ions remains immune to temperature changes from 2 to 300 K in this material.

3.5 Magnetic properties

All magnetic measurements were performed using a QUANTUM DESIGN SQUID MPMS-XL Magnetometer in the temperature range 5 - 330 K and field range ± 5 Tesla.

3.5.1 DC magnetization

The dc magnetic susceptibility (χ_{dc}) of our sample, measured at a magnetic field strength of 5 k Oe, as shown in Fig.3.4, exhibits a notable peak in the Zero-Field Cooled (ZFC) curve, along with a divergence between the ZFC and Field Cooled (FC) curves near T_f = 43 K, indicative of spin-glass (SG) like characteristics [167]. Typically, canonical spin glasses display a Field Cooled magnetization (M_{FC}) that is independent of temperature below T_f, a property commonly used to differentiate them from superparamagnets (SPM) [168]. But it's also feasible for SPMs with a narrow volume

distribution to exhibit a similar plateau below the blocking temperature[169]. In contrast, in our measurements the FC curve continues to rise even below T_f, a trait observed in various cluster glasses (CGs)[170,171,172].

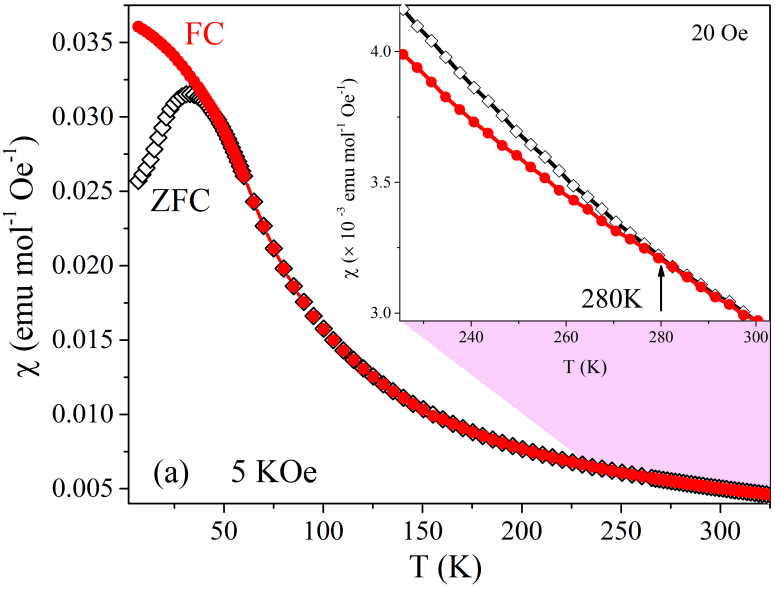
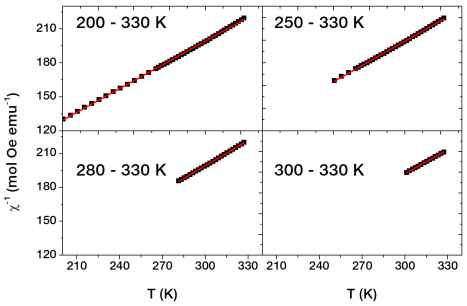


Figure 3.4: dc magnetic susceptibility (χ_{dc}) data from $T = 5 - 330$ K measured under an external magnetic field, $H = 5$ kOe showing irreversibility below 47 K. Inset shows χ_{dc} measured at low-field H = 20 Oe showing the onset of correlations $\sim$ 280 K.

Attempts to fit $\chi_{dc}^{-1}(T)$ to the Curie-Weiss (CW) law at high temperature did not yield satisfactory results as can be seen in Fig.3.5, where the Curie-Weiss temperature (θ_{CW}) and Curie constant (C) show a systematic variation with the fitting (temperature) range, indicative of a rounding of χ^{-1}. This deviation from the Curie-Weiss (CW) linearity is likely a result of spin clustering[168], and an absence of paramagnetic uncorrelated spins upto $T = 330$ K. This assertion is corroborated by the observation of irreversibility close to 280 K in low-field χ_{dc} H = 20 Oe) (inset (a) of Fig.3.4). In both SGs and SPMs, existence of a finite dipolar interaction can cause the ZFC and FC curves to split at temperatures much higher than T_F (or T_B) and continue to rise as the sample is cooled[169,173]. This separation of ZFC and FC curves above the ZFC maxima with growing M_{FC} below the bifurcation point has also been observed in many other cluster glasses[174,169,175,170,171,176].

Magnetization isotherms were also measured in the field range $H \in$ [-5 T,5 T] to study the magnetic behaviour under field cycling at constant temperature. At $T = 150$ K, 200 K and 300 K,



Range (K)	Adj. R^2	intercept (mol Oe emu^{-1})	slope (mol Oe emu^{-1} K^{-1})	C (emu K mol^{-1})	θ_{cw} (K)
200-330	0.999528	-10.53 ± 0.64	0.6995 ± 0.0023	1.43 ± 0.005	15.05 ± 0.92
250-330	0.999387	-16.06 ± 0.9	0.718 ± 0.003	1.393 ± 0.006	22.36 ± 1.25
280-330	0.999726	-23.14 ± 0.78	0.741 ± 0.003	1.349 ± 0.005	31.23 ± 1.06
300-330	0.999982	-29.82 ± 0.29	0.762 ± 0.001	1.312 ± 0.002	39.12 ± 0.38

Figure 3.5: Left: Linear fits attempted for inverse susceptibility $\chi^{-1}(T)$ in various temperature ranges. Right: Variation in fit parameters and derived values of Curie constant (C) and Curie-Weiss temperature θ_{CW} with fitting range.

the curves are purely linear with no signs of saturation. However for $T < T_f$, a slight S-shaped curve is seen to develop with a finite loop opening whose size increases at lower temperatures. The widest curve is observed for the lowest measured T = 2 K, with an average coercive field of $H_C \approx 0.19$ T and a remnant magnetization $M_R \approx 0.011$ emu/g. This shows the presence of active ferromagnetic correlations at low temperature which compete with the predominant anti-ferromagnetic clusters and inhibit a long-range magnetic order.

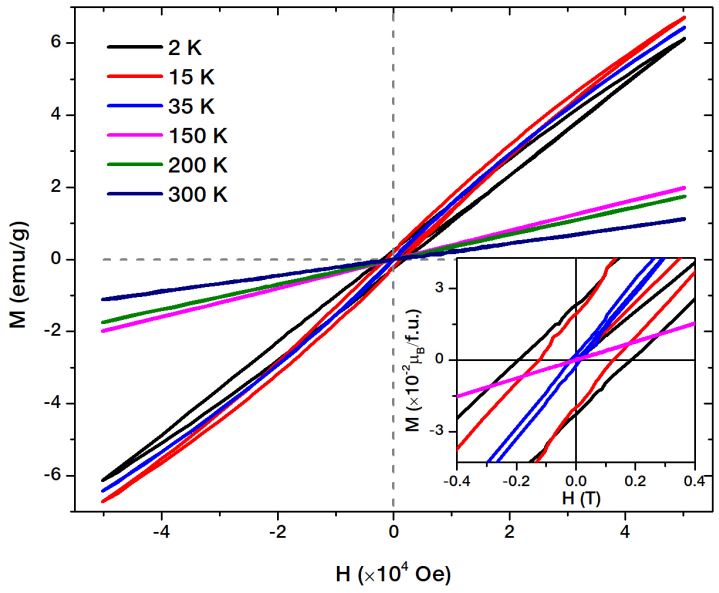


Figure 3.6: Linear magnetization isotherms $M(H)$ for $T \geq 150$ K without any signs of saturation. Development of an S-shaped curvature and a finite hysteresis loop below 47 K, indicating the presence of finite ferromagnetic correlations.

3.5.2 AC MAGNETIC SUSCEPTIBILITY

To confirm the glassy state, we measure the frequency dependence of the ac magnetic susceptibility ($\chi_{ac}(T)$). Fig.3.7 (a) shows a broad peak in the real part of χ_{ac} (ZFC) measured under an excitation field of $H = 2.6$ Oe. With increasing frequency, the cusp moves toward higher temperatures. The magnitude of this shift is characterized by the Mydosh Parameter (δT_f)[177],

$$\delta T_f = \frac{\Delta T_f}{T_f \Delta(log\omega)} \tag{3.1}$$

which in our case is 0.0136. T_f is the temperature at which Re(χ_{ac}) peaks and ω is the angular frequency ($\omega = 2\pi f$, f being the applied frequency in Hz) of the applied ac magnetic field. δT_f for Ba_2CoRuO_6 is more than double that of canonical spin glasses like CuMn ($\delta T_f \sim 0.005$) but is consistent with the values reported for reentrant spin glasses[177] and cluster glasses[178,176,179,180]. This value rules out the possibility of a SPM where δT_f is expected to be at least an order higher (> 0.1)[177]. This claim is further supported by the deviation of the relaxation time $\ln\tau$ ($\tau = \frac{1}{\omega}$) from the Néel-Arrhenius equation used to describe the relaxation of uncorrelated spins (Eq.3.2[181]).

$$\tau = \tau_0 \cdot exp\left(\frac{E_a}{k_B T}\right) \tag{3.2}$$

where τ_0 is the *attempt* frequency, and E_a the activation energy of the blocked clusters. Shown in inset of Fig.3.7(a) $\ln\tau$ defies linearity when plotted against $1000/T_f$ ruling out thermally-activated superparamagnetism here.

A modification to the equation 3.2 by introducing T_0 to account for cooperative behaviour leads to the Vogel-Fulcher-Tamman (VFT) equation

$$\tau = \tau_0 \cdot exp\left(\frac{E_a}{k_B(T - T_0)}\right) \tag{3.3}$$

generally used to describe the viscosity of supercooled liquids and real glasses[182]. A $\tau(T_f)$ fit to eq. 3.3 returns the parameters $\tau_0 \approx 10^{-4}$s, $T_0 = 45.21 \pm 0.11$ K and $E_a = 0.65 \pm 0.18$ meV. E_a corresponds to a temperature of $\sim$7.5 K putting Ba_2CoRuO_6 in the weak interaction regime ($\frac{E_a}{k_B} << T_0$)[183]. Although eq.3.3 fits the observed $\tau(T_f)$ reasonably as a nonlinear curve, (Fig.3.7(b)), on converting into a linear plot using $T_0 = 45.21$K (inset of Fig.3.7(b)) it becomes apparent that this model is insufficient in describing the dynamic behaviour in the glassy state.

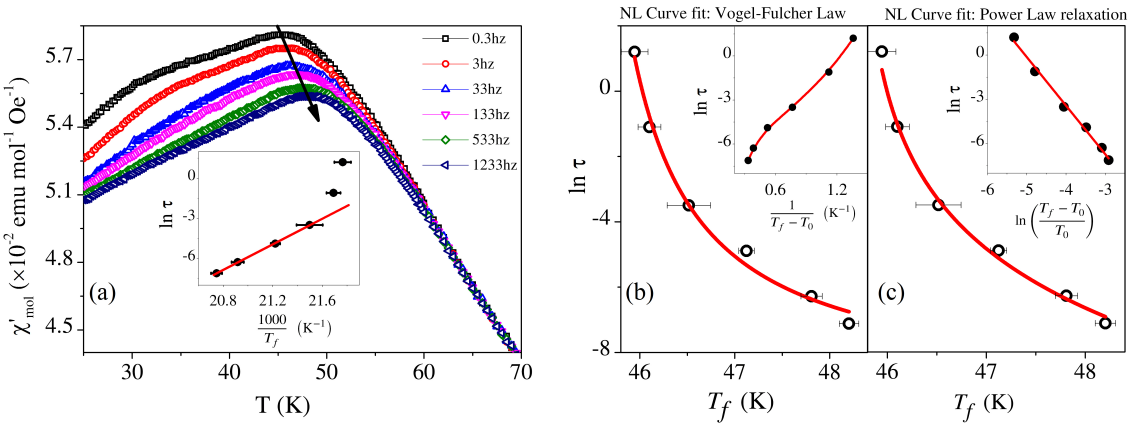


Figure 3.7: (a) Real part of $\chi_{ac}(T)$ showing a dispersive cusp below 60 K. Inset shows the variation of the cusp temperature ($10^3 T_f^{-1}$) with lnτ. (b) shows a non-linear (NL) curve fit to the VFT equation and the inset shows the linear scaling done using T_0 returned by the NL fit, (c) shows the fit to mean-field power law model and the inset shows the excellent fit to the linearized plot.

In the mean-field theory phase transitions, dynamical scaling near the transition expects τ to vary as a power law instead of an exponential function:

$$\tau = \tau_0 \cdot \left(\frac{T_f}{T_0} - 1 \right)^{-z\nu} \tag{3.4}$$

where, τ_0 is the characteristic relaxation time, T_0 the *true* glass transition temperature ($T \rightarrow T_0$ as $t \rightarrow \infty$) and $z\nu$ the dynamical exponent that encapsulates the critical slowing down of relaxation dynamics near the phase transition [184]. A non-linear fit to eq. 3.4, along with its linear scaling, is presented in Fig. 3.7 (c) and its inset, respectively. It's clear that the linear fit improves significantly when using eq. 3.4. The fitting yields the following parameters: $T_0 = 45.72 \pm 0.03$ K, $\tau_0 = 6.22(\pm 0.19) \times 10^{-8}$ s, and $z\nu = 3.29 \pm 0.12$. Comparing these values to those typical of a canonical spin glass like CuMn (4.6 at.%) - which has $\tau_0 = 10^{-12}$ s and $z\nu = 5.5$ - we see that the relaxation times of the two systems differ by nearly four orders of magnitude. This suggests that, in this system, the entities responding to external perturbations are not individual spins but correlated groups of spins. The $z\nu$ value is also lower than the usual range observed for spin glasses (4-12)[177]. However, values of $z\nu < 4$ have been reported in some cluster glass (CG) systems[185,186,180]. A $z\nu$ value approaching that for a mean-field phase transition ($z\nu = 2$) has been identified as a sign of strong interactions, which enable cooperative freezing of magnetic moments at T_f[187].

3.5.3 Thermoremnant magnetization

Thermoremnant magnetization measurements involve cooling a sample in presence of a magnetic field below the transition, switching off the field at the lowest T and then measuring the change in $M(T)$ while warming, but without any field applied. Tracking M without the influence of H provides enhanced sensitivity to the thermal evolution of the magnetic state, since T is the sole perturbation, particularly useful in revealing antiferromagnetic order within clusters, which would otherwise be obscured by the paramagnetic contribution. This method has been valuable in studying glassy behaviour[188,189,190] in various frustrated materials. We observe that along with the expected increase in magnetization at T_f, there is also subtle change in slope around 280 K (inset (b) of Fig. 3.8), suggesting that the antiferromagnetic correlations start developing close to room temperature and grow stronger as the sample is cooled.

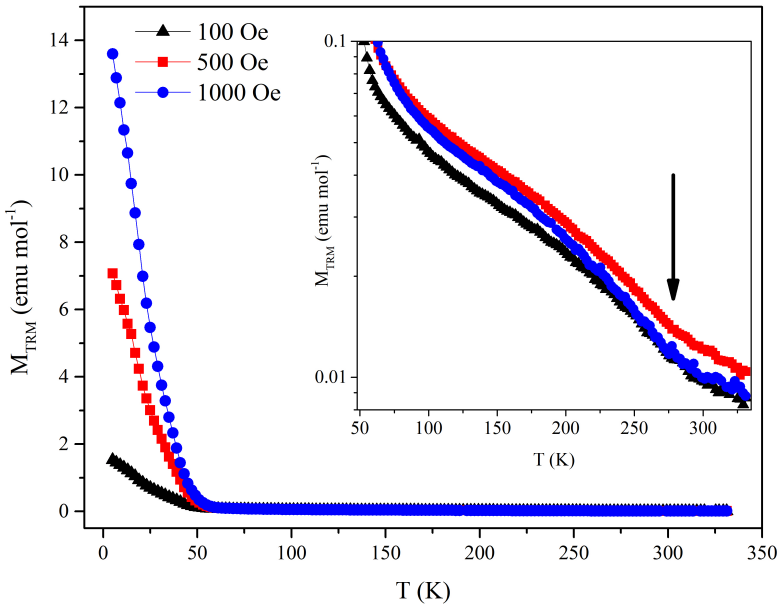


Figure 3.8: The thermal evolution of thermoremnant magnetization ($M_{TRM}(T, H = 0)$) measured for different cooling fields. The inset shows the same data as a semi-log plot, highlighting the slope change seen close to room temperature.

3.5.4 Aging, memory and rejuvenation

One of the most fascinating features exhibited by glasses is the *memory effect*. In this experiment, a reference field-cooled (FC) curve is first measured by cooling the sample in a finite magnetic field (here, $H = 100$ Oe). The sample is then cooled once again in the same field, but this time, at a certain $T < T_f$ (here, $T = 28$ K), the field is switched off, allowing the system to relax.

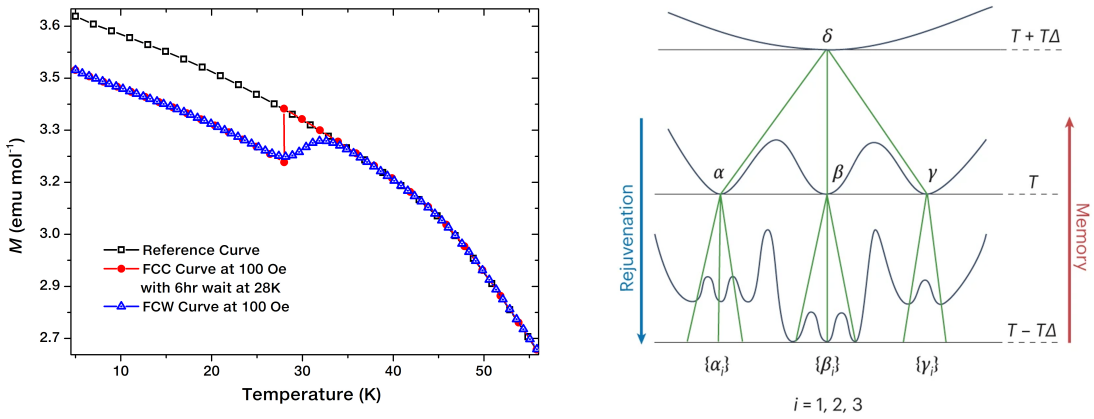


Figure 3.9: Left: The FC memory effect observed at $T = 28$ K with a waiting time of 6 hours and applied magnetic field of 100 Oe. Right: The ultrametric order in the spin glass phase space. Reproduced with permission from Springer Nature [19].

This is called *aging*. After a certain waiting period, t_w (usually several hours) (here, $t_w = 6$h), the sample is cooled further with $H \neq 0$, and the magnetization immediately starts rising again, as if it never relaxed. This is called *rejuvenation*. After reaching the lowest T, $M(T)$ is measured continuously while warming and exactly at the aging temperature M switches direction to merge into the pre-aging FC curve Fig.3.9 (left). The glass *remembers* the relaxation that occured at 28 K. This is an elegant illustration of the complicated phase space of spin glasses Fig.3.9 (right). A spin glass is a system that is technically always out-of-equilibrium, with a plethora of degenerate metastable states available, separated by a random distribution of energy. This is why it shows such a wide distribution of relaxation times (from 10^{-12} to 10^{4} s)[177,191] and extremely slow dynamics. As the glass is cooled, the energy states subdivide into smaller valleys, with new energy barriers developing to separate them. For a given ΔT the system can only shuffle between the sub-valleys (manifesting as rejuvenation) such that the population rates of the parent state (at T) is preserved.[19] (manifesting as aging memory). This hierarchical division of the free-energy landscape of a glass was discovered by Giorgio Parisi[192] in his seminal work as the equilibrium solution to the Sherington-Kirkpatrick model[193] of spin glasses by using replica symmetry breaking and is termed *ultrametric* order in the phase space of an otherwise disordered system. In other words, the arrangement of energy states is equivalent to that of length scales[194]. A larger energy barrier corresponds to a longer correlation length. Different time scales govern dynamics of distinct length scales, allowing seemingly counter-intuitive features like rejuvenation (subvalleys) and memory (parent states) to coexist[19,195].

We further investigated the field (H) and waiting time (t_w) dependence of the aging behaviour using the following protocol: the sample is cooled in a finite field from below T_f, and after waiting for a time t_w, the field is switched off, and the relaxing magnetization is measured as a function of time. This isothermal remnant magnetization (M_{IRM}) follows a stretched exponential function:

$$M_{IRM}(t) = M_0 + A \cdot exp\left[- \left(\frac{t}{\tau} \right)^{1-n} \right] \tag{3.5}$$

which is commonly used to model the slow dynamics of spin glasses. M_0 is the static magnetization, A is the relaxing component, τ is the characteristic relaxation time, and n is the time-stretching exponent. The value of n, which governs the relaxation rate, is typically around 0.5 for spin glasses. For all our fits at different t_w and H (Fig. 3.10(a), (c), and (e)), we consistently find n values between 0.5 and 0.6, confirming that the relaxation is slower than exponential. At a given temperature, t_w is proportional to the size of the frozen domains, meaning that longer waiting times allow for probing the aging behaviour of larger domain sizes[196], or that, the dynamics are dictated by the *age* t_w[19,195]. As a result, increasing waiting times leads to longer effective response times of the larger clusters[197].

The response function $S(t)$, given by:

$$S(t) = \frac{d}{dln(t)} \left[\frac{-M_{IRM}(t, t_w)}{H} \right] \tag{3.6}$$

is expected to peak at a time on the order of t_w, like a bell curve. This is evident in Fig. 3.10(b), where $S(t)$ peaks shift to longer timescales as waiting times increase. An exception is observed for $t_w = 100$ s, where the $S(t)$ peak occurs at a similar time to that for $t_w = 1000$ s, though slightly earlier. This may be related to the time required for temperature and field stabilization during measurement, which would affect shorter waiting times more, as these two timescales are comparable. This also highlights how extremely long measurement time is needed to even begin probing the timescales of glass dynamics.

We also explored the magnetic field dependence of aging to estimate the spin glass (SG) correlation length by analyzing the variation of the effective waiting time t_w^{eff} - the time at which $S(t)$ peaks - with H^2. The response function $S(t)$ is connected to the height of the energy barriers, which change as a function of the external magnetic field. As the field increases, the effective barrier heights decrease, leading to smaller t_w^{eff} values[198,199]. Interestingly, we observe that $S(t)$ peaks

at slightly longer timescales as H increases (Fig. 3.10(d), (f)). However, the change is minimal, only a few tens of seconds. This indicates that $S(t)$ does not shift appreciably from its peak near t_w in fields ranging from 20 to 500 Oe, and the characteristic relaxation time τ remains essentially unchanged (around 10^3 s) across different external fields.

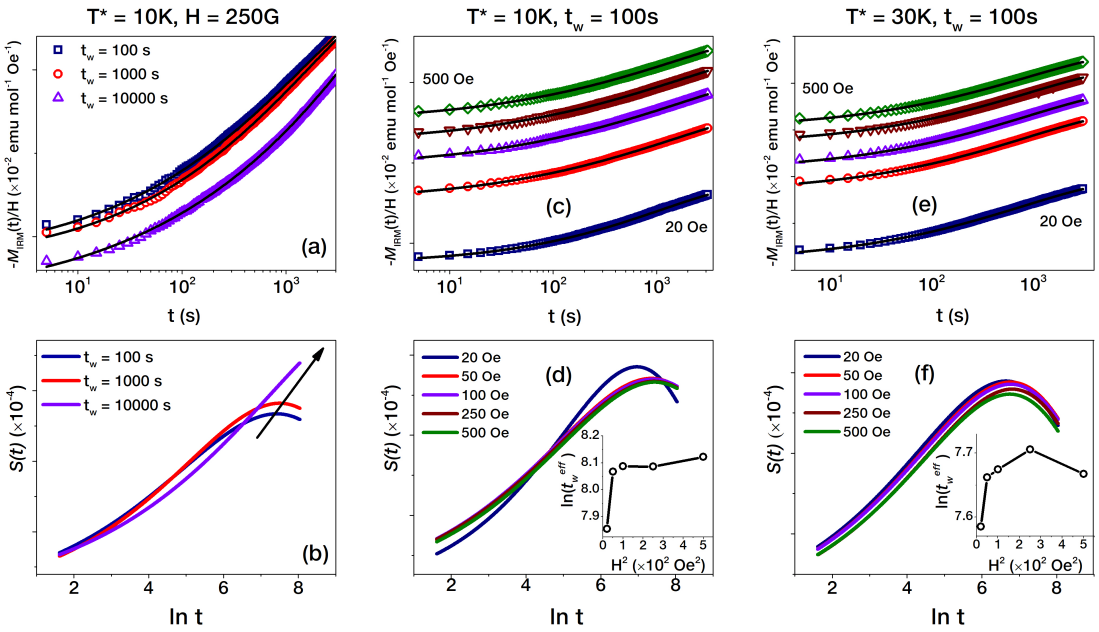


Figure 3.10: Aging behaviour of Ba_2CoRuO_6. The isothermal remnant magnetization $-M_{IRM}(t)$ plotted against t for (a) different waiting periods t_w at $T = 10$ K and $H = 250$ Oe, (c) different fields at $T = 10$ K and $t_w = 100$ s, and (e) different fields at $T = 30$ K and $t_w = 100$ s. Solid lines show fits to the modified stretched exponential function. The derivative of $-M_{IRM}(t)$ shown in (a), (c) and (e) with respect to t is shown in (b), (d) and (f), respectively. Insets of (d) and (f) show the (lack of) dependence of t_w^{eff} on H.

This is an important observation, as the magnetic (Zeeman) energy (E_z) associated with a field change H is related to the volume over which the spins are locked for barrier hopping (N_s) via the relation $E_z = N_s \chi_{FC} H^2$, where χ_{FC} is the field-cooled susceptibility per spin. The spin glass correlation length ξ represents the radius of this volume, N_s. If N_s consists of smaller clusters, the activation energy corresponds to lower barrier heights, and $S(t)$ would always peak near the waiting time t_w, yielding similar t_w^{eff} for different fields[198]. This is exactly what our measurements show, reinforcing our claim of a cluster-glass ground state for this system. This indicates that the spin-glass correlation length is far longer than can be probed using the length scale ξ associated with E_z.

3.5.5 Exchange anisotropy

Magnetization measurements under various applied fields show that T_f is significantly suppressed at higher fields (Fig. 3.11). By fitting $T_f(H)$ (Fig. 3.11) to the mean-field relation for vector spin glasses with random anisotropy[200]:

$$T_f(H) = T_f(0)(1 - AH^p) \tag{3.7}$$

we obtain $p \approx 0.45$ and $T_f(0) \approx 42.8$ K. Here, $T_f(0)$ represents the temperature at which the zero-field cooled (ZFC) curve is expected to peak in the absence of an external magnetic field, A is a constant that characterizes the randomly distributed exchange interactions, and p is an exponent that depends on the strength of anisotropy relative to the magnetic field. In cases of strong anisotropy, $p = \frac{2}{3} \approx 0.67$ is expected, corresponding to the A-T (de Almeida & Thouless) line for Ising spins[201]. For Heisenberg spin systems with weak anisotropy, the G-T (Gabay & Toulouse) line[202] with $p \approx 2$ is expected, where two distinct transitions occur for the freezing of transverse and longitudinal spins. Our value of $p \sim 0.45$ is closer to the A-T value, suggesting that we are in the strong anisotropy regime. This anisotropy likely arises from the globally disordered distribution of various exchange interactions in the system, forming short-range ordered regions of different sizes, which compete with each other down to the lowest temperatures, preventing the establishment of a long-range ordered ground state.

3.6 Influence of temperature on structure

Temperature-dependent x-ray diffraction was also performed at PF-18B at PHOTON FACTORY between 15 - 300 K to observe the changes in structure across the transition. No change in crystal symmetry was observed as the $P6_3/mmc$ structure was preserved down to 15 K. The analysis of peak profile parameters performed using the Le-Bail method[203] showed a sharp change in unit cell dimensions occurring across the freezing transition T_f suggestive of the magnetic transition's significant on the structure despite the absence of a magnetostructural transition. This is highlighted in Fig.3.12 where the axial ratio (c/a) of the hexagonal close-packed (hcp) structure is plotted as a function of temperature and drops sharply for $T < 50$ K.

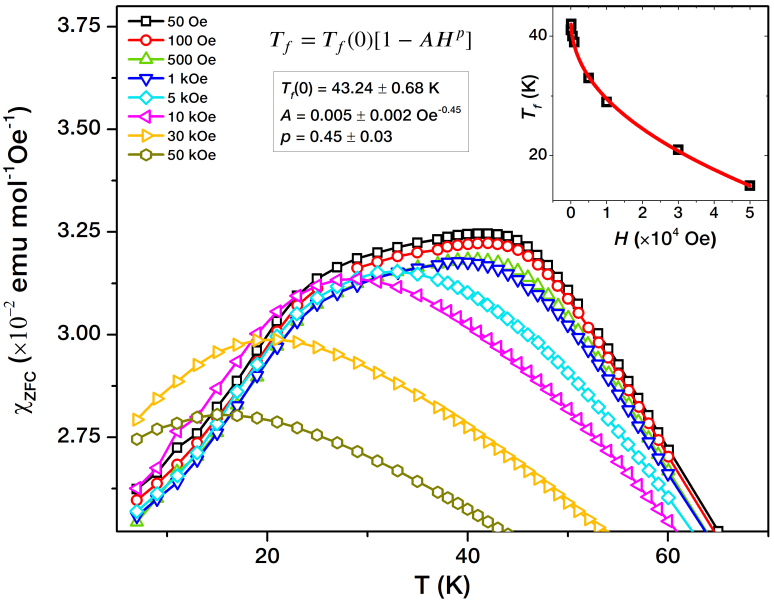


Figure 3.11: The field dependence of the cusp in static χ_{ZFC} . The inset shows the nonlinear fit to $T_f(H)$ using eq.3.7

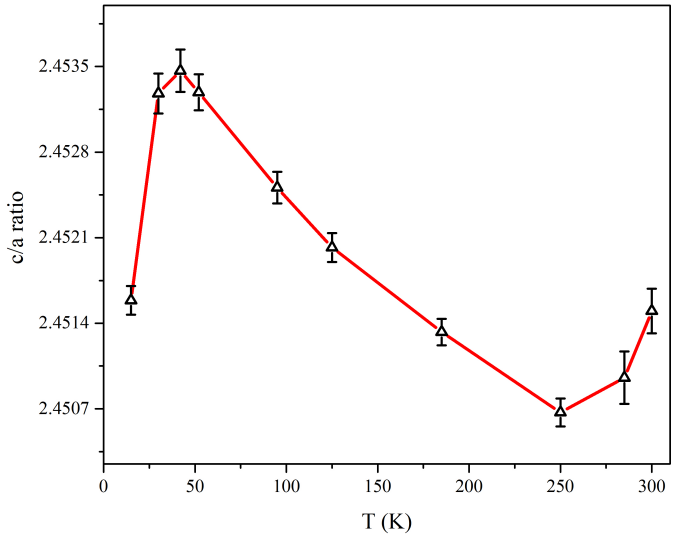


Figure 3.12: The c/a ratio as a function of temperature showing two distinct features across T_N and 250 K.

Apart from the more pronounced transition at low temperature, there is also an apparent change in the c/a ratio across 250 K. We believe this feature to be a structural manifestation of the development of short-range magnetic correlations in this system also seen in magnetic measurements (sections 3.5.1 and 3.5.3) .

NPD patterns were also measured at temperatures 150 K, 20 K and 1.7 K to probe the magnetic structure below T_f. In the 20 K and 1.7 K datasets, two additional weak reflections are observed at $2\theta = 17.5°$and $39.5°$ (Fig.3.13) indicative of antiferromagnetic order. These peaks were found to be consistent with a k-vector ($\frac{1}{2}$,0,0) (equivalent to (0,$\frac{1}{2}$,0) and ($\frac{1}{2}$,$\frac{1}{2}$,0)), found using the K-SEARCH module in the FULLPROF SUITE[20]. This meant that the frozen spin clusters comprised of antiferromagnetically ordered ions with a magnetic unit cell of dimensions ($2a, 2a, c$), a and c being the crystallographic lattice parameters. No significant enhancement of the nuclear peaks is observed, ruling out long range ferromagnetic order.

Magnetic representation analysis was conducted using SARAh[204,205], revealing that only odd irreducible representations (IRs) survived at the corner sites (with 6 basis vectors projected), while all IRs survived at the dimer sites (with 12 basis vectors projected). The finite IRs of the little group G_k calculated for each magnetic site along with their respective basis vectors ψ_n are shown in Tables A.1 and A.2. A detailed procedure of calculating magnetic structures using FULLPROF SUITE is also given in Appendix A.

Γ	No. of basis vectors	R_{mag}	$\mu(2a)$ (μ_B)	$\mu(4f)$ (μ_B)
Γ_1	1	85.1	0.53	0.18
Γ_3	2	58.8	0.83	0.41
Γ_5	1	89.1	0.06	0.41
Γ_7	2	68.4	0.78	0.48

Table 3.3: Summary of magnetic structure models obtained from refining neutron powder diffraction data measured at 1.7 K.

On testing the applicability of various combinations of the common IRs for both sites, it was ascertained that Γ_1 and Γ_5 both, with 1 basis vector could not accurately describe the peaks. However, Γ_3 and Γ_7 provided decent fits to the magnetic peaks, as illustrated in Fig.3.13. For comparison, the fits obtained using Γ_3 and Γ_5 are also shown, demonstrating that their inability to generate any intensity at 2θ =39.5°. Despite the difference between the R_{mag} of Γ_3 and Γ_7, due to their visual similarity to the observed magnetic intensities, we reckon both models to be of similar quality. Because the magnetic reflections are weak and limited in resolution, relying on the rel-

atively high R_{mag} values as a benchmark for selecting the accurate model would not be prudent, especially when the estimated moment values for both 2*a* and 4*f* sites are so close. A summary of the magnetic R-factors, and moment values obtained is given in Table 3.3.

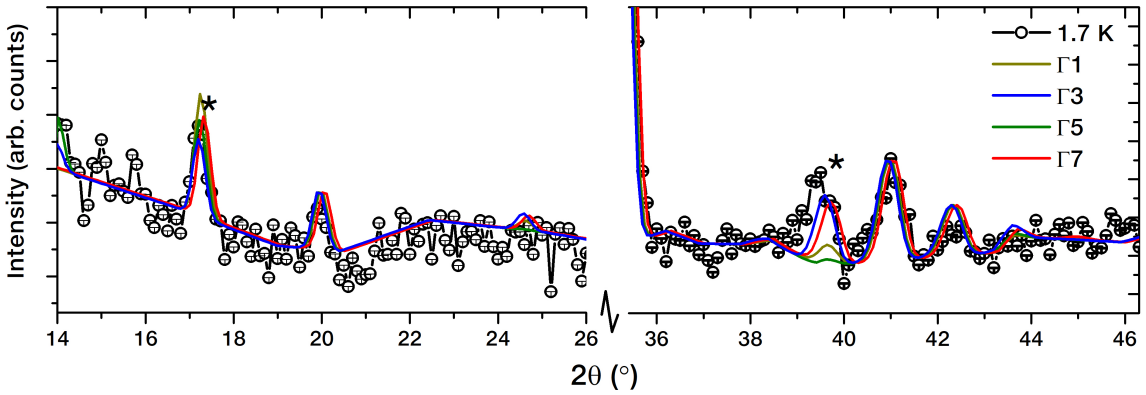


Figure 3.13: CW NPD data collected at 1.7 K showing presence of additional magnetic peaks (marked by ∗). Solid lines show fits to these peaks corresponding to three different irreps: Γ1, Γ5, and Γ7.

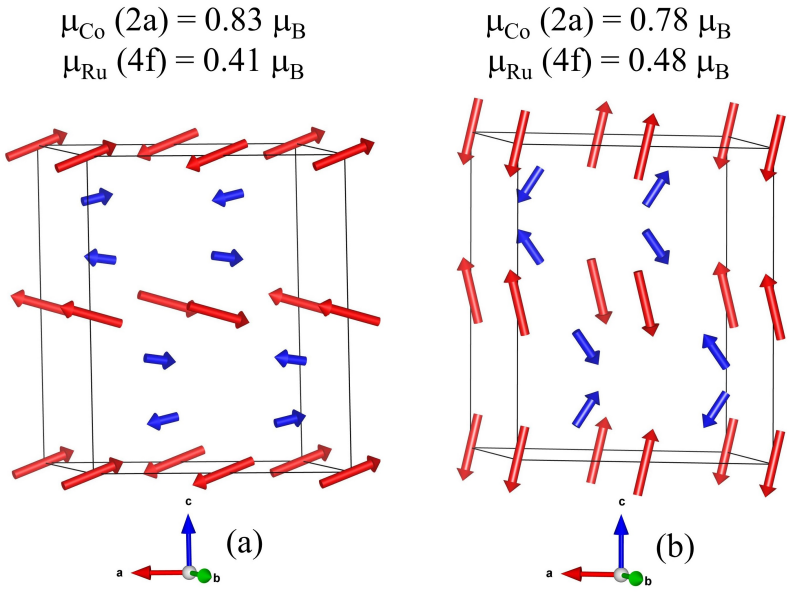


Figure 3.14: Magnetic structure within frozen antiferromagnetically correlated spin clusters corresponding to irreps (a) Γ3 and (b) Γ7.

Fig.3.14 visualizes the structures generated from these IRs, both showing antiferromagnetically aligned canted spins along the *c*-axis and ferromagnetically linked spins along *b*. The primary difference between the two models lies in the direction of canting: Γ_1 exhibits spins canted in

the *ab* plane, while Γ_3 expects a canting about the *c* axis. Both models give similar values of magnetic moments and goodness of fits, presenting both as plausible solutions within the current diffraction resolution. In both cases, the moments within the dimers are antiferromagnetically coupled, explaining the extremely small moments observed at these sites. Moment suppression is also noted at the corner sites, likely due to strong disorder and exchange randomness present in this material[206].

3.8 Electronic and thermal transport behaviour

3.8.1 Specific heat

Specific Heat capacity (C_P) measurements were performed on a QUANTUM DESIGN PPMS in collaboration with Prof. Surjeet Singh.

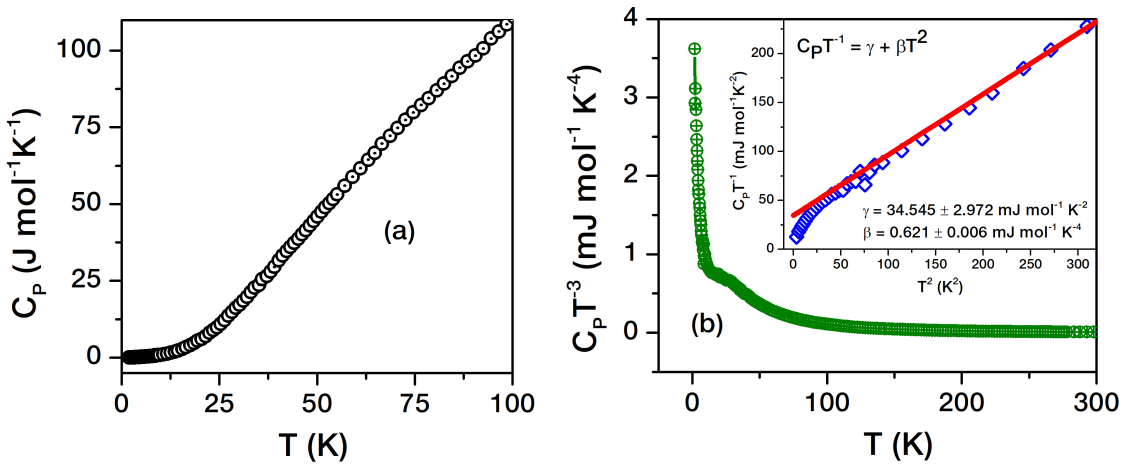


Figure 3.15: (a) The featureless molar heat capacity $C_P(T)$ shown upto 100 K, (b) $\frac{C_P}{T^3}$ vs T showing a strong upturn at low-temperatures. Inset: linear fit to $\frac{C_P}{T}$ vs T^2 showing the low-temperature deviation from the Debye Law.

$C_P(T)$ shows no features associated with long-range ordering in the vicinity of T_N (Fig. 3.15(a)), indicating that the entropy change associated with cluster freezing is negligible. A linear fit to C_P/T vs T^2 at low temperatures (inset of Fig. 3.15(b)) yields $\gamma = 34.55 \pm 2.97$ mJ mol^{-1} K^{-2} and $\beta = 0.62 \pm 0.01$ mJ mol^{-1} K^{-4}. The γ value is unusually large for an insulating system, but this, and the downturn below ~10K, can be attributed to the glassy ground state. Similar high γ values have been reported in other frustrated systems, including *6H* triple perovskites[190,207,208] and half-doped manganites[209,210]. Using these parameters, the Debye temperature (θ_D) can be

calculated from the relation:

$$\theta_D = \left(\frac{12\pi^4 pR}{5\beta}\right)^{1/3} \tag{3.8}$$

where p is the number of atoms per formula unit (10 for double perovskites) and R is the gas constant. This yields $\theta_D = 315.14 \pm 1.01$ K, which is consistent with typical values for perovskites (350-400K)[210,211]. Additionally, C_P/T^3 plotted against T (Fig. 3.15(b)) shows an upturn below 10K, reminiscent of two-level tunneling systems, a characteristic often observed in glassy or phase-separated systems[190,212,209]. In contrast, in Debye materials with expected periodicity, C_P/T^3 is expected to plateau at low temperatures.

3.8.2 Resistivity

Temperature dependence of resistivity was measured in the two-probe mode using a KEITHLEY DAQ6510 between 20 - 300 K by making thin contacts with Silver conductive paste (Sigma Aldrich, No. 735825) on a $3.9 \times 3.44 \times 1.18$ mm^3 sintered pellet. A semiconducting behaviour was observed between 20-300K with a small feature near 50 K in the vicinity of T_f. Generally, no features are expected from spin glasses in resisitivity measurements[177]. lnρ vs 1/T shows non-linearity well above the T_f (not shown here) and could be fitted to a linear relation only in the region 280 K$\leq$ T $\leq$300 K. This makes sense since below this temperature range, electron correlations become significant enough to influence transport behaviour as well as magnetism and the conduction mechanism cannot be described by thermal activation alone. Linearity upto temperatures approaching T_f is obtained when lnρ is plotted against $1/T^{\frac{1}{4}}$ (Fig.3.16), suggesting that the 3D Mott Variable Range Hopping model

$$\rho = \rho_0 \cdot exp\left(\frac{T_0}{T}\right)^{1/4} \tag{3.9}$$

governs the transport. This mechanism is used to describe the low temperature conduction in disordered systems with localized charge carrier states[213] and similar behaviour has been reported in other *6H* perovskites[143,214,215,216,217]. The three-dimensional conduction suggests that both inter- and intra-layer hopping energies are significant and participate in conduction. Below T_f the materials becomes highly insulating due to increased localization of these hopping electrons and resistivity increases beyond the measurement limit. It is interesting to compare this behaviour with $Ba_3CoRu_2O_9$ where unlike the present case, the transport behaviour changes from lnρ $\propto$

$T^{-1/2}$ to $\ln\rho \propto T^{-1/4}$, marking an electronic transition co-occuring with the magnetostructural transition at $T_N = 93$ K[148].

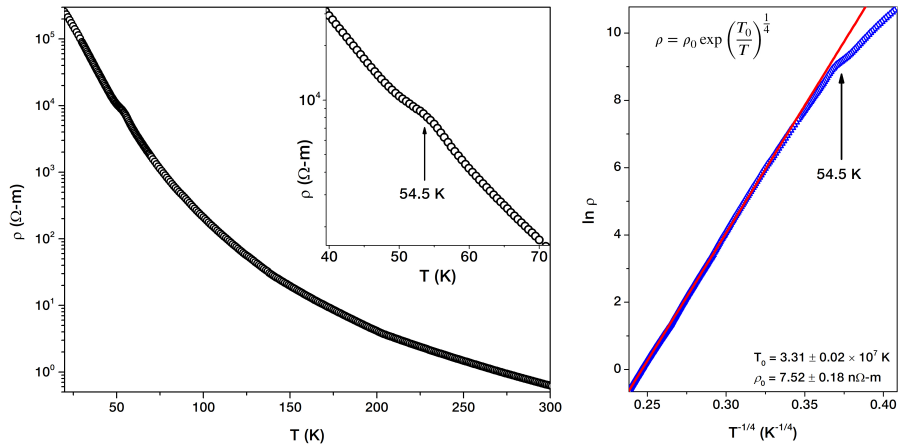


Figure 3.16: Left: Temperature dependence of resistivity ρ. The inset shows a zoomed view of the feature close to T_f. Right: The 3D VRH model fit to lnρ vs $1/T^{1/4}$.

3.9 Dielectric spectroscopy

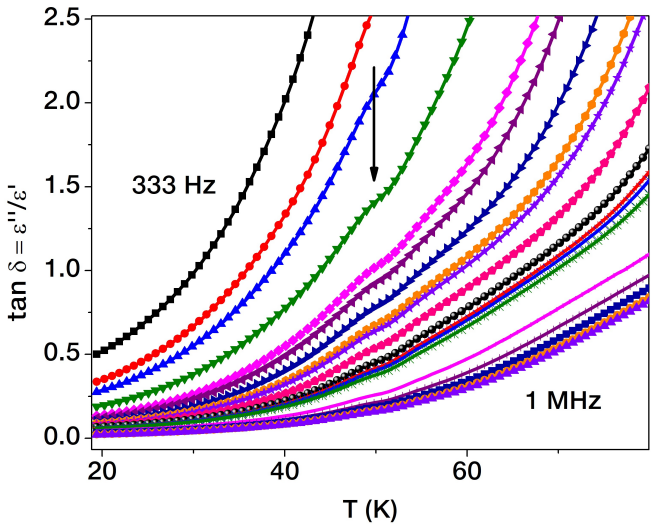


Figure 3.17: Dielectric loss tangent tan$\delta = \varepsilon''/\varepsilon'$ plotted as a function of T for frequencies $f =$ 333 Hz - 1 MHz

Broadband Dielectric spectroscopy was performed using NOVOCONTROL ALPHA-A IMPEDANCE ANALYZER with a voltage amplitude of $V_{ac} = 1$V, across a frequency range of 0.3 kHz to 1 MHz. The observations shown in Fig.3.17 indicate that Ba_2CoRuO_6 behaves as a lossy dielectric for

temperatures above 150K. Below 150K, both ε' and ε'' decrease smoothly without any significant features. However, on closer inspection, a subtle frequency-dependent feature appears near 50 K in the loss tangent ($\tan\delta = \varepsilon''/\varepsilon'$) (Fig. 3.17). This might suggest the presence of weak magnetodielectric coupling, but extensive magnetic field-dependent dielectric measurements would be necessary to confirm this possibility.

3.10 Conclusions

In this chapter, we present a comprehensive study of the *6H* disordered double perovskite Ba_2CoRuO_6, employing Synchrotron and Neutron Powder Diffraction, ac and dc magnetization, resistivity, specific heat, and dielectric measurements to probe the interplay of lattice, electronic and spin degrees of freedom in this system. We determine that the magnetic ground state of this material is a cluster spin glass with pronounced exchange anisotropy, promoted by the significant site-disorder between Co and Ru within face-shared octahedra. Ba_2CoRuO_6 demonstrates typical features of a glassy phase, including a frequency-dependence in ac magnetization, magnetic irreversibility strongly influenced by applied field, absence of saturation even under high magnetic fields, and remarkable memory and aging effects. Additionally, the specific heat at low temperatures shows non-Debye behaviour without any features consistent with ordering. Assessment of the ac susceptibility data points to the frozen components being clusters of spins that begin coalescing close to room temperature and grow on cooling. Evidence of AFM ordering within the clusters is observed in NPD data as additional peaks at 2 K and the presence of competing weak FM interactions is documented in magnetic hysteresis measurements. The magnetic unit cell is doubled with respect to the crystallographic unit cell along the *ab* plane with the canted spins aligned anti-parallel (either in the *ab* plane or along *c*-axis) and parallel along *b* axis. Average magnetic moment calculated from NPD analysis is less than $1\mu_B$ for both corner and dimer sites. This necessary competition between FM and AFM interactions coupled with the site disorder stabilize the magnetic glass state. The analysis of the temperature-field ($T_f - H$) phase diagram aligns with the presence of strong random anisotropy in the system ($p \sim 0.45$), despite not confirming A-T line ($p \sim 0.67$). The substantial disorder in the system enhances the exchange anisotropy, resulting in a highly frustrated network of Co^{3+} and Ru^{5+} ions. As the system is cooled, enhanced local correlations lead to the formation of AFM ordered domains interrupted by smaller regions of FM order which collectively freeze at T $\sim$ 43 K, culminating in a cluster glass ground state.

The only true wisdom is in knowing you know nothing.

Socrates

4

Nonlinear dielectric response of $A_3MRu_2O_9$ (A = Ba, Sr), (M = Co, Bi, Ca)

This work has been published as Chakravarty & Nair, "*Exploring low-temperature dynamics in triple perovskite ruthenates using nonlinear dielectric susceptibility measurements*", *Journal of Applied Physics* **135**, 104103 (2024)[218]

4.1 Introduction

According to the Landau-Ginzburg-Devonshire (LGD) theory of ferroelectric (FE) phase transitions, the higher-order susceptibilities of a dielectric material χ_i for $i \geq 1$ are related to the polarization developed in response to an external electric field as[219]:

$$\chi_1 = \frac{1}{\varepsilon_0[A(T - T_c) + 3BP^2]} \tag{4.1}$$

$$\chi_2 = -3\varepsilon_0 BP\chi_1^3 \tag{4.2}$$

$$\chi_3 = -(1 - 18\varepsilon_0 BP^2\chi_1)\varepsilon_0^3 B\chi_1^4 \tag{4.3}$$

where ε_0 is the vacuum permittivity, A is a constant, T_c is the critical temperature of the phase transition, and B and C are smoothly varying functions of temperature[220]. The sign of B specifies the type of phase transition: $B < 0$ corresponds to a discontinuous (1st order) transition, $B > 0$ for a continuous (2nd order) phase transition.

Equation 4.2 highlights that χ_2 is directly proportional to the net-induced polarization in the system, reflecting both its orientation and magnitude. As a result, in the paraelectric (PE) state, χ_2 is should vanish and reverse its sign when the polarity of the applied field is switched. In contrast, χ_1 and χ_3 are related to P^2 and, therefore, remain finite even above the critical temperature (T_c). In the PE phase, where $P = 0$, equation 4.3 simplifies to:

$$\chi_3 = -\varepsilon_0^3 B \chi_1^4$$

meaning $\chi_3 < 0$ for $B > 0$. However, in the ferroelectric (FE) phase,

$$\chi_3 = 8\varepsilon_0^3 B \chi_1^4$$

and should be positive for $B > 0$. Thus, we expect χ_3 to change signs across a continuous FE transition. Measuring both χ_1 and χ_3 simultaneously, also allows the estimation of the scaled nonlinear susceptibility, a_3, which is given by:

$$a_3 = \frac{-1}{\varepsilon_0^3} \frac{\chi_3}{\chi_1^4} \tag{4.4}$$

In the PE state, a_3 is simply equal to B, but in the FE state of a continuous transition, $a_3 = -8B$, which means, a_3 also should reverse its sign across a continuous PT. This prediction has been experimentally verified for various materials like Triglycine Sulphate (TGS, $(NH_2CH_2COOH)_3 \cdot H_2SO_4$)[221] and Lead Germanate ($Pb_5Ge_3O_{11}$)[222].

Likewise, for a discontinuous transition ($B, C < 0$), $\chi_3 > 0$ and $a_3 < 0$ is expected on both sides of T_c[219,223]. This has again been confirmed experimentally in measurements on $BaTiO_3$, a model ferroelectric showing multiple temperature-dependent first-order transitions. This demonstrates the importance of χ_3 and a_3 as essential parameters for differentiating 1st and 2nd order ferroelectric transitions[223].

In relaxor ferroelectrics (FEs), where there is no spontaneous symmetry breaking, the Spherical

Random Bond Random Field (SRBRF) model[224] assumes that the polar nanoregions (PNRs) interact through a spin-glass-like random-exchange coupling, influenced by quenched random local electric fields. According to this model, under a dynamic external perturbation, the PNRs realign with a characteristic timescale τ, resulting in a negative χ_3 and two distinct extrema: one at the freezing temperature T_f and another at T_m, where χ_1 peaks. Consequently, a_3 should remain positive at all temperatures. However, experiments on typical relaxor FEs, such as 2% Ba-doped LGO, $PbMg_{1/3}Nb_{2/3}O_3$ (PMN), and $Sr_{0.61}Ba_{0.39}Nb_2O_6$, have yielded contrasting results, showing positive, frequency-dependent χ_3 and a negative a_3 across all temperatures[223]. In dipolar glasses, a_3 is expected to diverge strongly at T_f, where $\chi_3 \propto (T-T_f)^{-\gamma}$ with $\gamma = 1$ as the mean field exponent[225,226]. Partial confirmation of this has been observed in $K_{0.989}Li_{0.011}TaO_3$ (KLT1.1), where frequency-dependent peaks in χ_3 have been followed by a sign change and a drop to zero. However, full confirmation of these theoretical predictions remains elusive.

This highlights that measuring nonlinear susceptibilities can offer significant insights into the critical dynamics near phase transitions. Since the hypersusceptibilities are more sensitive to dipolar orders, they can also help differentiate between dipolar and quadrupolar interactions. For instance, in the quantum paraelectric $SrTiO_3$, measurements of χ_3 provided experimental evidence of the onset of a coherent tunneling ground state below 33 K by directly probing ferroelectric (FE) pair correlations between dipole moments[227]. Additionally, phenomenological theories suggest that χ_3 could also probe amplitude modes in a type-II incommensurate phase, showing a jump and sign change at the incommensurate transition point[228]. These examples underscore the vast potential of exploring the nonlinear response in disordered ferroelectrics, an area still full of open questions worth investigating. Focusing on these quantities could lead to new discoveries in quantum materials.

So far, most nonlinear studies on relaxors have been concentrated on model FE systems, such as A/B-site substituted perovskites[229,230,231,232], or tungsten-bronze-based compounds[233]. Hardly any reports focus on double- or triple-perovskite systems, which are known to exhibit a variety of unconventional physical properties due to their inherent geometrical frustration. In this chapter, we will use nonlinear dielectric susceptibility to explore the correlated orders in three triple-perovskite systems: $Ba_3CoRu_2O_9$, $Ba_3BiRu_2O_9$, and $Sr_3CaRu_2O_9$.

$Ba_3CoRu_2O_9$, as described in Chapter 3, shows strong coupling between spin, charge, and lattice degrees of freedom and undergoes simultaneous antiferromagnetic (AFM) and hexagonal-

to-orthorhombic structural transitions, along with a semiconductor-semiconductor electronic transition (related to a change in the number of charge carriers) at $\sim$ 93 K. These coinciding transitions have been linked to orbital ordering in the Ru^{5+} t_{2g} manifold[148], which distorts the RuO_6 octahedra within the Ru_2O_9 dimers and explains the observed suppression of the magnetic moment.

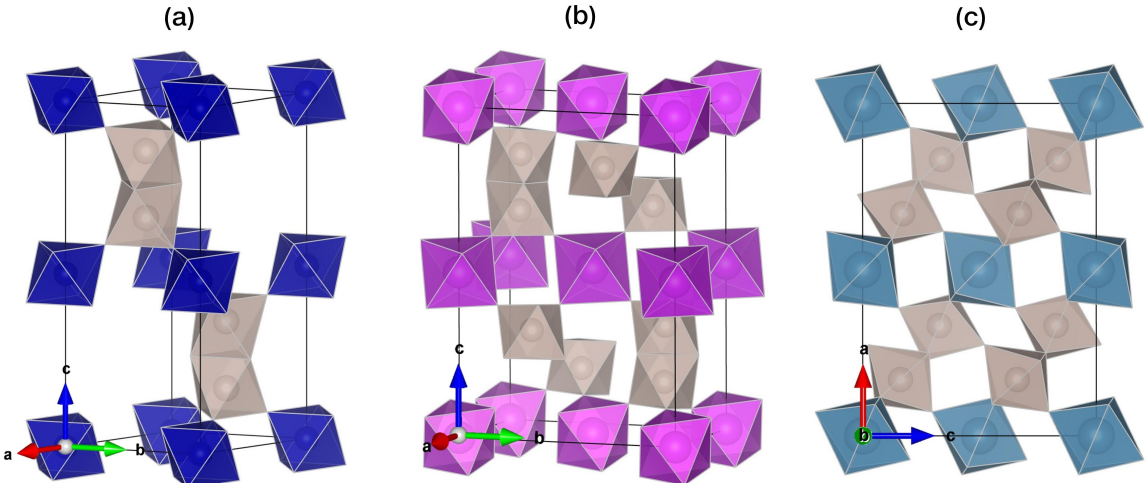


Figure 4.1: The room temperature crystal structures of (a) $Ba_3CoRu_2O_9$, (b) $Ba_3BiRu_2O_9$, and (c) $Sr_3CaRu_2O_9$

	$Ba_3CoRu_2O_9$	$Ba_3BiRu_2O_9$	$Sr_3CaRu_2O_9$
Space group	*$P6_3/mmc$*	*$C2/c$*	*$P2_1/c$*
a (Å)	5.754	5.9436	17.1433
b (Å)	5.754	10.2825	5.6836
c (Å)	14.130	14.7447	9.8485
γ (°)	120	91.010	125.077

Table 4.1: Structural parameters of the three compounds under investigation[2,3,4]

$Ba_3BiRu_2O_9$ is another intriguing system, showing a magnetoelastic transition around 175 K, accompanied by the opening of a spin gap. This material also exhibits unusual dielectric behavior, such as the suppression of frequency dispersion at the magnetoelastic transition and relaxor-like characteristics above the spin-gap opening regime[3].

Lastly, $Sr_3CaRu_2O_9$ is the first reported ruthenate with a 2:1 perovskite ordering and a d^0 ion at the B-site. While Nb^{5+} and Ta^{5+} compounds with similar structures are known to be good

dielectrics for microwave applications[2,3,4], $Sr_3CaRu_2O_9$ remains relatively unexplored. Recent research has revealed two successive magnetic transitions at ~ 160 K and 190 K, with corresponding features in dielectric permittivity, $\varepsilon(T)$, suggesting possible magnetodielectric coupling[4]. These results substantiate each of these compounds as a unique subject for nonlinear dielectric studies.

4.2 Sample preparation

All the materials discussed in this chapter were prepared as polycrystalline powders using the solid-state route using stoichiometric amounts of high-purity reagents (Ba/Sr)CO_3, $CaCO_3$, RuO_2, Bi_2O_3, and Co_3O_4. $Ba_3CoRu_2O_9$ was prepared by heating the reactant mixture at 900°C, 1000°C and 1100°C for 24 hours each with intermediate regrinding and pelletizing[2]. For preparing $Ba_3BiRu_2O_9$, samples were fired at 800°C, 1000°C and 1100°C for 24, 48 and 24 hours respectively, also with regrinding and pelletizing in between treatments[3]. The mixture of $Sr_3CaRu_2O_9$ reagents underwent calcinations at 850°C for 12 hours and at 1200°C for 48 hours, twice. The samples were finally pelletized and sintered at 1225°C for 12 hours to obtain the final phase[4].

4.3 The Measurement Setup

The custom-built setup used for performing these measurements has been described in Chapter 2 (Fig.2.16). To measure the sample's response, we apply a conductive silver paste on both sides of the pellets, effectively creating a parallel-plate capacitor configuration. We also performed measurements on samples with gold electrodes deposited onto them via sputtering, however, no significant improvement was observed. Consequently, conductive silver paste of appropriate consistency, applied uniformly onto flat and polished pellet surfaces, was selected as the electrode of choice. This step is very important since the quality of electrode contacts is crucial for dielectric measurements. An uneven coating results in a non-uniform electric field within the sample. The coating should also cover as much of the sample surface area as possible to avoid contributions due to edge capacitances. Through the lock-in amplifier's phase-sensitive detection capabilities, we separate and measure both the real and imaginary components of the susceptibility. However, since the SR830 is limited to sourcing and measuring frequencies of ≤ 100 kHz, our maximum applied frequency is limited to 33.3 kHz such that the second harmonic signal (I_3) is measured at the 99.9 kHz limit of the lock-in. The magnitudes of the applied ac fields are also constrained by the voltage levels at the lock-in's input where beyond 1.4 V_{pk} the input is over-

loaded. Consequently, the induced effective ac fields in the samples discussed in this chapter are are 4.54 kV/m for KDP, 42.73 V/m for $Ba_3CoRu_2O_9$, 57.7 V/m for $Ba_3BiRu_2O_9$, and 136 V/m for $Sr_3CaRu_2O_9$.

4.4 Calibration

The setup was initially calibrated using the standard ferroelectric KH_2PO_4 (KDP), a material widely used in optoelectronic and piezoelectric applications.

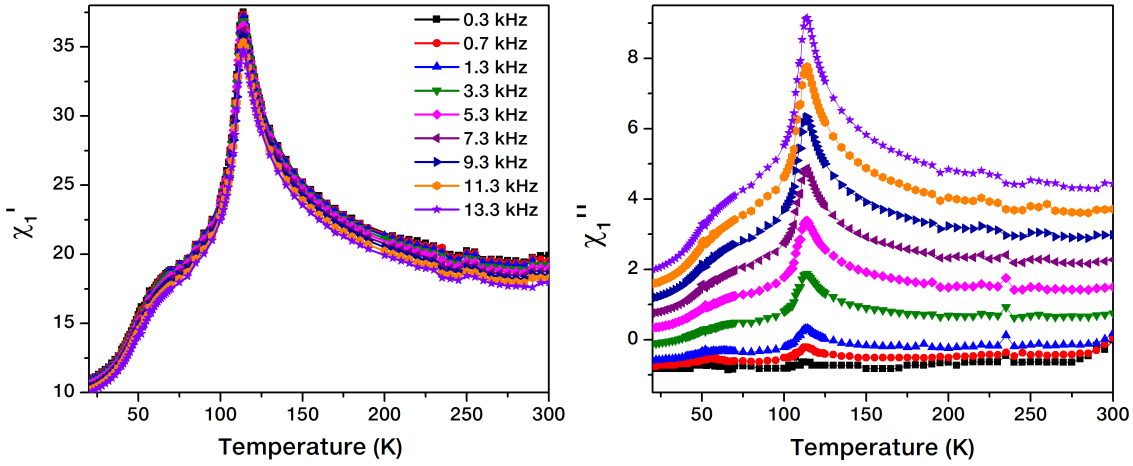


Figure 4.2: Temperature dependence of real (left) and imaginary (right) parts of fundamental susceptibility χ_1 of KDP (KH_2PO_4). Both the discontinuous FE transition and the shoulder peak associated with the domain freezing are measured, attesting to the accuracy of the setup.

KDP undergoes a paraelectric-to-ferroelectric (PE $\rightarrow$ FE) phase transition around 123 K, followed by a domain freezing at lower temperatures[235]. In Fig. 4.2, both the real and imaginary components of the linear susceptibility, χ_1' and χ_1'', measured on a 1.1 mm-thick circular KDP pellet, clearly display this FE transition. A frequency-independent discontinuity around 118 K marks the transition. The slight broadening of the cusp is attributed to the polycrystalline nature of the sample. As the temperature drops, a hump appears between 50 and 100 K, indicating the onset of domain freezing.

Fig. 4.3 presents the real part of the second-order susceptibility, χ_2', in a dimensionless form ($\chi_2' E$) to account for the harmonic distortion. χ_2' serves as a direct measure of the total polarization (P) (eq.4.2) within the material at any given time, making it useful for detecting changes in polarization with respect to temperature or frequency. A finite χ_2' is only expected in macroscopically

noncentrosymmetric systems[236]. Both the paraelectric ($I\bar{4}2d$) and ferroelectric ($Fdd2$) phases of KDP are non-centrosymmetric[237], which explains the finite second-order polarization observed throughout the measurement range, with noticeable frequency dependence. χ_2' remains negative across the temperature range (except at the highest measured frequency of 13.3 kHz) and peaks at the FE transition. The sign of χ_2' is not particularly important as it can simply be reversed by changing the polarity of the electrodes[223]. The magnitude of the negative peak at the FE transition increases up to 5.3 kHz but then gradually decreases, crossing into positive values at 13.3 kHz, while maintaining the same qualitative trend. This might be due to the presence of uncompensated domains within the FE phase that are oppositely aligned with the applied field and become noticeable only at higher frequencies, where larger domains aligned with the field contribute less to the response. As temperature rises, χ_2' decreases to a constant finite value. The loss response, χ_2'', although not shown here, is much more pronounced, being almost two orders of magnitude larger than the real part, and closely mirrors the fundamental response.

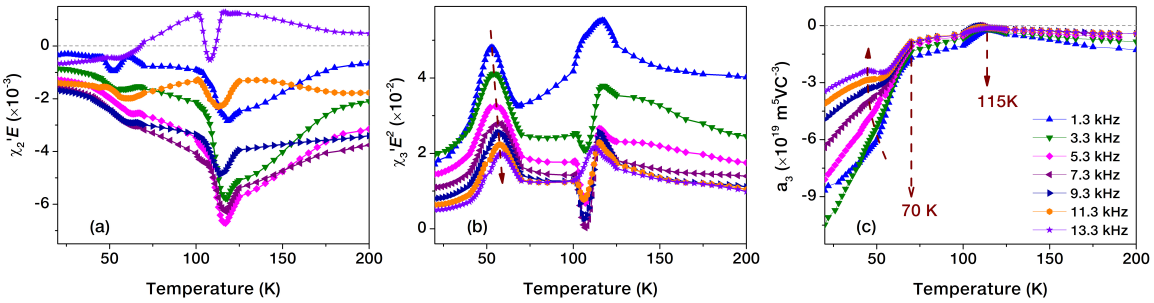


Figure 4.3: The nonlinear dielectric response of KDP (a) Real part of $\chi_2'(T)$ for KDP. Polarization remains negative throughout for all frequencies except 13.3 kHz. (b) Real part of $\chi_3'(T)$ for KDP. The first-order FE transition as well as the domain freezing process are captured. (c) Scaled nonlinear susceptibility a_3 of KDP as a function of temperature. Arrows mark the two distinct features. Frequency dispersion is present for $T < 70$ K. $a_3 < 0$ for all temperatures.

Figure 4.3 (b) displays the real third-order susceptibility of KDP, $\chi_3'(T)$, shown in the dimensionless form $\chi_3' E^2$. This captures the domain freezing process and the discontinuous ferroelectric (FE) transition for applied frequencies 1.3 - 13.3 kHz. The frequency dependence observed between 50 - 60K and the positive value of χ_3' resembles the behaviour of relaxor materials like $PbMg_{1/3}Nb_{2/3}O_3$ (PMN) and $Sr_{0.61}Ba_{0.39}Nb_2O6$ (SBN61)[223], which also challenges predictions of the SRBRF model[224]. Conversely, $\chi_3' > 0$ at all temperatures is consistent with the Landau-Ginzburg-Devonshire (LGD) theory for a discontinuous FE transition[223]. Although a frequency dependence is evident, the relaxation time derived from the peak positions (τ, T_{peak}) does not

follow the typical relaxation models of Arrhenius[238], Vogel-Fulcher (VF)[239], or critical slowing-down dynamics[184].

Additionally, the scaled nonlinear susceptibility, a_3, is shown in Fig. 4.3 (c), revealing features that correspond to both the FE transition (around 115 K) and domain freezing below 70 K. Like χ_3, a_3 exhibits greater frequency dispersion at lower temperatures. These measurements confirm the accuracy of our setup, demonstrating the first-order nature of the FE transition, followed by the freezing of FE domains as the temperature decreases. In agreement with LGD theory for a discontinuous transition, χ_3 remains positive throughout, while a_3 stays negative across the measured temperature range.

4.5 Nonlinear dielectric susceptibilities of $Ba_3CoRu_2O_9$

Figure 4.4 presents the real part of the linear susceptibility of $Ba_3CoRu_2O_9$, showing a distinct slope change around 100K, which mirrors its resistivity ($\rho(T)$) behavior[148]. This marks the antiferromagnetic (AFM) ordering and coincides with the electronic transition, indicating a strong coupling between magnetic, electronic, and polar orders in the material. This is expected, as the structural distortion of the RuO_6 octahedra within the Ru_2O_9 dimers at this temperature drives a structural phase transition from a higher-symmetry hexagonal phase ($P6_3/mmc$) to a lower-symmetry orthorhombic phase ($Cmcm$). The electronic transition is further confirmed by the presence of two distinct activation energies required to describe conduction above and below the Néel temperature, $T_N = 100$ K[148].

This transition is examined in more detail through the real part of the second-order susceptibility, χ_2' (Fig. 4.4), which shows a sharp increase in negative polarization above 100K, followed by the appearance of frequency-dependent peaks. The relaxation dynamics of these peaks follow the VF equation[239,182]. As shown in the inset of Fig. 4.4 (b), the relaxation time $\tau = \frac{1}{2\pi f}$ (where f is the applied frequency) is plotted as a function of $1/(T - T_0)$, with $T_0 = 162$K obtained from the nonlinear fit. The parameters obtained suggest a negative $\frac{E_a}{k_B}$ and a characteristic relaxation time $\tau_0 \approx 10^{-7}$s. Unlike typical glassy or relaxor-like systems, the temperature at which the peak occurs shifts to lower values with increasing frequency, presenting an unusual behavior that remains unresolved.

Throughout the measurement, χ_2' remains negative (Fig. 4.4(b)) and above 150 K, it drops sharply by up to two orders of magnitude. Since the crystal structure of $Ba_3CoRu_2O_9$ is centrosymmet-

ric in both phases, χ_2' should ideally be zero both above and below T_N. However, the observed non-zero values might be due to the polycrystalline nature of the samples, where free charges accumulate at grain boundaries, contributing strongly to the dielectric response as the sample is warmed. Similar finite χ_2' values have been reported in other materials like La_2NiMnO_6 and $Ca_3Mn_2O_7$[240]. Another possible explanation is that the non-zero χ_2' originates from incomplete averaging of the total polarization of polar nanoregions (PNRs), which may form due to significant bond distortion in the RuO_6 octahedra near the transition.

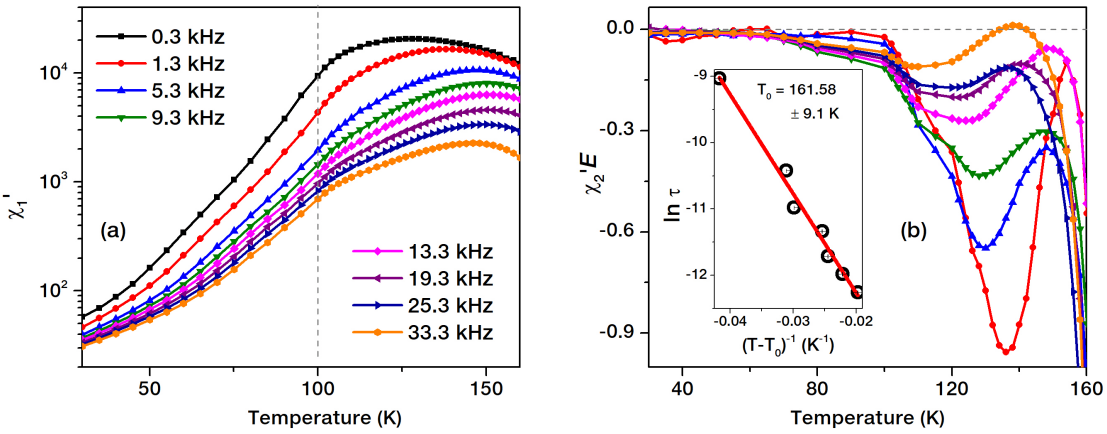


Figure 4.4: Fundamental and first harmonic dielectric response of $Ba_3CoRu_2O_9$. (a) $\chi_1'(T)$ plotted for various frequencies on a log scale. The magnetoelastic transition is captured as a distinct slope changed marked by the dashed line. For $T > 150$ K, the dielectricity is lost as conduction effects become dominant. (b) $\chi_2'(T)$ for various frequencies plotted on a log scale. P drops sharply above 100 K and shows intense frequency dependence. Beyond 150 K, conduction effects dominate.

A similar trend is observed in χ_3' (Fig. 4.5), where strong frequency dependent peaks are observed above T_N between 130 K and 150 K. As with χ_2', these peaks shift to lower temperatures with increasing frequency. However, this time, the variation does not match common relaxation models like the Arrhenius[238], VF[239], or the mean-field critical slowing-down model[184] (inset of Fig. 4.5 (a)). The peak height decreases with increasing frequency until it is washed out completely at 33.3 kHz. At certain frequencies, χ_3' becomes positive, peaks and eventually drops back to negative values above ~210K.

The negative values of χ_3' at temperatures above T_N for most frequencies are consistent with the predictions of the SRBRF model for relaxor FEs. The negative peaks around 150 K likely correspond to the peak in χ_1', with the magnetostructural transition taking over the local polarization before the polar orders freeze. Additionally, the scaled nonlinear susceptibility a_3 (Fig. 4.5 (b))

highlights two key discontinuities - a sharp slope change at T_N and a sharp peak around 160K. The latter possibly results from the crossover of χ_1' to negative values due to enhanced conduction at high temperatures. This is expected, given the low resistivity of this semiconducting material at room temperature (0.07 Ω-cm)[148]. Between these two temperatures, a_3 remains positive, aligning with the predictions of the SRBRF model.

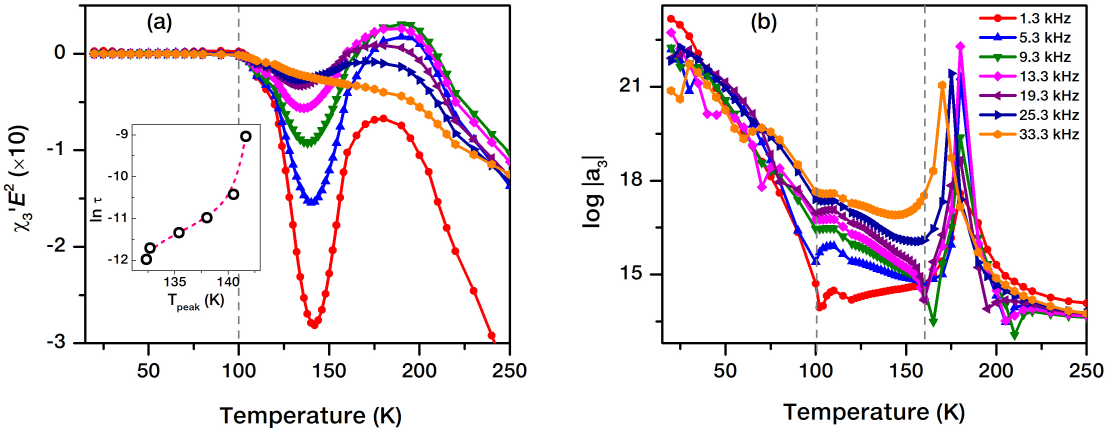


Figure 4.5: The second harmonic dielectric response of $Ba_3CoRu_2O_9$. (a) $\chi_3'(T)$ plotted for frequencies 1.3 - 33.3 kHz in log scale. χ_3' falls sharply above 100 K with similar dynamics as χ_2'. Inset shows the variation of τ with the temperature corresponding to χ_3 (negative) peaks. The dotted line is a guide to the eye. (b) Log of the absolute nonlinear susceptibility, log $|a_3(T)|$ plotted for frequencies 1.3 - 33.3 kHz. Dashed arrows mark the transition temperatures

4.6 Nonlinear dielectric susceptibilities of $Ba_3BiRu_2O_9$

Figure 4.6(a) presents the fundamental dielectric susceptibility (χ_1') measured for $Ba_3BiRu_2O_9$, plotted on a logarithmic scale. The curves show frequency dispersion across a broad temperature range, with changes in susceptibility spanning several orders of magnitude. Similar to $Ba_3CoRu_2O_9$, the sample's conductivity dominates the linear response above 175 K, driving χ_1' to negative values. This behavior contrasts with earlier reports, where the permittivity (ε', proportional to χ_1') remained positive up to room temperature[3]. A potential reason for this could be defect formation due to variations in synthesis or sintering conditions, as these strongly influence grain boundary formation, which, in turn, affects bulk conduction and charge polarization response.

This issue complicates the study of the magnetoelastic transition and the spin-gap opening, expected to occur within this temperature range. To address this, we plot the derivative of χ_1' with respect to temperature (Fig. 4.6(b)). Despite the proximity to the leakage current-dominated

region, this method successfully highlights the transition point. Figure 4.6(c) zooms into the transition region, revealing a subtle slope change at 175 K, indicating the spin-gap opening transition. Meanwhile, the upturn near 200 K marks the onset of leakage current dominance.

A strong frequency dependence between 100 – 150 K corresponds to an exponential divergence-like feature in χ_1', which diminishes at lower frequencies. This feature was noted in earlier linear dielectric measurements, though previously dismissed as an artifact[3]. Finally, the τ vs T_{peak} plot derived from the relaxation peaks shows a linear trend with a negative slope (Fig. 4.6(d)), which does not align with known relaxation models[238,239,184].

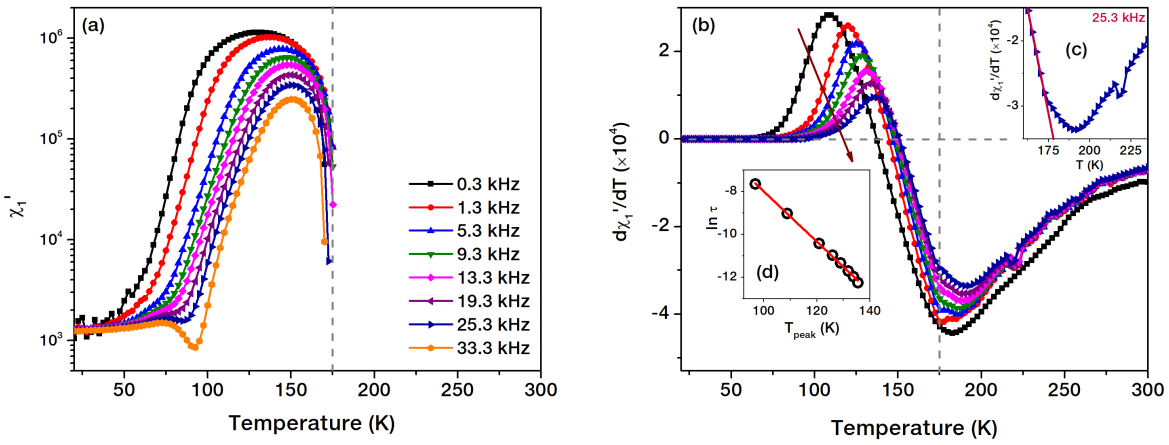


Figure 4.6: Linear dielectric response of $Ba_3BiRu_2O_9$. (a) $\chi_1'(T)$ plotted for various frequencies on a log scale. χ_1' sharply drops to negative values close to 175 K due to conduction. Feature below 100 K is most pronounced at 33.3 kHz and is suppressed at lower frequencies. (b) Derivative $d\chi_1'/dT$ plotted as a function of temperature for frequencies 0.3 - 33.3 kHz to discern the spin-gap opening transition. (c) Zoom-in of $d\chi_1'/dT$ at $f = 33.33$ kHz showing the slope change marking the spin-gap transition. (d) relaxation below 100 K seen to follow an exponential T-dependence.

The frequency dependence is clearly reflected in the χ_2' curves shown in Fig. 4.7(a), where three distinct types of dispersion peaks are observed. The first peak appears around 100 K, coinciding with the development of polar nanoregions (PNRs) as the system is warmed. At this point, the net polarization increases, reaching a peak at T_{P1} that increases with increasing frequency. The dynamic behavior of these PNRs follows the critical slowing down equation, as seen in Fig. 4.7 (b,c), where T_{P1} is plotted against the natural log of $\tau = \frac{1}{2\pi f}$. The fit yields the parameters: $z\nu = 4.03 \pm 0.5$ (the dynamical exponent), $T_0 = 51.06 \pm 5.14$ K (the *true* critical temperature), and the characteristic relaxation time $\tau_0 = (2.68 \pm 0.07) \times 10^{-5}$ s. Notably, τ_0 is about two orders of magnitude larger than previously reported values for temperatures above the phase transition[3],

suggesting that even below the magnetoelastic transition, the electric dipoles remain dynamic forming larger correlated domains on cooling until freezing below 100 K, when $P \rightarrow 0$.

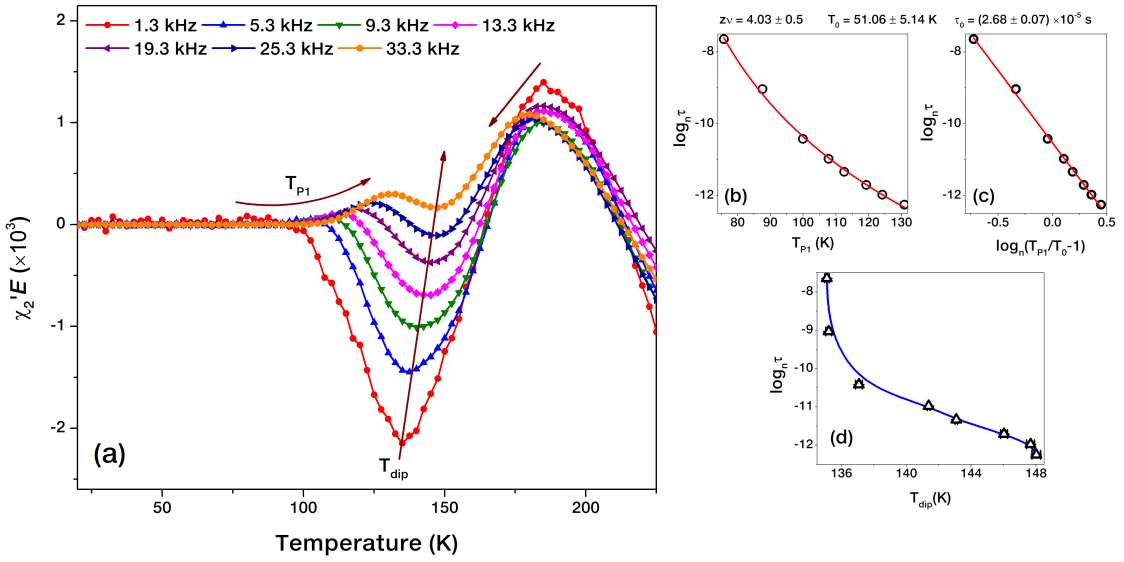


Figure 4.7: First harmonic response of $Ba_3BiRu_2O_9$. (a) $\chi_2'(T)$ is plotted for frequencies 1.3 - 33.3 kHz. Three features are noticeable: peak $\rightarrow$ dip $\rightarrow$ peak ($T_{P1} \rightarrow T_{dip} \rightarrow T_{P2}$) shown with arrows. (b) Critical slowing down behavior followed by $\tau(T_{P1})$ (c): linearity in lnτ vs ln(T_{P1}/T_0-1) confirming the validity of the nonlinear fit. (d) Relaxation process across T_{dip}, dotted lines are only a guide to the eye (not a fit)

The second dispersion appears in the negative polarization peaks (T_{dip}) (Fig. 4.7(a)) which do not ascribe to standard relaxation models. However, the reduction in the magnitude of the negative peak with increasing frequency suggests that larger polar domains are negatively polarized, while smaller ones align along the applied electric field. This type of χ_2' response is similar to what is observed in relaxor ferroelectrics such as $PbMg_{1/3}Nb_{2/3}O_3$ (PMN) and $Sr_{0.61}Ba_{0.39}Nb_2O_6$ (SBN61)[223].

The third dispersion is seen in the positive maxima following the negative-to-positive polarization crossover at all frequencies Fig. 4.7(a), indicating an inversion in the dominant direction of polarization in the system. Interestingly, the frequency dependence of these peaks is reversed — similar to the behavior seen in $Ba_3CoRu_2O_9$ — and quite subtle, suggesting a possible convergence of two relaxation processes at the crossover point.

A similar behavior is observed in the χ_3' curves (Fig. 4.8(a)), where two distinct anomalies shift with temperature and frequency. At the lowest frequency (0.3 kHz), a broad peak appears below 125 K (T_1), along with a subtle slope change around 175 K (T_2). At 1.33 kHz, the peak shifts slightly to the right, while the 175 K feature becomes more pronounced and shifts leftward. At

5.33 kHz, both the features are distinctly visible with nearly equal magnitude. As frequency increases, the two features begin to converge until only one peak remains around 150 K. This behavior seems to indicate multiple relaxation processes acting on the polar domains within the spin-gap phase, making characterization difficult. The dynamic nature of these processes is represented in Fig. 4.8(b,c), where $\log_n \tau$ is plotted as a function of both T_1 and T_2. The linear relationship shows that at the highest frequencies, the two peaks merge between 130 K and 150 K.

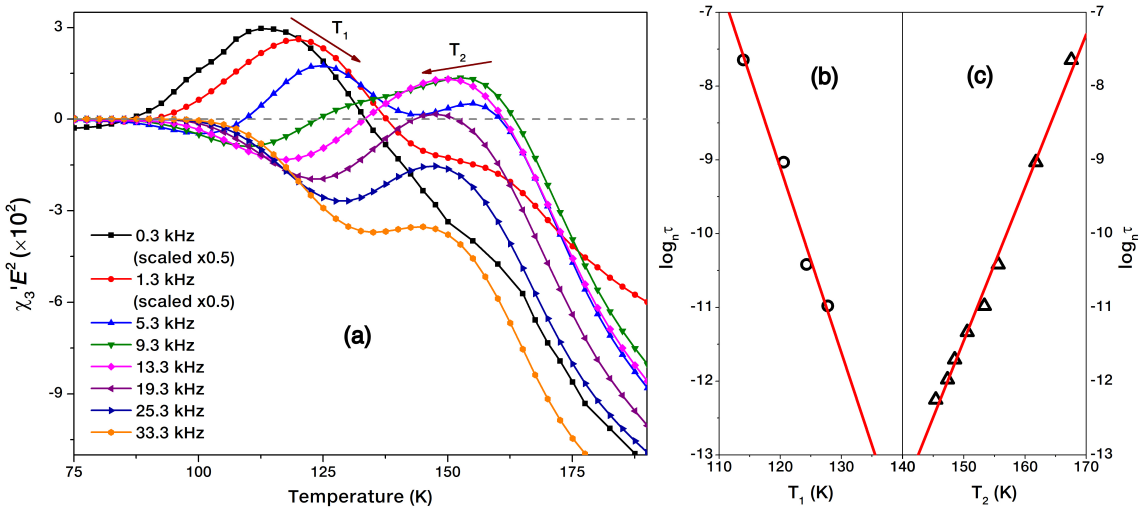


Figure 4.8: Second harmonic response of $Ba_3BiRu_2O_9$. (a) $\chi_3'(T)$ as a function of temperature for various frequencies in the temperature range 75 - 190 K. The coexistence of two types of relaxation processes is captured in the dynamics of the two observed features. The inset shows τ plotted as a function of T_1 and T_2.

4.7 Nonlinear dielectric susceptibilities of $Sr_3CaRu_2O_9$

Our final system of interest, $Sr_3CaRu_2O_9$, is a relatively unexplored triple-perovskite. Recent reports on its linear dielectric permittivity (ε) suggest the potential for magnetodielectric behavior[4]. Figure 4.9(a) displays the first-order susceptibility χ_1' on a logarithmic scale, revealing a sharp dispersion-like feature at 160 K, more distinct at higher frequencies. This behavior closely resembles that observed in $Ba_3BiRu_2O_9$ (Fig. 4.6(a)), with a more pronounced feature at the magnetic transition. The relaxation in this regime follows critical slowing down, with extracted parameters: $T_0 = 87.9 \pm 5.1$ K, $\tau_0 \approx (2.4 \pm 0.5) \times 10^{-6}$ s, and $z\nu \approx 2.6 \pm 0.5$ (inset of Fig.4.9(a)).

Additionally, a broad dispersion is visible in the peaks near room temperature. However, the extremely high susceptibility values and dispersion in this region are likely due to extrinsic effects,

such as significant surface contributions to polarization caused by delocalized surface charges. Since these materials are semiconducting rather than insulating dielectrics, leakage current near room temperature is unavoidable. Even though $Sr_3CaRu_2O_9$ has a relatively high room temperature resistivity of around 0.9 Ω-m—higher than the other two compounds in this study [ρ(Co,300K) = 7×10^{-4} Ω-m, ρ(Bi,300K) = 0.3 Ω-m] — leakage current still affects the measurements when the sample becomes more conducting. This is also why the lossy behavior emerges at the lowest temperature for the most conductive sample, $Ba_3CoRu_2O_9$.

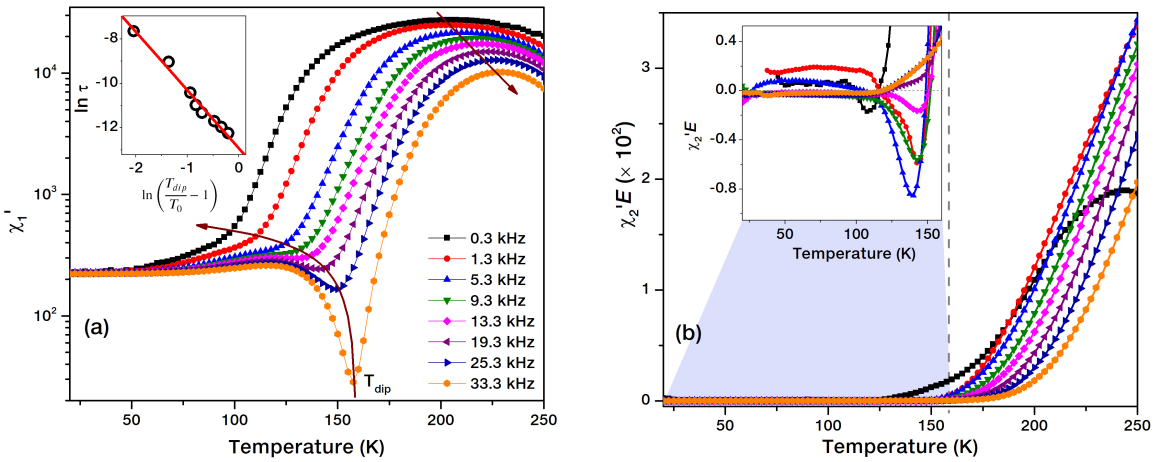


Figure 4.9: The fundamental and first harmonic response of $Sr_3CaRu_2O_9$. (a) $\chi_1'(T)$ is shown for frequencies 0.3 - 33.3 kHz. The sharp feature (T_dip) corresponding to the magnetic transition at $\sim$ 160 K. (b) $\chi_2'(T)$ for frequencies 0.3 - 33.3 kHz. Inset: zoomed view of $T < 150$ K, highlighting the small frequency-dependent negative polarization observed before $\chi_2'(T)$ rose sharply.

As shown in Fig. 4.9(b), the polarization drops sharply as the system cools and transitions into the magnetically ordered phase below approximately 200 K. The inset highlights a small crossover to negative values near 150 K at the lowest frequencies. This slight negative cusp diminishes with increasing frequency and disappears entirely above 13.3 kHz. At higher frequencies, the polarization vanishes below 125 K, which is expected given the global crystal symmetry of $P2_1/c$, a centrosymmetric structure. The persistence of the small negative polarization at lower frequencies likely arises from cluster-like dipolar segments with longer response times. These segments take more time to equilibrate to the zero-polarization state, leading to a small persistent negative polarization.

Figure 4.10(a) presents χ_3' as a function of temperature for $Sr_3CaRu_2O_9$. The inset reveals that across all frequencies, χ_3' exhibits a crossover from a tiny positive to large negative values, spanning

4–5 decades. This crossover has a strong frequency dependence. The increase in the third-order polarization is gradual, occurring between 100 and 200 K, and begins to slow beyond 200 K, eventually decreasing near room temperature. The predominantly negative χ_3' value above the magnetic transition is consistent with predictions from the SRBRF model for relaxors. Similar behavior of χ_3' has been observed in materials such as La_2NiMnO_6, a partially disordered double perovskite manganite, and $Ca_3Mn_2O_7$, a layered perovskite with hybrid-improper ferroelectricity (HIF)[240].

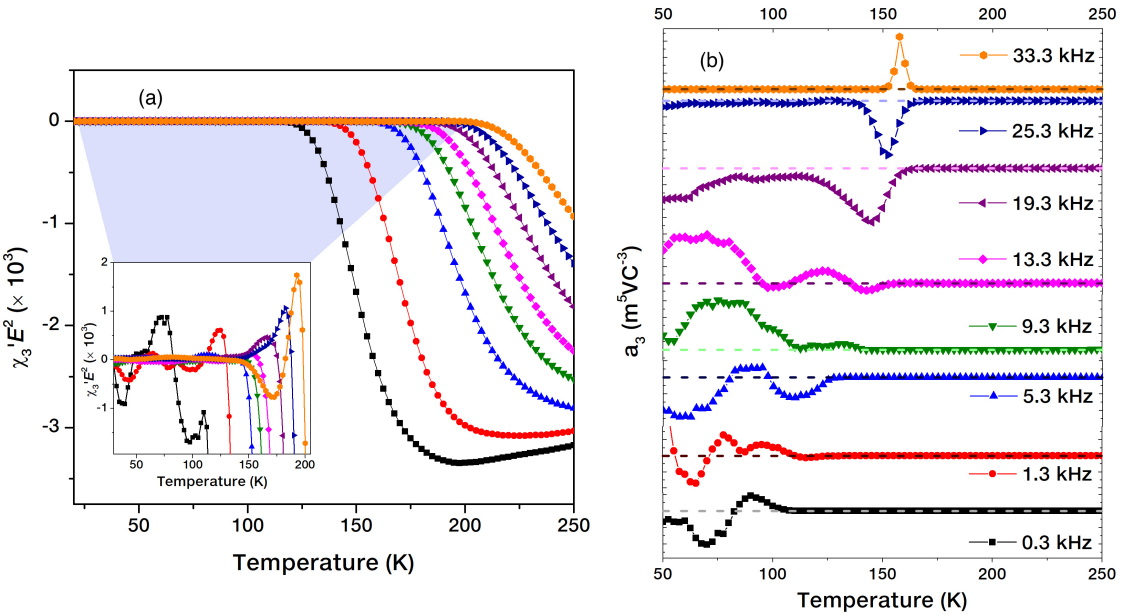


Figure 4.10: (a) Second harmonic response of $Sr_3CaRu_2O_9$. (a) $\chi_3'(T)$ measured at frequencies 0.3 - 33.3 kHz. Inset: zoomed view of $T < 150$ K, highlighting the minuscule magnitude of χ_3 maxima on a positive scale, (b) The scaled nonlinear susceptibility, $a_3(T)$ shown for frequencies 0.3 - 33.3 kHz. Horizontal dotted lines show the position of zero for each curve.

Figure 4.10(b) shows the frequency-dependent variation of the scaled nonlinear susceptibility a_3, measured from 0.3 to 33.3 kHz. As the frequency increases, a negative peak emerges near 150 K, corresponding to the positive peaks in χ_3' just before the crossover to negative values. At the highest frequency, however, the peak unexpectedly reverses sign, accompanied by a strong divergence. Notably, a_3 rapidly diminishes beyond the divergence point. According to previous studies, a_3 should exhibit a critical singularity at T_f in dipolar glasses[225]. This suggests that $Sr_3CaRu_2O_9$ exhibits characteristics of both dipolar glasses and relaxor ferroelectrics at the magnetic phase transition. The frequency dependence of the anomaly in $a_3(T)$ likely reflects the fact that larger, more correlated domains with longer relaxation times dominate the polarization re-

sponse at lower frequencies. Additionally, multiple features emerge at low temperatures, as seen in χ_3' (inset of Fig. 4.9(c)), indicating the presence of uncompensated short-range correlated domains within the magnetically ordered state. These features only become apparent when probing higher-order polarization responses. Further study of this material will be crucial to determining which of these states—dipolar glass or relaxor ferroelectric—dominates the low-temperature dipolar ground state in this system.

4.8 Conclusion

This chapter summarizes the first comprehensive nonlinear dielectric measurements on polycrystalline samples of three triple perovskite ruthenates: $Ba_3CoRu_2O_9$, $Ba_3BiRu_2O_9$, and $Sr_3CaRu_2O_9$. Through these measurements, we explored the dynamic behavior of underlying polar orders using higher harmonics of the electric polarization response. Each system revealed intriguing, previously unreported features in their higher-order susceptibilities.

In $Ba_3CoRu_2O_9$, the magnetostructural transition near 100 K is captured in $\chi_{1,2,3}'$. The hypersusceptibilities $\chi_{2,3}'$ and a_3 reveal frequency-dependent dynamics just above the transition, which have no counterpart in the linear susceptibility. As the transition is approached from above, χ_2' displays negative peaks which move toward lower temperatures with increasing frequency, and are sharply suppressed below T_N. Despite being linear in a Vogel-Fulcher (VF) plot, the dispersion yields an unexpected activation energy $E_a < 0$, warranting further investigation. Additionally, χ_3' shows frequency-dependent negative peaks between 130 and 150 K that defy typical relaxation models, such as Arrhenius, VF, or critical slowing down. The negative values of χ_3' and a_3 for most frequencies align with the SRBRF model for relaxor ferroelectric systems, a behavior rarely observed in real materials. This relaxor-like behavior may result from strong distortions in the RuO_6 octahedra within the Ru_2O_9 dimers, leading to a breaking of the t_{2g} orbital degeneracy of Ru^{5+} ions below 100 K. The frequency dispersion above this temperature reflects the thermal evolution of this distortion, which is expressed in the polarization response.

In $Ba_3BiRu_2O_9$, χ_2' and χ_3' reveal a dipolar regime within the spin-gap phase, where multiple relaxation processes seem to coexist. The frequency dependence of the peaks in $d\chi_1'/dT(\log_n \tau(T_P))$ is linear with a negative slope, the reasons for which are still unknown. Similarly, in χ_2', $\log_n \tau(T_{P2})$ follows the same trend. Broad, dispersive peaks just above 100 K ($\log_n \tau(T_{P1})$) in χ_2' exhibit critical slowing down, with a relaxation time around 10^{-5} s, $z\nu = 4.03$, and $T_0 \approx 51$ K. The neg-

ative peaks ($\log_n \tau(T_{dip})$), however, do not conform to standard relaxation models. In χ_3', both peak temperatures exhibit an exponential dependence on frequency, described by $\tau = ke^{\beta T}$ with $\beta = -0.25$ for T_1 and $\beta = +0.21$ for T_2, suggesting two inversely behaving relaxation processes below the spin-gap opening across a broad temperature range. This implies that interlayer charge transfer, which may drive the relaxor-like behavior in this system, does not cease at the spin-gap opening but continues subtly down to around 100 K.

In $Sr_3CaRu_2O_9$, distinct anomalies are observed near the magnetic phase transitions (160 K and 190 K) in $\chi_{1,2,3}'$, along with strong dispersion effects. The dispersive peaks in χ_1' follow critical slowing down behavior, with parameters $T_0 \approx 88$ K, $\tau_0 \approx 2.5\mu$s, and $z\nu = 2.6$. Both hypersusceptibilities drop across the transition and nearly vanish in the magnetically ordered state. Small oscillations around zero persist at low temperatures and low frequencies, likely indicating larger, uncompensated domains responding to low-frequency perturbations. Features in χ_3' and a_3 suggest a mixture of dipolar-glass and relaxor ferroelectric-like behavior. Further nonlinear measurements, potentially on single crystals, are necessary to clearly define the true polar order behavior in this system.

Additionally, the agreement with the SRBRF model found in χ_3' for both $Sr_3CaRu_2O_9$ and $Ba_3BiRu_2O_9$ suggests that materials with polar orders strongly correlated with spin, lattice, or orbital orders represent a new class of systems beyond classic or relaxor ferroelectrics. These systems can be explored to investigate concurrent phase transitions and serve as potential testbeds for theoretical models in the future.

But still try for who knows what is possible!

Michael Faraday

5

Evolution of the magnetism in $Ba_4NaRu_3O_{12}$

5.1 Introduction

Continuing in our exploration of layered ruthenate systems, we reach the 1:3 substitution limit of the perovskite system where the option of substituting either the A or B-site in this ratio generates highly anisotropic crystal systems with very interesting material properties.

The A-site substituted class of these systems have recently gained traction due to their excellent dielectric[241] and catalytic properties[73]. They are categorized as distorted cubic perovskites and their structures are strongly influenced by the type of tilt system involved. For example, large $a^+a^+a^+$ tilts produce the AA'$_3$B$_4$O$_{12}$ structure where the strong tilting of the B octahedra forces the A' sites to settle in a square planar geometry. On the other hand, strong tilting in the $a^+a^+c^-$ directions generates the A$_2$A'A"B$_4$O$_{12}$ structure possessing an inherent columnar-order[242]. These materials, although with a huge potential for the exploration of symmetry-influenced physical properties, require the use of simultaneous high-pressure and high-temperature environments to be stabilized.

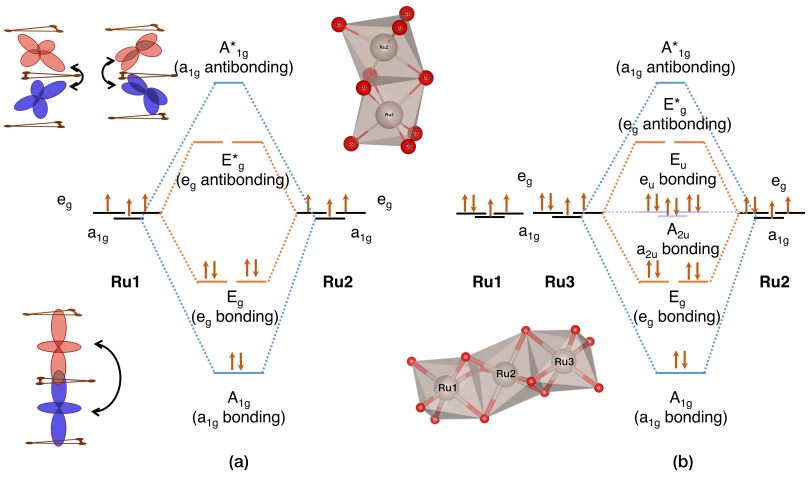


Figure 5.1: Formation of molecular orbitals in a (a) $Ru_2^{5+}O_9$ dimer, and (b) a $Ru_3^{4+}O_{12}$ trimer. The structural geometry of the dimer/trimer and the hopping within the a_{1g} (bottom) and e_g (top) orbitals is also shown.

The B-site substituted systems, conversely, show very interesting *quasimolecular* physics from having cation dimers and trimers govern their magnetism. For example, in systems like $Ba_3NbRu_3O_{12}$ [76] and $Ba_4LnM_3O_{12}$ [243,244] (M = Ru, Ir), Ru trimers isolated by nonmagnetic layers show fascinating frustration-based physics with either long-range order developing at extremely low temperatures or not at all. The relative proximity of the transition-metal (TM) cations within these trimers leads to the formation of molecular orbitals which govern the physics. We can understand this by considering a simpler case of a dimer first, where the atomic d-orbitals of two TM cations, in a local D_{3h} symmetry linearly combine to produce bonding and antibonding molecular orbitals. A schematic visualizing such a scenario for a $Ru_2^{5+}O_9$ dimer comprising of two d^3 Ru ions with inter-site hopping in a trigonal local field is shown in Fig. 5.1(a) [245,246,247]. The 6 electrons occupying the nondegenerate a_{1g} and doubly-degenerate e_g^π atomic orbitals (created due to degeneracy breaking of the t_{2g} orbitals by the weak trigonal field), populate the new low-lying hybridized A_{1g} and E_g orbitals according to Hund's coupling and stabilize a low-spin $S = 0$ state. Similar molecular orbitals are formed in the case of $Ru_3^{4+}O_{12}$ (d^4) trimers as shown in Fig. 5.1 (b), where the two outer ions can combine with the middle ion and lead to a low-spin $S = 0$ state against the $S = 1$ state (2 unpaired electrons) in the atomic orbital scenario. These states are strongly influenced by the geometry of the local field and the electron hopping probablities between them, and thus make d-orbital compounds with the ability for direct exchange possess high degree of tunability and a very attractive platform to study instabilities leading to quantum phase transitions [247]. Additionally, compounds containing isolated groups of magnetic

ions as repeating motifs have often surprised physicists with their exotic properties and complex magnetic ground states[248,79] despite disruptions in the exchange pathway. This highlights the importance of next-nearest neighbour superexchange mediated interactions in these materials.

$Ba_4NaRu_3O_{12}$ uniquely stands out in this family of B-site substituted quadruple perovskites in that it is neither a network of isolated or connected Ru/Ir trimers like $Ba_5Ru_3O_{12}$[248] and $Ba_4(Ru/Ir)_3O_{10}$[249,250] nor of isolated Ru dimers like its sister triple-perovskite $Ba_3NaRu_2O_9$[79]. The repeating motif of this structure is a set of one RuO_6 octahedra connected via a corner shared oxygen to a Ru_2O_9 dimer separated by layers of nonmagnetic NaO_6 octahedra. In our knowledge, no other layered ruthenate is known to possess such a motif. This material has also been scarcely studied in the literature, with only three reports on it from nearly 20 years ago[251,252,253], leaving much to be explored, especially its complex magnetism at low T. This motivates us to investigate this compound in-depth and explore its ground state's evolution as a function of temperature and characterize its correlation with lattice and charge degrees of freedom. In this chapter, we summarize our findings from a combination of bulk physical and magnetic characterization measurements with high-resolution neutron and synchrotron x-ray powder diffraction, helping us correlate the macroscopic response with the microscopic changes in structure that occur under external perturbation.

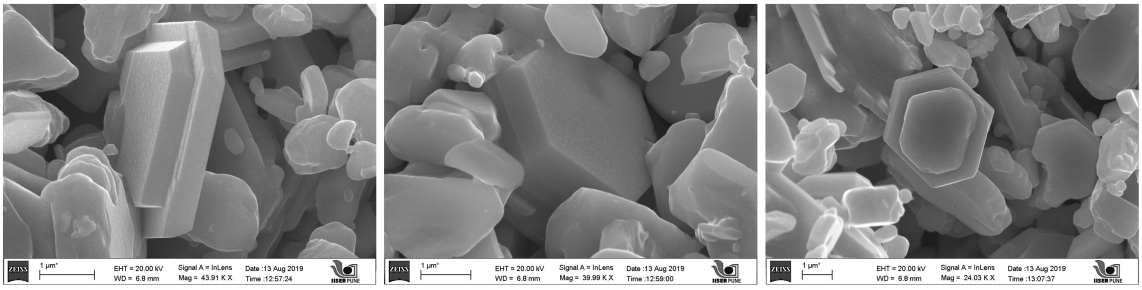


Figure 5.2: FESEM image $Ba_4NaRu_3O_{12}$ showing micron-sized hexagonal crystallites.

5.2 Synthesis and preliminary characterization

Polycrystalline samples of $Ba_4NaRu_3O_{12}$ were prepared via solid state synthesis method using stoichiometric amounts of raw materials ($BaCO_3$, Na_2CO_3 and RuO_2) following the procedure detailed by Battle et al.[251]. To compensate for the volatility of Na, a 15% excess of Na_2CO_3 was used and RuO_2 was heated for 2 - 3 hours at 250°C before weighing to remove any moisture. The precursors were mixed and ground in a mortar using ethanol until a fine, homogeneous mixture

was obtained. The entire mixture was then pelletized into a thick pellet to further reduce the loss of Na, placed in an alumina crucible and heated at 800°C for 12 hours in air. Hard, black pellets obtained at the end of the reaction were crushed and checked for phase purity through laboratory x-ray diffraction (XRD) using the BRUKER D8 ADVANCE DIFFRACTOMETER (CuK_α λ=1.5406Å). Elemental compositions and their homogeneity was also confirmed by using an energy dispersive X-ray spectrometer (EDS) (Ziess Ultra Plus). The average stoichiometry calculated from the statistical analysis of the EDS data is $Ba_4Na_{0.87\pm0.1}Ru_{3.02\pm0.2}O_{12}$, confirming the homogeneity and single phase nature of the sample. FESEM images of hexagonal microstructure are shown in Fig.5.2

Synchrotron x-ray powder diffraction (SXRD) was performed at the Swiss Light Source (PSI) on the ADDAMS beamline[12]. The wavelength of the x-ray was calculated by refining LaB_6 standard to be $\lambda = 0.49343$ Å and an instrument-resolution file (IRF) file was created (FWHM (°) vs 2θ). Using this IRF file, the profile parameters were fixed and only microstructural and atomic parameters were refined for diffraction patterns collected at each $T = 5 - 300$ K. This allowed us to estimate changes in maximum strain (%) with temperature. (details in Appendix B). Rietveld refinement of the diffraction patterns were performed using the FULLPROF SUITE[20]. Crystal Structures were generated using VESTA[115]. Neutron time-of-flight (*tof*) measurements were performed at the WISH diffractometer of ISIS Pulsed Neutron and Muon source in the T range 13 - 300 K. Data collected on 5 banks was simultaneously refined using FULLPROF and Bank 4-7 (2θ =121.66°) was chosen to be the pattern of choice with acceptable $q-$range and resolution. Specific Heat and Magnetization measurements were performed in a Quantum Design PPMS Dynacool. Resisitivity measurements were performed in a Cryogenic Limited Cryogen Free Measurement System (CFMS) using a VTI-based resistivity option.

5.3 Crystal structure

$Ba_4NaRu_3O_{12}$ crystallizes in a rare 8-layered hexagonal structure described by the non-centrosymmetric space group $P6_3mc$ (No. 186) as shown in Fig. 5.4, with lattice parameters $a = b = 5.797(2)$ Å and $c = 19.211(6)$ Å . The Ba ions have 4 crystallographically distinct sites and occupy corner and edges of the unit-cell as well as the voids between the octahedra. The Ru ions have three unique positions as well, two of them (Ru2, Ru3) forming a face-shared octahedra located on the unit cell edges, while one (Ru1) sits at the centre of an octahedra corner-linking the Ru_2O_9

and the NaO_6 octahedra. This structure is visually presented in Fig. 5.4 (a). Viewed along the *a*-axis the 8-layers (2 formula units, so $Z = 2$) forming the unit cell can be seen in Fig. 5.4 (d). Fig. 5.4 (b) and (c) show the Ru1(/Na) and Ru2(/Ru3) layers in the *ab*-plane, highlighting the triangular arrangement of Ru cations in each layer. The structural and bond parameters obtained from the Rietveld refinement of this structure are tabulated in Tables 5.1 and 5.2. The values obtained are consistent with previous reports[251,252].

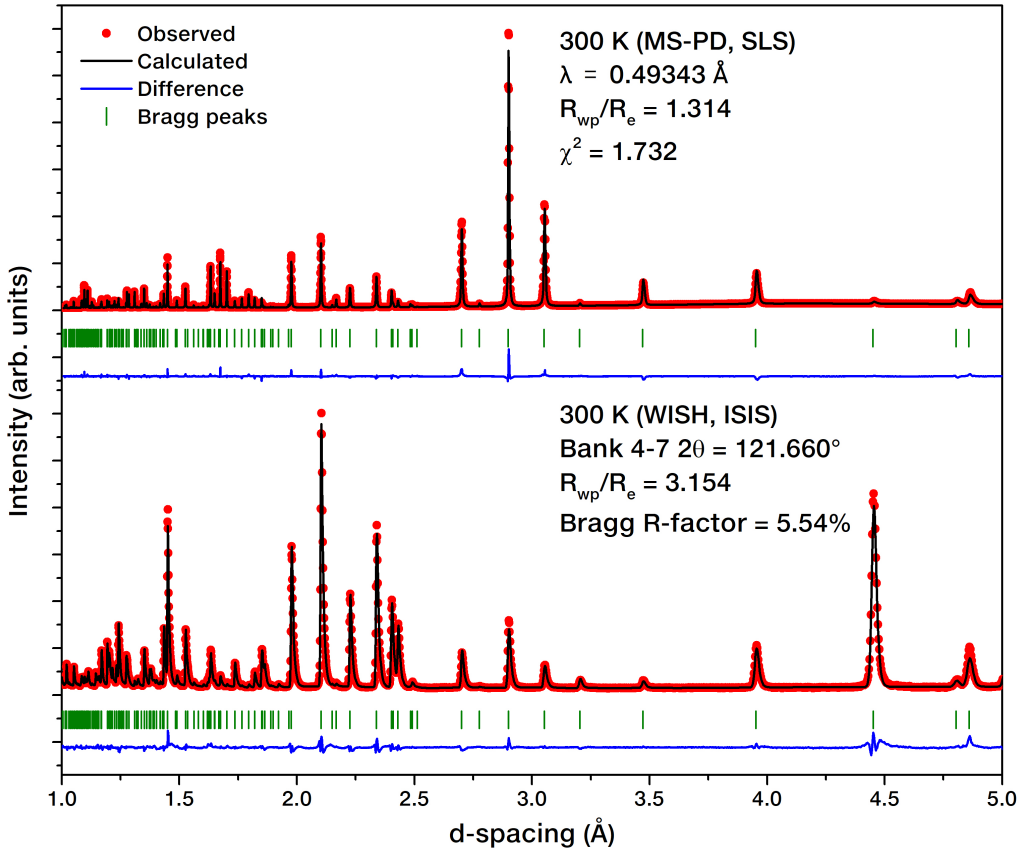


Figure 5.3: Room temperature synchrotron XRD (top) and neutron (bottom) powder diffraction patterns of $Ba_4NaRu_3O_{12}$ refined using FULLPROF SUITE[20]

Since the ionic radii of Na^+ (1.02 Å[254]) and Ru^{5+} (0.565 Å[254]) vastly differ, no site disorder is expected and all ions fully occupy their sites. The refinement results confirm this too and return a total cell content of $Ba_8Na_2Ru_6O_{23.99}$. However, since Ba2, Ba3, Ba4, Na and Ru1 - all lie on the same plane [Wyckoff site: 2*b* (1/3,2/3,*z*)], the positions and thermal parameters required constraints to prevent the fit from diverging. The three Ru sites are inequivalent, but have the same site multiplicity 2. Fig. 5.3 shows the fit to the structural model in Table 5.1 for synchrotron x-ray (top panel) and neutron (bottom panel) powder diffraction data at room temperature. The

goodness of fits obtained are reasonable and confirm the accuracy of the model.

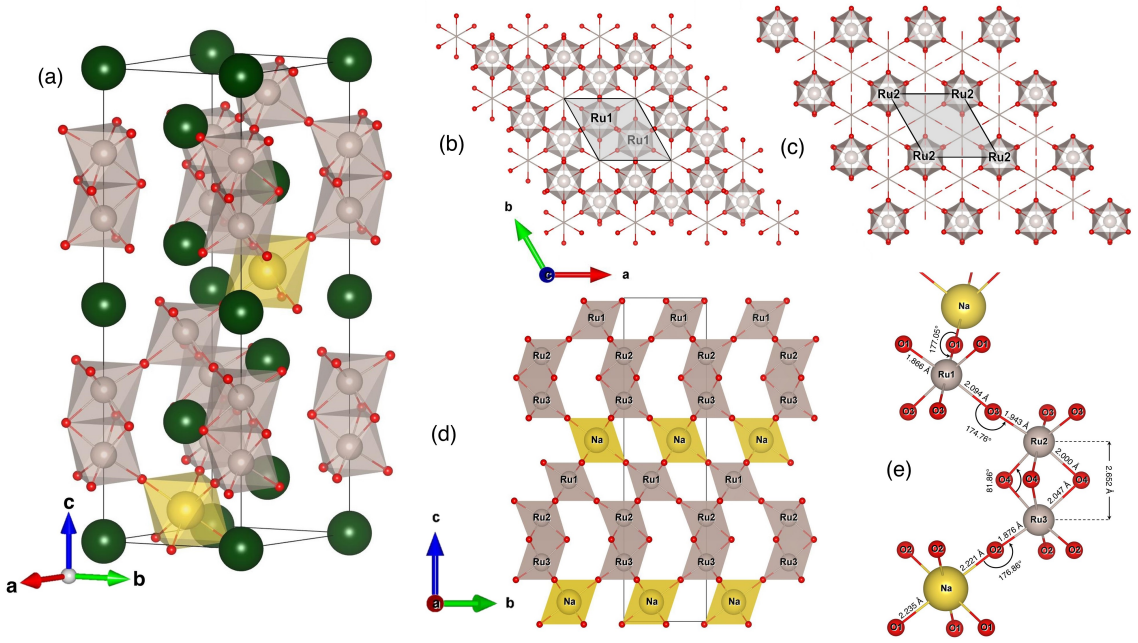


Figure 5.4: (a) Crystal structure of $Ba_4NaRu_3O_{12}$. The triangular network formed in the ab-plane by (b) Ru1/Na and (c) Ru2/Ru3 ions viewed along the *c*-axis. (d) The 8-layered unit cell viewed along the *a*-axis, (e) Bond lengths and angles of the exchange path calculated from at room temperature neutron diffraction data.

It can be seen from Table 5.2 that the distance between the Ru ions within the Ru_2O_9 is 2.652 Å, shorter than the Ru-Ru metallic bond length (2.6725Å [116]), suggesting a strong antiferromagnetic (AFM) direct interaction between Ru2 and Ru3. The observed average Ru-O bond length ≈1.97 Å is very close to that expected for an Ru^{5+}—O^{2-} bond (1.964Å [151]), thus confirming the pentavalent oxidation state of Ru. The Ru octahedra are also slightly distorted as evidenced by the difference in the distances of the two uniquely located O^{2-} ions forming each of the Ru octahedra. Ru2 and Ru3 are both farther away from the O^{2-} connecting them (O4) than the anions on the opposite side (O3, O2 respectively) due to Coulomb repulsion. Due to the same reason, the Ru2—O3 bond is longer than the Ru3—O2 bond which experiences repulsion from Na^+ instead of the more electropositive Ru^{5+}. Distortion is present for the NaO_6 octahedra as well, likely due to its large size.

The Ru2—O4—Ru3 superexchange ($\angle_{ROR} = 81.86°$) competes with the direct exchange by favoring a weak ferromagnetic (FM) coupling. There will be an AFM exchange across the Ru1—Ru2 path as well ($\angle_{ROR} = 174.76°$) due to the half filled t_{2g}^3 of Ru^{5+}. These three magnetic ions are separated by non-magnetic NaO_6 layers. Thus, for the exchange path to extend throughout

the crystal, a robust next-nearest-neighbour (NNN) exchange between Ru1 and Ru3 is imperative.

Space Group: $P6_3mc$ (Hexagonal, No. 186)
a = b = 5.797(2) Å c = 19.211(6) Å $\alpha = \beta = 90°$ $\gamma = 120°$

Atom	Wyckoff site	x	y	z	B_{iso}
Ba1	2a	0	0	0	0.8(3)
Ba2	2b	1/3	2/3	0.123(33)	0.8(3)
Ba3	2b	1/3	2/3	0.371(03)	0.8(3)
Ba4	2b	1/3	2/3	0.746(93)	0.8(3)
Na	2b	1/3	2/3	0.559(93)	0.8(3)
Ru1	2b	1/3	2/3	0.937(03)	0.8(3)
Ru2	2a	0	0	0.320(31)	0.8(3)
Ru3	2a	0	0	0.182(41)	0.8(3)
O1	6c	0.488(03)	0.511(97)	-0.009(27)	1.0(2)
O2	6c	0.844(21)	0.155(79)	0.128(71)	1.0(2)
O3	6c	0.834(51)	0.165(59)	0.372(51)	1.0(2)
O4	6c	0.847(91)	0.152(09)	0.753(21)	1.0(2)

Table 5.1: Lattice and structural parameters of $Ba_4NaRu_3O_{12}$ calculated from combined synchrotron x-ray and neutron powder diffraction.

5.4 Magnetic properties

dc magnetic susceptibility measurements were performed under an applied field of $H = 1$ kOe in the zero field-cooled (ZFC), field-cooled cooling (FCC) and field-cooled warming (FCW) modes. A clear cusp at ∼265 K marks the onset of long-range antiferromagnetic order. A significant hysteresis is seen between the magnetization measured during heating and cooling, suggesting the possibility of the transition being of the first-order. It is interesting to note that the triple perovskite version of this compound $Ba_3NaRu_2O_9$ exhibits a first-order charge-ordering transition at 210 K, accompanied by a $P6_3/mmc \rightarrow P2/c$ symmetry transformation [79,255] stabilized by a combination of single-ion and molecular degrees of freedom with the Ru_2O_9 clusters being the physically meaningful units. For $Ba_4NaRu_3O_{12}$, the Néel temperature is calculated by plotting the derivative of the ZFC susceptibility with respect to temperature (Fig.3.4 (a)) and found to be $T_N = 257.42 \pm 0.07$ K.

The derivative also reveals several features below T_N, likely related to octahedral distortions compensating for the growing strength of the antiferromagnetic exchange in order to minimize the global free energy. The observation of more than one transition is consistent with previous re-

ports. Although, qualitatively the $M(T)$ curves look different, both Battle et al.[251] and Kim et al.[252] observe various features in the magnetic susceptibility below T_N. The former reported a χ_{ZFC} showing an irreversibility below T_N, a pleateau (or a very broad peak) till ∼150 K, below which a broad peak would develop before finally decreasing continuously till the base temperature was reached. Kim et al.[252] had performed a magnetic field-dependence analysis and come to the conclusion that all the features except for T_N are suppressed at some critical field. They observed features at 180 K, 110 K and 30 K and assigned them to a development of a weak FM correlation between Ru1's, a spin-reorientation, and a dynamic crossover with long range antiferromagnetism across the NaO_6 orbital, respectively[252]. In the present work too, as shown in Fig. 5.5 (a), the derivative $d\chi/dT$ highlights various features below T_N - and we get more insights into these features on analyzing the temperature-dependent diffraction data, discussed in section 5.5.

Ba1 —O1	×6	2.9092(7) Å
Ba1 —O2	×6	2.9287(19) Å
Ba1 —O3	×3	2.9628(19) Å
Ba2 —O1	×3	2.986(4) Å
Ba2 —O2	×6	2.9052(5) Å
Ba2 —O4	×3	3.091(3) Å
Ba3 —O1	×3	2.919(4) Å
Ba3 —O3	×6	2.9017(5) Å
Ba3 —O4	×3	2.907(3) Å
Ba4 —O2	×3	2.890(3) Å
Ba4 —O3	×3	2.945(3) Å
Ba4 —O4	×6	2.9075(5) Å
Na —O1	×3	2.235(3) Å
Na —O2	×3	2.221(3) Å
Ru1 —O1	×3	1.866(3) Å
Ru1 —O3	×3	2.094(3) Å
Ru2 —O3	×3	1.9431(17) Å
Ru2 —O4	×3	2.000(3) Å
Ru3 —O4	×3	2.047(3) Å
Ru3 —O2	×3	1.8756(18) Å
Ru2 —Ru3		**2.652(3)** Å
Na —O1 —Ru1		177.05(16)°
Ru1 —O3 —Ru2		174.76(14)°
Ru2 —O4 —Ru3		81.86(8) °
Ru3 —O2 —Na		176.86(13)°

Table 5.2: Bond angles and lengths for $Ba_4NaRu_3O_{12}$ estimated from Rietveld refinement of neutron diffraction data collected at 300 K

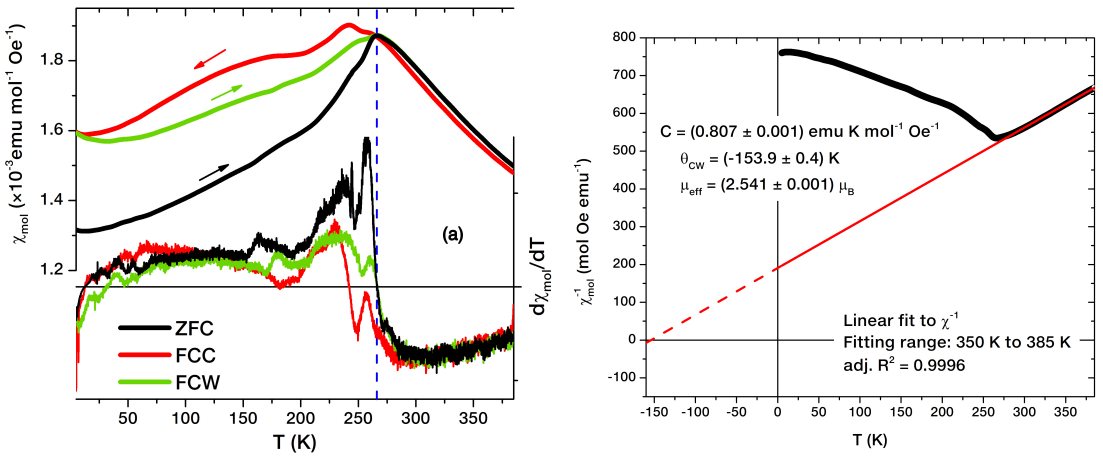


Figure 5.5: Magnetic Properties of $Ba_4MRu_3O_{12}$ (a) dc Molar susceptibility χ_{mol} measured as a function of T in ZFC, FCC and FCW protocols. The temperature derivative $d\chi_{mol}/dT$ shows the antiferromagnetic transition at $T_N \sim 265$ K along with other subtler features within the AFM phase. (b) Curie-Weiss fit to the inverse magnetic susceptibility $(\chi^{-1}_{mol}(T))$

The inverse molar susceptibility $1/\chi_{mol}$ as a function of temperature T is shown in Fig. 5.5 (b) showing Curie-Weiss (CW) behaviour down to $\sim$ 290 K, below which the system enters the transition region. To ensure the correct estimation of CW parameters, the fitting has been performed across the highest measured T range between 350 - 385 K (388 points). The Curie constant was calculated to be $C = 0.8$ emu K mol^{-1}Oe^{-1} and the CW temperature $\theta_{CW} = -153.9 \pm 0.4$ K confirming the dominant antiferromagnetic correlations. Kim et al.,[252] had performed high T magnetization measurements on this material and shown that above 520 K, a CW fit to χ^{-1} yields a θ_{CW} = -1332 K and an effective magnetic moment, $\mu_{eff} = 3.74\,\mu_B$, nearly equal to the spin-only moment expected for a Ru^{5+} $S = 3/2$ state ($\mu_{so} = 2\sqrt{S(S+1)} = 3.87\mu_B$). They noted a change of slope in χ^{-1} below $\sim$520 K resulting in a significant reduction in $\theta_{CW} = 221$ K and $\mu_{eff} = 2.32\,\mu_B$. This is attributed to the development of AFM correlations within the Ru_2O_9 dimers which lowers the measured bulk magnetization. Since our measurements were limited to 380 K, we likely probe this already correlated paramagnetic phase and calculate the (reduced) μ_{eff} per formula unit to be $2.541 \pm 0.001\,\mu_B$. The analysis also allows us to calculate the frustration parameter $f = \frac{\theta_{CW}}{T_N} = 0.6$ highlighting the absence of magnetic frustration in this material, in contrast to the suggestion by Kim et al. of the system having a frustration-induced spin glass ground state at low T[252]. Even comparing their reported value of θ_{CW} values obtained from the high-T susceptibility data with a $T_N \sim$260 K, $f = |\frac{1332}{260}| \sim 5$, far lesser than the benchmark of $f \geq 10$ for a magnetically frustrated system.

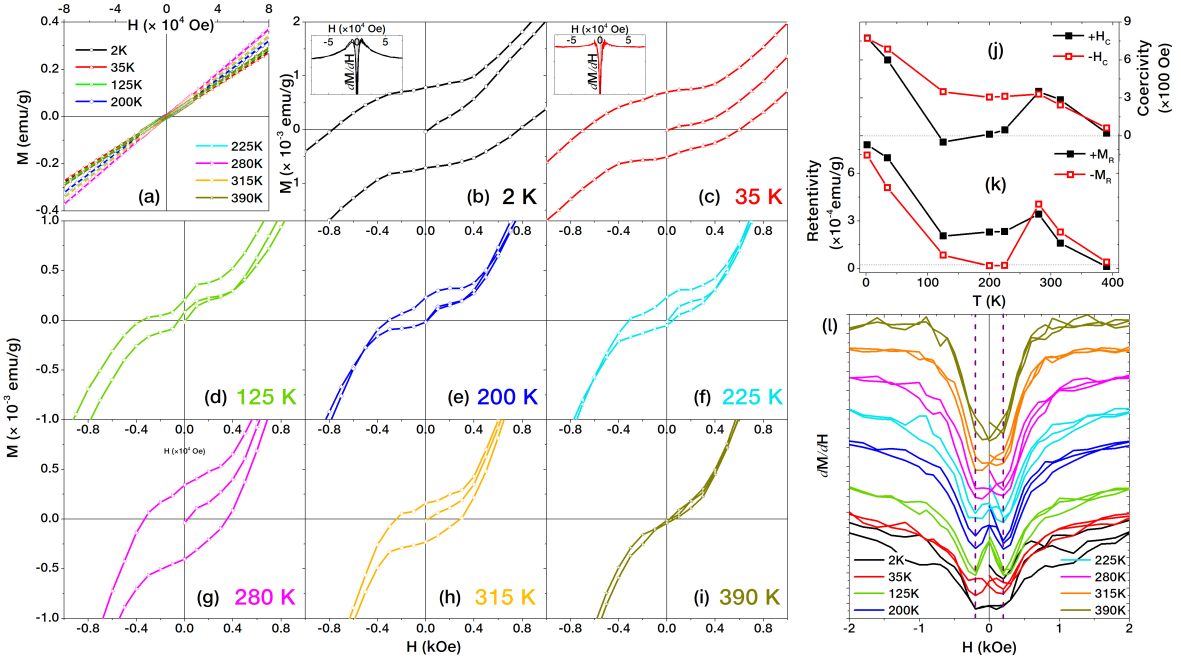


Figure 5.6: (a) $M(H)$ isotherms measured in the range [-8 T, 8T] for 8 temperatures between 2 - 400 K, (b) - (i) show low field regions showing a finite loop and low-field features, insets of (b) and (c) show dM/dH in the H range [-8 T, 8 T] and (l) for $H \in$ [-0.1 T, 0.1 T], (j) and (k) show the coercivity (H_c) and Retentivity (or Remnant Magnetization, M_R) as function of temperature.

Fig. 5.6 shows the $M(H)$ isotherms measured at various temperatures between 2 - 400 K. Overall, an antiferromagnetic behaviour is observed with a linear relationship between M and H without any saturation upto 8 T. A small loop opens up at low temperatures suggestive of weak ferromagnetic correlations. This is in line with a miniscule upturn we observe in χ_{DC} below 12.5 K. The origin of both the rise in χ_{DC} and the loop opening at 2 K could be a weak ferromagnetic contribution contributing to the magnetic response at low temperature. Insets of (b) and (c) show a sharp change in the slope dM/dH at about $\pm$8.5 kOe for $T = 2$ K and 35 K. This feature is suppressed as T increases and for $T =$ 125 K, 200 K and 225K, subtle step-like features are visible, reminiscent of metamagnetic behaviour. This also manifests in the dM/dH in the low-field limit (Fig. 5.6 (l)) where distinct features can be seen at $\pm$ 100 Oe which are washed out both at higher and lower temperatures. Tracking the variation in the coercivity (H_c) and remnant magnetization (M_R) with temperature brings out the sharp change in both parameters across T_N and subsequent increase below $\sim$ 100 K. This appearance of symmetric dips in dM/dH at low fields in an intermediate range of temperatures within the antiferromagnetically ordered phase suggests the possibility of a field-induced spin-flop like phenomenon. It will be interesting

to perform further magnetic field-dependent measurements on this system to closely study its metamagnetic behaviour.

5.5 Influence of temperature on structure

The analysis of structural parameters at various temperatures through synchrotron x-ray and neutron powder shed light on the variation in bond parameters that lay the foundation of the exchange pathway within this system. The strong spin-lattice coupling is revealed in Fig. 5.7 where the lattice parameters (a) and the axial ratio (c/a) (b) both show an anomaly across T_N.

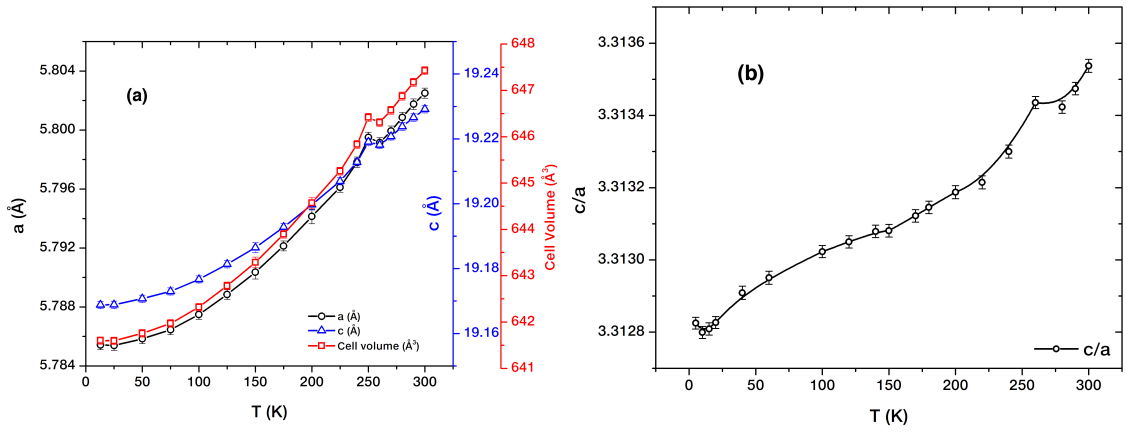


Figure 5.7: Thermal evolution of (a) lattice constants a, c and the unit cell volume (obtained from NPD) and (b) the axial ratio c/a obtained from SXRD.

As shown in Fig. 5.4 (e), there are three types of exchange mechanisms present here - the intradimer superexchange Ru2—O—Ru3, the interdimer superexchange Ru1—O—Ru2 and the intradimer direct exchange between Ru2 and Ru3. The T-dependence of the intra- and interdimer bond angles angles is shown in Fig. 5.8 (a). It is clear that the many subtler features seen in the bulk χ_{DC} are manifestations of the intrinsic bond distortions occurring on cooling. Across T_N, the Ru_2O_9 dimer contracts, accompanied by a simultaneous reduction of the corner angle between Ru1—O_6 and Ru_2O_9. On further cooling, the angles continue to decrease, but non-monotonically, with the Ru1—O—Ru2 angle showing peaks at 100 and 200 K. These features are even more clearly illustrated in the thermal dependence of the bond lengths of the Ru1—O_6 octahedra Fig.5.8 (b). After the first contraction, the Ru1—O bonds plateau for a small temperature region before contracting again below 200 K and then finally stabilizing below 100 K. When looking at the dimer bonds, as shown in Fig.5.8 (c) and (d), that although the changes below T_N

are also manifested in the dimer structure, but the changes in length are miniscule ($\sim 10^{-3}$Å). The largest changes even among these parameters are observed in the Ru2—O3 bond which is in the closest proximity to Ru1 and connects to the Ru1—O_6 octahedra.

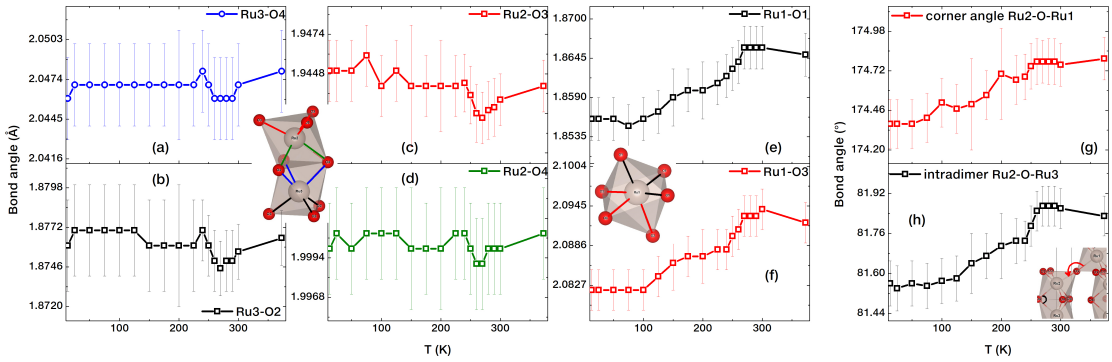


Figure 5.8: Thermal variation of the (a,b) Ru3—O, (c,d) Ru2—O and (e,f) Ru1—O bond lengths. The colors of the curves correspond to the color coding on the pictorial representation of the octahedral bonds. T dependence of the (g) inter- and (h) intra-dimer Ru—O—Ru bond angles.

The Ru-Ru intradimer bond, on the other hand, shows a rather smooth decrease below the room temperature until $\sim$ 100 K where is flattens till 50 K before decreasing further. This indicates that the Ru-Ru overlap strengthens on cooling thus increasing the AFM coupling. The dimers effectively become nonmagnetic as a result and wield no influence on the overall magnetic response of the material, as evidenced by the close correlation between the thermal dependence of the distortion in the isolated octahedra and the bulk magnetization response.

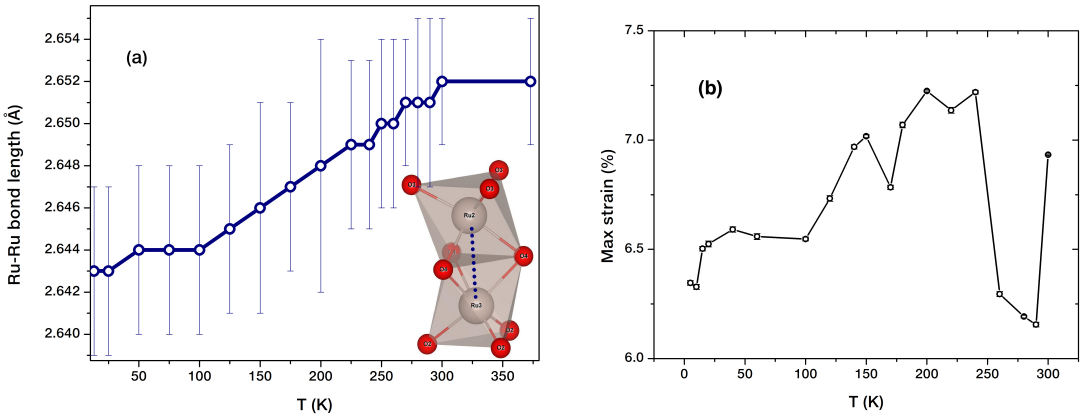


Figure 5.9: (a) T dependence of the Ru-Ru bond lengths. (b) Variation in maximum strain (%) calculated from synchrotron XRD microstructure analysis with Temperature

Microstructural analysis of the SXRD patterns also provide us with a way to estimate the maximum averaged strain in the powder sample. The thermal variation of the maximum strain % is shown in Fig. 5.9 (b). It is evident that the octahedral distortions are translated into the lattice strain. Following the sharp rise across T_N, the strain is reduced (the lattice relaxes). On further cooling, the strain becomes nearly independent of T below 100 K until another step-like change is observed below 25 K. The standard deviation - which measures the maximum strain anisotropy[123] - is very small and is represented by the y-error bars for both the plots. A description of the estimation of microstructural parameters from XRD data using FULLPROF is given in Appendix B for the benefit of beginners.

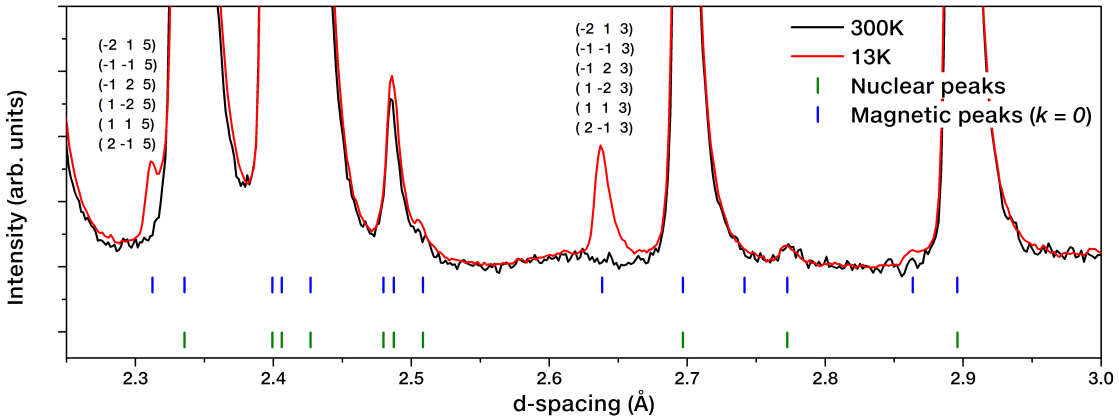


Figure 5.10: Additional reflections observed in NPD at $T = 13$ K corresponding to the magnetic structure.

5.6 Magnetic structure

The appearance of new reflections not allowed by the crystal symmetry $P6_3mc$ confirmed the existence of long-range magnetic order in the system. Fig. 5.10 shows comparison between the diffraction patterns collected at 300 and 13 K, clearly highlighting the two additional reflections at $d = 2.637$ Åand 2.311 Å which are indexed by the k-vector $\mathbf{k} = 0\,0\,0$.

In order to solve the magnetic structure corresponding to these reflections, we performed magnetic representational analysis using the program SARAh[204]. Although the three Ru sites are symmetrically unique, their site multiplicities are same (each generates two equivalent positions) which means that their magnetic representations (Γ_{Mag}) are the same. For each site $\Gamma_{Mag} = 0\Gamma_1^1 + 1\Gamma_2^1 + 0\Gamma_3^1 + 1\Gamma_4^1 + 1\Gamma_5^2 + 1\Gamma_6^2$. The basis vectors and their components, calculated for each site are illustrated in Appendix A. The point symmetry and Shubnikov Group corresponding to

each basis vector for each surviving Γ is given in Table 5.3.

IR	BV	Point Group	Shubnikov Group, BNS No.	
Γ_2	ψ_1	6	P6_3m'c'	$(P6_3m'c', 186.207)$
Γ_4	ψ_2	6	P6_3'm'c	$(P6_3'm'c, 186.205)$
Γ_5	ψ_3	6	C/B	
	ψ_4	3m	P1	$(P1, 1.1)$
Γ_6	ψ_5	6	C/B	
	ψ_6	3m	P1	$(P1, 1.1)$

Table 5.3: The point symmetries and Shubnikov space groups associated with each basis vector calculated from the parent space group $P6_3mc$ with $\mathbf{k} = (0,\ 0,\ 0)$.

The best fit to the magnetic peaks is obtained using the IR Γ_4 corresponding to the magnetic space group $P6_3'm'c$.* The Rietveld fit of this model to the observed diffraction pattern at 13 K is shown in Fig. 5.12 (a). The accuracy of the model is confirmed by the reasonable magnetic R-factor of 7.39% and the fits to the magnetic reflections (Fig. 5.12 (b) and (c)).

*The 230 crystallographic space groups are extended to form 1651 magnetic space groups by introducing the time inversion group $1' = \{e, e'\}$, containing the identity e and the time inversion operation e'. A symmetry g followed by a time reversal is denoted by g'. The action of $1'$ on a some crystallographic space group group $\mathcal{G}$ can result in four types of magnetic space groups, $\mathcal{G}_M$:
1. $\mathcal{G}_M = \mathcal{G}$. These 230 groups are called *colourless* groups and are equivalent to the crystallographic point groups.
2. $\mathcal{G}_M = \mathcal{G} \times 1'$, also written as $\mathcal{G}1'$ where every symmetry in G appears with and without time reversal. These 230 groups are called *grey* groups.
3. The nontrivial *black and white* magnetic space groups are of the form $\mathcal{G}_M = \mathcal{H} + (g'|\mathbf{t}_{g'})\mathcal{H}$, where $\mathcal{H}$ is a subgroup of $\mathcal{G}$ of order 2 and the primed symmetry g' may be followed by a translation $\mathbf{t}_{g'}$. These are further divided into two types based on their magnetic point group G_M:
(i) Given a nonmagnetic point group G, if $G_M = H + g'H$ such that H is a subgroup of G of index 2 and $g \notin H$ so that $G = H + gH$, then exactly half of the symmetries in G (belonging to H) appear in G_M as they are, and the other half are followed by time reversal. Here, $e' \notin G_M$. In this case, the point group H of $\mathcal{H}$ is a subgroup of index 2 of the point group G of $\mathcal{G}$, and the Bravais lattices of $\mathcal{G}$ and $\mathcal{H}$ are same. Symmetries in G excluded from H must be combined with time reversal to leave the magnetic crystal invariant within a translation. These 674 groups are called *lattice-equivalent magnetic space groups* and are denoted by taking the International (Hermann-Mauguin) symbol for $\mathcal{G}$ and adding a $'$ to the symmetries that do no belong to $\mathcal{H}$ and thus must be followed by a time inversion.
(ii) If $G_M = G \times 1'$, then the point groups of $\mathcal{G}$ and $\mathcal{H}$ are same and the Bravais lattice T of $\mathcal{H}$ is a sublattice of the Bravais lattice T_0 of $\mathcal{G}$. Translations in T_0 excluded from T must be combined with a time inversion to leave the magnetic crystal invariant. These 517 groups are called *class-equivalent magnetic space groups* and different notations are used to describe them depending on which of the two lattices – magnetic/nonmagnetic, is considered primary. In the *Opechowski-Guccione* (**OG**)[256] notation, the nonmagnetic T_0 is primary, and T is marked as a subscript. In the *Belov, Neronova, and Smirnova* (**BNS**)[257] setting, T is primary, T_0 is a subscript and only unprimed elements are used in the description. For example, the crystallographic space group $P432$ ($\mathcal{G}$) acted upon by $1'$ results in the magnetic space groups: colourless $P432$, grey $P4321'$, lattice-equivalent black and white $P4'32'$, and the class-equivalent black and white magnetic space group P_I432 (BNS)/I_P432 (OG). These four types of magnetic space groups form the *magnetic superfamily* of the nonmagnetic space group $P432$.[258].

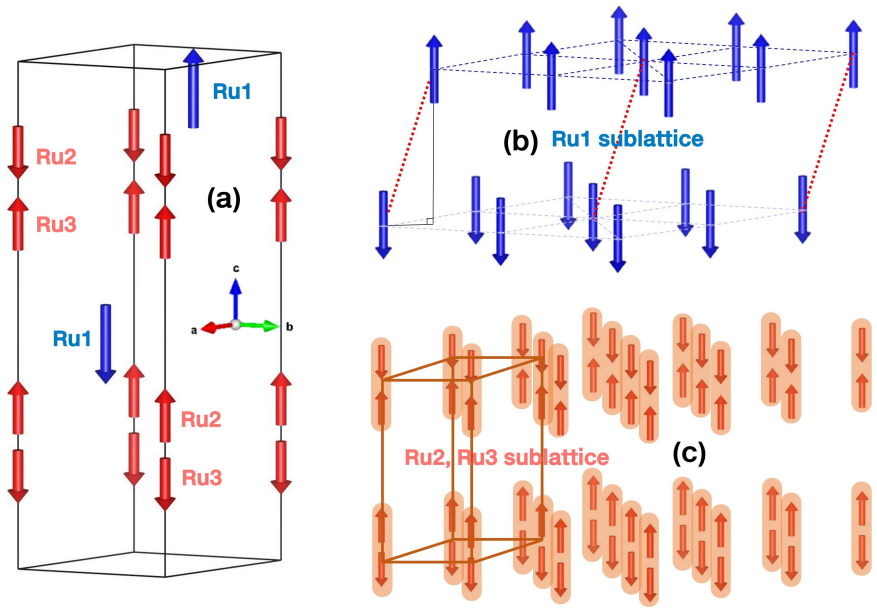


Figure 5.11: (a) The A-type AFM structure of $Ba_3NaRu_3O_{12}$ at 13 K. (b) The staggered arrangement of the Ru1 triangular layers, AFM coupled to each other along *c*. (c) The cubic packing of the Ru2,3 dimers - characterized by intra-dimer and inter-layed AFM coupling. Both sublattices are intra-layer FM coupled.

The magnetic structure (Fig. 5.11 (a)) exhibits an A-type arrangement with spins within each layer being ferromagnetically coupled, while AFM coupling is present between the NN layers. All the spins are aligned collinear to the crystalline easy axis *c*, a testament to the strong influence of the structure on the magnetic order. An interesting aspect of this structure is shown in Fig. 5.11 (b) and (c), which is the difference in the packing of the different layers. If the Ru1 and Ru2,3 sublattices are separated out, one can observe that the Ru1 layers have a staggered arrangement owing to the 6_3 axis running along *c*, while the Ru2,3 have a cubic packing, which cancels out their net moment. For the Ru1 moments to sustain the long-range AFM order, the exchange between them, which traverses 3 cation layers (Na–Ru3–Ru2), must be quite strong. Similar A-type orderings with spins locked in the *ab*-plane, have been found in other layered perovskite systems like $Ba_3Fe_2(W,Te)O_9$ [259,260] and $NdBaMn_2O_6$ [261], which have a structurally cubic packing. Ba_2CoTeO_6 also shows an A-type order but with spins canted at an angle of 24.5° with respect to the *c*-axis [262]. $Ba_3NdRu_2O_9$ shows a FM order of Nd spins collinear with the *c*-axis below 24 K which cant below 18 K accompanied by an AFM order of the dimer Ru spins [263]. This exemplifies the vast variation in magnetic stuctures possible and its strong dependence on the underlying crystal structure and the type of TM ions making up the exchange network. We note that this work is the first conclusive solution of the ground state magnetic structure of of a B-site

substituted non-trimer quadruple perovskite.

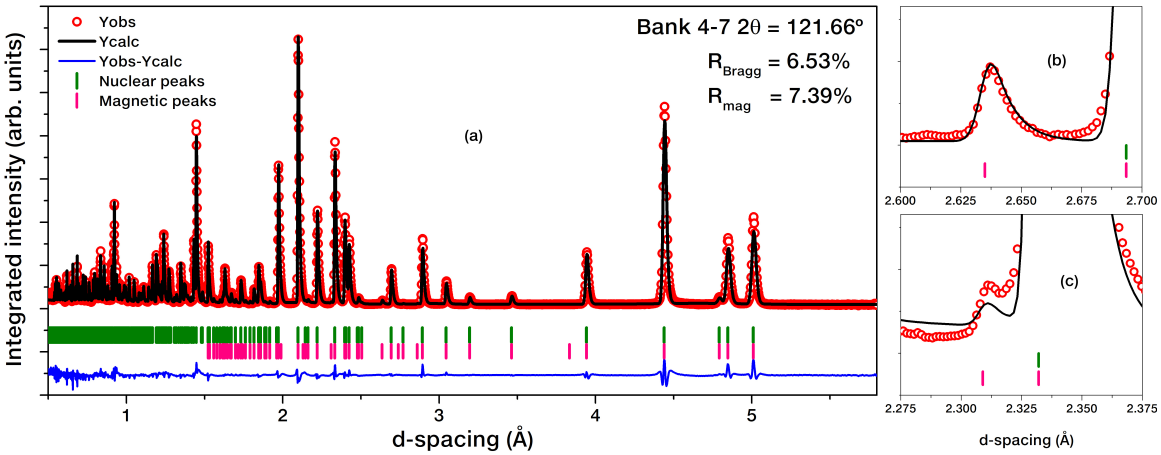


Figure 5.12: Rietveld fit of the IR Γ_4 magnetic model to neutron powder diffraction data collected at 13 K.

Fitting the model to NPD patterns collected at different temperatures allows us to track the development of the magnetic phase as a function of temperature. The rise in moment values at each magnetic site with cooling, is shown in Fig. 5.13. Both Ru moments record a qualitatively similar curve with Ru1 saturating at $\sim 2.25\,\mu_B$ and Ru2 (= Ru3) at $\sim 1.5\,\mu_B$. The overall magnetization response is governed by Ru1 and this is evident when we note that saturation moment of Ru1 matches almost perfectly to the μ_{eff} calculated from the bulk susceptibility measurements ($\sim 2.5\,\mu_B$).

We fit the growth of moment below T_N to a power-law function to ascertain the magnetic order parameter exponent β and the temperature of the phase transition. The mean-field equation is:

$$\mu(T) = \mu_0 \left(1 - \frac{T}{T_N}\right)^{\beta} \tag{5.1}$$

where μ_0 is the magnetic moment at $T = 0$, T_N the temperature of the phase transition and β the critical exponent capturing the behaviour of the order parameter (μ) at criticality. For Ru1, the parameters obtained are: μ_0 =2.38±0.03, matching the $\mu_{eff}/f.u.$ obtained from the magnetic susceptibility data and for Ru2,3 = μ_0 =1.59±0.03, elucidating the effect of Ru-Ru direct interaction within the Ru_2O_9 facilitating the suppression of the individual Ru values. The critical exponent for both sites, calculated independently, yield the same value of $\beta = 0.19 \pm 0.02$, placing $Ba_4NaRu_3O_{12}$ well within the universality window of two-dimensional critical exponents[264],

with its lower limit marked by the Ising 2D model ($\beta = 1/8 = 0.125$) and the upper limit by the unconventional critical exponent of the Kosterlitz–Thouless–Berezinskii (KTB) phase transition ($\tilde{\beta}$ =0.23) . Values of β for 3D magnetic models is expected to be much larger (β =0.33). $Fe(NCS)_2(pyrazine)_2$, a $S = 1/2$ 2D molecular antiferromagnet is reported to have the exact same value of β[265]. Similar values of β =0.18±0.03 and $\beta = 0.20 \pm 0.02$ are reported for $PdCrO_2$, an $S = 3/2$ triangular lattice antiferromagnet[266], and La_2CoO_4, a 2D $S = 1/2$ layered material with longitudinal Ising spin correlations[267]. A summary of known universality classes with their corresponding order parameter critical exponents β are given in Table 5.4. This attests to the layered, quasi-2D nature of the magnetism in $Ba_4NaRu_3O_{12}$ with ferromagnetic triangular layers of Ru ions are antiferromagnetically linked along the easy-axis (c) with out-of-plane collinear spins.

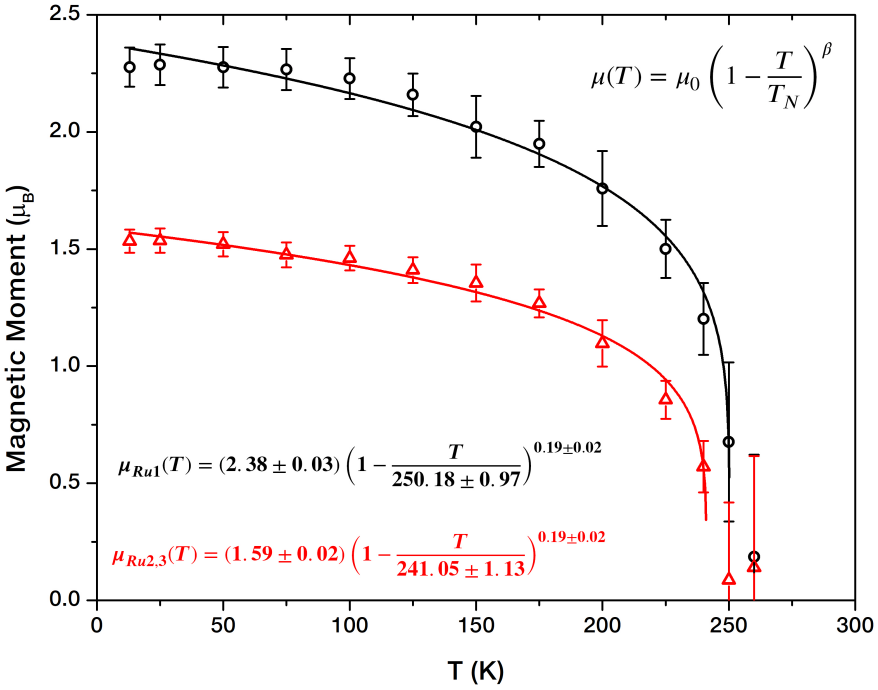


Figure 5.13: Increase in moment values with decreasing temperature

5.7 Electronic and thermal transport

5.7.1 Specific Heat

The specific heat measured as a function of temperature (C_P(T)) is shown in Fig. 5.14 (a). A clear λ-type anomaly is visible at 255 K, confirming the antiferromagnetic transition at T_N. The small magnitude of the peak likely suggests that the entropy change associated with this transi-

dim.	β	class
any	1/2	Mean field
2	1/8	Ising
3	0.32653(10)	
4+	1/2	
2	1/9	3-state Potts
2	1/12	Ashkin-Teller (4-state Potts)
3	0.3485(2)	XY
3	0.366(2)	Heisenberg
1	0	Ordinary percolation
2	5/36	
3	0.4181(8)	
4	0.657(9)	
5	0.830(10)	
6+	1	
1	0.276486(8)	Directed percolation
2	0.536(3)	
3	0.813(9)	
4+	1	

Table 5.4: Universality classes and their critical exponents[5]

tion is small. This observation also matches up with the absence of any symmetry lowering in the crystal structure of the compound as a function of temperature. Inset (i) of Fig.5.14 shows the data in the full T range highlighting the absence of any more features at lower temperature. This probably means that the octahedral distortions only affect the magnetic ground states and the overall energy of the state remains impervious to those local changes. Inset (ii) of Fig.5.14 highlights the region where Debye behaviour is observed, and a linearity is captured in the C_P vs T^3 plot. At low temperature, the deviation from the Debye behaviour attests to the frustration in this material and at high temperature C_P can be seen to approach the Dulong-Petit Limit, as expected.

Fig.5.14 (b) shows the low-temperature linear fit to C_P/T vs T^2, to estimate the electronic and lattice contributions to the specific heat. We obtain a Debye Temperature $\theta_D = 376.23 \pm 1.72$ K using eq. 3.8, consistent with reports for other layered perovskites[268,269]. The values obtained for $\gamma = 2.1 \pm 0.2$ mJ mol^{-1}K^{-2} and $\beta = 0.73 \pm 0.01$ mJ mol^{-1}K^{-4} are both miniscule, implying that most of the entropy of the system is lost in approaching low temperatures. This is further corroborated in the plot of C_P/T^3 vs T where a peak in C_P/T^3 is observed at ~ 21 K. This excess

phonon specific heat is a common feature in many perovskite systems and is attributed to the presence of low-lying optical (Einstein) modes that cause a departure from the phononic density of states and promote a pure T^3 dependence of C_P at T<θ_D. The position of the peak is said to be a manifestation of the *boson peak*[270] and can be used to estimate the vibration energy of the largest contribution to C_P at the peak temperature under the dominant phonon approximation[271]. For the observed peak in C_P/T^3 at ∼20.8 K, we obtain a vibrational energy of ∼ 55 cm^{-1} (using $\hbar\omega = 3.8k_BT_{max}$)[271].

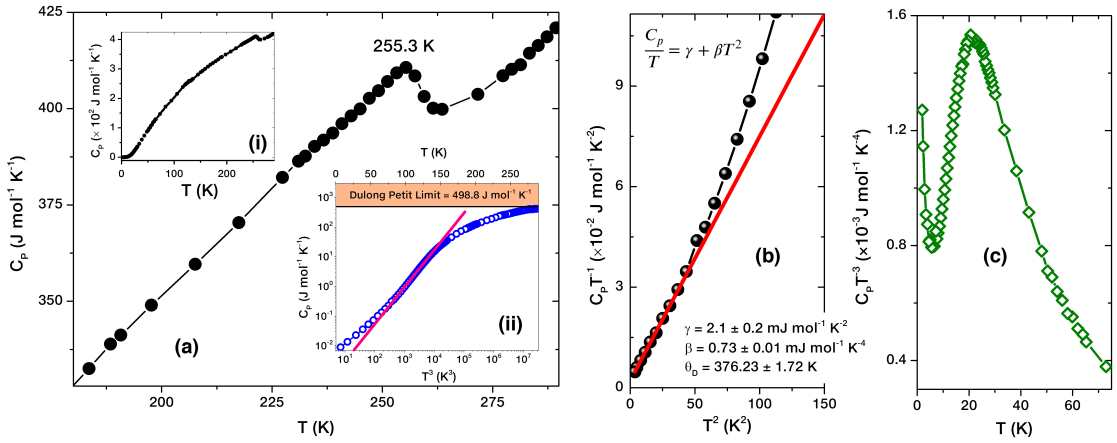


Figure 5.14: (a) Temperature dependence of specific heat capacity of $Ba_4NaRu_3O_{12}$ in the vicinity of T_N. Inset (i) shows $C_P(T)$ for the whole T range (2 - 300 K) and inset (ii) shows a plot of C_P vs T^3 showing the range of temperatures for which the Debye term is dominant. (b) A plot of C_P/T vs T^2 with the linear fit along with the parameters obtained from the fit. (c) A graph showing the variation in C_P/T^3 as a function of T.

5.7.2 Resistivity

Fig.5.15 (a) shows the semiconducting nature of the material along with a small discontinuity observed in the derivative $d\rho/dT$ at T_N. The charge transport shows a thermally activated behaviour above T_N with a linear lnρ against T^{-1}. Fig.5.15 (b) shows the linear fit in the T range 333 - 287 K. Deviation from this linearity begins close to the magnetic transition and is depicted more clearly in the zoomed inset of Fig.5.15 (b) and the derivative plot $d(ln\rho)/dT$ vs 10^3T^{-1} marking the onset of a declining slope below T_N. The linear fit returned an activation energy of E_a = 135.08 ± 0.04 meV and the minimum resistivity ρ_0 = 9.75 ± 0.01 mΩ-m.

Below T_N, when lnρ was found to be non-linear with respect to Mott's Variable Range Hopping

(VRH) behaviour[213], we employed the generalized VRH law given by:

$$\rho = \rho_0 exp\left(\frac{T_0}{T}\right)^p \tag{5.2}$$

where ρ_0 and T_0 define the minimum resistivity at T$\rightarrow\infty$, and characteristic temperature of the hopping behaviour, respectively. p is the *hopping exponent*, which takes the value 1/3 and 1/4 in Mott's law[213] for 2D and 3D systems, respectively, having noninteracting electrons and constant density of states $N(\varepsilon) = N_0$. However, in real materials, electron-electron interactions are often important and their inclusion modifies the Mott-VRH to the Efros-Shklovskii (ES) VRH[272] with $p = 1/2$ for both 2D and 3D systems. The density of states in this model has a quadratic dependence on the energy close to the Fermi energy (ε_F) given by[273,274]:

$$N(\varepsilon) = \frac{\pi}{3}\frac{\kappa^3(\varepsilon - \varepsilon_F)^m}{e^6} \tag{5.3}$$

with $m = 2$ in a 3D semiconductor where, κ is the dielectric constant of the material and encapsulates the effect of Coulomb interaction between the electrons. This leads to the opening of a soft gap in the single particle density of states, the width of which is known as the *Coulomb gap*. Fitting the lnρ to $1/T^{1/2}$ returns a reasonably linear fit across 7-8 orders of magnitude, however, the value $T_0 = 4.3 \times 10^4$ K obtained is significantly high. Similar results, with even higher values of T_0 have been reported for the 5*d* double perovskites A_2MnReO_6 (A = Ba, Sr, Ca)[275].

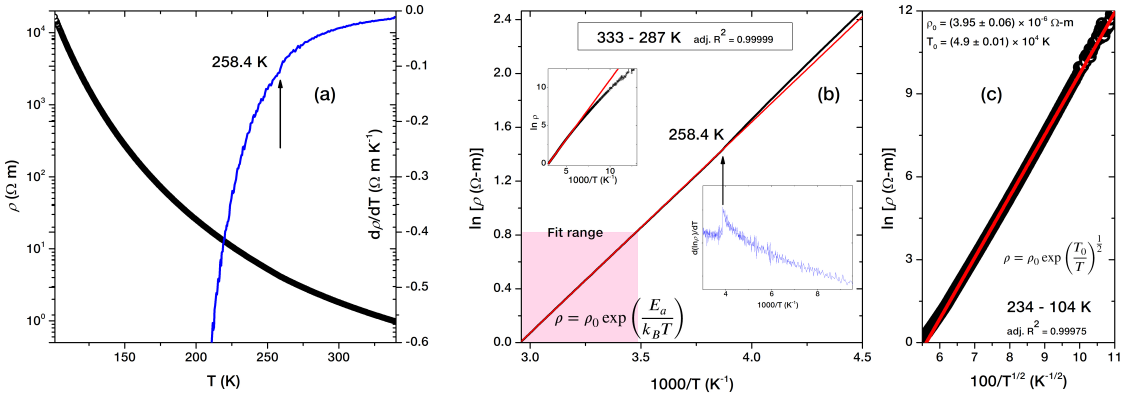


Figure 5.15: Transport behaviour of $Ba_4NaRu_3O_{12}$. (a) ρ vs T, showing a semiconducting behaviour, and the derivative dρ/dT shows the discontinuity at T_N. (b) Linear fit to ln ρ vs $10^3/T$ for $T > T_N$. Insets show the deviation from linearity and the sharp change in the slope below T_N. (c) Linear fit to the Efros-Shklovskit Variable Range Hopping (ES-VRH) model below T_N.

Now, the hopping exponent can be *a priori* extracted from the ρ vs T curve by plotting $\log\frac{d(ln\rho)}{d(ln(1/T))}$ vs $\log T$, the slope of which returns $-p$[276]. As shown in Fig.5.16 (a), the temperature regimes $T > T_N$ and $T < T_N$ are defined by two different slopes. For $T > T_N$, we find $p \approx 1$, as discussed earlier, and for $T < T_N, p = 0.642 \pm 0.004$, which is higher than the ES value. Generally, the exponent describing the dependence of $N(\varepsilon)$ on ε (m) is related to the hopping exponent as: $p = (m+1)/(m+4)$[277], so that for the ES model, when $p = 1/2$, $m = 2$ and $N(\varepsilon) \propto (\varepsilon - \varepsilon_F)^2$. In the present case, the obtained value of $p = 0.642$ yields the relation $N(\varepsilon) \propto (\varepsilon - \varepsilon_F)^{4.38}$, a far stronger dependence than proposed by ES-VRH. This scenario is likely if multi-particle excitations due to correlation effects are considered instead of the single-particle consideration of the ES model.[278]. Numerical calculations also have suggested that the Coulomb gap can have a quasiexponential energy dependence in presence of multi-electron transitions[279]. This attests to the strongly insulating low temperature state, where the total energy available to the system is greatly reduced and thus, so are the density of states close to Fermi level, leaving the system with little possibility to conduct.

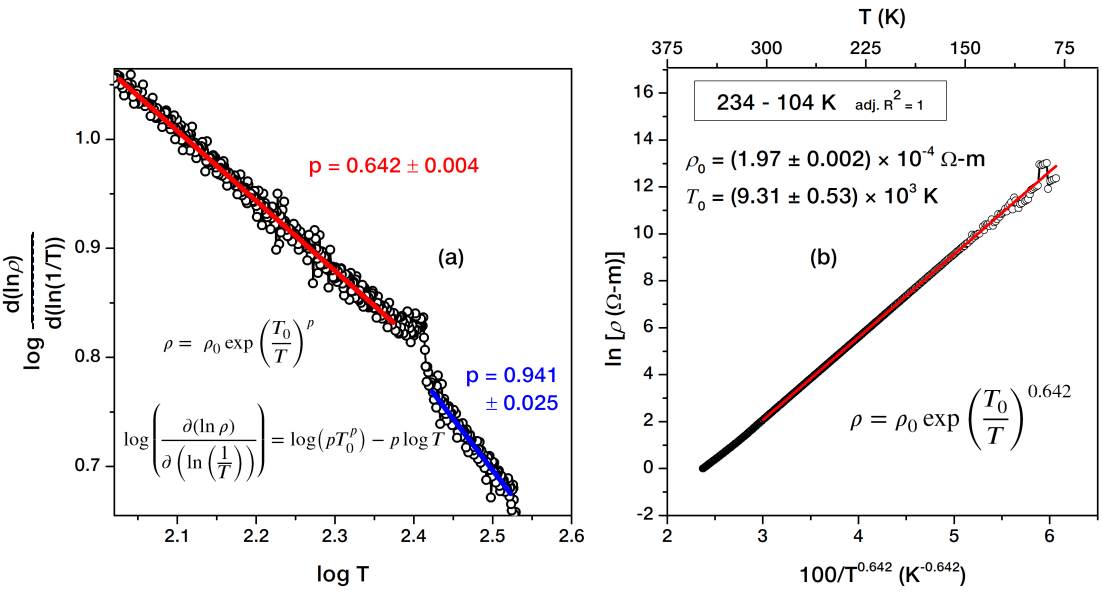


Figure 5.16: (a) log-log plot of $d(ln\rho)/d(ln(1/T))$ showing the two distinct transport regimes characterized by different slopes (p). (b) lnρ vs $100/T^{0.642}$ yielding an improved linear fit with a lower T_0

Another interesting aspect here is the lack of existence of the Mott regime. Generally, a gradual crossover from Mott to ESVRH regime is observed on cooling, and the Mott and ES characteristic temperatures T_0^M and $T_0^E S$ are related to the Coulomb gap width (Δ_{CG}) as $\Delta_{CG} = \sqrt{\frac{T_0^3}{T_M}}$[280]. But here, we bypass the Mott regime entirely to reach the ES hopping regime.

5.8 Conclusions

In this chapter, we have presented a thorough investigation of the magnetic ground state of $Ba_4NaRu_3O_{12}$, its revealed the robust spin-lattice coupling of its ground state. The system consists of a unique motif uncommon in layered perovskite systems - of three symmetrically unique magnetic ions occupying the centre of a corner octahedra connected to a dimer, isolated by a non-magnetic layer. Despite this separation of magnetic entities, it exhibits a long-range magnetic ordering at a fairly high temperature of $T_N \sim 257$ K which is corroborated in both specific heat as well as temperature-dependent diffraction measurements, attesting to the strong coupling between the magnetic and lattice degrees of freedom, and the robustness of the exchange mechanism. The magnetically ordered ground state is visualized by the neutron powder diffraction measurements at 13 K and it is found that the overall magnetic response is unaffected by the Ru2 and Ru3 moments - which are antiparallelly aligned and result in a net zero moment contribution from the dimer. The bulk magnetization mirrors the changes in octahedral distortions in the Ru1—O_6 suggestive of a strong lattice-spin coupling in the system. The magnetization isotherms show an interesting metamagnetic feature in the intermediate T-range of 125 - 225 K, concurring with the region where the Ru1—O_6 show the maximum change - pointing to some type of spin reorientation. This places $Ba_4NaRu_3O_{12}$ as an interesting material candidate for a theoretical investigation of the competing interactions influencing its ground state and the reason behind the strength of the antiferromagnetic exchange interaction. The low-T specific heat response is dominated by Einstein (optical) mode vibrations attested to by the peak seen in C_P/T^3 plots and the diminished electronic and Debye terms (γ and β). The charge transport shows a transition from a thermally activated behaviour above T_N to a $exp(T^{-p})$ VRH transport with $p = 0.642$ - implying the presence of a *soft* Coulomb gap with a stronger energy-dependence than the quadratic dependence suggested by the Efros-Shklovskii model with $p = 0.5$. This suggests that multiparticle effects might be active in this system due to strong correlation effects.

One never notices what has been done; one can only see what remains to be done.

Marie Curie

6

Summary and future scope

The aim of this work was to explore the intricate relationship between the spin, charge and lattice degrees of freedom in transition-metal oxides. To this end, we chose three different classes of layered hexagonal perovskites and explored the evolution of their magnetic state over a wide range of temperatures in conjunction with their structure. We also utilized a sparsely-used technique of measuring nonlinear dielectric susceptibilities to probe subtler effects in the electric polarization of these systems and correlate them with their known anomalies in the magnetic and transport properties.

We began with a study of the *6H* double perovskite Ba_2CoRuO_6, with a significant anti-site disorder of $\sim$30% where a combination of synchrotron x-ray and neutron powder diffraction, magnetization, resistivity, specific heat, and dielectric measurements revealed a cluster spin glass magnetic ground state. This behavior was attributed to significant Co/Ru site disorder of $\sim$30% in the face-shared octahedra. The system exhibited hallmark features of a glassy phase, including frequency-dependent ac magnetization, magnetic irreversibility, and memory and aging effects, without saturation even under high magnetic fields. At low temperatures, the specific heat data displayed a non-Debye behavior, indicating a lack of long-range ordering. NPD data at 2 K revealed antiferromagnetic (AFM) ordering within spin clusters, while magnetic hysteresis measure-

ments documented the competing weak ferromagnetic (FM) interactions. The magnetic unit cell was doubled along the *ab* plane, with canted spins, forming a highly frustrated network of Co^{3+} and Ru^{5+} ions, resulting in a cluster glass state stabilized by a combination of competing FM and AFM interactions, and site-disorder. The temperature-field phase diagram further highlighted the strong random exchange anisotropy in the system, although it did not confirm an A-T line.

We then turned to nonlinear dielectric measurements of three triple perovskite ruthenates: $Ba_3CoRu_2O_9$, $Ba_3BiRu_2O_9$, and $Sr_3CaRu_2O_9$. These investigations revealed intriguing behaviors in the higher harmonics of the electric polarization response, offering insights into their polar orders.

For $Ba_3CoRu_2O_9$, the magnetostructural transition near 100 K was reflected in the nonlinear susceptibilities $\chi'_{1,2,3}$. The hypersusceptibilities $\chi'_{2,3}$ showed frequency-dependent dynamics above the transition, and negative peaks in χ'_2 moved toward lower temperatures with increasing frequency, sharply diminishing below the Néel temperature (T_N). An unexpected activation energy $E_a < 0$ was found from Vogel-Fulcher plots, meriting further study. The third-order susceptibility χ'_3 exhibited unusual negative peaks that did not align with traditional relaxation models, suggesting relaxor-like behavior potentially caused by distortions in the RuO_6 octahedra and a breakdown of the t_{2g} orbital degeneracy below 100 K.

In $Ba_3BiRu_2O_9$, nonlinear susceptibilities χ'_2 and χ'_3 indicated the presence of multiple relaxation processes within the spin-gap phase. Frequency dependence showed critical slowing down near 100 K, with unusual negative peaks not conforming to typical relaxation models. The nonlinear response suggests that interlayer charge transfer persists across the spin-gap opening, potentially driving the observed relaxor-like behavior.

$Sr_3CaRu_2O_9$ exhibited anomalies near its magnetic phase transitions (160 K and 190 K), with strong dispersion effects in both linear and nonlinear susceptibilities. A critical slowing down behavior was observed, with low-temperature variations in χ'_3 pointing to dipolar-glass or relaxor ferroelectric-like behavior. The SRBRF model appears relevant for both $Sr_3CaRu_2O_9$ and $Ba_3BiRu_2O_9$, suggesting that polar orders in these systems are strongly influenced by spin, lattice, or orbital interactions, representing a novel class of materials beyond the canonical ferroelectrics.

Finally, we examined $Ba_4NaRu_3O_{12}$, revealing a robust spin-lattice coupled ground state with long-range magnetic ordering at $T_N \sim 257$ K. The system's unique structural motif of three symmetrically distinct magnetic ions, including Ru dimers separated by non-magnetic layers, is inti-

mately correlated with its magnetic behaviour, as evidenced by temperature-dependent diffraction measurements and specific heat data. The powder neutron diffraction patterns at 13 K showed that the dimer moments (Ru2 and Ru3) are antiparallel, leading to a net zero moment contribution from the dimers and a staggered arrangement of the Ru1 triangular layers along the *c*-axis. The low-temperature specific heat revealed an extra boson peak contribution from optical modes with a maximum vibrational energy of $\sim$55cm^{-1}, while the charge transport exhibited variable-range hopping (VRH) behaviour below T_N, with a stronger energy-dependence than expected from the Efros-Shklovskii model, suggesting the presence of multiparticle correlation effects.

Taken together, this comprehensive investigation highlights the delicate balance of competing interactions — frustration, structural disorder, anisotropy, and electronic correlations - that shape the ground states and dynamic responses of these layered hexagonal perovskite systems. The results open up significant avenues for further exploration, particularly in understanding the role of disorder and frustration in stabilizing unusual phases like spin glasses, relaxor ferroelectrics, and multiferroics/multiglasses, as well as the influence of strong correlations on charge transport mechanisms in such materials.

6.1 Ongoing and future work

Continuing the theme of this thesis, we are currently investigating other quadruple perovskite compounds with non-magnetic ions substituted on the B-site. As discussed in Chapter 1, structurally similar compounds with Na^+ and Li^+ on the B-site show very different properties and we still do not quite understand why. We observe the same dissimilarity in $Ba_4LiRu_3O_{12}$ which has a more symmetric crystal structure than its Na counterpart and is likely to possess a 6-layered stacking. Apart from this, its magnetization shows fewer features and indicates development of short-range correlations below 250 K and a bifurcation in ZFC and FC magnetization below 100 K - hinting at a cooperative freezing. It will be interesting to track the development and dynamics of this glass state to see what factors contribute to stabilize it and contrast its properties with its Na counterpart which shows a long-range magnetic ordering. The room temperature x-ray diffraction pattern and dc magnetization measurements for $Ba_4LiRu_3O_{12}$ are shown in Fig. 6.1

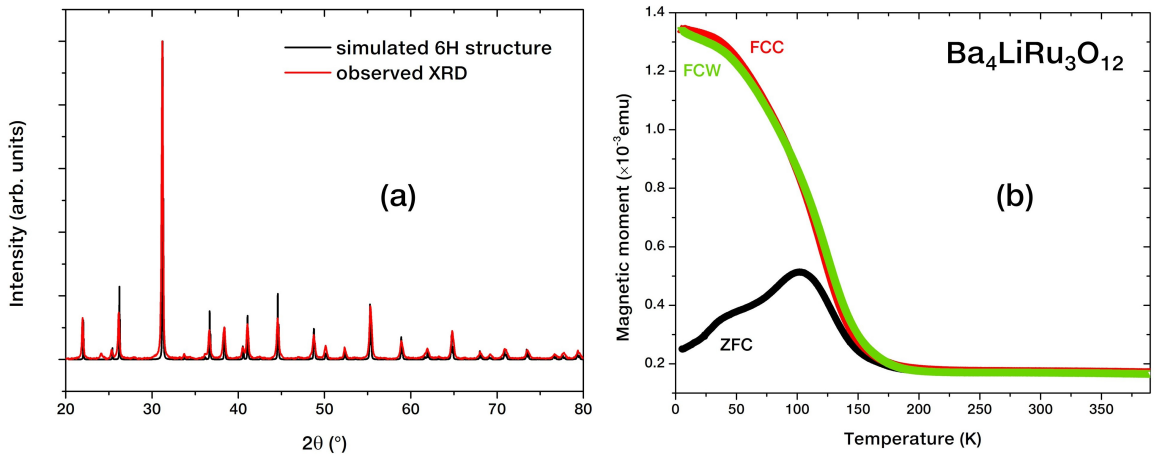


Figure 6.1: (a) Powder x-ray diffraction of $Ba_4LiRu_3O_{12}$ at room temperature compared to a simulated 6H structure (using vesta). (b) DC magnetization measurements showing magnetic irreversibility below 100 K.

We are also investigating the effect of substituting a divalent cation on the B-site. The first observation is obvious - the charge state of Ru is reduced from the stable pentavalence it had in the monovalent compounds. A divalent B imposes an effective charge of +4.67 on Ru. This allows the possibility of charge disproportionation as well as electron sharing within dimers/trimers. Structurally, $Ba_4(Mg,Zn)Ru_3O_{12}$ look similar to $Ba_4LiRu_3O_{12}$ and are likely to opt for the 6H structure too. Initial profile analysis indicates a hexagonal unit cell with a =5.7462 Å and c =14.0962 Å in the space group $P6_3/mmc$ (No. 194) for $Ba_4MgRu_3O_{12}$. A Le-Bail fit to this structure is shown in Fig. 6.2.

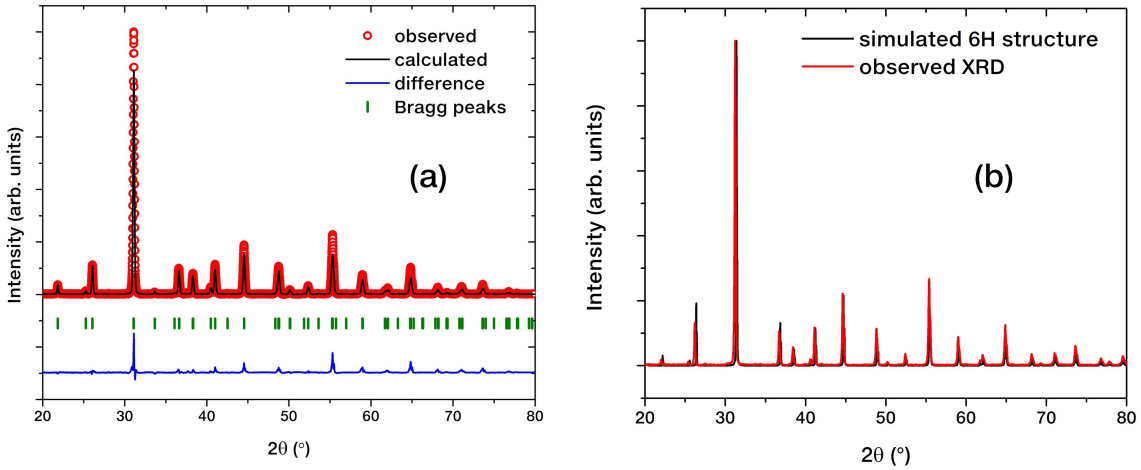


Figure 6.2: (a) Le-Bail fit performed on the room temperature XRD pattern to a hexagonal unit cell in space group $P6_3/mmc$ for $Ba_4MgRu_3O_{12}$. (b) Powder x-ray diffraction of $Ba_4ZnRu_3O_{12}$ at room temperature compared to a simulated 6H structure (using VESTA)

However, their magnetization follows a very different trend (Fig. 6.3) compared to the monovalent B-substituted compounds. Both Mg and Zn systems show a dimer-like susceptibility across a wide temperature range. Below 150 K $Ba_4MgRu_3O_{12}$ shows a bifurcation in ZFC and FC curve, and a broad peak at ∼36 K. The temperature of the upturn in M_{ZFC} is pushed to lower T for $Ba_4ZnRu_3O_{12}$ at ∼56 K. The rate of increase is visibly impeded below 38 K before decreasing slowly below 13.5 K. A finite hysteresis between the heating and cooling FC curves is present as well. The evolution of $M(T)$ in both of these compounds clearly exhibits the competition between the various exchange interactions becoming more intense at low T as they become comparable in magnitude. It will be very interesting to track the changes in bond parameters and magnetic moment values as a function of temperature to unveil the structure-property relationships in these materials. The NPD data for $Ba_4MgRu_3O_{12}$ reveals the presence of additional magnetic peaks (Fig.6.4) - implying the presence of ordered domains. Now whether that ordering is within large frozen domains (as in the case of Ba_2CoRuO_6 [136]), or a true long-range order (like $Ba_4NaRu_3O_{12}$ (Chapter 5)) - remains to be ascertained.

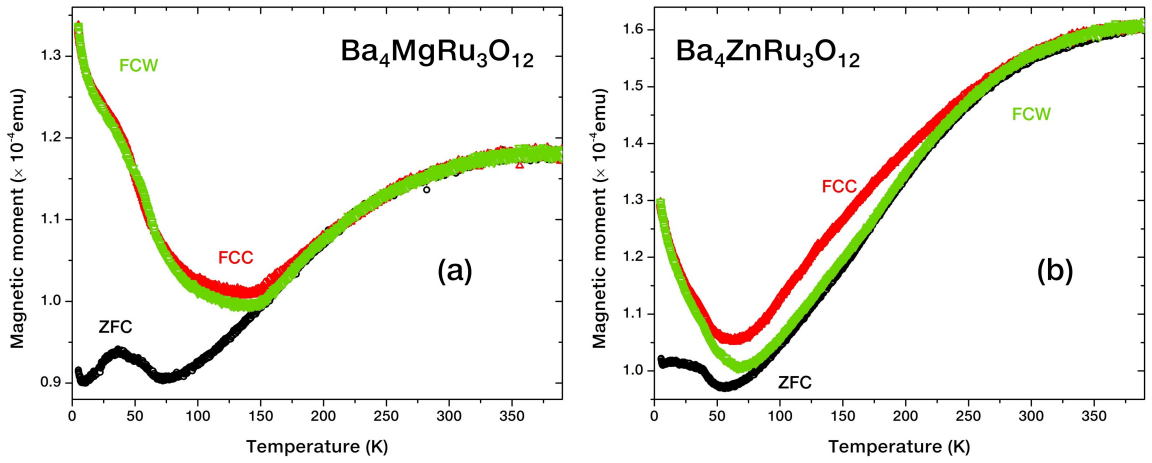


Figure 6.3: DC Magnetization measurements on (a) $Ba_4MgRu_3O_{12}$ and (b) $Ba_4ZnRu_3O_{12}$ showing absence of any paramagnetic region and a dimer-like susceptibility.

The B-site substituted quadruple perovskite ruthenate systems with nonmagnetic B cations, belong to the family of compounds where the overall magnetic behaviour is governed solely by the magnetic state of the Ru ions. As discussed extensively in this thesis, Ru is a particularly unpredictable element. Its dynamic charge, orbital and magnetic interaction with its local environment over a wide range of lengthscales, allows it to participate in stabilizing a plethora of unexpected magnetic ground states. These structurally anisotropic systems further present an appealing plat-

form to explore the physics of these isolated Ru clusters and see how their arrangement across the crystal, is related to the crossover from an ordered to a correlated, yet frustrated ground state. It would also be interesting to explore ways to control and manipulate these interactions to push the compound closer to critical points in its phase diagram.

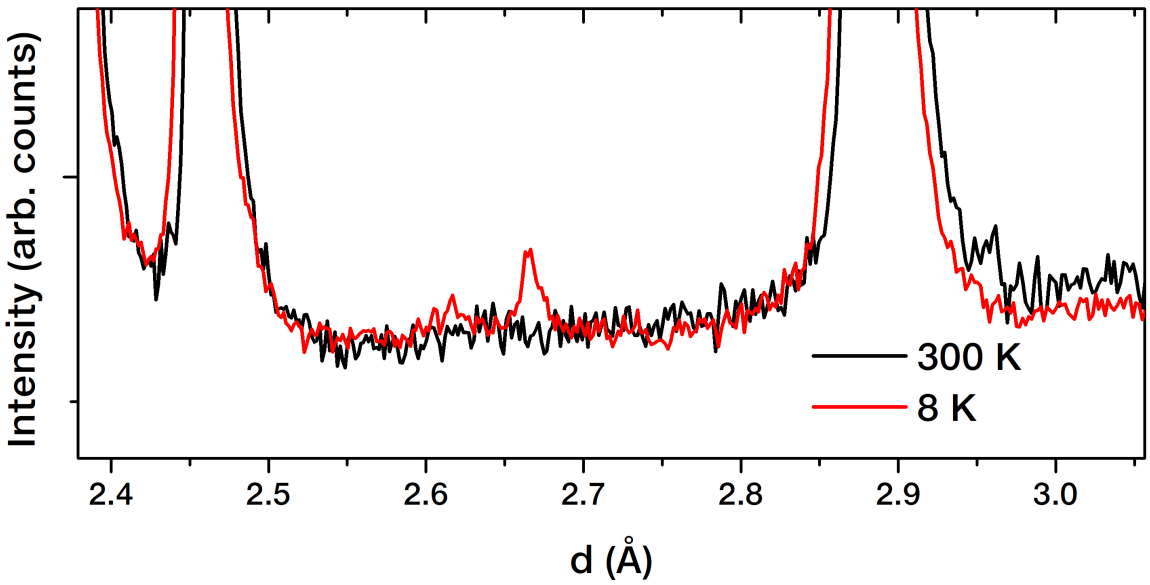


Figure 6.4: Additional reflections at low temperature corresponding to the magnetic structure at 8 K observed in NPD data.

A

Solving magnetic structures using FULLPROF

This appendix is meant to be a guide for beginners in magnetic structure solving, in addition to the already excellent tutorials available in literature[281,282,283,284,285]. We deal more with the technical aspects here, in order to determine the structure that best describes the diffraction pattern below the transition. The reader is advised to acquaint themselves with the group theoretical of magnetic representation analysis from the already mentioned resources. This awareness is important in order to understand the symmetry-based factors that drive the magnetic phase transitions. We will focus primarily on analysing data from DMC (PSI) and WISH (ISIS) as they represent two different ways (constant wavelength and time-of-flight) in which neutron powder diffraction is performed. In the following sections we will go through each step in the process.

A.1 The structure above the transition

The first step is to get the parent/crystal structure of the compound. This is typically the room temperature structure, but can be at lower temperature as well, depending on where the magnetic transition is expected. Till here, things are routine: you have a (neutron) diffraction pattern, you input a guess model into FULLPROF and refine the profile and atomic parameters until reasonable fit parameters are obtained. This refinement needs to be done well, since any errors here will

translate into the magnetic structure. You must be careful to have physically consistent values of thermal, atomic and occupancy parameters. The starting profile parameters and screenshot of a sample `.pcr` file for DMC are available here. For analysing data from WISH, it is best to modify an existing `.pcr` file (can be obtained by writing to the beamline managers) - since it simultaneously refines patterns from five data banks, each with specific parameters. An example `.pcr` file screenshot is shown in Fig. A.1

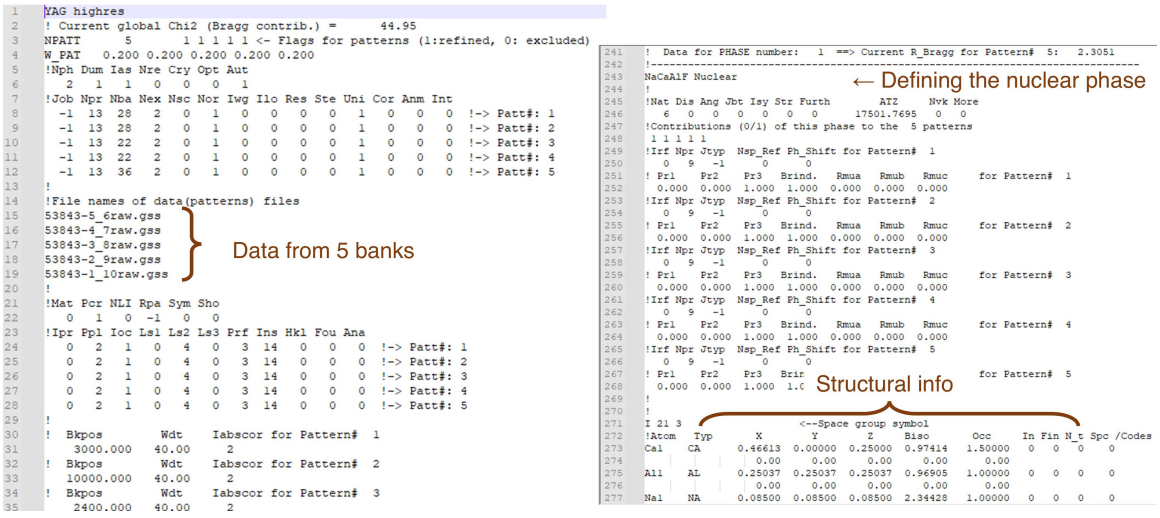


Figure A.1: `.pcr` file format for WISH

In most cases, when the background of the pattern is not flat, it is best to make a `.bgr` file manually, by visually selecting points from the observed pattern. This can be done using `WinPLOTR`, a module shipped with the FULLPROF SUITE.

The best fits for DMC data are obtained with a tripled-pseudo-Voigt function (`Npr=4` in FULLPROF) given by[123]:

$$\Omega(x) = X\,pV(x-D) + (1-X-Y)\,pV(x) + Y\,pV(x+D) \quad \text{with} \quad D = \frac{S_{b1}}{dcos\theta} \tag{A.1}$$

where $pV(x)$ is the pseudo-Voigt function, and X, Y, S_{b1} are all shape parameters.

On the other hand, time-of-flight reflections are described by the back-to-back exponential function convoluted with a pseudo-Voigt function (`Npr=9` in FULLPROF) given by[123]:

$$tof(\mu s) = \texttt{Zero} + \texttt{Dtt1} \times d + \texttt{Dtt2} \times d^2 + \texttt{Dtt_1overd}/d \tag{A.2}$$

with the Gaussian variance:

$$\sigma^2 = \texttt{sig-2} \times d^4 + \texttt{sig-1} \times d^2 + \texttt{sig-0} + \texttt{sig-q} \times \frac{1}{d^2}$$

and the Lorentzian FWHM given by:

$$\mathcal{G} = \texttt{gam-2} \times d^2 + \texttt{gam-1} \times d + \texttt{gam-0}$$

Each parameter in blue is refinable and their location in the `.pcr` file can be seen in Fig. A.1. However, the profile shape is strongly dependent on the undulator and the optics geometry of the neutron diffractometer, so different values are allowed to be refined depending on where the data was collected. For example, reflection profiles from WISH are primary Gaussian and so, the values of `gam-2,1,0` are kept fixed to the instrument values and not refined. There is also hardly any $1/d$ dependence observed, so `sig-2` and `Dtt_1overd` are also fixed to 0.

A.2 Adding the magnetic phase

Once you have the nuclear phase refined, you add the magnetic phase as a second phase. There are two ways to do this: (a) you can either use the EdPCR GUI provided with FULLPROF or (b) simply duplicate the first phase below and then modify it. You need to to take care of two things here - first, the profile parameters (lattice, background, scale etc.) are all constrained to the first (nuclear) phase, and second, only the magnetic atoms will be given in the atoms information section - each with occupancy 1. Neutron diffraction cannot differentiate between ions at equivalent sites, and gives an averaged moment value. So if you have anti-site disorder in your system - choose the dominant ion to represent the moment on that site and assign the occupancy 1.

Another modification required for the magnetic phase is the addition of the k-vector. This defines the orientation of the magnetic unit cell with respect to the crystallographic cell. For example, if you have a k-vector $(\frac{1}{3},\ 0,\ 0)$, it implies that the dimensions of the magnetic unit cell is $3a \times b \times c$ where a, b, c are the nuclear lattice parameters.

A.2.1 How to find the *k-vector*

For this, you need to identify the magnetic peaks. This is done by plotting together the patterns above and below the transition (for example, in WinPLOTR) and then observing the differences. If

no additional peaks are observed, and only intensities are enhanced, your k is likely (0,0,0). This is the case when the magnetic and nuclear unit cells are the same.

If new peaks are observed, use the `Select points` option in `WinPLOTR` to mark them and then click `Save as>>Save points for K_Search`. A dialogue box will appear where you will be asked to input parameters corresponding to the nuclear structure, the tolerance threshold and the range of k-values to search for, and the wavelength or `dtt1` value for the pattern being used for the analysis. `dtt1` is tied to the *tof* detector bank being used, so make sure you use the correct value for the pattern under study. This input file can then be used to run `K_Search` which will output a list of plausible commensurate and incommensurate k vectors compatible with the input parent structure and magnetic peak positions. It is advisable to try the highest symmetry k vectors first.

Once you have chosen a k vector, you add it to your `.pcr` file. But one task remains: you need to input the symmetry of the magnetic phase.

A.3 Magnetic representation analysis

Once you have the k-vector, you need to know what symmetries are going to survive into the ordered phase. There are specific group theoretical rules that dictate in how many ways this can happen, i.e. how many symmetries can be transformed from the parent crystallographic phase, to reach the magnetic phase. This analysis is called magnetic representational analysis[286,287,6,288,289,290] and it allows the determination of the symmetry-allowed magnetic structures that can result from a second-order magnetic phase transition, given the crystal structure before the transition and the propagation vector of the magnetic ordering. There are various softwares available which allow you to do this - most prominent of them - BASIREPS (which ships with the FULLPROF SUITE), ISODISTORT (web-based) and SARAh[204]. In the following sections, we will show the results of the magnetic representation analysis of the materials discussed in Chapter 3 and 5 performed using SARAh. They involve first the determination of the space group symmetry elements, g, that leave the propagation vector k invariant: these form the little group G_k. The magnetic representation of a crystallographic site can then be decomposed in terms of the irreducible representations (IRs) of G_k:

$$\Gamma_{Mag} = \sum_{\nu} n_{\nu} \Gamma_{\nu}^{\mu} \tag{A.3}$$

where n_ν is the number of times that the IR Γ_ν of order μ appears in the magnetic representation Γ_{Mag} for the chosen crystallographic site.

The general procedure involves two steps as briefed below:

A.3.0.1 STEP 1: SARAh Rep Analysis

This part is executed in the SARAh `Rep Analysis` module where you provide the parent (nuclear) space group, the *k*-vector and the positions of the magnetic atoms as the input. The program then performs the symmetry analysis and generates a `.mat` file which contains the results of the analysis.

A.3.0.2 STEP 2: SARAh Refine

Next, open the SARAH `Refine` module, and load the `.mat` file (this option is under the `Fullprof Controls` tab). A dialogue box similar to the one shown in Fig. A.2 should open. Here, $A(n)$ ($n = 1, 2, 3...$) denotes the sites of the magnetic atoms as defined in the input. For example, in Fig. A.2, three magnetic atoms were defined, so n runs over 1, 2, 3. $\Gamma(n)$ denotes all possible irreducible representations (IR) calculated for each site and $\Psi(n)$ denotes the basis vectors associated with each IR.

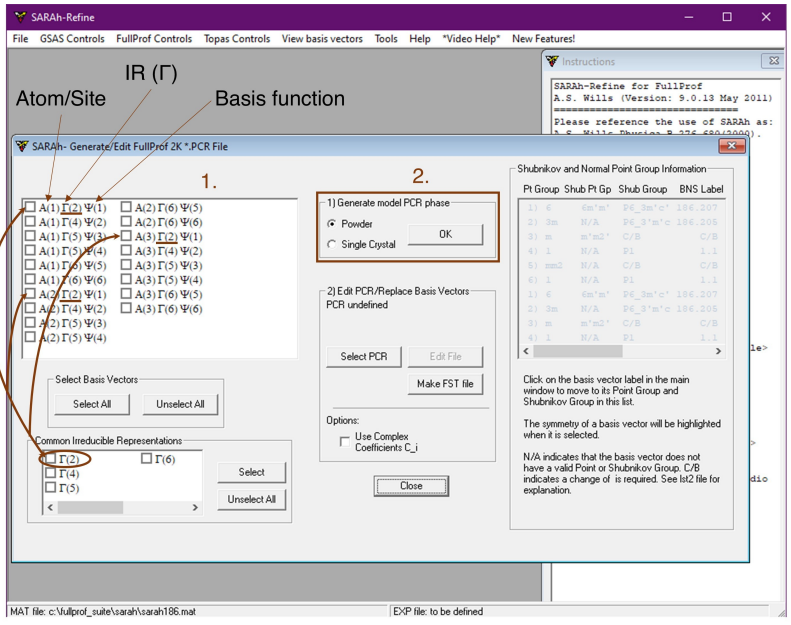


Figure A.2: SARAH Refine dialogue box with a `.mat` file loaded showing the basis vectors resulting from the representation analysis.

A.3.1 Which IR describes the magnetic structure?

Now begins the fun part, because you get to *visualize* the magnetic structure and see what the spins are up to at low temperature. This allows you to correlate the microscopic information with the macroscopic response you collect in a bulk magnetic susceptibility measurement.

Once you arrive at the dialogue box shown in Fig. A.2 you select various combinations of IRs for each site and check which one(s) are able to reproduce the magnetic peaks the best. It is advisable to start with the IRs common to all the defined magnetic sites. Check the desired basis vectors, click on `Select` and then click `OK` under the `Generate model PCR phase` with `Powder` selected. This will generate a `.pcr` file containing the symmetry and atoms information relevant to the basis vectors selected. Sections of this file are shown in Fig. A.3

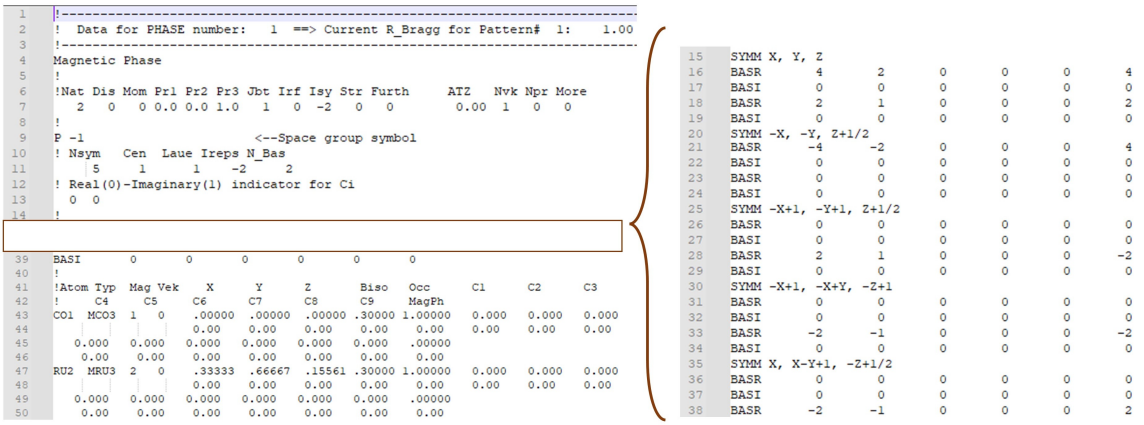


Figure A.3: The `.pcr` file output by SARAh

This `.pcr` file corresponds to FULLPROF's *User defined basis functions* mode (`Isy=-2`). In this case, the program reads the basis functions of the irreducible representations of the propagation vector group in the form shown in lines 15-38 in Fig. A.3. The 3 digits following the keyword `BASR` are the components of the vectors corresponding to the real part of the atomic basis functions. Similarly, `BASI` denotes the imaginary basis vector components. There are three components (columns) for each basis vector. So, since `N_bas` in Fig.A.3 is 2, there are 6 columns defined for each symmetry element. Also note that, the space group for the magnetic phase is $P-1$, i.e. there is no inherent symmetry, except the point of inversion. All symmetries are user defined (lines 15-38). In line 10-11, `Nsym` = 5 means there are 5 symmetry elements specified, `Cen` = 1 that the parent space group is centrosymmetric (`Cen=2` for noncentrosymmetric case), `Laue` =

1 means the Laue class is also not defined (since there is no predefined symmetry) *, `Ireps` = -2 implies that there are two irreducible representations given and the minus sign implies that the basis functions are complex, `N_bas` = 2 means there are 2 basis vectors defined and that in this case, you can refine two coefficients (`C1` and `C2` in lines 41-44). Also `Nat`=2 in lines 6-7 means there are two magnetic atoms defined.

Once you make a note of all of this information about the basis vectors you are testing, you simply copy everything between lines 1-50 and paste it under the last line of the nuclear phase (i.e. where the absorption correction parameters are defined - ends with `ABS: ABSCOR1 ABSCOR2`). Right below the last line of the magnetic atoms information (line 50), you should have the profile parameters corresponding to the magnetic phase. These values are the same as the nuclear phase and they should be constrained so, during the refinement.

You must also remember to modify the `Biso` of the atoms in the magnetic phase to match that of the nuclear phase and constrain them (as well as the atoms positions) to vary with the same codewords. The SARAh output `.pcr` files have a default `Biso` value of 0.3.

Once all of this is done, you run the program, ideally only varying the coefficients `Cn` at first, to see if the fit converges or looks visually good. The acid-tests are the visual fit of the magnetic peaks (as shown in Figs. 5.12, 3.13) and the R_{mag} % (Eq.2.10).

Each refinement run generates a `.mcif` file and two *.fst* files which can be opened in VESTA and `FPStudio`, respectively. The *.mcif* format is slowly gaining popularity among crystallographers as a program-independent format detailing the magnetic structures, although it continues to be riddled by bugs. For example,VESTA somehow is unable to reproduce the inversion symmetry of the ordered phase. For this, it is advisable to confirm the magnetic structure corresponding to the refined Γ by visualizing it in both `FPStudio` and VESTA. The magnetic moment value on each magnetic site can also be extracted by navigating to `Magnetic structure>>List magnetic moments`. This generates a text file containing the components of the magnetic moment vectors on each magnetic site as shown in Fig. A.4. Note that these values are different from the values of `Cn` since the latter are coefficients of the basis functions from which the magnetic moment values are calculated - but they are the same quantity. A small initial value of ∼0.5-1 is generally a good point to start refining the `Cn`. The values to which the fit converges, tells you about the moment

*The Laue classes as denoted by `Laue` on line 10 are: $1 \rightarrow$ -1, $2 \rightarrow 2/m$, $3 \rightarrow mmm$, $4 \rightarrow 4/m$, $5 \rightarrow 4/mmm$, $6 \rightarrow -3R$, $7 \rightarrow -3mR$, $8 \rightarrow -3$, $9 \rightarrow -3m1$, $10 \rightarrow -31m$, $11 \rightarrow 6/m$ $12 \rightarrow 6/mmm$ $13 \rightarrow m3$, and $14 \rightarrow m3m$ [123]

orientation. For example, if the Cn for the two atoms converges to values close in magnitude but opposite in sign, it probably indicates the twos sites being AFM coupled - and a better fit might be obtained by introducing a constraint.

Once a structure is found to be satisfactory, refine the profile and atomic parameters of the nuclear+magnetic phase with appropriate constraints. Remember that for *tof* data, each pattern (1-5) of each phase (1-2) must be constrained to the same codewords. Once a stable and convergent fit is obtained, the refinement can be deemed complete. The `.out` file lists all the varied parameters and their standard deviations - which can be used for further data analysis.

```
 Magnetic lattice type : P
 Unit Cell:       5.7921      5.7921     19.1928     90.0000     90.0000    120.0000

 Current Box:    0   1   0   1   0   1

 Magnetic k-vectors :
  0.00000  0.00000  0.00000

 Symmetry operations :
SYMM x,y,z
u,v,w,0.0

Atom : RU1_1     Ru
------------------------------------------------------------------------------
        x         y         z        Translation    k MSYM     m(a)     m(b)     m(c)     Mtot
  0.33333   0.66667   0.93664
                              (   0,   0,  -1)
                                                    1    1  0.00000  0.00000  1.94928
                                                             ---------------------------------
                                                             0.00000  0.00000  1.94928  1.94928
                              (   0,   0,   0)
                                                    1    1  0.00000  0.00000  1.94928
                                                             ---------------------------------
                                                             0.00000  0.00000  1.94928  1.94928
Atom : RU1_2     Ru
------------------------------------------------------------------------------
        x         y         z        Translation    k MSYM     m(a)     m(b)     m(c)     Mtot
  0.66667   0.33333   0.43664
                              (   0,   0,   0)
                                                    1    1  0.00000  0.00000 -1.94928
                                                             ---------------------------------
                                                             0.00000  0.00000 -1.94928  1.94928
Atom : RU1_3     Ru
------------------------------------------------------------------------------
```

Figure A.4: Magnetic moment values obtained from FPStudio for a given refined Γ

The following sections provide a summary of the results obtained from SARAh's representation analysis for the parent space groups $P6_3/mmc$ (#194) and $P6_3mc$ (#186) for Ba_2CoRuO_6 and $Ba_4NaRu_3O_{12}$, respectively.

A.3.2 FOR Ba_2CoRuO_6

The crystal structure of Ba_2CoRuO_6 above the transition is described in the space group $P6_3/mmc$ (#194). This space group involves 1 centering operation and 24 symmetry operations (section A.3.2.1). Of these symmetry operations 8 leave the propagation k invariant or transform it into an equivalent vector (section A.3.2.2).

The decomposition of the magnetic representation Γ_{Mag} in terms of the non-zero IRs of G_k for each crystallographic site examined, and their associated basis vectors, ψ_n, are given in Tables A.1 and A.2. The labeling of the propagation vector and the IRs follows the scheme used by Kovalev[291].

IR	BV	Atom	BV components					
			$m_{\|a}$	$m_{\|b}$	$m_{\|c}$	$im_{\|a}$	$im_{\|b}$	$im_{\|c}$
Γ_1	ψ_1	1	0	-2	0	0	0	0
		2	0	2	0	0	0	0
Γ_3	ψ_2	1	4	2	0	0	0	0
		2	-4	-2	0	0	0	0
	ψ_3	1	0	0	4	0	0	0
		2	0	0	4	0	0	0
Γ_5	ψ_4	1	0	-2	0	0	0	0
		2	0	-2	0	0	0	0
Γ_7	ψ_5	1	4	2	0	0	0	0
		2	4	2	0	0	0	0
	ψ_6	1	0	0	4	0	0	0
		2	0	0	-4	0	0	0

Table A.1: Basis vectors for the space group $P6_3/mmc$ with $k = (\frac{1}{2},\ 0,\ 0)$.The decomposition of the magnetic representation for the $Co1$ site $(0,\ 0,\ 0)$ is $\Gamma_{Mag} = 1\Gamma_1^1 + 0\Gamma_2^1 + 2\Gamma_3^1 + 0\Gamma_4^1 + 1\Gamma_5^1 + 0\Gamma_6^1 + 2\Gamma_7^1 + 0\Gamma_8^1$. Atoms of the non-primitive basis are defined according to 1: $(0,\ 0,\ 0)$, 2: $(0,\ 0,\ \frac{1}{2})$.

IR	BV	Atom	BV components					
			$m_{\|a}$	$m_{\|b}$	$m_{\|c}$	$im_{\|a}$	$im_{\|b}$	$im_{\|c}$
Γ_1	ψ_1	1	0	-1	0	0	0	0
		2	0	-1	0	0	0	0
		3	0	1	0	0	0	0
		4	0	1	0	0	0	0
Γ_2	ψ_2	1	2	1	0	0	0	0
		2	2	1	0	0	0	0
		3	2	1	0	0	0	0
		4	2	1	0	0	0	0

IR	BV	Atom	BV components					
			$m_{\parallel a}$	$m_{\parallel b}$	$m_{\parallel c}$	$im_{\parallel a}$	$im_{\parallel b}$	$im_{\parallel c}$
	ψ_3	1	0	0	2	0	0	0
		2	0	0	-2	0	0	0
		3	0	0	2	0	0	0
		4	0	0	-2	0	0	0
Γ_3	ψ_4	1	2	1	0	0	0	0
		2	2	1	0	0	0	0
		3	-2	-1	0	0	0	0
		4	-2	-1	0	0	0	0
	ψ_5	1	0	0	2	0	0	0
		2	0	0	-2	0	0	0
		3	0	0	-2	0	0	0
		4	0	0	2	0	0	0
Γ_4	ψ_6	1	0	-1	0	0	0	0
		2	0	-1	0	0	0	0
		3	0	-1	0	0	0	0
		4	0	-1	0	0	0	0
Γ_5	ψ_7	1	0	-1	0	0	0	0
		2	0	1	0	0	0	0
		3	0	1	0	0	0	0
		4	0	-1	0	0	0	0
Γ_6	ψ_8	1	2	1	0	0	0	0
		2	-2	-1	0	0	0	0
		3	2	1	0	0	0	0
		4	-2	-1	0	0	0	0
	ψ_9	1	0	0	2	0	0	0
		2	0	0	2	0	0	0
		3	0	0	2	0	0	0
		4	0	0	2	0	0	0
Γ_7	ψ_{10}	1	2	1	0	0	0	0
		2	-2	-1	0	0	0	0
		3	-2	-1	0	0	0	0
		4	2	1	0	0	0	0

IR	BV	Atom	BV components					
			m_a	m_b	m_c	im_a	im_b	im_c
	ψ_{11}	1	0	0	2	0	0	0
		2	0	0	2	0	0	0
		3	0	0	-2	0	0	0
		4	0	0	-2	0	0	0
Γ_8	ψ_{12}	1	0	-1	0	0	0	0
		2	0	1	0	0	0	0
		3	0	-1	0	0	0	0
		4	0	1	0	0	0	0

Table A.2: Basis vectors for the space group $P6_3/mmc$ with $k = (\frac{1}{2},\ 0,\ 0)$. The decomposition of the magnetic representation for the Ru site $(\frac{1}{3},\ \frac{2}{3},\ 0.15561)$ is $\Gamma_{Mag} = 1\Gamma_1^1 + 2\Gamma_2^1 + 2\Gamma_3^1 + 1\Gamma_4^1 + 1\Gamma_5^1 + 2\Gamma_6^1 + 2\Gamma_7^1 + 1\Gamma_8^1$. The atoms of the nonprimitive basis are defined according to 1: $(\frac{1}{3},\ \frac{2}{3},\ 0.15561)$, 2: $(\frac{1}{3},\ \frac{2}{3},\ 0.65561)$, 3: $(\frac{1}{3},\ \frac{2}{3},\ 0.84439)$, 4: $(\frac{1}{3},\ \frac{2}{3},\ 0.34439)$.

A.3.2.1 Elements in the group G_0

Element g_n	Rotation matrix R	IT notation $g_n = \{R \mid \tau\}$	Kovalev notation $g_n = \{h_n \mid \tau\}$	Jones symbol
g_1	$\begin{pmatrix} 1 & 0 & 0 \\ 0 & 1 & 0 \\ 0 & 0 & 1 \end{pmatrix}$	$\{E\mid 0\,0\,0\}$	$\{h_1 \mid 0\,0\,0\}$	x, y, z
g_2	$\begin{pmatrix} 0 & \bar{1} & 0 \\ 1 & \bar{1} & 0 \\ 0 & 0 & 1 \end{pmatrix}$	$\{C_3^+\mid 0\,0\,0\}$	$\{h_3 \mid 0\,0\,0\}$	$-y, x-y, z$
g_3	$\begin{pmatrix} \bar{1} & 1 & 0 \\ \bar{1} & 0 & 0 \\ 0 & 0 & 1 \end{pmatrix}$	$\{C_3^-\mid 0\,0\,0\}$	$\{h_5 \mid 0\,0\,0\}$	$-x+y, -x, z$
g_4	$\begin{pmatrix} \bar{1} & 0 & 0 \\ 0 & \bar{1} & 0 \\ 0 & 0 & 1 \end{pmatrix}$	$\{C_2\mid 0\,0\,\frac{1}{2}\}$	$\{h_4 \mid 0\,0\,\frac{1}{2}\}$	$-x, -y, z+\frac{1}{2}$
g_5	$\begin{pmatrix} 0 & 1 & 0 \\ \bar{1} & 1 & 0 \\ 0 & 0 & 1 \end{pmatrix}$	$\{C_6^-\mid 0\,0\,\frac{1}{2}\}$	$\{h_6 \mid 0\,0\,\frac{1}{2}\}$	$y, -x+y, z+\frac{1}{2}$

Element g_n	Rotation matrix R	IT notation $g_n = \{R \mid \tau\}$	Kovalev notation $g_n = \{h_n \mid \tau\}$	Jones symbol
g_6	$\begin{pmatrix} 1 & \bar{1} & 0 \\ 1 & 0 & 0 \\ 0 & 0 & 1 \end{pmatrix}$	$\{C_6^+ \mid 0\,0\,\frac{1}{2}\}$	$\{h_2 \mid 0\,0\,\frac{1}{2}\}$	$x-y, x, z+\frac{1}{2}$
g_7	$\begin{pmatrix} 0 & 1 & 0 \\ 1 & 0 & 0 \\ 0 & 0 & \bar{1} \end{pmatrix}$	$\{C_{23} \mid 0\,0\,0\}$	$\{h_{11} \mid 0\,0\,0\}$	$y, x, -z$
g_8	$\begin{pmatrix} 1 & \bar{1} & 0 \\ 0 & \bar{1} & 0 \\ 0 & 0 & \bar{1} \end{pmatrix}$	$\{C_{21} \mid 0\,0\,0\}$	$\{h_9 \mid 0\,0\,0\}$	$x-y, -y, -z$
g_9	$\begin{pmatrix} \bar{1} & 0 & 0 \\ \bar{1} & 1 & 0 \\ 0 & 0 & \bar{1} \end{pmatrix}$	$\{C_{22} \mid 0\,0\,0\}$	$\{h_7 \mid 0\,0\,0\}$	$-x, -x+y, -z$
g_{10}	$\begin{pmatrix} 0 & \bar{1} & 0 \\ \bar{1} & 0 & 0 \\ 0 & 0 & \bar{1} \end{pmatrix}$	$\{C_{23} \mid 0\,0\,\frac{1}{2}\}$	$\{h_8 \mid 0\,0\,\frac{1}{2}\}$	$-y, -x, -z+\frac{1}{2}$
g_{11}	$\begin{pmatrix} \bar{1} & 1 & 0 \\ 0 & 1 & 0 \\ 0 & 0 & \bar{1} \end{pmatrix}$	$\{C_{21} \mid 0\,0\,\frac{1}{2}\}$	$\{h_{12} \mid 0\,0\,\frac{1}{2}\}$	$-x+y, y, -z+\frac{1}{2}$
g_{12}	$\begin{pmatrix} 1 & 0 & 0 \\ 1 & \bar{1} & 0 \\ 0 & 0 & \bar{1} \end{pmatrix}$	$\{C_{22} \mid 0\,0\,\frac{1}{2}\}$	$\{h_{10} \mid 0\,0\,\frac{1}{2}\}$	$x, x-y, -z+\frac{1}{2}$
g_{13}	$\begin{pmatrix} \bar{1} & 0 & 0 \\ 0 & \bar{1} & 0 \\ 0 & 0 & \bar{1} \end{pmatrix}$	$\{I \mid 0\,0\,0\}$	$\{h_{13} \mid 0\,0\,0\}$	$-x, -y, -z$
g_{14}	$\begin{pmatrix} 0 & 1 & 0 \\ \bar{1} & 1 & 0 \\ 0 & 0 & \bar{1} \end{pmatrix}$	$\{S_6^- \mid 0\,0\,0\}$	$\{h_{15} \mid 0\,0\,0\}$	$y, -x+y, -z$
g_{15}	$\begin{pmatrix} 1 & \bar{1} & 0 \\ 1 & 0 & 0 \\ 0 & 0 & \bar{1} \end{pmatrix}$	$\{S_6^+ \mid 0\,0\,0\}$	$\{h_{17} \mid 0\,0\,0\}$	$x-y, x, -z$
g_{16}	$\begin{pmatrix} 1 & 0 & 0 \\ 0 & 1 & 0 \\ 0 & 0 & \bar{1} \end{pmatrix}$	$\{\sigma_h \mid 0\,0\,\frac{1}{2}\}$	$\{h_{16} \mid 0\,0\,\frac{1}{2}\}$	$x, y, -z+\frac{1}{2}$

Element g_n	Rotation matrix R	IT notation $g_n = \{R \mid \tau\}$	Kovalev notation $g_n = \{h_n \mid \tau\}$	Jones symbol
g_{17}	$\begin{pmatrix} 0 & \bar{1} & 0 \\ 1 & \bar{1} & 0 \\ 0 & 0 & \bar{1} \end{pmatrix}$	$\{S_3^+ \mid 0\,0\,\frac{1}{2}\}$	$\{h_{18} \mid 0\,0\,\frac{1}{2}\}$	$-y, x-y, -z+\frac{1}{2}$
g_{18}	$\begin{pmatrix} \bar{1} & 1 & 0 \\ \bar{1} & 0 & 0 \\ 0 & 0 & \bar{1} \end{pmatrix}$	$\{S_3^- \mid 0\,0\,\frac{1}{2}\}$	$\{h_{14} \mid 0\,0\,\frac{1}{2}\}$	$-x+y, -x, -z+\frac{1}{2}$
g_{19}	$\begin{pmatrix} 0 & \bar{1} & 0 \\ \bar{1} & 0 & 0 \\ 0 & 0 & 1 \end{pmatrix}$	$\{\sigma_{v3} \mid 0\,0\,0\}$	$\{h_{23} \mid 0\,0\,0\}$	$-y, -x, z$
g_{20}	$\begin{pmatrix} \bar{1} & 1 & 0 \\ 0 & 1 & 0 \\ 0 & 0 & 1 \end{pmatrix}$	$\{\sigma_{v1} \mid 0\,0\,0\}$	$\{h_{21} \mid 0\,0\,0\}$	$-x+y, y, z$
g_{21}	$\begin{pmatrix} 1 & 0 & 0 \\ 1 & \bar{1} & 0 \\ 0 & 0 & 1 \end{pmatrix}$	$\{\sigma_{v2} \mid 0\,0\,0\}$	$\{h_{19} \mid 0\,0\,0\}$	$x, x-y, z$
g_{22}	$\begin{pmatrix} 0 & 1 & 0 \\ 1 & 0 & 0 \\ 0 & 0 & 1 \end{pmatrix}$	$\{\sigma_{d3} \mid 0\,0\,\frac{1}{2}\}$	$\{h_{20} \mid 0\,0\,\frac{1}{2}\}$	$y, x, z+\frac{1}{2}$
g_{23}	$\begin{pmatrix} 1 & \bar{1} & 0 \\ 0 & \bar{1} & 0 \\ 0 & 0 & 1 \end{pmatrix}$	$\{\sigma_{d1} \mid 0\,0\,\frac{1}{2}\}$	$\{h_{24} \mid 0\,0\,\frac{1}{2}\}$	$x-y, -y, z+\frac{1}{2}$
g_{24}	$\begin{pmatrix} \bar{1} & 0 & 0 \\ \bar{1} & 1 & 0 \\ 0 & 0 & 1 \end{pmatrix}$	$\{\sigma_{d2} \mid 0\,0\,\frac{1}{2}\}$	$\{h_{22} \mid 0\,0\,\frac{1}{2}\}$	$-x, -x+y, z+\frac{1}{2}$

Table A.3: Symmetry operators of the space group $P6_3/mmc$. The notations used are of the International Tables, where the elements are separated into rotation[6] and translation components, and the *Jones faithful representations*[7].

A.3.2.2 Elements in the group G_k

Element g_n	Rotation matrix R	IT notation $g_n = \{R \mid \tau\}$	Kovalev notation $g_n = \{h_n \mid \tau\}$	Jones symbol
g_1	$\begin{pmatrix} 1 & 0 & 0 \\ 0 & 1 & 0 \\ 0 & 0 & 1 \end{pmatrix}$	$\{E\mid 0\,0\,0\}$	$\{h_1 \mid 0\,0\,0\}$	x, y, z
g_4	$\begin{pmatrix} \bar{1} & 0 & 0 \\ 0 & \bar{1} & 0 \\ 0 & 0 & 1 \end{pmatrix}$	$\{C_2\mid 0\,0\,\frac{1}{2}\}$	$\{h_4 \mid 0\,0\,\frac{1}{2}\}$	$-x, -y, z+\frac{1}{2}$
g_9	$\begin{pmatrix} \bar{1} & 0 & 0 \\ \bar{1} & 1 & 0 \\ 0 & 0 & \bar{1} \end{pmatrix}$	$\{C_{22}\mid 0\,0\,0\}$	$\{h_7 \mid 0\,0\,0\}$	$-x, -x+y, -z$
g_{12}	$\begin{pmatrix} 1 & 0 & 0 \\ 1 & \bar{1} & 0 \\ 0 & 0 & \bar{1} \end{pmatrix}$	$\{C_{22}\mid 0\,0\,-\frac{1}{2}\}$	$\{h_{10} \mid 0\,0\,-\frac{1}{2}\}$	$x, x-y, -z-\frac{1}{2}$
g_{13}	$\begin{pmatrix} \bar{1} & 0 & 0 \\ 0 & \bar{1} & 0 \\ 0 & 0 & \bar{1} \end{pmatrix}$	$\{I\mid 0\,0\,0\}$	$\{h_{13} \mid 0\,0\,0\}$	$-x, -y, -z$
g_{16}	$\begin{pmatrix} 1 & 0 & 0 \\ 0 & 1 & 0 \\ 0 & 0 & \bar{1} \end{pmatrix}$	$\{\sigma_h\mid 0\,0\,-\frac{1}{2}\}$	$\{h_{16} \mid 0\,0\,-\frac{1}{2}\}$	$x, y, -z-\frac{1}{2}$
g_{21}	$\begin{pmatrix} 1 & 0 & 0 \\ 1 & \bar{1} & 0 \\ 0 & 0 & 1 \end{pmatrix}$	$\{\sigma_{v2}\mid 0\,0\,0\}$	$\{h_{19} \mid 0\,0\,0\}$	$x, x-y, z$
g_{24}	$\begin{pmatrix} \bar{1} & 0 & 0 \\ \bar{1} & 1 & 0 \\ 0 & 0 & 1 \end{pmatrix}$	$\{\sigma_{d2}\mid 0\,0\,\frac{1}{2}\}$	$\{h_{22} \mid 0\,0\,\frac{1}{2}\}$	$-x, -x+y, z+\frac{1}{2}$

Table A.4: Symmetry elements of the little group $G_{\mathbf{k}}$. The notations used are of the International Tables, where the elements are separated into rotation[6] and translation components, and the *Jones faithful representations*[7].

A.3.3 For $Ba_4NaRu_3O_{12}$

The same method described in the previous section gives the following representations for $Ba_4NaRu_3O_{12}$ with the noncentrosymmetric space group $P6_3mc$ at room temperature.

IR	BV	Atom	BV components					
			$m_{\|a}$	$m_{\|b}$	$m_{\|c}$	$im_{\|a}$	$im_{\|b}$	$im_{\|c}$
Γ_2	ψ_1	1	0	0	6	0	0	0
		2	0	0	6	0	0	0
Γ_4	ψ_2	1	0	0	6	0	0	0
		2	0	0	-6	0	0	0
Γ_5	ψ_3	1	0	-1.5	0	0	0	0
		2	0	-1.5	0	0	0	0
	ψ_4	1	-1.732	-0.866	0	0	0	0
		2	-1.732	-0.866	0	0	0	0
Γ_6	ψ_5	1	0	-1.5	0	0	0	0
		2	0	1.5	0	0	0	0
	ψ_6	1	-1.732	-0.866	0	0	0	0
		2	1.732	0.866	0	0	0	0

Table A.5: Basis vectors for the space group $P6_3mc$ with $\mathbf{k} = (0,\ 0,\ 0)$. Decomposition of the magnetic representation for the sites $Ru1(\frac{1}{3},\ \frac{2}{3},\ 0.93858)$, $Ru2(0,\ 0,\ 0.32126)$, and $Ru3(0,\ 0, 0.18269)$ is $\Gamma_{Mag} = 0\Gamma_1^1 + 1\Gamma_2^1 + 0\Gamma_3^1 + 1\Gamma_4^1 + 1\Gamma_5^2 + 1\Gamma_6^2$

The atoms of the nonprimitive basis for each site are defined according to:

Site	Atom 1	Atom 2
Ru1	$\frac{1}{3},\ \frac{2}{3},\ 0.93858$	$\frac{2}{3},\ \frac{1}{3},\ 0.43858$
Ru2	$0,\ 0,\ 0.32126$	$0,\ 0,\ 0.82126$
Ru3	$0,\ 0,\ 0.18269$	$0,\ 0,\ 0.68269$

Table A.6: Atoms of the nonprimitive cell of $Ba_4NaRu_3O_{12}$

A.3.3.1 Elements in the group G_0

Element g_n	Rotation matrix R	IT notation $g_n = \{R \mid \tau\}$	Kovalev notation $g_n = \{h_n \mid \tau\}$	Jones symbol
g_1	$\begin{pmatrix} 1 & 0 & 0 \\ 0 & 1 & 0 \\ 0 & 0 & 1 \end{pmatrix}$	$\{E\mid 0\,0\,0\}$	$\{h_1 \mid 0\,0\,0\}$	x, y, z

Element g_n	Rotation matrix R	IT notation $g_n = \{R \mid \tau\}$	Kovalev notation $g_n = \{h_n \mid \tau\}$	Jones symbol
g_2	$\begin{pmatrix} 0 & \bar{1} & 0 \\ 1 & \bar{1} & 0 \\ 0 & 0 & 1 \end{pmatrix}$	$\{C_3^+ \mid 0\,0\,0\}$	$\{h_3 \mid 0\,0\,0\}$	$-y, x-y, z$
g_3	$\begin{pmatrix} \bar{1} & 1 & 0 \\ \bar{1} & 0 & 0 \\ 0 & 0 & 1 \end{pmatrix}$	$\{C_3^- \mid 0\,0\,0\}$	$\{h_5 \mid 0\,0\,0\}$	$-x+y, -x, z$
g_4	$\begin{pmatrix} \bar{1} & 0 & 0 \\ 0 & \bar{1} & 0 \\ 0 & 0 & 1 \end{pmatrix}$	$\{C_2 \mid 0\,0\,.5\}$	$\{h_4 \mid 0\,0\,.5\}$	$-x, -y, z+\frac{1}{2}$
g_5	$\begin{pmatrix} 0 & 1 & 0 \\ \bar{1} & 1 & 0 \\ 0 & 0 & 1 \end{pmatrix}$	$\{C_6^- \mid 0\,0\,.5\}$	$\{h_6 \mid 0\,0\,.5\}$	$y, -x+y, z+\frac{1}{2}$
g_6	$\begin{pmatrix} 1 & \bar{1} & 0 \\ 1 & 0 & 0 \\ 0 & 0 & 1 \end{pmatrix}$	$\{C_6^+ \mid 0\,0\,.5\}$	$\{h_2 \mid 0\,0\,.5\}$	$x-y, x, z+\frac{1}{2}$
g_7	$\begin{pmatrix} 0 & \bar{1} & 0 \\ \bar{1} & 0 & 0 \\ 0 & 0 & 1 \end{pmatrix}$	$\{\sigma_{v3} \mid 0\,0\,0\}$	$\{h_{23} \mid 0\,0\,0\}$	$-y, -x, z$
g_8	$\begin{pmatrix} \bar{1} & 1 & 0 \\ 0 & 1 & 0 \\ 0 & 0 & 1 \end{pmatrix}$	$\{\sigma_{v1} \mid 0\,0\,0\}$	$\{h_{21} \mid 0\,0\,0\}$	$-x+y, y, z$
g_9	$\begin{pmatrix} 1 & 0 & 0 \\ 1 & \bar{1} & 0 \\ 0 & 0 & 1 \end{pmatrix}$	$\{\sigma_{v2} \mid 0\,0\,0\}$	$\{h_{19} \mid 0\,0\,0\}$	$x, x-y, z$
g_{10}	$\begin{pmatrix} 0 & 1 & 0 \\ 1 & 0 & 0 \\ 0 & 0 & 1 \end{pmatrix}$	$\{\sigma_{d3} \mid 0\,0\,.5\}$	$\{h_{20} \mid 0\,0\,.5\}$	$y, x, z+\frac{1}{2}$
g_{11}	$\begin{pmatrix} 1 & \bar{1} & 0 \\ 0 & \bar{1} & 0 \\ 0 & 0 & 1 \end{pmatrix}$	$\{\sigma_{d1} \mid 0\,0\,.5\}$	$\{h_{24} \mid 0\,0\,.5\}$	$x-y, -y, z+\frac{1}{2}$

Element g_n	Rotation matrix R	IT notation $g_n = \{R \mid \tau\}$	Kovalev notation $g_n = \{h_n \mid \tau\}$	Jones symbol
g_{12}	$\begin{pmatrix} \bar{1} & 0 & 0 \\ \bar{1} & 1 & 0 \\ 0 & 0 & 1 \end{pmatrix}$	$\{\sigma_{d2} \mid 0\,0\,.5\}$	$\{h_{22} \mid 0\,0\,.5\}$	$-x, -x+y, z+\frac{1}{2}$

Table A.7: Symmetry operators of the space group P 63 m c. The notations used are of the International Tables, where the elements are separated into rotation[6] and translation components, and the *Jones faithful representations*[7].

A.3.3.2 Elements in the group G_k

Element g_n	Rotation matrix R	IT notation $g_n = \{R \mid \tau\}$	Kovalev notation $g_n = \{h_n \mid \tau\}$	Jones symbol
g_1	$\begin{pmatrix} 1 & 0 & 0 \\ 0 & 1 & 0 \\ 0 & 0 & 1 \end{pmatrix}$	$\{E \mid 0\,0\,0\}$	$\{h_1 \mid 0\,0\,0\}$	x, y, z
g_6	$\begin{pmatrix} 1 & \bar{1} & 0 \\ 1 & 0 & 0 \\ 0 & 0 & 1 \end{pmatrix}$	$\{C_6^+ \mid 0\,0\,.5\}$	$\{h_2 \mid 0\,0\,.5\}$	$x-y, x, z+\frac{1}{2}$
g_2	$\begin{pmatrix} 0 & \bar{1} & 0 \\ 1 & \bar{1} & 0 \\ 0 & 0 & 1 \end{pmatrix}$	$\{C_3^+ \mid 0\,0\,0\}$	$\{h_3 \mid 0\,0\,0\}$	$-y, x-y, z$
g_4	$\begin{pmatrix} \bar{1} & 0 & 0 \\ 0 & \bar{1} & 0 \\ 0 & 0 & 1 \end{pmatrix}$	$\{C_2 \mid 0\,0\,.5\}$	$\{h_4 \mid 0\,0\,.5\}$	$-x, -y, z+\frac{1}{2}$
g_3	$\begin{pmatrix} \bar{1} & 1 & 0 \\ \bar{1} & 0 & 0 \\ 0 & 0 & 1 \end{pmatrix}$	$\{C_3^- \mid 0\,0\,0\}$	$\{h_5 \mid 0\,0\,0\}$	$-x+y, -x, z$
g_5	$\begin{pmatrix} 0 & 1 & 0 \\ \bar{1} & 1 & 0 \\ 0 & 0 & 1 \end{pmatrix}$	$\{C_6^- \mid 0\,0\,.5\}$	$\{h_6 \mid 0\,0\,.5\}$	$y, -x+y, z+\frac{1}{2}$
g_9	$\begin{pmatrix} 1 & 0 & 0 \\ 1 & \bar{1} & 0 \\ 0 & 0 & 1 \end{pmatrix}$	$\{\sigma_{v2} \mid 0\,0\,0\}$	$\{h_{19} \mid 0\,0\,0\}$	$x, x-y, z$

Element g_n	Rotation matrix R	IT notation $g_n = \{R \mid \tau\}$	Kovalev notation $g_n = \{h_n \mid \tau\}$	Jones symbol
g_{10}	$\begin{pmatrix} 0 & 1 & 0 \\ 1 & 0 & 0 \\ 0 & 0 & 1 \end{pmatrix}$	$\{\sigma_{d3} \mid 0\,0\,.5\}$	$\{h_{20} \mid 0\,0\,.5\}$	$y, x, z + \frac{1}{2}$
g_8	$\begin{pmatrix} \bar{1} & 1 & 0 \\ 0 & 1 & 0 \\ 0 & 0 & 1 \end{pmatrix}$	$\{\sigma_{v1} \mid 0\,0\,0\}$	$\{h_{21} \mid 0\,0\,0\}$	$-x + y, y, z$
g_{12}	$\begin{pmatrix} \bar{1} & 0 & 0 \\ \bar{1} & 1 & 0 \\ 0 & 0 & 1 \end{pmatrix}$	$\{\sigma_{d2} \mid 0\,0\,.5\}$	$\{h_{22} \mid 0\,0\,.5\}$	$-x, -x + y, z + \frac{1}{2}$
g_7	$\begin{pmatrix} 0 & \bar{1} & 0 \\ \bar{1} & 0 & 0 \\ 0 & 0 & 1 \end{pmatrix}$	$\{\sigma_{v3} \mid 0\,0\,0\}$	$\{h_{23} \mid 0\,0\,0\}$	$-y, -x, z$
g_{11}	$\begin{pmatrix} 1 & \bar{1} & 0 \\ 0 & \bar{1} & 0 \\ 0 & 0 & 1 \end{pmatrix}$	$\{\sigma_{d1} \mid 0\,0\,.5\}$	$\{h_{24} \mid 0\,0\,.5\}$	$x - y, -y, z + \frac{1}{2}$

Table A.8: Symmetry elements of the little group $G_{\mathbf{k}}$. The notations used are of the International Tables, where the elements are separated into rotation[6] and translation components, and the *Jones faithful representations*[7].

It must be noted that there are many more ways of treating magnetic structures in FULLPROF - depending on how the symmetry operators are defined in the `.pcr` file. However, the above described method to refine the coefficients of the basis functions is the most user-friendly and compatible with representation analysis software. BASIREPS also outputs a similar `.pcr` fragment that can be copied and pasted into the main `.pcr` file. ISODISTORT works slightly differently as it models magnetic distortions in terms of amplitude modes and is more compatible with JANA - another refinement software. ISODISTORT, however, is very useful for visualizing the different types of magnetic distortions that can occur in a given space groups and at what k-points, especially when magnetic transitions co-occur with strain and atomic displacement distortions.

B

Microstructure Analysis in FULLPROF

Bragg peaks diffracted by powder samples have a finite width which limits resolution. The main contributors to this width are the sample microstructure, the optical elements in the beam path and the detector. This is why the knowledge of instrumental resolution is imperative to the calculation of the sample microstructure.

The instrumental contribution is a convolution of that due to the optics chain that precedes the sample and the geometrical broadening due to the sample. In the absence of a diffracted beam analyzer, the latter occurs due to the sample size and the detector strip pitch[8].

The instrumental broadening (unlike the sample microstructure) is generally well modeled as pure Gaussian profiles.

If the shape of a peak at angle θ be defined by $\Omega(x)$ where $x = (\theta - \theta_B)$ and θ_B is the Bragg position, and its total broadening is denoted by σ then,

$$\sigma^2 = \sigma^2_{sample} + \sigma^2_{opt} + \sigma^2_{geom}$$

where σ_{sample}, σ_{opt} and σ_{geom} signify the broadening coming from the sample microstructure, optics

chain and the sample geometry, respectively[8]. σ is in units of ° (2θ).

B.1 Contributions to broadening

B.1.1 Optics

σ_{opt} is primarily due to the beam divergence and has a 2θ dependence given by:

$$\sigma_{opt} = \frac{1}{\sqrt{2ln2}}\sqrt{Utan^2(2\theta) + Vtan(2\theta) + W}$$

where U, V, W are Caglioti half-width parameters and $\frac{1}{\sqrt{2ln2}}$ converts the half-width at half-maximum (HWHM) of a Gaussian curve to its standard deviation. Caglioti's work modeled neutron diffraction line shapes in terms of collimator and monochromator transmission functions in the Gaussian approximation[292,293].

B.1.2 Sample Geometry

Contributions to σ_{geom} depend on how the diffraction experiment is set up. Generally, in such an experiment a glass capillary is loaded with the powder sample such that no air gaps exist and are rotated about their axis normal to the beam direction to increase isotropy. This is called the *Debye-Scherrer Geometry*. This contribution will differ between beamlines.

The four main contributions to σ_{geom} are:

$$\sigma^2_{geom} = \sigma^2_{pix} + \sigma^2_{cap} + \sigma^2_{wob} + \sigma^2_{axial}$$

B.1.2.1 Intrinsic resolution of the detector

The detector contribution, σ_{pix} is defined by the strip pitch of the sensor. For example for MYTHEN, a 1D single photon counting detector developed at PSI SLS-MS, at $E_{photon} = 8$ keV and energy threshold at 4 keV, $\sigma_{pix} = 16 \pm 2\,\mu m$[106]. This is different from the ideal standard deviation of a 50 μm wide box function (=14.4 μm) due to charge sharing between neighbouring strips[8].

Using the sample-to-detector distance R_{SDD} = 760 mm, in terms of 2θ, $\sigma_{pix} = 1.21 \pm 0.15$ mdeg[8].

B.1.2.2 Capillary size

The finite diameter of the capillary adds to the broadening and is estimated by considering the projection of the cylindrical capillary on the flat detector surface as

$$\sigma_{cap} = \frac{45}{\pi}\frac{d}{R_{SDD}}$$

where d is the capillary diameter and R_{SDD} the sample-to-detector distance, and σ_{cap} is in degrees.

This relation holds when the sample absorption is small. This can be ensured by adjusting the loading density of the sample so that the absorption depth of x-rays remains greater than the capillary diameter.

Typically, σ_{cap} increases linearly with sample capillary size from about 0.002°for a 0.1mm capillary to about 0.019°for a 1mm capillary[8].

B.1.2.3 Wobbling

Misalignment of the capillary axis with respect to its rotation axis causes *wobbling*. This is estimated by convolution of the cylindrical capillary shape and the periodic wobbling function, projecting it onto the flat detector surface and averaging it

$$\sigma_{wob} = \frac{90\sqrt{2}}{\pi}\frac{w}{R_{SDD}} = \sqrt{8}\frac{w}{d}\sigma_{cap}$$

where w is the capillary displacement.

Smaller capillaries are more likely to be affected by wobbling than medium ones. Severe wobbling ($w > 0.5d$) can change the peak shape to bimodal and in such cases, analysis becomes non-trivial. It is important to align capillaries to within 0.05 mm or better. At $w \approx 0.1d$, wobbling contributes to $\sim 4\%$ of σ_{geom}.

B.1.2.4 Axial divergence

This is a contribution that arises in case of 1D detectors and shows up as an asymmetric broadening at low angles. It also causes negative peak shifts for $2\theta \leq 90°$and positive above. Soller slits and/or capillary lenses are used to reduce this effect. This broadening σ_{axial} is modeled by the Finger-Cox-Jephcoat (FCJ) lineshape, and is proportional to $\cot\theta$. This formalism describes

the divergence in terms of finite sample and detector sizes[294]. For MYTHEN, the detector axial dimension is 8 mm (given by the strip length)[8].

B.1.3 Microstructure

The above two sections make it clear that in order to extract any microstructural information from XRD data, it is imperative to first isolate the instrumental contribution coming from the optics and geometry.

Diffractometers at large facilities usually do this analysis very precisely as shown in the following section where we look at specific results for the MYTHEN diffractometer at SLS (PSI).

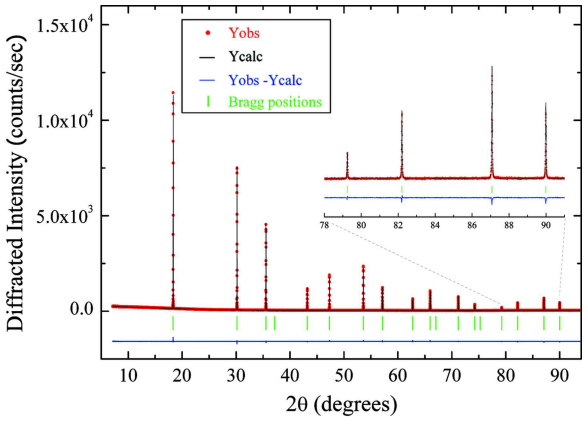


Figure B.1: Refinement of Si NIST 640C using FULLPROF. Reproduced with permission from Bergamaschi et al., 2010[8]. Copyright IUCr Journals.

Capillary diameter, d = 0.5 mm
E = 12.4 keV, acquisition time = 2.4 s
Profile = TCH-PV (Npr=7 for FULLPROF)
χ^2 = 1.4

	Si NIST 640C
λ (Å)	1.000003
2θ Zero-error	-0.01202
U	0.00029
V	0.00037
W	0.00030
X	0.01516
Y	0.00099
S/L	0.00841
D/L	0.00427

Table B.1: Si refinement values[8]

B.1.3.1 Experimental Results for MYTHEN at SLS XRPD

Bergamaschi et al., 2010[8] report the experimental values obtained on SLS XRPD station using the MYTHEN detector for the standard samples Si NIST 640C and $Na_2Ca_2Al_2F_{14}$ (NAC). Si NIST 640C, being a well-defined NIST standard, is the preferred choice for wavelength and zero-error calibration before measurements. NAC, due to its small intrinsic line width, is the preferred choice for estimation of instrumental contribution. Results obtained from structural refinement[117] of Si NIST 640C and Whole Powder Pattern Matching (WPPM)[203,295,296] of NAC

are summarized in Figs **??**, **??** and Tables B.1, B.2*:

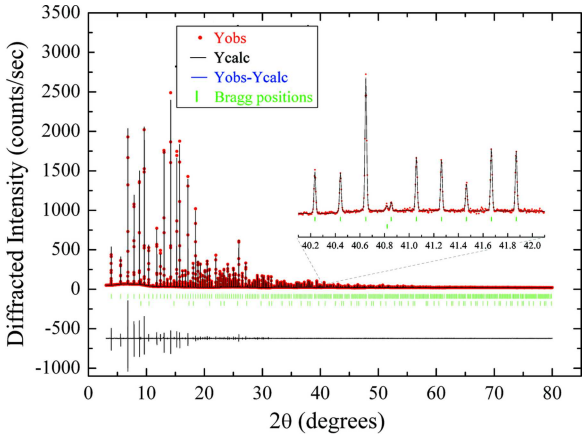


Figure B.2: WPPM of $Na_2Ca_3Al_2F_{14}$ (NAC) using FULLPROF. Reproduced with permission from Bergamaschi et al., 2010[8]. Copyright IUCr Journals.

Capillary diameter, d = 0.2 mm
E = 25 keV, acquisition time = 120 s
Profile = TCH-PV (Npr=7 for FULLPROF)
χ^2 (WPPM) = 1.1
Estimated grain size ∼ 1.3 - 1.4 μm [297]

	NAC	CaF_2
λ (Å)	0.495747	0.495747
2θ Zero-error	0.02167	0.02167
U	0.001487	0.005221
V	-0.000266	-0.000841
W	0.000109	0.000057
X	0.006916	0.000039
Y	0.000025	0.000025
S/L	0.00300	0.00300
D/L	0.01190	0.01190

Table B.2: NAC refinement values[8]

NAC is not a NIST standard reference material, hence, starting parameters taken from [298]. Known impurity: CaF_2.[8]

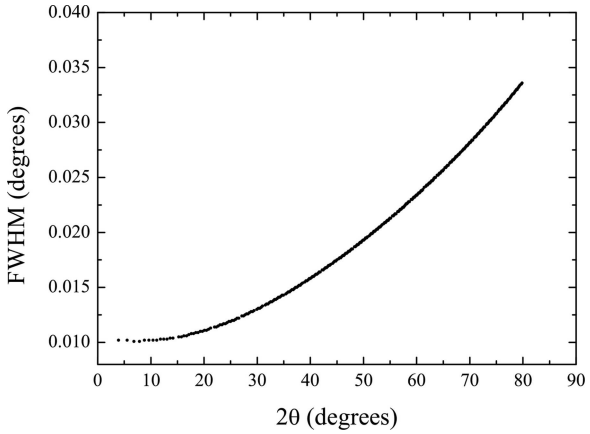


Figure B.3: IRF measured using NAC for a 0.2 mm capillary at 25 keV[8]

So, in order to start with microstructural analysis, one should have this IRF file (*FWHM* vs 2θ), specific to the instrument. Providing FULLPROF with this information, allows it to estimate the

*All samples were mounted in *Lindemann* capillaries and spun at a frequency of 10 hz in Debye-Scherrer (Transmission) Geometry.

instrumental broadening and subtract it from the total peak broadening to calculate apparent size and strain parameters.

B.2 Format of the *.irf file

Some sample `.irf` files are provided in with the `FULLPROF` download. The path for Windows systems should be `C:\FullProf_Suite\IRF_Files`. The format of one of these files is shown in Fig.B.4.

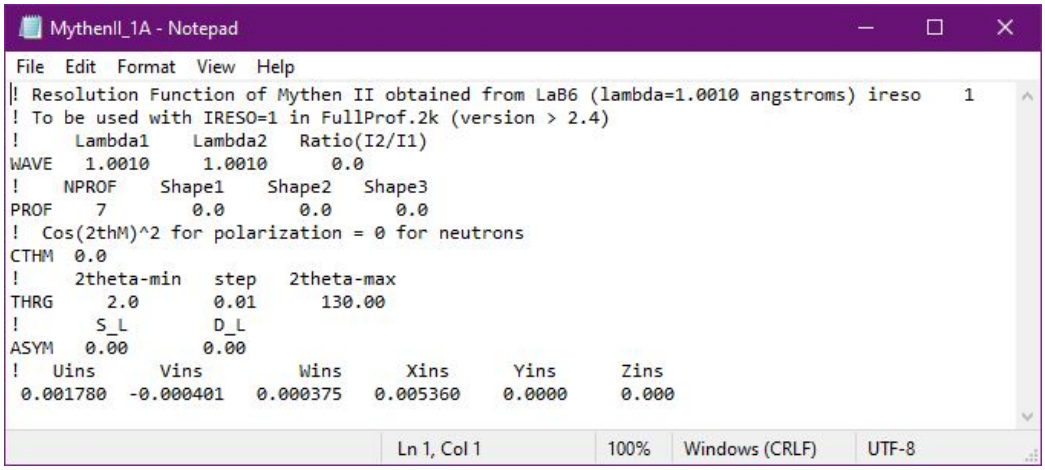


Figure B.4: Format of `.irf` files provided in `FullProf_Suite` folder

It is also possible to create your own `.irf` files which is a list of peak positions (2θ), the Gaussian contribution H_G, and the Lorentzian contribution H_L from the instrument, if you have collected a pattern for a standard sample like NAC or LaB_6 on it. The format of such a file generated using the `WinPLOTR` module of `FULLPROF` is shown in Fig. B.6. To do this, you open the pattern file (`.dat`) and zoom into well-resolved and strong intensity peaks, over a 2θ range of $\sim$100° and then navigate to `Calculations>>Profile Fitting`. With this, the plot frame becomes active for peak selection. The first and second clicks are for the left and the right edge of the FWHM, respectively - a line will form on between the two points to show this. The third click marks the height of the peak. Each peak included in the profile fitting is defined by these three clicks and you continue to do this until a reasonable number of peaks has been identified. It is advisable to select the strongest reflections over the widest angular range in the pattern, to minimise the resolution errors. Once done, a right-click on the mouse will bring you back to the profile-fitting dialogue box which looks like Fig. B.5

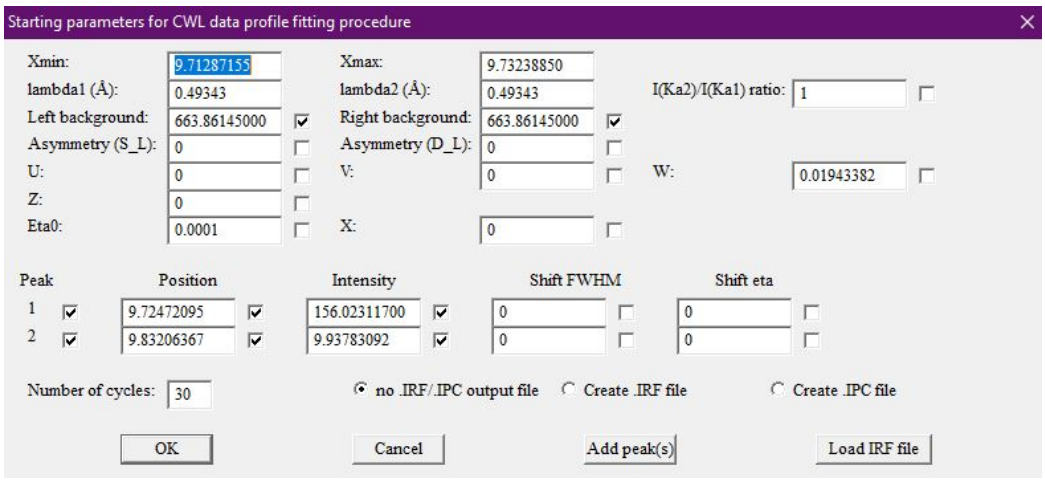


Figure B.5: Profile fitting dialogue box in `WinPLOTR` for manually creating an IRF file

Selecting `Create .IRF file` and the pressing `OK` generates an `.irf` file that looks like Fig. B.6

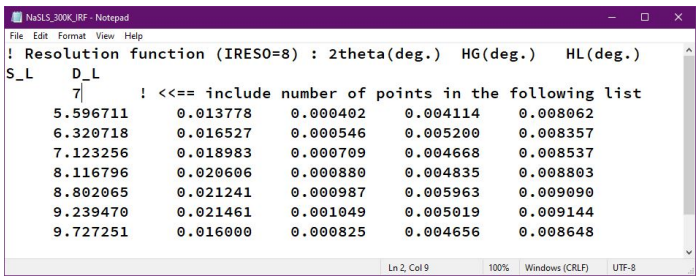


Figure B.6: Format of `.irf` file generated using `WinPLOTR`

This file can then be used as an input in the `.pcr` file for the refinement. One must we aware that when using an IRF file, only the strain and size parameters (U, I_G, X, YD_{ST}, ξ and $F(S_Z)$) should be varied since the instrumental broadening is calculated according to the input IRF file.

B.2.1 Profile functions in FULLPROF and calculation of Size and Strain

A normalized Gaussian function,

$$G(x) = a_G\, exp(-b_G\, x^2) \quad \text{with} \quad a_G = \frac{2}{H}\sqrt{\frac{ln2}{\pi}} \quad \text{and} \quad b_G = \frac{4ln2}{H^2}$$

The Gaussian integral breadth,

$$\beta_G = \frac{1}{a_G} = \frac{H}{2}\sqrt{\frac{\pi}{ln2}}$$

A normalized Lorentzian function,

$$L(x) = \frac{a_L}{1 + b_L x^2} \quad \text{with} \quad a_L = \frac{2}{\pi H} \quad \text{and} \quad b_L = \frac{4}{H^2}$$

Lorentzian integral breadth,

$$\beta_L = \frac{1}{a_L} = \frac{\pi H}{2}$$

A Voigt function is a convolution of a Gaussian and a Lorentzian, defined as:

$$V(x) = L(x) \otimes G(x) = \int_{-\infty}^{+\infty} L(x-u)G(u)du$$

It can be written in terms of the individual Gaussian and Lorentzian FWHMs (H_G, H_L) or integral breadths (β_G, β_L) as

$$V(x) = V(x, H_L, H_G) = V(x, \beta_G, \beta_L) = \frac{1}{\beta_G} \mathrm{Re}\left[erf\left(\frac{\sqrt{\pi}}{\beta_G}|x| + i\frac{\beta_L}{\beta_G\sqrt{\pi}} \right) \right]$$

where

$$erf(x) = \frac{2}{\sqrt{\pi}} \int_0^x e^{-t^2} dt$$

is the complex error function.

Pseudo-Voigt function approximates $V(x)$ by converting the individual FWHMs (H_L, H_G) into one FWHM (H) and one mixing parameter η so that

$$pV(x) = \eta L'(x) + (1-\eta)G'(x) = pV(x, \eta, H) \qquad 0 \leq \eta \leq 1$$

Now $pV(x)$, $L'(x)$ and $G'(x)$ all have the same FWHM (H)

Pseudo-Voigt integral breadth,

$$\beta_{pV} = \frac{\int \Omega(x)dx}{\Omega(0)} = \frac{1}{pV(0)} = \frac{\pi H/2}{\eta + (1-\eta)\sqrt{\pi ln2}}$$

The TCH-PV (Thompson-Cox-Hastings Pseudo-Voigt) profile function (`Npr=7`)[299] is a must if physically significant microstructure information is to be obtained from the data. It mimics $V(x)$

and includes Finger's treatment[294] of the axial divergence. `FULLPROF` uses the integral breadth method to obtain a volume average of sizes and strains and outputs a microstructural file (`*.mic`) containing analysis of size and strain contribution to each reflection.

The independent Gaussian and Lorentzian FWHMs (H_G, H_L) for `Npr=7` is calculated by the following expressions:

$$H_G^2 = [U + (1-\xi^2)\cdot D_{ST}^2]\, tan^2\theta + V tan\theta + W + \frac{I_G}{cos^2\theta}$$

and

$$H_L = (X + \xi \cdot D_{ST})\, tan\theta + \frac{Y + F(S_Z)}{cos\theta}$$

where U, V, W are the Caglioti parameters[293]

The TCH expressions provide for a mapping between (H_L, H_G) and (H, η) by numerical approximation as follows:

$$(H, \eta) = F(H_G, H_L)$$

$$H^5 = H_G^5 + 2.69269\, H_G^4 H_L + 2.42843\, H_G^3 H_L^2 + 4.47163\, H_G^2 H_L^3 + 0.07842\, H_G H_L^4 + H_L^5$$

$$\eta = 1.36603 \left(\frac{H_L}{H}\right) - 0.47719 \left(\frac{H_L}{H}\right)^2 + 0.11116 \left(\frac{H_L}{H}\right)^3$$

Inverting the above relations gives:

$$(H_G, H_L) = F^{-1}(H, \eta)$$

$$\frac{H_L}{H} = 0.72928\,\eta + 0.19289\,\eta^2 + 0.07783\,\eta^3$$

$$\frac{H_G}{H} = \sqrt{1 - 0.74417\,\eta - 0.24781\,\eta^2 - 0.0081\,\eta^3}$$

The Lorentzian and Gaussian contributions of size and microstrains are represented by the following tabulated parameters:

	Isotropic		Anisotropic	
	Gaussian	Lorentzian	Gaussian	Lorentzian
Strain	U	X	D_{ST}	ξ
Size	I_G	Y	$\times$	$F(S_Z)$

Table B.3: Size and microstrain parameters in FULLPROF

The Gaussian and Lorentzian size contribution to the peak width are

$$H_{GS}^2 = \frac{I_G}{cos^2\theta} \qquad \text{and} \qquad H_{LS} = \frac{Y + F(S_Z)}{cos\theta}$$

respectively.

Since a pseudo-Voigt function is a convolution of these two components given as:

$$pV(x) = \eta L(x) + (1-\eta)G(x) \qquad \text{with} \qquad \eta = \eta_0 + X \cdot 2\theta$$

the overall size contribution (H_S) can be written as a function of H_{GS} and H_{LS} as

$$(H_S, \eta_S) = F(H_{GS}, H_{LS})$$

Rewrite $H_S = \frac{Z_S}{cos\theta}$ to get

$$Z_S^5 = \sqrt{I_G}^5 + 2.69269\sqrt{I_G}^4 Y_L + 2.42843\sqrt{I_G}^3 Y_L^2 + 4.47163\sqrt{I_G}^2 Y_L^3 + 0.07842\sqrt{I_G} Y_L^4 + Y_L^5$$

and

$$\eta_S = 1.36603\left(\frac{Y_L}{Z_S}\right) - 0.47719\left(\frac{Y_L}{Z_S}\right)^2 + 0.11116\left(\frac{Y_L}{Z_S}\right)^3$$

which then give the integral breadth for a normalized pseudo-Voigt function, β_{pV}, corresponding to size effects :

$$\beta_{pV}\,(Size) = \frac{\pi\,(Z_S/2)}{\eta_S + (1-\eta_S)\sqrt{\pi ln 2}} \cdot \frac{\pi}{180} \cdot \frac{1}{cos\theta} \quad \text{(radians)}$$

The refined parameters in FULLPROF relevant for this calculation are `(GauSiz, Y, LorSiz)`

which are related to Z_S and η_S through I_G and Y_L as:

$$I_G = \texttt{GauSiz} \qquad \text{and} \qquad Y_L = \texttt{Y} + \texttt{LorSiz}$$

Equating the expression obtained for β_{pV} $(Size)$ to the Scherrer formula:

$$\frac{\lambda}{D_h\, cos\theta} = \frac{\pi\,(Z_S/2)}{\eta_S + (1-\eta_S)\sqrt{\pi ln2}} \cdot \frac{\pi}{180} \cdot \frac{1}{cos\theta}$$

gives the apparent size D_h

$$D_h = \frac{\eta_S + (1-\eta_S)\sqrt{\pi ln2}}{Z_S} \cdot \frac{360\lambda}{\pi^2}$$

Anisotropic contributions: D_{ST} and $F(S_Z)$

For calculating these functions, FULLPROF contains the following set of micro-structural models:

For Size:

Only the Lorentzian component is considered for anisotropic size broadening via $F(S_Z)$.

For `STR = 0` $\rightarrow$ `IsizeModel` $\neq 0$

For `STR > 1` $\rightarrow$ generalized formulation of the size effect (up to six) size parameters given in line 11-14 of pcr file.

$$F(S_Z) = F(S_{z1}, S_{z2}, ..., S_{z6}) = \frac{360\lambda}{\pi^2} \cdot d^2_{hkl} \cdot \zeta(S_{z1}, S_{z2}, ..., S_{z6}) \qquad \text{and}$$

$$\zeta = S_{z1}h^2 + S_{z2}k^2 + S_{z3}l^2 + S_{z4}kl + S_{z5}hl + S_{z6}hk$$

where the size parameters are $S_{z1}, S_{z2}, ..., S_{z6}$.

This formulation assumes that the average diameter can be expressed as an ellipsoid of refinable parameters $S_{z1}, S_{z2}, ..., S_{z6}$. Thus

$$d_{avg} = d_{hkl} \cdot \zeta(S_{z1}, S_{z2}, ..., S_{z6})$$

Size-Model #	Model
1	*Platelet coherent domains.* $F(S_Z) = S_Z \cdot cos\varphi$ $S_Z \rightarrow$ refined parameter, $\varphi \rightarrow$ acute angle between the scattering vector hkl and the vector defining the platelet shape of domains $[S_{z1}, S_{z2}, S_{z3}]$ in line 11-9 of pcr file
-1	*Needle-like coherent domains.* $F(S_Z) = S_Z \cdot sin\varphi$ $S_Z \rightarrow$ refined parameter, $\varphi \rightarrow$ acute angle between the scattering vector hkl and the vector defining the needle shape of domains $[S_{z1}, S_{z2}, S_{z3}]$ in line 11-9 of pcr file
2 to 7	Broadening only considered for reflections: $(00l)$, $(0k0)$, $(h00)$, $(hk0)$, $(h0l)$ and $(0kl)$ $F(S_Z) = S_Z$
8	Only satellite reflections broadened. $F(S_Z) = S_Z$
9	Only reflections (hkl) with $h = 2n + 1$ and $k = 2m + 1$ broadened. $F(S_Z) = S_Z$
10	Only reflections $(h0l)$ with $h + l = 2$ broadened. $F(S_Z) = S_Z$
11	All reflections (hkl) except (hhl) are broadened. $F(S_Z) = S_Z$
12	All reflections (hkl) with $h = 2n + 1$ are broadened. $F(S_Z) = S_Z$
13	All reflections (hkl) with $h = 2n$ and $k = 2m + 1$ are broadened. $F(S_Z) = S_Z$

Table B.4: Models for Anisotropic Size broadening

For Strain:

Only the Gaussian component is considered for anisotropic size broadening via D_{ST}(STR).

For STR = 0 $\rightarrow$ IstrainModel $\neq 0$

$$(FWHM)_{strain} = D_{ST}\, tan\theta = c \left(\frac{\Sigma(\frac{1}{d^2})}{\frac{1}{d^2}} \right) tan\theta$$

$$c = 2\sqrt{Ln2}\left(\frac{180}{\pi}\right)$$

Effective values used in program = $c \times 10^{-3}$

Thus, refined strain parameters must be divided by 1000[300].

Strain-Model #	Model
1	*Orthorhombic strain in a tetragonal lattice.* Refined $\rightarrow$ only STR1
2	*Strain along "a" in an orthorhombic lattice.* Refined $\rightarrow$ only STR1
3	*Strain along a diagonal of the ab plane in an orthorhombic lattice for which an equivalent monoclinic double cell has been used.* Refined $\rightarrow$ only STR1
4	*Same as 3 but strains along the two diagonals.* Refined $\rightarrow$ STR1, STR2
5	*Strain in an orthorhombic lattice with fluctuations along "a" and "b" and correlation between "a" and "b".* Refined $\rightarrow$ STR1, STR2, STR3
6	*Strain in an orthorhombic lattice with fluctuations along "a", "b" and "c" and corr(a,b)=-1, corr(a,c)=1, and corr(b,c)=0.* Refined $\rightarrow$ STR1, STR2, STR3

Strain-Model #	Model
7	*Uniaxial microstrain.* $D_{STR} = STR1 \cdot cos\varphi$ Refined → STR1 φ → angle between the scattering vector (h,k,l) and the vector defining the axial direction of strain (Str1, Str2, Str3)
8	*General anisotropic strain of hexagonal symmetry.*[300] $STR1 = S_{aa} = Sigma(A),\ STR2 = S_{cc} = Sigma(C),\ STR3 = S_{ac} = Correl(A, C)$ $\left(\frac{1}{d^2}\right) = S_Q = A(h^2 + k^2 + hk) + Cl^2 = Am^2 + Cl^2$ $Var(S_Q) = S_{aa}^2 m^2 + S_{cc}^2 l^4 + 2S_{aa}S_{cc}C_{ac}ml^2$ $FWHM^2(strain) = Var(S_Q)\left(\frac{P}{S_Q}\right)^2$ $P = \left(\frac{180}{\pi}\right) \cdot \sqrt{8ln2}\left(\frac{tan\theta}{1000}\right)$
9	*Strain adapted for compounds $LaNi_5$-like*[301] **4 parameters:** $FWHM(Gaussian) = \sqrt{Sum_j(S(j))}\, tan\theta$ STR1 → S(1) = × Par(1) STR2 → S(2) = $\frac{l^4}{(h^2+k^2+l^2)}$ × Par(2) STR3 → S(3) = $\frac{(h^2k^2+k^2l^2}{(h^2+k^2+l^2)}$ × Par(3) STR4 → S(2) = $\frac{h^2k^2}{(h^2+k^2+l^2)}$ × Par(4)
10	*General anisotropic strain for orthorhombic symmetry*[300] **6 strain parameters:** $STR1 = S_{aa} = Sigma(A)\quad STR2 = S_{bb} = Sigma(B)\quad STR3 = S_{cc} = Sigma(C)$ $STR4 = C_{ab} = Corr(A, B)\quad STR5 = C_{ac} = Corr(A, C)\quad STR6 = C_{bc} = Corr(B, C)$ $S_Q = A\,h^2 + B\,k^2 + C\,l^2$ and $Var(S_Q) = S_{aa}^2 h^4 + S_{bb}^2 k^4 + S_{cc}^2 l^4 + 2S_{aa}S_{bb}C_{ab}h^2k^2 + 2S_{aa}S_{cc}C_{ac}h^2l^2 + 2S_{bb}S_{cc}C_{bc}k^2l^2$ $FWHM^2 = Var(S_Q)(\frac{P}{S_Q})^2$ $P = \frac{180}{\pi}\sqrt{8ln2}\left(\frac{tan\theta}{1000}\right)$

Strain-Model #	Model
11	*General anisotropic strain for monoclinic symmetry being the setting $\gamma \neq 0$: 2-fold axis along (001)*[300] (limited to 8 parameters by putting arbitrarily zero two correlation values ($C_{ad} = C_{bd} = 0$)) **8 strain parameters:** $STR1 = S_{aa} = Sigma(A)$ $STR2 = S_{bb} = Sigma(B)$ $STR3 = S_{cc} = Sigma(C)$ $STR4 = S_{dd} = Sigma(D)$ $STR5 = C_{ab} = Corr(A,B)$ $STR6 = C_{ac} = Corr(A,C)$ $STR7 = C_{bc} = Corr(B,C)$ $STR7 = C_{cd} = Corr(C,D)$ $S_Q = A\,h^2 + B\,k^2 + C\,l^2 + Dhk$ and $Var(S_Q) = S_{aa}^2 h^4 + S_{bb}^2 k^4 + S_{cc}^2 l^4 + 2S_{aa}S_{bb}C_{ab}h^2k^2 + 2S_{aa}S_{cc}C_{ac}h^2l^2 + 2S_{bb}S_{cc}C_{bc}k^2l^2$ $FWHM^2 = Var(S_Q)(\frac{P}{S_Q})^2$ $P = \frac{180}{\pi}\sqrt{8ln2}\left(\frac{tan\theta}{1000}\right)$

Table B.8: Models for Anisotropic Strain broadening

For `ISTR=1,3` $\rightarrow$ Generalized formulation of the strain broadening $\rightarrow$ **10 parameters**[300].

The strain parameters correspond to the fluctuations and correlations of direct cell parameters.

The lower symmetry is monoclinic with the conventional setting.

The hexagonal lattice is treated as a special case.

Strain parameters:

$$P_x = sigma(x) \qquad x,y = a,b,c,\beta \qquad corr(x,y) = sin(P_{xy})$$

$$P_{xy} \rightarrow \text{angle } (^\circ) \quad ; \quad corr(x,y) = \frac{covar(x,y)}{(sigma(x)\cdot sigma(y))} \in [-1,1].$$

The strain parameters read in the following order: $P_a, P_b, P_c, P_\beta, P_{ab}, P_{ac}, P_{a\beta}, P_{bc}, P_{b\beta}, P_{c\beta}$

NOTE:

In some cases, when the program uses size-strain options, the computing time is greatly increased. This is related to the fact that the number of reflections contributing to each particular point of the diagram increases because the broadening is quite important. An excessive computing time may indicate a divergence of the refinement that has attributed a too large FWHM to some reflections.

Bibliography

[1] A. M. Glazer, Acta Crystallographica Section B **28**, 3384 (1972), URL https://doi.org/10.1107/S0567740872007976.

[2] K. Dey, Ph.D. thesis, Indian Institute of Science Education and Research, Pune, India (2016).

[3] J. Kumar, K. Dey, S. N. Panja, and S. Nair, Journal of Physics: Condensed Matter **34**, 465401 (2022), URL https://dx.doi.org/10.1088/1361-648X/ac8f7c.

[4] A. Kumar, P. Manuel, and S. Nair, Physical Review Materials **8**, 024405 (2024).

[5] G. Ódor, Reviews of modern physics **76**, 663 (2004).

[6] C. J. Bradley and A. P. Cracknell, *The Mathematical Theory of Symmetry in Solids* (Clarendon Press, Oxford, 1972).

[7] While the *Jones faithful representations* conventionally correspond to the vector formed from the operation of the rotation part of the element, R, on the site coordinates $(x,\ y,\ z)$, here we use it to demonstrate the effect of the complete symmetry operator, g.

[8] A. Bergamaschi, A. Cervellino, R. Dinapoli, F. Gozzo, B. Henrich, I. Johnson, P. Kraft, A. Mozzanica, B. Schmitt, and X. Shi, Journal of synchrotron radiation **17**, 653 (2010), URL https://journals.iucr.org/s/issues/2010/05/00/gf5028/gf5028.pdf.

[9] A. A. Belik, Dalton Transactions **47**, 3209 (2018).

[10] High Energy Accelerator Research Organization (KEK) - Institute of Materials Science Structure (IMSS), *Beamlines of Photon Factory*, URL https://www2.kek.jp/imss/pf/eng/apparatus/bl/.

[11] Saha Institute of Nuclear Phyics, *Low Temperature Powder Diffraction at Photon Factory*, URL https://www.saha.ac.in/web/home-photon-factory/powder-diffraction-at-lt.

[12] P. Willmott, D. Meister, S. Leake, M. Lange, A. Bergamaschi, M. Böge, M. Calvi, C. Cancellieri, N. Casati, A. Cervellino, et al., Journal of synchrotron radiation **20**, 667 (2013).

[13] Science and U. Technology Facilities Council (STFC), *Materials to help you talk about ISIS*, URL https://www.isis.stfc.ac.uk/Pages/Things-to-help-you-talk-about-ISIS.aspx.

[14] C. Ltd., *Cryogen-free measurement system (cfms) brochure*, URL https://cryogenic.co.uk/sites/default/files/product_files/cryogenic_cfms_brochure_v5.0_may_2020_compressed_5.pdf.

[15] Novocontrol Technologies GmbH, *Alpha-A High Resolution Dielectric, Conductivity, Impedance and Gain Phase Modular Measurement System User's Manual*.

[16] Stanford Research Systems, *MODEL SR830 DSP Lock-In Amplifier User's Manual* (2011), URL https://www.thinksrs.com/downloads/pdfs/manuals/SR830m.pdf.

[17] Stanford Research Systems, *MODEL SR570 Low-Noise Current Preamplifier User's Manual* (2015), URL https://www.thinksrs.com/downloads/pdfs/manuals/SR570m.pdf.

[18] Stanford Research Systems, URL https://www.thinksrs.com/products/sr570.html.

[19] E. Vincent, Nature Physics **19**, 926 (2023).

[20] J. Rodriguez-Carvajal, in *satellite meeting on powder diffraction of the XV congress of the IUCr* (Toulouse, France, 1990), vol. 127.

[21] Y. Tokiwa, M. Mchalwat, R. S. Perry, and P. Gegenwart, Phys. Rev. Lett. **116**, 226402 (2016), URL https://link.aps.org/doi/10.1103/PhysRevLett.116.226402.

[22] Y. Maeno, S. Yonezawa, and A. Ramires, *Still mystery after all these years – unconventional superconductivity of sr2ruo4* (2024), 2402.12117, URL https://arxiv.org/abs/2402.12117.

[23] O. Fedchenko, J. Minár, A. Akashdeep, S. W. D'Souza, D. Vasilyev, O. Tkach, L. Odenbreit, Q. Nguyen, D. Kutnyakhov, N. Wind, et al., Science advances **10**, eadj4883 (2024).

[24] S. Maekawa, T. Tohyama, S. E. Barnes, S. Ishihara, W. Koshibae, and G. Khaliullin, *Physics of transition metal oxides*, vol. 144 (Springer Science & Business Media, 2013).

[25] A. Fert, M. Chshiev, A. Thiaville, and H. Yang, Journal of the Physical Society of Japan **92**, 081001 (2023).

[26] A. J. Lee, A. S. Ahmed, J. Flores, S. Guo, B. Wang, N. Bagués, D. W. McComb, and F. Yang, Physical Review Letters **124**, 107201 (2020).

[27] D. Bercioux and P. Lucignano, Reports on Progress in Physics **78**, 106001 (2015).

[28] J. Van Vleck, *The Theory of Electric and Magnetic Susceptibilities*, International series of monographs on physics (Clarendon Press, 1932), URL https://books.google.co.in/books?id=yaBh6WVYLgwC.

[29] P. A. M. Dirac and R. H. Fowler, Proceedings of the Royal Society of London. Series A, Containing Papers of a Mathematical and Physical Character **112**, 661 (1926), URL https://royalsocietypublishing.org/doi/abs/10.1098/rspa.1926.0133.

[30] W. Heisenberg, Zeitschrift für Physik **38**, 411 (1926).

[31] M. Kato, S. Harada, M. Fukatsu, and K. Hirota, in *Journal of Physics: Conference Series* (IOP Publishing, 2011), vol. 273, p. 012152.

[32] S. Streltsov, I. Mazin, and K. Foyevtsova, Physical Review B **92**, 134408 (2015).

[33] H.-L. Huang and H.-T. Jeng, Scientific Reports **10**, 7089 (2020).

[34] M. Hossain, B. Bohnenbuck, Y. Chuang, M. Haverkort, I. Elfimov, A. Tanaka, A. Cruz Gonzalez, Z. Hu, H.-J. Lin, C. Chen, et al., Physical Review B—Condensed Matter and Materials Physics **86**, 041102 (2012).

[35] J. Lee, Y. Lee, T. Noh, S. Nakatsuji, H. Fukazawa, R. Perry, Y. Maeno, Y. Yoshida, S. Ikeda, J. Yu, et al., Physical Review B—Condensed Matter and Materials Physics **70**, 085103 (2004).

[36] S. Riegg, S. Widmann, B. Meir, S. Sterz, A. Günther, N. Büttgen, S. G. Ebbinghaus, A. Reller, H.-A. K. von Nidda, and A. Loidl, Physical Review B **93**, 115149 (2016).

[37] J. Kim, M. Daghofer, A. Said, T. Gog, J. Van den Brink, G. Khaliullin, and B. Kim, Nature communications **5**, 4453 (2014).

[38] J. B. Goodenough, Phys. Rev. **100**, 564 (1955), URL https://link.aps.org/doi/10.1103/PhysRev.100.564.

[39] J. Kanamori, Journal of Physics and Chemistry of Solids **10**, 87 (1959), ISSN 0022-3697, URL https://www.sciencedirect.com/science/article/pii/0022369759900617.

[40] C. Zener, Phys. Rev. **82**, 403 (1951), URL https://link.aps.org/doi/10.1103/PhysRev.82.403.

[41] P. W. Anderson, Physical Review **102**, 1008 (1956).

[42] K. Kitagawa, T. Takayama, Y. Matsumoto, A. Kato, R. Takano, Y. Kishimoto, S. Bette, R. Dinnebier, G. Jackeli, and H. Takagi, Nature **554**, 341 (2018).

[43] W.-H. Kao, J. Knolle, G. B. Halász, R. Moessner, and N. B. Perkins, Physical Review X **11**, 011034 (2021).

[44] H. Yao, L. Tanzi, L. Sanchez-Palencia, T. Giamarchi, G. Modugno, and C. D'Errico, Phys. Rev. Lett. **133**, 123401 (2024), URL https://link.aps.org/doi/10.1103/PhysRevLett.133.123401.

[45] A. A. Patel, H. Guo, I. Esterlis, and S. Sachdev, Science **381**, 790 (2023), URL https://www.science.org/doi/abs/10.1126/science.abq6011.

[46] A. S. Bhalla, R. Guo, and R. Roy, Materials research innovations **4**, 3 (2000).

[47] N.-G. Park, Materials today **18**, 65 (2015).

[48] R. Cava, B. Batlogg, J. Krajewski, R. Farrow, L. Rupp Jr, A. White, K. Short, W. Peck, and T. Kometani, nature **332**, 814 (1988).

[49] J. Goodenough, W. Gräper, F. Holtzberg, D. Huber, R. Lefever, J. Longo, T. McGuire, and S. Methfessel, *Magnetic and other properties of oxides and related compounds* (Springer, 1970).

[50] H. Yamamoto, O. Ikeda, T. Honda, K. Kimura, T. Aoyama, K. Ohgushi, A. Suzuki, K. Ishii, D. Matsumura, T. Tsuji, et al., Phys. Rev. Mater. **8**, 094402 (2024), URL https://link.aps.org/doi/10.1103/PhysRevMaterials.8.094402.

[51] S.-W. Cheong and M. Mostovoy, Nature Materials **6**, 13 (2007), ISSN 1476-4660, URL https://doi.org/10.1038/nmat1804.

[52] S. Vasala and M. Karppinen, Progress in Solid State Chemistry **43**, 1 (2015), URL https://www.sciencedirect.com/science/article/pii/S0079678614000338?via%3Dihub.

[53] C. J. Howard and H. T. Stokes, Acta Crystallographica Section B: Structural Science **54**, 782 (1998).

[54] C. J. Howard, B. J. Kennedy, and P. M. Woodward, Acta Crystallographica Section B: Structural Science **59**, 463 (2003).

[55] C. J. Howard and Z. Zhang, Acta Crystallographica Section B: Structural Science **60**, 249 (2004).

[56] B. F. Grosso and N. A. Spaldin, Phys. Rev. Mater. **5**, 054403 (2021), URL https://link.aps.org/doi/10.1103/PhysRevMaterials.5.054403.

[57] C.-Q. Jin, J.-S. Zhou, J. Goodenough, Q. Liu, J. Zhao, L. Yang, Y. Yu, R. Yu, T. Katsura, A. Shatskiy, et al., Proceedings of the National Academy of Sciences **105**, 7115 (2008).

[58] H. Seung-Tae and A. W. Sleight, Journal of Solid State Chemistry **128**, 251 (1997).

[59] J. Zhao, L. Yang, Y. Yu, F. Li, R. Yu, Z. Fang, L. Chen, and C. Jin, Journal of Solid State Chemistry **180**, 2816 (2007).

[60] P. C. Donohue, L. Katz, and R. Ward, Inorganic Chemistry **4**, 306 (1965).

[61] D. Sarma, Current Opinion in Solid State and Materials Science **5**, 261 (2001), ISSN 1359-0286, URL https://www.sciencedirect.com/science/article/pii/S1359028601000146.

[62] D. Serrate, J. De Teresa, and M. Ibarra, Journal of Physics: Condensed Matter **19**, 023201 (2006).

[63] C. Meneghini, S. Ray, F. Liscio, F. Bardelli, S. Mobilio, and D. Sarma, Physical Review Letters **103**, 046403 (2009).

[64] P. M. Woodward, *Structural distortions, phase transitions, and cation ordering in the perovskite and tungsten trioxide structures* (Oregon State University, 1997).

[65] D. Cox and A. Sleight, Acta Crystallographica Section B: Structural Crystallography and Crystal Chemistry **35**, 1 (1979).

[66] J. Alonso, J. García-Muñoz, M. Fernández-Díaz, M. Aranda, M. Martínez-Lope, and M. Casais, Physical Review Letters **82**, 3871 (1999).

[67] P. Woodward, D. Cox, E. Moshopoulou, A. Sleight, and S. Morimoto, Physical Review B **62**, 844 (2000).

[68] R. K. Sahu and S. S. Manoharan, Journal of applied physics **92**, 4831 (2002).

[69] R. A. Ricciardo, H. L. Cuthbert, P. M. Woodward, Q. Zhou, B. J. Kennedy, Z. Zhang, M. Avdeev, and L.-Y. Jang, Chemistry of Materials **22**, 3369 (2010).

[70] M. Retuerto, F. Jiménez-Villacorta, M. Martínez-Lope, Y. Huttel, E. Roman, M. Fernández-Díaz, and J. Alonso, Physical Chemistry Chemical Physics **12**, 13616 (2010).

[71] C. Sakai, Y. Doi, Y. Hinatsu, and K. Ohoyama, Journal of Physics: Condensed Matter **17**, 7383 (2005).

[72] N. T. Taylor, F. H. Davies, S. G. Davies, C. J. Price, and S. P. Hepplestone, Advanced Materials **31**, 1904746 (2019).

[73] W. Liu, K. Kawano, M. Kamiko, Y. Kato, Y. Okazaki, I. Yamada, and S. Yagi, Small **18**, 2202439 (2022), https://onlinelibrary.wiley.com/doi/pdf/10.1002/smll.

202202439, URL https://onlinelibrary.wiley.com/doi/abs/10.1002/smll.202202439.

[74] A. Poddar, S. Das, and B. Chattopadhyay, Journal of applied physics **95**, 6261 (2004).

[75] K.-I. Kobayashi, T. Kimura, H. Sawada, K. Terakura, and Y. Tokura, Nature **395**, 677 (1998).

[76] L. T. Nguyen, T. Halloran, W. Xie, T. Kong, C. L. Broholm, and R. J. Cava, Phys. Rev. Mater. **2**, 054414 (2018), URL https://link.aps.org/doi/10.1103/PhysRevMaterials.2.054414.

[77] P. Battle, G. Blake, T. Gibb, and J. Vente, Journal of Solid State Chemistry **145**, 541 (1999).

[78] A. Dos santos García, C. Ritter, E. Solana-Madruga, and R. Sáez-Puche, Journal of Physics: Condensed Matter **25**, 206004 (2013).

[79] S. A. Kimber, M. S. Senn, S. Fratini, H. Wu, A. H. Hill, P. Manuel, J. P. Attfield, D. N. Argyriou, and P. F. Henry, Physical Review Letters **108**, 1 (2012), ISSN 00319007, URL https://journals.aps.org/prl/abstract/10.1103/PhysRevLett.108.217205.

[80] H. Samata, M. Kai, T. Uchida, M. Ohtsuka, G. Tanaka, S. Sawada, T. Taniguchi, and Y. Nagata, Journal of alloys and compounds **350**, 77 (2003).

[81] G. Cao, T. Qi, L. Li, J. Terzic, S. Yuan, L. E. DeLong, G. Murthy, and R. K. Kaul, Physical review letters **112**, 056402 (2014).

[82] M. d. C. Viola, M. Martinez-Lope, J. Alonso, P. Velasco, J. Martínez, J. Pedregosa, R. Carbonio, and M. Fernández-Díaz, Chemistry of materials **14**, 812 (2002).

[83] R. Morrow, R. Mishra, O. D. Restrepo, M. R. Ball, W. Windl, S. Wurmehl, U. Stockert, B. Büchner, and P. M. Woodward, Journal of the American Chemical Society **135**, 18824 (2013).

[84] S. Yáñez-Vilar, E. Mun, V. Zapf, B. Ueland, J. S. Gardner, J. Thompson, J. Singleton, M. Sánchez-Andújar, J. Mira, N. Biskup, et al., Physical Review B—Condensed Matter and Materials Physics **84**, 134427 (2011).

[85] J. Hwang, E. S. Choi, F. Ye, C. R. Dela Cruz, Y. Xin, H. D. Zhou, and P. Schlottmann, Phys. Rev. Lett. **109**, 257205 (2012), URL https://link.aps.org/doi/10.1103/PhysRevLett.109.257205.

[86] A. A. Aczel, D. Bugaris, L. Li, J.-Q. Yan, C. De la Cruz, H.-C. Zur Loye, and S. E. Nagler, Physical Review B—Condensed Matter and Materials Physics **87**, 014435 (2013).

[87] S. Vasala, J.-G. Cheng, H. Yamauchi, J. Goodenough, and M. Karppinen, Chemistry of Materials **24**, 2764 (2012).

[88] S. Vasala, H. Saadaoui, E. Morenzoni, O. Chmaissem, T.-S. Chan, J.-M. Chen, Y.-Y. Hsu, H. Yamauchi, and M. Karppinen, Physical Review B **89**, 134419 (2014).

[89] I. Raevski, S. Kubrin, S. Raevskaya, V. Titov, D. Sarychev, M. Malitskaya, I. Zakharchenko, and S. Prosandeev, Physical Review B—Condensed Matter and Materials Physics **80**, 024108 (2009).

[90] Y. Maeno, S. Kittaka, T. Nomura, S. Yonezawa, and K. Ishida, Journal of the Physical Society of Japan **81**, 011009 (2011), URL https://journals.jps.jp/doi/abs/10.1143/JPSJ.81.011009.

[91] H. Suzuki, L. Wang, J. Bertinshaw, H. U. R. Strand, S. Käser, M. Krautloher, Z. Yang, N. Wentzell, O. Parcollet, F. Jerzembeck, et al., Nature Communications **14**, 7042 (2023), ISSN 2041-1723, URL https://doi.org/10.1038/s41467-023-42804-3.

[92] H. Suzuki, H. Gretarsson, H. Ishikawa, K. Ueda, Z. Yang, H. Liu, H. Kim, D. Kukusta, A. Yaresko, M. Minola, et al., Nature Materials **18**, 563 (2019), ISSN 1476-4660, URL https://doi.org/10.1038/s41563-019-0327-2.

[93] H. T. Dang, J. Mravlje, A. Georges, and A. J. Millis, Phys. Rev. B **91**, 195149 (2015), URL https://link.aps.org/doi/10.1103/PhysRevB.91.195149.

[94] H.-T. Jeng, S.-H. Lin, and C.-S. Hsue, Phys. Rev. Lett. **97**, 067002 (2006), URL https://link.aps.org/doi/10.1103/PhysRevLett.97.067002.

[95] A. Banerjee, C. Bridges, J.-Q. Yan, A. Aczel, L. Li, M. Stone, G. Granroth, M. Lumsden, Y. Yiu, J. Knolle, et al., Nature materials **15**, 733 (2016), URL https://www.nature.com/articles/nmat4604.

[96] L. J. Sandilands, Y. Tian, K. W. Plumb, Y.-J. Kim, and K. S. Burch, Phys. Rev. Lett. **114**, 147201 (2015), URL https://link.aps.org/doi/10.1103/PhysRevLett.114.147201.

[97] J. P. Attfield, APL Materials **3**, 041510 (2015), ISSN 2166-532X, URL https://doi.org/10.1063/1.4913736.

[98] Y. Horibe, M. Shingu, K. Kurushima, H. Ishibashi, N. Ikeda, K. Kato, Y. Motome, N. Furukawa, S. Mori, and T. Katsufuji, Phys. Rev. Lett. **96**, 086406 (2006), URL https://link.aps.org/doi/10.1103/PhysRevLett.96.086406.

[99] M. S. Senn, A. M. Arevalo-Lopez, T. Saito, Y. Shimakawa, and J. P. Attfield, Journal of Physics: Condensed Matter **25**, 496008 (2013).

[100] T. Kajita, T. Kanzaki, T. Suzuki, J. Kim, K. Kato, M. Takata, and T. Katsufuji, Physical Review B—Condensed Matter and Materials Physics **81**, 060405 (2010).

[101] M. S. Senn, J. P. Wright, and J. P. Attfield, Nature **481**, 173 (2012).

[102] B. Cullity and S. Stock, *Elements of X-ray Diffraction*, Pearson custom library (Pearson Education, 2014), ISBN 9781292040547, URL https://books.google.co.in/books?id=F81wngEACAAJ.

[103] W. H. Bragg and W. L. Bragg, Proceedings of the Royal Society of London. Series A, Containing Papers of a Mathematical and Physical Character **88**, 428 (1913), URL https://royalsocietypublishing.org/doi/abs/10.1098/rspa.1913.0040.

[104] P. Debye and P. Scherrer, Physikalische Zeitschrift **17**, 277 (1916).

[105] A. W. Hull, Physical Review **10**, 661 (1917).

[106] A. Bergamaschi, C. Broennimann, R. Dinapoli, E. E, F. Gozzo, B. Henrich, M. Kobas, P. Kraft, B. Patterson, and B. Schmitt, Nuclear Instruments and Methods in Physics Research Section A: Accelerators, Spectrometers, Detectors and Associated Equipment **591**, 163 (2008).

[107] A. Bergamaschi, A. Cervellino, R. Dinapoli, F. Gozzo, B. Henrich, I. Johnson, P. Kraft, A. Mozzanica, B. Schmitt, and X. Shi, Nuclear Instruments and Methods in Physics Re-

search Section A: Accelerators, Spectrometers, Detectors and Associated Equipment **604**, 136 (2009).

[108] M. Andrä, R. Barten, A. Bergamaschi, M. Brückner, N. Casati, A. Cervellino, S. Chiriotti, R. Dinapoli, E. Fröjdh, D. Greiffenberg, et al., Journal of Instrumentation **14**, C11028 (2019), URL https://dx.doi.org/10.1088/1748-0221/14/11/C11028.

[109] M. Andrä, R. Dinapoli, A. Bergamaschi, R. Barten, M. Brückner, S. Chiriotti Alvarez, E. Fröjdh, D. Greiffenberg, C. Lopez-Cuenca, D. Mezza, et al., Nuclear Instruments and Methods in Physics Research Section A: Accelerators, Spectrometers, Detectors and Associated Equipment **936**, 383 (2019), ISSN 0168-9002, frontier Detectors for Frontier Physics: 14th Pisa Meeting on Advanced Detectors, URL https://www.sciencedirect.com/science/article/pii/S0168900218315729.

[110] A. Bergamaschi, M. Andrä, R. Barten, F. Baruffaldi, M. Brückner, M. Carulla, S. Chiriotti, R. Dinapoli, E. Fröjdh, D. Greiffenberg, et al., Journal of Instrumentation **17**, C11012 (2022), URL https://dx.doi.org/10.1088/1748-0221/17/11/C11012.

[111] L. Brügemann and E. K. Gerndt, Nuclear Instruments and Methods in Physics Research Section A: Accelerators, Spectrometers, Detectors and Associated Equipment **531**, 292 (2004), ISSN 0168-9002, proceedings of the 5th International Workshop on Radiation Imaging Detectors, URL https://www.sciencedirect.com/science/article/pii/S0168900204011842.

[112] C. Broennimann, E. F. Eikenberry, B. Henrich, R. Horisberger, G. Huelsen, E. Pohl, B. Schmitt, C. Schulze-Briese, M. Suzuki, T. Tomizaki, et al., Journal of Synchrotron Radiation **13**, 120 (2006), URL https://doi.org/10.1107/S0909049505038665.

[113] P. S. Institute, *The SINQ Facility*, URL https://www.psi.ch/de/sinq/the-neutron-source.

[114] Paul Scherrer Institute, *DMC Instrument description*, URL https://www.psi.ch/en/sinq/dmc/description.

[115] K. Momma and F. Izumi, J. Appl. Crystallogr **44**, 1272 (2011), URL https://scripts.iucr.org/cgi-bin/paper?db5098.

[116] A. Jain, S. P. Ong, G. Hautier, W. Chen, W. D. Richards, S. Dacek, S. Cholia, D. Gunter, D. Skinner, G. Ceder, et al., APL Materials **1**, 011002 (2013), ISSN 2166532X, URL https://aip.scitation.org/doi/abs/10.1063/1.4812323.

[117] H. M. Rietveld, Journal of applied Crystallography **2**, 65 (1969).

[118] A. C. Larson and R. Von Dreele, Los Alamos National Laboratory: Santa Fe, NM, USA **86** (2004).

[119] B. H. Toby, Journal of applied crystallography **34**, 210 (2001).

[120] A. A. Coelho, Journal of Applied Crystallography **51**, 210 (2018), URL https://doi.org/10.1107/S1600576718000183.

[121] V. Petříček, M. Dušek, and L. Palatinus, Zeitschrift für Kristallographie - Crystalline Materials **229**, 345 (2014), URL https://doi.org/10.1515/zkri-2014-1737.

[122] F. Izumi, The Rigaku Journal **6**, 10 (1989).

[123] J. Rodríguez-Carvajal, Laboratoire Léon Brillouin (2001).

[124] L. McCusker, R. Von Dreele, D. Cox, D. Louër, and P. Scardi, Journal of Applied Crystallography **32**, 36 (1999).

[125] B. Toby (2019).

[126] R. Young, *The Rietveld Method*, IUCr monographs on crystallography (Oxford University Press, 1995), ISBN 9780198559122, URL https://books.google.co.in/books?id=k4EvAQAAIAAJ.

[127] B. H. Toby, Powder Diffraction **21**, 67–70 (2006).

[128] J. I. Goldstein, D. E. Newbury, J. R. Michael, N. W. Ritchie, J. H. J. Scott, and D. C. Joy, *Scanning electron microscopy and X-ray microanalysis* (springer, 2017).

[129] S. Blundell, *Magnetism in Condensed Matter*, Oxford Master Series in Condensed Matter Physics (OUP Oxford, 2001), ISBN 9780191586644, URL https://books.google.co.in/books?id=zP9QEAAAQBAJ.

[130] F. Kremer and A. Schönhals, *Broadband Dielectric Spectroscopy* (Springer Berlin Heidelberg, 2012), ISBN 9783642561207, URL https://books.google.co.in/books?id=z5LzCAAAQBAJ.

[131] A. K. Jonscher, Journal of Physics D: Applied Physics **32**, R57 (1999), URL https://dx.doi.org/10.1088/0022-3727/32/14/201.

[132] S. Miga, J. Dec, and W. Kleemann, Review of Scientific Instruments **78**, 033902 (2007), ISSN 0034-6748, URL https://doi.org/10.1063/1.2712792.

[133] Lake Shore Cryotronics, Inc., *Model 335 Temperature Controller User's Manual* (2019), URL https://www.lakeshore.com/docs/default-source/product-downloads/335_manual.pdf?sfvrsn=9f5c5b7f_7.

[134] Lake Shore Cryotronics, Inc., *Appendix C: Sensor Packaging and Installation*, URL https://www.lakeshore.com/docs/default-source/product-downloads/literature/lstc_appendixc_l.pdf?sfvrsn=9e24ceb1_4.

[135] Lake Shore Cryotronics, Inc., *Accessories - Coaxial Cable*, URL https://www.lakeshore.com/docs/default-source/product-downloads/catalog/lstc_cable_l.pdf?sfvrsn=d59fb2e3_5.

[136] S. Chakravarty, O. S. Fjellvåg, A. Bhattacharyya, L. Keller, and S. Nair, Physical Review B **107**, 134414 (2023), URL https://link.aps.org/doi/10.1103/PhysRevB.107.134414.

[137] L. Shlyk, S. Kryukov, V. Durairaj, S. Parkin, G. Cao, L. De Long, et al., Journal of Magnetism and Magnetic Materials **319** (2007), URL https://doi.org/10.1016/j.jmmm.2007.04.033.

[138] L. T. Nguyen and R. J. Cava, Chemical Reviews **121**, 2935 (2021), URL https://dx.doi.org/10.1021/acs.chemrev.0c00622.

[139] D. Ziat, A. A. Aczel, R. Sinclair, Q. Chen, H. D. Zhou, T. J. Williams, M. B. Stone, A. Verrier, and J. A. Quilliam, Physical Review B **95**, 184424 (2017), URL https://link.aps.org/doi/10.1103/PhysRevB.95.184424.

[140] Q. Chen, S. Fan, K. M. Taddei, M. B. Stone, A. I. Kolesnikov, J. Cheng, J. L. Musfeldt, H. Zhou, and A. A. Aczel, Journal of the American Chemical Society **141**, 9928 (2019), URL https://pubs.acs.org/doi/10.1021/jacs.9b03389.

[141] A. A. Aczel, P. J. Baker, D. E. Bugaris, J. Yeon, H. C. Zur Loye, T. Guidi, and D. T. Adroja, Physical Review Letters **112**, 117603 (2014), ISSN 10797114, 1401.1496, URL https://journals.aps.org/prl/abstract/10.1103/PhysRevLett.112.117603.

[142] W. Xia, Q. Zhou, H. Xu, L. Chen, and J. He, Physica B: Condensed Matter **403**, 2189 (2008), ISSN 09214526, URL https://www.sciencedirect.com/science/article/pii/S0921452607012835.

[143] R. Phatak, K. Krishnan, S. K. Sali, A. Das, and A. K. Nigam, Journal of Magnetism and Magnetic Materials **344**, 129 (2013), ISSN 03048853, URL https://www.sciencedirect.com/science/article/pii/S0304885313004058.

[144] J. P. Carlo, J. P. Clancy, K. Fritsch, C. A. Marjerrison, G. E. Granroth, J. E. Greedan, H. A. Dabkowska, and B. D. Gaulin, Physical Review B **88**, 024418 (2013), ISSN 10980121, URL https://journals.aps.org/prb/abstract/10.1103/PhysRevB.88.024418.

[145] K. Yoshii, N. Ikeda, and M. Mizumaki, physica status solidi (a) **203**, 2812 (2006), URL https://onlinelibrary.wiley.com/doi/abs/10.1002/pssa.200669549.

[146] I. Terasaki, T. Igarashi, T. Nagai, K. Tanabe, H. Taniguchi, T. Matsushita, N. Wada, A. Takata, T. Kida, M. Hagiwara, et al., Journal of the Physical Society of Japan **86** (2017), ISSN 13474073, URL https://journals.jps.jp/doi/10.7566/JPSJ.86.033702.

[147] M. DeMarco, H. A. Blackstead, J. D. Dow, M. K. Wu, D. Y. Chen, F. Z. Chien, M. Haka, S. Toorongian, and J. Fridmann, Physical Review B **62**, 14301 (2000), ISSN 01631829, URL https://journals.aps.org/prb/abstract/10.1103/PhysRevB.62.14301.

[148] H. D. Zhou, A. Kiswandhi, Y. Barlas, J. S. Brooks, T. Siegrist, G. Li, L. Balicas, J. G. Cheng, and F. Rivadulla, Phys. Rev. B **85**, 041201 (2012), URL https://link.aps.org/doi/10.1103/PhysRevB.85.041201.

[149] S. Kim and P. Battle, Journal of Solid State Chemistry **114**, 174 (1995), URL https://www.sciencedirect.com/science/article/pii/S0022459685710250.

[150] U. Hira, J. W. G. Bos, A. Missyul, F. Fauth, N. Pryds, and F. Sher, Inorganic Chemistry **60**, 17824 (2021), ISSN 1520510X, URL https://pubs.acs.org/doi/full/10.1021/acs.inorgchem.1c02442.

[151] O. C. Gagné and F. C. Hawthorne, IUCrJ **7**, 581 (2020), URL https://doi.org/10.1107/S2052252520005928.

[152] A. Santoro, I. Natali Sora, and Q. Huang, Journal of Solid State Chemistry **151**, 245 (2000), ISSN 0022-4596, URL https://www.sciencedirect.com/science/article/pii/S002245960098647X.

[153] P. Lightfoot and P. D. Battle, Journal of Solid State Chemistry **89**, 174 (1990), ISSN 0022-4596, URL https://www.sciencedirect.com/science/article/abs/pii/002245969090309L.

[154] P. Kayser, S. Injac, B. Ranjbar, B. J. Kennedy, M. Avdeev, and K. Yamaura, Inorganic Chemistry **56**, 9009 (2017), ISSN 1520510X, URL https://pubs.acs.org/doi/full/10.1021/acs.inorgchem.7b00983.

[155] M. Oku, Journal of Solid State Chemistry **23**, 177 (1978), URL https://www.sciencedirect.com/science/article/abs/pii/0022459678900634.

[156] Z. Hu, C. Mazumdar, G. Kaindl, F. De Groot, S. Warda, and D. Reinen, Chemical physics letters **297**, 321 (1998), URL https://www.sciencedirect.com/science/article/pii/S000926149801135X.

[157] N. Hollmann, Z. Hu, M. Valldor, A. Maignan, A. Tanaka, H. Hsieh, H.-J. Lin, C. Chen, and L. Tjeng, Physical Review B **80**, 085111 (2009), URL https://journals.aps.org/prb/abstract/10.1103/PhysRevB.80.085111.

[158] Z. Hu, H. Wu, M. Haverkort, H. Hsieh, H.-J. Lin, T. Lorenz, J. Baier, A. Reichl, I. Bonn, C. Felser, et al., Physical Review Letters **92**, 207402 (2004), URL https://journals.aps.org/prl/pdf/10.1103/PhysRevLett.92.207402.

[159] A. A. Belik, S. Iikubo, K. Kodama, N. Igawa, S.-i. Shamoto, S. Niitaka, M. Azuma, Y. Shimakawa, M. Takano, F. Izumi, et al., Chemistry of materials **18**, 798 (2006), URL https://pubs.acs.org/doi/10.1021/cm052334z.

[160] M. W. Haverkort, Z. Hu, J. C. Cezar, T. Burnus, H. Hartmann, M. Reuther, C. Zobel, T. Lorenz, A. Tanaka, N. B. Brookes, et al., Physical Review Letters **97**, 176405 (2006), URL https://journals.aps.org/prl/abstract/10.1103/PhysRevLett.97.176405.

[161] S. Tsubouchi, T. Kyomen, M. Itoh, P. Ganguly, M. Oguni, Y. Shimojo, Y. Morii, and Y. Ishii, Physical Review B **66**, 052418 (2002), URL https://journals.aps.org/prb/abstract/10.1103/PhysRevB.66.052418.

[162] C. Martin, A. Maignan, D. Pelloquin, N. Nguyen, and B. Raveau, Applied Physics Letters **71**, 1421 (1997), URL https://aip.scitation.org/doi/10.1063/1.119912.

[163] Z. Hu, H. Wu, T. Koethe, S. Barilo, S. Shiryaev, G. Bychkov, C. Schüßler-Langeheine, T. Lorenz, A. Tanaka, H. Hsieh, et al., New Journal of Physics **14**, 123025 (2012), URL https://iopscience.iop.org/article/10.1088/1367-2630/14/12/123025.

[164] W. Kobayashi, S. Ishiwata, I. Terasaki, M. Takano, I. Grigoraviciute, H. Yamauchi, and M. Karppinen, Physical Review B **72**, 104408 (2005), URL https://journals.aps.org/prb/abstract/10.1103/PhysRevB.72.104408.

[165] J.-M. Chen, Y.-Y. Chin, M. Valldor, Z. Hu, J.-M. Lee, S.-C. Haw, N. Hiraoka, H. Ishii, C.-W. Pao, K.-D. Tsuei, et al., Journal of the American Chemical Society **136**, 1514 (2014), URL https://pubs.acs.org/doi/10.1021/ja4114006.

[166] Y.-Y. Chin, H.-J. Lin, Z. Hu, C.-Y. Kuo, D. Mikhailova, J.-M. Lee, S.-C. Haw, S.-A. Chen, W. Schnelle, H. Ishii, et al., Scientific reports **7**, 1 (2017), URL https://www.nature.com/articles/s41598-017-03950-z.

[167] K. Binder and A. P. Young, Reviews of Modern Physics **58**, 801 (1986), ISSN 00346861, URL https://link.aps.org/doi/10.1103/RevModPhys.58.801.

[168] M. Giot, A. Pautrat, G. André, D. Saurel, M. Hervieu, and J. Rodriguez-Carvajal, Physical Review B **77**, 134445 (2008), ISSN 10980121, URL https://journals.aps.org/prb/abstract/10.1103/PhysRevB.77.134445.

[169] S. Nair and A. K. Nigam, Physical Review B **75** (2007), ISSN 10980121, URL https://journals.aps.org/prb/pdf/10.1103/PhysRevB.75.214415.

[170] D. A. Pejaković, J. L. Manson, J. S. Miller, and A. J. Epstein, Physical Review Letters **85**, 1994 (2000), ISSN 10797114, URL https://journals.aps.org/prl/abstract/10.1103/PhysRevLett.85.1994.

[171] M. Koyano, M. Suezawa, H. Watanabe, and M. Inoue, Journal of the Physical Society of Japan **63**, 1114 (2013), ISSN 13474073, URL https://journals.jps.jp/doi/abs/10.1143/JPSJ.63.1114.

[172] S. Mukherjee, R. Ranganathan, P. Anilkumar, and P. Joy, Physical Review B **54**, 9267 (1996), ISSN 1550235X, URL https://journals.aps.org/prb/abstract/10.1103/PhysRevB.54.9267.

[173] W. Luo, S. R. Nagel, T. F. Rosenbaum, and R. E. Rosensweig, Physical Review Letters **67**, 2721 (1991), ISSN 00319007, URL https://journals.aps.org/prl/pdf/10.1103/PhysRevLett.67.2721.

[174] S. Middey, S. Ray, K. Mukherjee, P. L. Paulose, E. V. Sampathkumaran, C. Meneghini, S. D. Kaushik, V. Siruguri, K. Kovnir, and D. D. Sarma, Physical Review B **83**, 144419 (2011), ISSN 10980121, URL https://journals.aps.org/prb/abstract/10.1103/PhysRevB.83.144419.

[175] R. S. Freitas, L. Ghivelder, F. Damay, F. Dias, and L. F. Cohen, Physical Review B **64**, 1444041 (2001), ISSN 01631829, URL https://journals.aps.org/prb/abstract/10.1103/PhysRevB.64.144404.

[176] P. M. Shand, A. L. Meyer, M. Streicher, A. Wilson, T. Rash, M. W. Roth, T. E. Kidd, and L. H. Strauss, Physical Review B **85**, 144432 (2012), ISSN 10980121, URL https://journals.aps.org/prb/abstract/10.1103/PhysRevB.85.144432.

[177] J. A. Mydosh, *Spin glasses : an experimental introduction* (Taylor and Francis, 1993), ISBN 0748400389, URL https://books.google.co.in/books/about/Spin_Glasses.html?id=lRpmQgAACAAJ.

[178] J. Lago, I. Živković, J. O. Piatek, P. Álvarez, D. Hüvonen, F. L. Pratt, M. Díaz, and T. Rojo, Physical Review B **89**, 024421 (2014), ISSN 10980121, URL https://journals.aps.org/prb/abstract/10.1103/PhysRevB.89.024421.

[179] N. Marcano, J. C. Gómez Sal, J. I. Espeso, L. Fernández Barquín, and C. Paulsen, Physical Review B **76**, 224419 (2007), ISSN 10980121, URL https://journals.aps.org/prb/abstract/10.1103/PhysRevB.76.224419.

[180] S. Harikrishnan, C. M. Naveen Kumar, H. L. Bhat, S. Elizabeth, U. K. Rößler, K. Dörr, S. Rößler, and S. Wirth, Journal of Physics: Condensed Matter **20**, 275234 (2008), ISSN 0953-8984, URL https://iopscience.iop.org/article/10.1088/0953-8984/20/27/275234.

[181] W. F. Brown, Phys. Rev. **130**, 1677 (1963), URL https://link.aps.org/doi/10.1103/PhysRev.130.1677.

[182] R. Balian, R. Maynard, and G. Toulouse, *ILL-condensed Matter*, ECOLE D'ETE DE PHYSIQUE THEORETIQUE LES HOUCHES//PROCEEDINGS (North-Holland Publishing Company, 1979), ISBN 9789971950590, URL https://books.google.co.in/books?id=J4Q9oElF9h8C.

[183] S. Shtrikman and E. Wohlfarth, Physics Letters A **85**, 467 (1981).

[184] J. Souletie and J. Tholence, Physical Review B **32**, 516 (1985).

[185] T. Chakrabarty, A. V. Mahajan, and S. Kundu, Journal of Physics: Condensed Matter **26**, 405601 (2014), URL https://iopscience.iop.org/article/10.1088/0953-8984/26/40/405601.

[186] M. K. Warshi, A. Kumar, A. Sati, S. Thota, K. Mukherjee, A. Sagdeo, and P. R. Sagdeo, Chemistry of Materials **32**, 1250 (2020), URL https://pubs.acs.org/doi/full/10.1021/acs.chemmater.9b04703.

[187] J. Alonso, M. L. Fdez-Gubieda, J. M. Barandiarán, A. Svalov, L. Fernández Barquín, D. Alba Venero, and I. Orue, Physical Review B **82**, 054406 (2010), URL https://link.aps.org/doi/10.1103/PhysRevB.82.054406.

[188] R. Mathieu, P. Jönsson, D. N. Nam, and P. Nordblad, Physical Review B **63** (2001), ISSN 1550235X, URL https://journals.aps.org/prb/pdf/10.1103/PhysRevB.63.092401.

[189] J. Kumar, S. N. Panja, S. Dengre, and S. Nair, Physical Review B **95**, 54401 (2017), ISSN 24699969, URL https://journals.aps.org/prb/pdf/10.1103/PhysRevB.95.054401.

[190] C. Garg, A. Cervellino, and S. Nair, Journal of Physics: Condensed Matter **34**, 285602 (2022), ISSN 0953-8984, URL https://iopscience.iop.org/article/10.1088/1361-648X/ac6923.

[191] L. Lundgren, P. Svedlindh, and O. Beckman, Physical Review B **26**, 3990 (1982), ISSN 01631829, URL https://link.aps.org/doi/10.1103/PhysRevB.26.3990.

[192] G. Parisi, Phys. Rev. Lett. **50**, 1946 (1983), URL https://link.aps.org/doi/10.1103/PhysRevLett.50.1946.

[193] D. Sherrington and S. Kirkpatrick, Phys. Rev. Lett. **35**, 1792 (1975), URL https://link.aps.org/doi/10.1103/PhysRevLett.35.1792.

[194] J.-P. Bouchaud, V. Dupuis, J. Hammann, and E. Vincent, Physical review B **65**, 024439 (2001).

[195] E. Vincent, F. Bert, J.-P. Bouchaud, V. Dupuis, J. Hammann, D. Hérisson, F. Ladieu, M. Ocio, and D. Parker, Lecture Notes in Physics **716**, 7 (2007), ISSN 00758450, URL https://link.springer.com/chapter/10.1007/3-540-69684-9_2.

[196] I. S. Suzuki and M. Suzuki, Physical Review B **78** (2008), ISSN 10980121, URL https://journals.aps.org/prb/pdf/10.1103/PhysRevB.78.214404.

[197] L. Lundgren, P. Svedlindh, P. Nordblad, and O. Beckman, Physical Review Letters **51**, 911 (1983), ISSN 00319007, URL https://journals.aps.org/prl/pdf/10.1103/PhysRevLett.51.911.

[198] Y. G. Joh, R. Orbach, G. G. Wood, J. Hammann, and E. Vincent, Physical Review Letters **82**, 438 (1999), ISSN 10797114, URL https://journals.aps.org/prl/pdf/10.1103/PhysRevLett.82.438.

[199] E. Vincent, J. Bouchaud, D. Dean, and J. Hammann, Physical Review B **52**, 1050 (1995), ISSN 01631829, URL https://link.aps.org/doi/10.1103/PhysRevB.52.1050.

[200] G. Kotliar and H. Sompolinsky, Physical Review Letters **53**, 1751 (1984), ISSN 00319007, URL https://journals.aps.org/prl/abstract/10.1103/PhysRevLett.53.1751.

[201] J. R. L. de Almeida and D. J. Thouless, Journal of Physics A: Mathematical and General **11**, 983 (1978), ISSN 0305-4470, URL http://stacks.iop.org/0305-4470/11/i=5/a=028?key=crossref.c94e59ef7ba0b393e3ee582dcdd0c876.

[202] M. Gabay and G. Toulouse, Physical Review Letters **47**, 201 (1981), URL https://link.aps.org/doi/10.1103/PhysRevLett.47.201.

[203] A. Le Bail, H. Duroy, and J. L. Fourquet, Materials Research Bulletin **23**, 447 (1988).

[204] A. Wills, Physica B: Condensed Matter **276**, 680 (2000), URL https://www.sciencedirect.com/science/article/pii/S0921452699017226.

[205] A. Wills, in *Eleventh European Powder Diffraction Conference: Warsaw, September 19-22, 2008* (Walter de Gruyter GmbH & Co KG, 2015), vol. 30, pp. 39–44, URL https://www.degruyter.com/document/doi/10.1524/9783486992588-011/html?lang=en.

[206] T. Saha-Dasgupta and D. Sarma, Physical Review B **64**, 064408 (2001), URL https://journals.aps.org/prb/abstract/10.1103/PhysRevB.64.064408.

[207] A. Nag, S. Middey, S. Bhowal, S. K. Panda, R. Mathieu, J. C. Orain, F. Bert, P. Mendels, P. G. Freeman, M. Mansson, et al., Physical Review Letters **116**, 097205 (2016), ISSN 10797114, URL https://journals.aps.org/prl/abstract/10.1103/PhysRevLett.116.097205.

[208] H. D. Zhou, E. S. Choi, G. Li, L. Balicas, C. R. Wiebe, Y. Qiu, J. R. Copley, and J. S. Gardner, Physical Review Letters **106**, 147204 (2011), ISSN 00319007, URL https://journals.aps.org/prl/abstract/10.1103/PhysRevLett.106.147204.

[209] A. Banerjee, R. Rawat, K. Mukherjee, and P. Chaddah, Physical Review B **79**, 212403 (2009), ISSN 10980121, URL https://link.aps.org/doi/10.1103/PhysRevB.79.

212403.

[210] V. Hardy, A. Maignan, S. Hébert, and C. Martin, Physical Review B **67** (2003), ISSN 0163-1829, URL https://journals.aps.org/prb/pdf/10.1103/PhysRevB.67.024401.

[211] W. Prellier, V. Smolyaninova, A. Biswas, C. Galley, R. Greene, W. Prellier, K. Ramesha, and J. Gopalakrishnan, Journal of Physics: Condensed Matter **12**, 965 (2000), ISSN 02729172, URL https://iopscience.iop.org/article/10.1088/0953-8984/12/6/318/pdf.

[212] C. Garg, D. Roy, M. Lonsky, P. Manuel, A. Cervellino, J. Müller, M. Kabir, and S. Nair, Physical Review B **103**, 014437 (2021), URL https://journals.aps.org/prb/abstract/10.1103/PhysRevB.103.014437.

[213] N. F. Mott, Philosophical Magazine **19**, 835 (1969), ISSN 00318086, URL http://www.tandfonline.com/doi/abs/10.1080/14786436908216338.

[214] P. M. Woodward, J. Goldberger, M. W. Stoltzfus, H. W. Eng, R. A. Ricciardo, P. N. Santhosh, P. Karen, and A. R. Moodenbaugh, Journal of the American Ceramic Society **91**, 1796 (2008), ISSN 1551-2916, URL https://onlinelibrary.wiley.com/doi/full/10.1111/j.1551-2916.2008.02412.x.

[215] S. Savitha Pillai, S. Narayana Jammalamadaka, and P. N. Santhosh, IEEE Transactions on Magnetics **43**, 3076 (2007), ISSN 00189464, URL https://ieeexplore.ieee.org/abstract/document/4202879/.

[216] K. Naveen, M. Reehuis, P. Adler, P. Pattison, A. Hoser, T. K. Mandal, U. Arjun, P. K. Mukharjee, R. Nath, C. Felser, et al., Physical Review B **98**, 224423 (2018), ISSN 24699969, URL https://journals.aps.org/prb/pdf/10.1103/PhysRevB.98.224423.

[217] S. Kumar, S. K. Panda, M. M. Patidar, S. K. Ojha, P. Mandal, G. Das, J. W. Freeland, V. Ganesan, P. J. Baker, and S. Middey, Physical Review B **103**, 184405 (2021), ISSN 24699969, URL https://journals.aps.org/prb/abstract/10.1103/PhysRevB.103.184405.

[218] S. Chakravarty and S. Nair, Journal of Applied Physics **135**, 104103 (2024), ISSN 0021-8979, URL https://doi.org/10.1063/5.0182471.

[219] S. Ikeda, H. Kominami, K. Koyama, and Y. Wada, Journal of applied physics **62**, 3339 (1987), URL https://doi.org/10.1063/1.339294.

[220] M. Fujimoto, *The Physics of Structural Phase Transitions* (Springer New York, 2005), ISBN 9780387268330, URL https://books.google.co.in/books?id=uCOYhbqNKH4C.

[221] S. Miga, J. Dec, and K. Ćwikiel, Phase Transitions **80**, 95 (2007), URL https://doi.org/10.1080/01411590601096010.

[222] S. Miga, J. Dec, A. Molak, and M. Koralewski, Journal of Applied Physics **99** (2006), URL https://doi.org/10.1063/1.2206267.

[223] S. Miga, J. Dec, and W. Kleemann, in *Ferroelectrics*, edited by M. Lallart (IntechOpen, Rijeka, 2011), chap. 10, URL https://doi.org/10.5772/20380.

[224] R. Pirc and R. Blinc, Phys. Rev. B **60**, 13470 (1999), URL https://link.aps.org/doi/10.1103/PhysRevB.60.13470.

[225] R. Pirc, B. Tadić, and R. Blinc, Physica B: Condensed Matter **193**, 109 (1994), URL https://doi.org/10.1016/0921-4526(94)90001-9.

[226] K. Binder and J. Reger, Advances in Physics **41**, 547 (1992), URL https://doi.org/10.1080/00018739200101553.

[227] J. Hemberger, P. Lunkenheimer, R. Viana, R. Böhmer, and A. Loidl, Phys. Rev. B **52**, 13159 (1995), URL https://link.aps.org/doi/10.1103/PhysRevB.52.13159.

[228] M. Iwata, H. Orihara, and Y. Ishibashi, Journal of the Physical Society of Japan **67**, 3130 (1998), URL https://doi.org/10.1143/JPSJ.67.3130.

[229] J. Dec, S. Miga, W. Kleemann, and B. Dkhil, Ferroelectrics **363**, 141 (2008), URL https://doi.org/10.1080/00150190802025947.

[230] V. Bobnar, Z. Kutnjak, and A. Levstik, Journal of the European Ceramic Society **21**, 1319 (2001), URL https://doi.org/10.1016/S0955-2219(01)00009-7.

[231] W. Kleemann, S. Miga, Z. Xu, S. Lu, and J. Dec, Applied Physics Letters **104** (2014), URL https://doi.org/10.1063/1.4875595.

[232] W. Kleemann, S. Miga, J. Dec, and J. Zhai, Applied Physics Letters **102** (2013), URL https://doi.org/10.1063/1.4811089.

[233] J. Dec, W. Kleemann, S. Miga, C. Filipic, A. Levstik, R. Pirc, T. Granzow, and R. Pankrath, Phys. Rev. B **68**, 092105 (2003), URL https://link.aps.org/doi/10.1103/PhysRevB.68.092105.

[234] J. T. Rijssenbeek, S. Malo, V. Caignaert, and K. R. Poeppelmeier, Journal of the American Chemical Society **124**, 2090 (2002), URL https://doi.org/10.1021/ja017586p.

[235] K. Kuramoto, Journal of the Physical Society of Japan **56**, 1859 (1987), URL https://doi.org/10.1143/JPSJ.56.1859.

[236] C. Bottcher, *Theory of electric polarization* (Elsevier, Amsterdam, London, New York, 1973).

[237] M. Jia, X. Cheng, M.-H. Whangbo, M. Hong, and S. Deng, RSC Advances **10**, 26479 (2020), URL https://doi.org/10.1039/D0RA03136D.

[238] S. Arrhenius, Z. Phys. Chem. **4**, 226 (1889).

[239] H. Vogel, Phys. Z. **22**, 645 (1921).

[240] P. Sahlot, S. Pandey, A. Pandey, and A. Awasthi, Journal of Applied Physics **127** (2020), URL https://pubs.aip.org/aip/jap/article/127/15/154103/156846.

[241] M. Ahmadipour, M. F. Ain, and Z. A. Ahmad, Nano-Micro Letters **8**, 291 (2016).

[242] A. A. Belik, D. D. Khalyavin, Y. Matsushita, and K. Yamaura, Inorganic Chemistry **61**, 14428 (2022).

[243] Y. Shimoda, Y. Doi, M. Wakeshima, and Y. Hinatsu, Journal of Solid State Chemistry **183**, 1962 (2010).

[244] Y. Shimoda, Y. Doi, Y. Hinatsu, and K. Ohoyama, Chemistry of Materials **20**, 4512 (2008).

[245] Y. Shimoda, Y. Doi, M. Wakeshima, and Y. Hinatsu, Inorganic chemistry **48**, 9952 (2009).

[246] Y. Li, A. A. Tsirlin, T. Dey, P. Gegenwart, R. Valentí, and S. M. Winter, Phys. Rev. B **102**, 235142 (2020), URL https://link.aps.org/doi/10.1103/PhysRevB.102.235142.

[247] B. Yuan, B. H. Kim, Q. Chen, D. Dobrowolski, M. Azmanska, G. Luke, S. Fan, V. Bisogni, J. Pelliciari, and J. Clancy, arXiv preprint arXiv:2405.09418 (2024).

[248] T. Basu, F. Y. Wei, Q. Zhang, Y. Fang, and X. Ke, Phys. Rev. Mater. **4**, 114401 (2020), URL https://link.aps.org/doi/10.1103/PhysRevMaterials.4.114401.

[249] Y. Klein, G. Rousse, F. Damay, F. Porcher, G. André, and I. Terasaki, Phys. Rev. B **84**, 054439 (2011), URL https://link.aps.org/doi/10.1103/PhysRevB.84.054439.

[250] G. Cao, H. Zheng, H. Zhao, Y. Ni, C. A. Pocs, Y. Zhang, F. Ye, C. Hoffmann, X. Wang, M. Lee, et al., npj Quantum Materials **5**, 26 (2020), ISSN 2397-4648, URL https://doi.org/10.1038/s41535-020-0232-6.

[251] P. Battle, S. Kim, and A. Powell, Journal of Solid State Chemistry **101**, 161 (1992), ISSN 0022-4596, URL https://www.sciencedirect.com/science/article/pii/002245969290212E.

[252] I.-S. Kim, T. Nakamura, and M. Itoh, Bulletin of the Chemical Society of Japan **71**, 2247 (1998), URL https://doi.org/10.1246/bcsj.71.2247.

[253] K. E. Stitzer, W. R. Gemmill, M. D. Smith, and H.-C. zur Loye, Journal of Solid State Chemistry **175**, 39 (2003), ISSN 0022-4596, special Issue on Metal Oxides - From Proceedings of the ACS Symposium on Metal Oxides, URL https://www.sciencedirect.com/science/article/pii/S0022459603001129.

[254] R. D. Shannon, Acta Crystallographica Section A **32**, 751 (1976), URL https://doi.org/10.1107/S0567739476001551.

[255] K. E. Stitzer, M. D. Smith, W. R. Gemmill, and H.-C. zur Loye, Journal of the American Chemical Society **124**, 13877 (2002), ISSN 0002-7863, URL https://doi.org/10.1021/ja0271781.

[256] W. Opechowski, Magnetism (1965).

[257] A. Shubnikov and N. Belov, *Colored Symmetry* (Macmillan, 1964), URL https://books.google.co.in/books?id=QKk9AAAAIAAJ.

[258] R. Lifshitz, in *Encyclopedia of Condensed Matter Physics (Second Edition)*, edited by T. Chakraborty (Academic Press, Oxford, 2024), pp. 1–10, second edition ed., ISBN 978-0-323-91408-6, URL https://www.sciencedirect.com/science/article/pii/B9780323908009000822.

[259] Y. Tang, R. P. Sena, M. Avdeev, P. D. Battle, J. Cadogan, J. Hadermann, and E. C. Hunter, Journal of Solid State Chemistry **253**, 347 (2017), URL https://www.sciencedirect.com/science/article/pii/S0022459617302396#bib16.

[260] S. Ivanov, S.-G. Eriksson, J. Erikssen, R. Tellgren, and H. Rundlof, Materials research bulletin **39**, 615 (2004), URL https://www.sciencedirect.com/science/article/pii/S0025540803003702.

[261] D. Akahoshi, Y. Okimoto, M. Kubota, R. Kumai, T. Arima, Y. Tomioka, and Y. Tokura, Physical Review B—Condensed Matter and Materials Physics **70**, 064418 (2004), URL https://journals.aps.org/prb/pdf/10.1103/PhysRevB.70.064418#page=5.60.

[262] S. Ivanov, P. Nordblad, R. Mathieu, R. Tellgren, and C. Ritter, Dalton Transactions **39**, 5490 (2010), URL https://pubs.rsc.org/en/content/articlehtml/2010/dt/b927498g.

[263] M. S. Senn, S. A. Kimber, A. M. Arevalo Lopez, A. H. Hill, and J. P. Attfield, Physical Review B—Condensed Matter and Materials Physics **87**, 134402 (2013), URL https://journals.aps.org/prb/pdf/10.1103/PhysRevB.87.134402.

[264] A. Taroni, S. T. Bramwell, and P. C. Holdsworth, Journal of Physics: Condensed Matter **20**, 275233 (2008).

[265] H. N. Bordallo, L. Chapon, J. L. Manson, J. Hernández-Velasco, D. Ravot, W. M. Reiff, and D. N. Argyriou, Phys. Rev. B **69**, 224405 (2004), URL https://link.aps.org/doi/10.1103/PhysRevB.69.224405.

[266] H. Takatsu, H. Yoshizawa, S. Yonezawa, and Y. Maeno, Physical Review B—Condensed Matter and Materials Physics **79**, 104424 (2009).

[267] K. Yamada, M. Matsuda, Y. Endoh, B. Keimer, R. J. Birgeneau, S. Onodera, J. Mizusaki, T. Matsuura, and G. Shirane, Phys. Rev. B **39**, 2336 (1989), URL https://link.aps.org/doi/10.1103/PhysRevB.39.2336.

[268] T. Igarashi, R. Okazaki, H. Taniguchi, Y. Yasui, and I. Terasaki, Journal of the Physical Society of Japan **84**, 094601 (2015), https://doi.org/10.7566/JPSJ.84.094601, URL https://doi.org/10.7566/JPSJ.84.094601.

[269] G. Radtke, A. Saúl, Y. Klein, and G. Rousse, Phys. Rev. B **87**, 054436 (2013), URL https://link.aps.org/doi/10.1103/PhysRevB.87.054436.

[270] G. D'Angelo, G. Carini, C. Crupi, M. Koza, G. Tripodo, and C. Vasi, Phys. Rev. B **79**, 014206 (2009), URL https://link.aps.org/doi/10.1103/PhysRevB.79.014206.

[271] R. Berman, *Thermal Conduction in Solids*, Oxford studies in physics (Clarendon Press, 1976), ISBN 9780198514299, URL https://books.google.co.in/books?id=rUh5AAAAIAAJ.

[272] A. L. Éfros and B. I. Shklovskii, Journal of Physics C: Solid State Physics **8**, L49 (1975).

[273] B. Shklovskiĭ and A. Ėfros, *Electronic Properties of Doped Semiconductors*, Solid-State Sciences Series (Springer-Verlag, 1984), ISBN 9783540129950, URL https://books.google.co.in/books?id=o8PvAAAAMAAJ.

[274] B. I. Shklovskii, *Half century of Efros-Shklovskii Coulomb gap. Romance with Coulomb interaction and disorder* (2024), 2403.19793, URL https://arxiv.org/abs/2403.19793.

[275] B. Fisher, J. Genossar, K. B. Chashka, A. Knizhnik, L. Patlagan, and G. M. Reisner, Journal of Applied Physics **104**, 033716 (2008), ISSN 0021-8979, URL https://doi.org/10.1063/1.2967820.

[276] J. Massey and M. Lee, Physical Review Letters **75**, 4266 (1995).

[277] M. Pollak, Journal of Non-Crystalline Solids **11**, 1 (1972).

[278] M. Pollak, Journal of Non-Crystalline Solids **35**, 83 (1980).

[279] J. Davies, P. Lee, and T. Rice, Physical Review B **29**, 4260 (1984).

[280] R. Rosenbaum, Phys. Rev. B **44**, 3599 (1991), URL https://link.aps.org/doi/10.1103/PhysRevB.44.3599.

[281] J. Rodríguez-Carvajal, *Tutorial on magnetic structure determination and refinement using neutron powder diffraction and fullprof* (2014), URL https://neutrons2.ornl.gov/conf/2014/magstr/docs/Tutorial_Magnetic_Structures.pdf.

[282] J. Rodríguez-Carvajal (????), URL https://workshops.ill.fr/event/332/attachments/243/1035/Magnetic_structure_determination_refinement-FullProf.pdf#page=4.53.

[283] J. Rodríguez-Carvajal, Physica B: Condensed Matter **192**, 55 (1993), URL https://www.sciencedirect.com/science/article/abs/pii/092145269390108I.

[284] J. Rodríquez-Carvajal, in *Materials Science Forum* (Transtec Publications; 1999, 2001), vol. 378, pp. 268–273, URL https://www.scientific.net/MSF.378-381.268.

[285] P. L. Bernardo and H. S. de Amorim, Handbook of Materials Characterization pp. 1–35 (2018), URL https://link.springer.com/chapter/10.1007/978-3-319-92955-2_1.

[286] E. F. Bertaut, J. Appl. Phys. **33**, 1138 (1962).

[287] Y. A. Izyumov, V. E. Naish, and R. P. Ozerov, *Neutron Diffraction of Magnetic Materials* (Consultants Bureau, New York, 1991).

[288] A. P. Cracknell, *Magnetism in Crystalline Materials* (Pergamon Press, Oxford, 1975).

[289] A. S. Wills, J. de Physique (2001), in press.

[290] A. S. Wills, Phys. Rev. B **63**, 064430 (2001).

[291] O. V. Kovalev, *Representations of the Crystallographic Space Groups* (Gordon and Breach Science Publishers, Switzerland, 1993), 2nd ed.

[292] D. Balzar and N. C. Popa, Rigaku J **22**, 16 (2005), URL https://mysite.du.edu/~balzar/Rigaku-2005.pdf.

[293] G. Caglioti, A. Paoletti, and F. Ricci, Nuclear Instruments **3**, 223 (1958), URL https://www.sciencedirect.com/science/article/abs/pii/0369643X5890029X.

[294] L. Finger, Journal of Applied Crystallography **31**, 111 (1998).

[295] G. S. Pawley, Journal of Applied Crystallography **14**, 357 (1981).

[296] H. Toraya, Journal of Applied Crystallography **19**, 440 (1986).

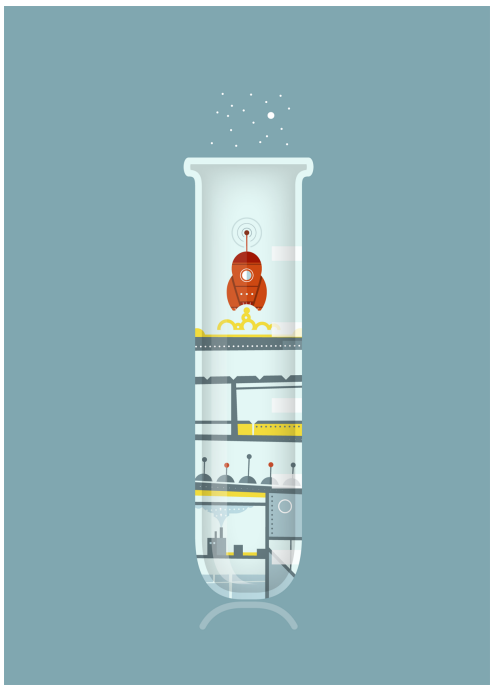
[297] F. Gozzo, L. De Caro, C. Giannini, A. Guagliardi, B. Schmitt, and A. Prodi, Journal of applied crystallography **39**, 347 (2006), URL https://journals.iucr.org/j/issues/2006/03/00/hx5036/index.html.

[298] G. Courbion and G. Ferey, Journal of Solid State Chemistry **76**, 426 (1988), URL https://www.sciencedirect.com/science/article/abs/pii/0022459688902393.

[299] P. Thompson, D. Cox, and J. Hastings, Journal of Applied Crystallography **20**, 79 (1987).

[300] J. Rodriguez-Carvajal, M. Fernandez-Diaz, and J. Martinez, Journal of Physics: Condensed Matter **3**, 3215 (1991).

[301] P. Thompson, J. Reilly, and J. Hastings, Journal of the Less Common Metals **129**, 105 (1987).



This thesis was typeset using LaTeX, originally developed by Leslie Lamport and based on Donald Knuth's TeX. The body text is set in 11 point Egenolff-Berner Garamond, a revival of Claude Garamont's humanist typeface. The above illustration, *Science Experiment 02*, was created by Ben Schlitter and released under CC BY-NC-ND 3.0. A template that can be used to format a PhD dissertation with this look & feel has been released under the permissive AGPL license, and can be found online at github.com/suchow/Dissertate or from its lead author, Jordan Suchow, at suchow@post.harvard.edu.